MORPHOLOGICAL STUDIES IN POLYMER-FULLERENE BLENDS

A Dissertation
Presented to
The Academic Faculty

by

Nabankur Deb

In Partial Fulfillment
of the Requirements for the Degree of
Doctor of Philosophy in the
School of Materials Science and Engineering

Georgia Institute of Technology
December, 2015

MORPHOLOGICAL STUDIES IN POLYMER-FULLERENE BLENDS

Approved by:

Dr. David G. Bucknall, Advisor
School of Materials Science and Engineering
Georgia Institute of Technology

Dr. Seth R. Marder
School of Chemistry and Biochemistry
Georgia Institute of Technology

Dr. Elsa Reichmanis
School of Chemical and Biochemical Engineering
Georgia Institute of Technology

Dr. John R. Reynolds
School of Materials Science and Engineering
Georgia Institute of Technology

Dr. Zhiqun Lin
School of Materials Science and Engineering
Georgia Institute of Technology

Date Approved: 10/28/15

To my family

ACKNOWLEDGEMENTS

I would first like to acknowledge Prof. David Bucknall for his guidance throughout these five years of graduate school, not only for his mentoring and scientific input, but also promoting constant creative as well as critical thinking. I have learnt immensely more than I expected during my tenure here at Georgia Tech and for this I am very grateful to him. From his encouragement towards writing research proposals right from my inception in the group, to the opportunity to present the research at numerous conferences, Dr. Bucknall has truly helped cultivate a strong scientific understanding combined with overall development as a researcher. I would also like to thank my thesis committee members Prof. Seth Marder, Prof. John Reynolds, Prof. Elsa Reichmanis and Prof. Zhiqun Lin for their scientific guidance and input as well as opportunities. Most of this work would not have been possible, if not for the countless contributions from collaborators from all over the place and a number of different disciplines.

Firstly, I'd like to thank Dr. Gabriel Bernardo at the University of Minho who provided an excellent repository of knowledge in the field of organic electronics to help me acclimatize into this field as a new graduate student. Also, a special thanks to Dr. Alamgir Kamir and Dr. Xiong Gong at the University of Akron and Dr. Bobby Sumpter at ORNL for their contributions and important feedback for our collaborative Department of Energy funded project.

I would like to thank Dr. Maximilian Skoda and Dr. Sarah Rogers at ISIS, UK and Candice Halbert at ORNL for their help and thoughtful comments regarding the neutron reflectivity, SANS and GISANS experiments.

Also, many thanks to Dr. Chris Tassone and Dr. Chad Miller and the SSRL, Stanford for their help with the GIWAXS experiments and Dr. An-Ting Chien for always being available and providing ready assistance for the use of the in-house WAXS systems.

TABLE OF CONTENTS

LIST OF TABLES

LIST OF FIGURES

LIST OF SYMBOLS AND ABBREVIATIONS

AFM	Atomic force microscopy
ann	Annealed
BHJ	Bulk Heterojunction
Bis-$PC_{60}BM$/bis-PCBM	Bis(1-[3-(methoxycarbonyl)propyl]-1-phenyl)-[6,6]C62
CB	Chlorobenzene
CT	Charge Transfer
CV	Cyclic voltammetry
DAB/DB	Debye-Anderson-Brumberger/Debye Bueche
DCM	Dichloromethane
DFT	Density functional theory
DSC	Differential scanning calorimetry
FF	Fill factor
GISANS	Grazing incidence small angle neutron scattering
GISAXS	Grazing incidence small angle X-ray scattering
GIWAXS	Grazing incidence wide angle X-ray scattering
HOMO	Highest occupied molecular orbital
HPLC	High performance liquid chromatography
ITO	Indium Tin oxide
J_{sc}	Short circuit current
LUMO	Lowest unoccupied molecular orbital
NMR	Nuclear magnetic resonance
NR	Neutron reflectivity

o-DCB	Ortho-dichlorobenzene
OFET	Organic field effect transistor
OPV	Organic Photovoltaic
P3AT	Poly(3-alkylthiophene)
P3BT	Poly(3-butylthiophene)
P3HT	Poly(3-hexylthiophene)
P3OT	Poly(3-octylthiophene)
$PC_{60}BM$/PCBM	[6,6]-phenyl-C61-butyric acid methyl ester
PCE	Power conversion efficiency
PEDOT: PSS	Poly(3,4ethylenedioxythiophene):poly(styrenesulfonate)
SANS	Small angle neutron scattering
SAXS	Small angle X-ray scattering
SCLC	Space charge limited current
SLD	Scattering length density
unann	Unannealed
V_{oc}	Open circuit voltage
WAXS	Wide angle X-ray scattering
XPS	X-ray photoelectron spectroscopy
W	Electronic bandwidth
h	Period in Heisenberg's uncertainty principle
η_{EQE}	External quantum efficiency
η_{IQE}	Internal quantum efficiency
η	Device efficiency/Power conversion efficiency
P	Radiated power

q	Particle charge
a	Particle acceleration
v	Particle velocity
c	Speed of light
ε_o	Permittivity of vacuum
ε_r	Relative permittivity of material
r	Radius of a particle
λ	Wavelength
d_{hkl}	d-spacing
ψ_i	Incident wave
ψ_s	Scattered wave
b	Nuclear or electron scattering length
ρ	Scattering length density
V	Volume
q/q_{hkl}	Scattering vector
τ	Mean size of crystal domain
K	Crystal shape factor
θ	Scattering/diffraction angle
Φ	Azimuthal angle
f_H	Herman's orientation factor
n	Refractive index
$P(q)$	Form factor
$S(q)$	Shape factor
θ_c	Critical angle

μ_e	Electron mobility
μ_h	Hole mobility
L	Layer thickness
Φ_i	Volume fraction of component i
ξ	Correlation length - DAB model
C_{DB}	Scale factor – DAB model
D_m	Fractal dimension
γ	Surface energy
δ	Solubility parameter
$\Delta\rho^2$	SLD contrast factor
r	Hard sphere radius
m	Porod constant

SUMMARY

The advent of organic semiconductor materials has opened up the possibility of expanding the area of solar technology to more easily processable and cost-effective techniques. However, for solar technology based on organic photovoltaics to be ubiquitous and commercially viable, improvements are required to enhance the device efficiencies. Currently the best performing solar cells exploiting a bulk heterojunction (BHJ) architecture have efficiencies in the range of 10%. [1]

These are significantly less efficient than their inorganic counterparts and also have the drawback of having lower long term stability owing to the environmental degradation. Thus in order to improve the device efficiency, fundamental studies need to be conducted into the parameters which control the performance of these devices. These include opto-electronic properties of the materials, thin film morphology and the device architecture. While synthesizing new materials with desirable electronic properties is essential for improving device performances, it is equally important to understand the complex phase morphology in these systems and their effect on the device performance. Consequently, understanding of the morphology could then be used to design new materials and device architectures to help improve the device efficiency as well as its long term stability. In particular, this thesis focuses primarily on the morphology in series of model polyalkylthiophene-fullerene blend systems both in bulk and thin films and how this relates to the device performance. These studies utilized various advanced characterization techniques, the results of which have been exploited to demonstrate a possible approach for controlling the morphology development.

This thesis is divided into 6 main chapters, the first of which is a literature survey summarizing prior work in OPV development and in particular aspects of morphology and its

relationship to the device performance. The following chapter (Chapter 2) outlines the experimental methodologies undertaken for the thesis studies and their background. The next chapter (Chapter 3) details the studies undertaken on the miscibility of a modified fullerene PCBM in various amorphous polymers in bulk drop cast films. The miscibility of fullerenes in polymers is a significant property determining the phase morphology development in the eventual polymer-fullerene blend systems or bulk heterojunction thin films. Thus, in this segment the miscibility of the PCBM is first measured in a series of polystyrene based polymers with varying aromaticity on the side chain. The use of differential scanning calorimetry is applied in determining the miscibility level which is seen to be correlated to the level of aromaticity. Following this, small angle neutron scattering is used to determine the phase behavior of these systems going from the miscible to immiscible state. Few standard shape independent models are seen to appropriately describe the phase morphology in these systems and give estimates of phase dimensions and compositions in the various polymer-fullerene blends.

The understanding of the morphology in amorphous polymer-fullerene blends, leads on to the studies of semi-crystalline polyalkylthiophene-fullerene based blends used in BHJ based OPV devices (Chapters 4 and 5). The chosen polyalkylthiophenes and fullerenes had varying lengths of the side chains to look at the effect of side chain interaction on the blend morphology.These studies are divided into two parts. In Chapter 4, the through thickness phase segregation behavior is studied with the use of neutron reflectometry (NR) and corroborated with X-ray photoelectron spectroscopy (XPS). The samples show various trends in terms of the degree of phase segregation and composition at the different interfaces. These values for the amount of segregated compounds are quantified in turn correlated to the device performance parameters, which were measured with the exact same configuration of the polymer-fullerene BHJs.

In Chapter 5, studies on the phase morphology differences in bulk and thin films of the polyalkylthiophene-fullerene blends are discussed. The bulk measurements are carried out using wide angle X-ray scattering (WAXS) and small angle neutron scattering (SANS). This provides phase information over all the different length scales, from crystal spacing ~1-2 nm to the large segregated amorphous, crystalline and mixed phases ~100-200 nm. Subsequently, similar measurements are shown for thin films as well, but using these techniques in grazing incidence mode. That in turn generates information about the in-plane phase morphology, but also at different depths of the thin film active layer. The results from the bulk and thin film measurement are then compared to derive the scale of influence between thermodynamic and kinetic factors on the phase development. This is also used to hypothesize an overall morphological structure in the bulk heterojunction devices through the entire depth of the active layer.

In the last chapter (Chapter 6), having observed the effects of fullerene diffusion in polyalkylthiophenes on the morphology and device performance, a modified fullerene is shown to be synthesized with the purpose of having controlled diffusion in the BHJ. A thermo cross-linking strategy is adopted to allow processing the BHJ from the precursor and coupling the cross-linking reaction with the post-processing annealing step. The cross-linked fullerene did show reduced diffusion in bilayers made with the polyhexylthiophene and superior long term stability in the devices without compromising much on the electronic properties (device mobilities and efficiencies).

A final chapter at the end (Chapter 7) binds together all the conclusions from the thesis work and discusses the potential for future directions of research in this area.

1 INTRODUCTION

The potential for solar energy to provide a green, renewable energy source has been well understood for many years. For solar technology to be pervasive and simultaneously provide a large segment of the global energy, new and innovative concepts pertaining to photovoltaic systems need to be derived. This has led to a large interest in trying to achieve scalable production of highly efficient organic photovoltaics (OPVs)[2, 3] mainly due to the ease with which OPVs can be manufactured at much lower costs compared to inorganic PVs. Currently the most efficient laboratory-produced OPV devices (at ~11%)[4] are still a long way from a technologically useful efficiency from other commercially available devices – 15 % for Si based, 29.1% for a single junction GaAs based cell and 44.1% for a multi-junction device made by Sharp.[5] A lot of early research on OPVs had been dedicated to developing materials and devices having improved electronic properties with the blends of semiconducting polymers and small molecules acceptors such as fullerene. More recently though, groups have also started dedicating research towards the understanding of the structure and morphology of these blend system based OPVs. One may argue that without complete understanding of the structure and morphology, it will be difficult to realize the theoretical maximum of the device efficiency. At the same time, these devices also degrade with time and under inclement conditions. Thus an understanding of the changes in the device morphology under different simulated environmental conditions and over long periods of time should also be considered important. A thorough understanding of the structure and morphology of the polymer blends with fullerene, their processing conditions, and how this affects device efficiency is thus vital to achieve the full potential of OPVs.[6] OPV devices with efficiencies close to the theoretical maximum, coupled with the inherent low cost processing techniques (inkjet

printing, roll to roll processing) will surely give us a technology capable of challenging other conventional energy sources for power generation.

1.1 ORGANIC SEMICONDUCTORS IN ELECTRONIC APPLICATIONS

1.1.1 Charge generation in Organic Photovoltaics (OPVs)

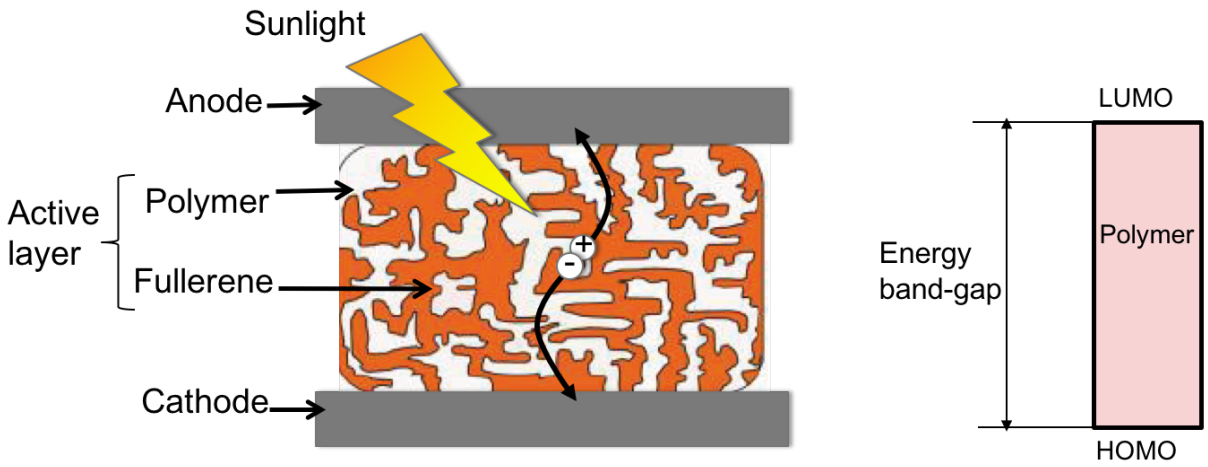

Figure 1.1 Charge generation in an organic photovoltaic device and energy level band diagram of a semiconducting polymer

Organic semiconductors usually have a wide band gap (around 1.4 eV and above up to 3 eV) which is the energy gap between the highest occupied molecule orbital (HOMO) and the lowest unoccupied molecular orbital (LUMO) energy levels (Figure 1.1). HOMO – LUMO energy levels are analogous to the top of the valence band (at which the valence electrons are present) and the lowest level of the conduction band (at which the electrons are mobile charge carriers) in inorganic semiconductors. Organic semiconductor materials can absorb energy to excite an electron from the HOMO energy level to the LUMO energy level in order to generate a bound

electron-hole pair (exciton) which in turn can dissociate to generate and transport free carriers. Thus organic semiconductors have a negligible charge carrier density at room temperature. They need an external source (either through chemical, or photochemical) of doping to generate extrinsic charge carriers in the semiconductor. One such method is photo-induced charge transfer. Due to the low dielectric constant of organic semiconductors compared to their inorganic counterparts, its harder to separate the electron-hole bound pair (exciton) and consequently the excitons have a high binding energy. The excitons thus require the presence of an acceptor species with a suitable LUMO lower that the LUMO of the acceptor to accept the electron and lead to the splitting of the charges.[7] Upon approaching an electron accepting species, the bound pair can split into free charges (with positive on the donor and negative charge on the acceptor) and be collected as electrodes. This serves as the basis of building organic photovoltaic devices. Donor-acceptor-type built in the form of bilayers devices (one on top of the other) can thus work like classical p-n junctions (Figure 1.2).

In 1985, Tang built a bilayer device with sequentially stacked layers of a p-type (copper pthalocyanine) and n-type (perylene tetracarboxylic derivative) organic semiconductors (through vacuum deposition).[8] Subsequently a number of other materials combinations (both by vacuum deposition and solution processed) were used to make similar OPV devices.[9-11] The efficiencies in these bilayer devices however got limited at around 1 % due to a number of factors. Firstly, due to the short diffusion length of the excitons in organic semiconductors, the thickness of the layers was limited to 10-20 nm. Thicker films would suffer from considerable recombination leading to drop in efficiencies. At the same time, the thinness of the films (10-20 nm) limited the absorbance leading to collection of lower amount of photons and photocurrent, again negatively affecting the device performance.

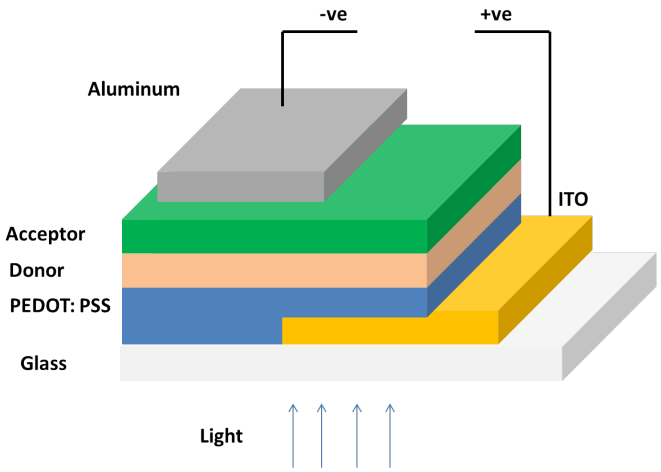

Figure 1.2 Schematic for a bilayer configuration OPV device (reproduced from reference[12])

With the ability of organic molecules to dissolve easily in solution, a lot of research started focusing on solution processing of small molecules and polymers for OPV applications beside vacuum deposition techniques. [13] At the same time, having weighed the limitations of the bilayer devices (layer thickness, absorbance and efficiency), there came a need to develop a new architecture for better charge generation capabilities.

1.1.2 Bulk Heterojunction (BHJ) based Organic Photovoltaics (OPVs)

A new architecture of OPVs, the bulk heterojunction (BHJ) was designed by a heterogeneous mixture of a donor and an acceptor in the active layer (Figure 1.3)[14-16] which addressed a number of drawbacks of the bilayer based OPV systems. Yu et al.[14] first made such a system with a mixture of poly(2-methoxy-5-(2′-ethyl-hexyloxy)-1,4-phenylene vinylene) (MEH-PPV) as the donor and C_{60} fullerene as the acceptor with efficiencies reaching values up to 2.9%. Replacing the polymer with with poly(3hexylthiophene) and the fullerene with a more soluble form, Meeskers et al.[17] managed to make devices with internal quantum efficiency (IQE) approaching unity making the devices even more efficient. This in turn with suitable post production treatment led to the evolution of P3HT-PCBM based BHJ as one of the most popular

and widely studied combination with even higher efficiency values.[16, 18, 19] In the conventional form, BHJs were formed by dissolving donor and acceptor components in a common solvent (or solvent mixture) and subsequently spinning them onto the electrode (anode). This is the active layer in the device (Figure 1.3). The complementary electrode (cathode) is then deposited on the active layer to complete the structure. Unlike bilayers where the donor and acceptor phases (layers) are separated and directly in contact with the anode and cathode, they are intermixed in a BHJ.[16, 20, 21] This allows for easier exciton dissociation since the exciton needs to travel a shorter distance before encountering an interface, and also allows for thicker active layers giving us greater photon absorption. But the intermixed nature of the active layer also means that the electrons and holes have no internal fields to direct them towards opposing ends. Thus the electrodes need to be chosen with appropriate work function differences to generate the internal field for charge separation. Work function of a material is the energy required to move an electron from its surface to vacuum. Thus difference in work function of the two electrode materials builds up an overall potential between the two and thus sets up an internal field in the active layer. The necessity of one of the sides to be transparent (for light to approach) led to the use of a transparent thin layers of Indium tin oxide (ITO) and its modification with a water soluble organic hole transport layer, poly(3,4-ethylenedioxythiophene) polystyrene sulfonate (PEDOT PSS) gave even higher efficiencies.[22, 23] The presence of an organic layer also made it easier to spin the active layer onto the substrate. Consequently, it was also important to have a good ohmic contact of the top electrode with the active layer and the introduction of a LiF interlayer between the Aluminum cathode and active layer led to significant improvements in the device performance.[21, 24]

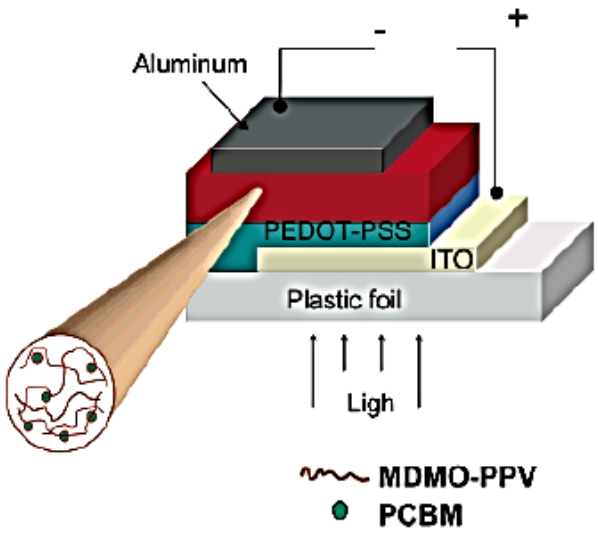

Figure 1.3 Schematic for bulk heterojunction type organic photovoltaic devices (reproduced from reference[12])

Within the BHJ, a number of steps are involved in the process of charge generation. [13] They could be broadly divided into

1) Absorption of photon by the active layer leading to the formation of an exciton
2) Diffusion of the exciton to an interface
3) Charge separation of an exciton leading to formation of free charges
4) Transport of the free charges to the respective electrodes.

The total efficiency (η) of charge collection could thus be attributed to the efficiency of each of these steps:

$$\eta = \eta_1 \times \eta_2 \times \eta_3 \times \eta_4 \qquad [1.2]$$

It is thus important to understand these steps and try and optimize each one of them to get the desired maximum device efficiency.

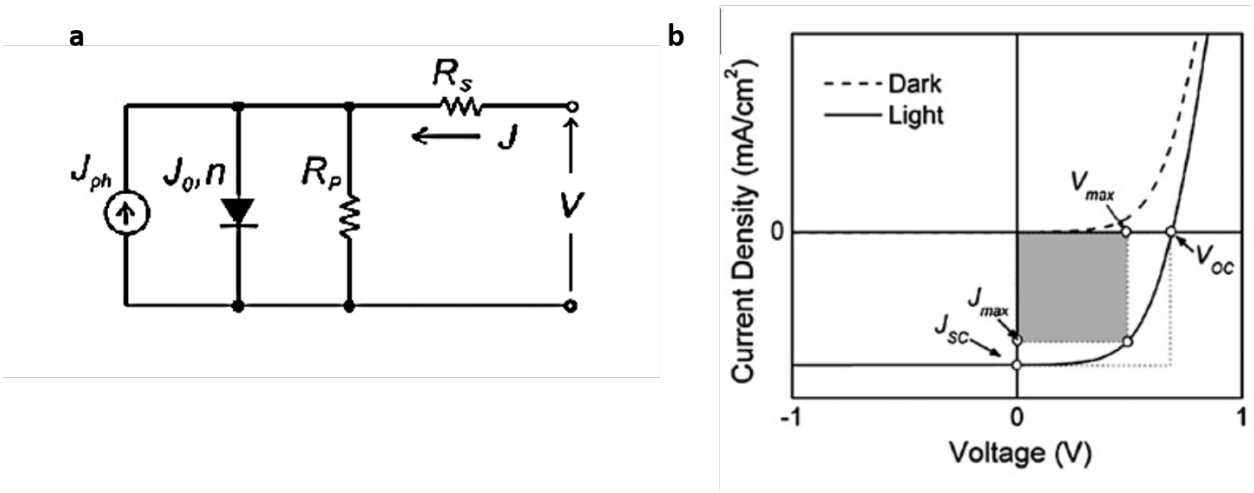

Figure 1.4 a) Circuit to model organic solar cells b) typical current voltage statistics for OPVs (reproduced from reference[25])

To model the overall efficiency of the device it was necessary to look at the device current voltage statistics while in operation. The current-voltage characteristics were thus modeled as shown in Figure 1.4a. The current and voltage was thus derived to be related by the Shockley equation to give a profile as in Figure 1.4b.[26] From the J-V curve, two parameters that could be defined easily, were the short circuit current (J_{sc}) and the open circuit voltage (V_{oc}). In addition, the power derived at each J-V point by the circuit could be maximized at a point P_{max} corresponding to specific values of current J_{max} and voltage V_{max}. From these values and the incident power P_{inc}, the device efficiency (η) was defined as:

$$\eta = \frac{P_{max}}{P_{inc}} = \frac{FF \times J_{sc} \times V_{oc}}{P_{inc}} \qquad [1.6]$$

Where FF is the fill factor and is representative of the squareness of the plot. Most of the effort in this fields research has gone into improving these parameters (J_{sc}, V_{oc} , FF), but it is non trivial since they are interlinked and often with have opposing trends. The maximum photocurrent (*Jsc*) is dependent on the absorption spectrum,[27] and a possibly larger or broader absorption spectrum

would generally affect the J_{sc} positively. Thus a lot of focus has gone into developing low band-gap polymers. However it is known that the V_{oc} also depends on the difference between the HOMO of the polymer and the LUMO of the fullerene.[28] Raising the HOMO of the polymer (or lowering the LUMO of the acceptor) would in turn reduce the bandgap and negatively affect the V_{oc}. In addition, the fill factor is determined by the amount of charge carriers that actually reach the electrodes.[29] So improving the fill factor is dependent on minimizing the recombination losses in the thin films primarily due to uncontrolled morphological development. The enhancement of the device efficiency thus depend on careful understanding and designing of devices, starting from synthesis of optimal material to controlling the final device morphology and finally optimizing device architecture and interfaces.

1.2 DONOR-ACCEPTOR INTERACTIONS IN OPVS

Currently, one of the most popular forms of OPVs are donor-acceptor based BHJs which produce charge carriers through photo-generation. As discussed previously, due to the variety of mechanisms by which photocurrent is generated and subsequently collected, it is affected by the composition and structure of the device. Thus it is important to study the inherent properties and nature of interactions between the donor and acceptor in the heterojunction in order to predict an optimal composition of the same.

1.2.1 Donor-Acceptor Electronic Properties in BHJs

While choosing appropriate donor and acceptor systems for constructing BHJs focus lay on chemically synthesizing them so as to obtain maximum absorption of incident photons as well a better matching of the energy bands to ensure maximum collection of photo-generated charges. This would ensure optimal inherent electronic properties of the device. Thus the bandgap of the

polymers would have to be low, (~ 1.3 eV) to absorb the maximum possible spectrum. At the same time, the energy level difference between the HOMO of the donor polymer and the LUMO of the acceptor needs to be maximized so as to maximize the V_{OC} and ensure efficient charge transport from the donor to the acceptor.[30] One of the first conjugated polymers used in OPVs were poly(1,4-phenylene vinylene) (PPV)-based polymers. Poly(2-methoxy-5-(30,70-dimethyloctyloxy)-p-phenylenevinylene) (MDMO-PPV), was mixed with $PC_{70}BM$ to give one of the first high performing OPV with efficiencies approaching 3%. Some research was also done in this period to study the morphology of these systems to understand its effect on the device efficiency. Studies observed formation of an interpenetrating network of the polymer and fullerene, whose phase sizes could be controlled by changing the type of solvent, post processing conditions, ratio of the donor-acceptors etc.[31]

Subsequently, with the synthesis of polyhexylthiophene, a soluble form of polythiophene semiconductor, scientists achieved one of the most commonly used and most-studied forms of organic semiconductor for OPV applications. Its ease in processing along with the relatively high achievable device efficiencies made it a model polymer for these devices. With the introduction of a post-annealing process (solvent and thermal based), [18, 32] BHJ based OPVs containing P3HT (donor) and PCBM (acceptor) was seen to reach up to 4-5% efficiency. The efficiencies for P3HT based systems however plateaued out at that value, mainly due to limitations of its bandgap, leading to lower absorption in the near IR regions, and thus limiting the photocurrent produced.

In recent years, newer polymers have been synthesized to produce variable band-gaps which allow the absorption of a larger section of solar spectrum.[31] By combining different repeating units of electron donating and accepting capabilities, the HOMO and LUMO levels could be varied. Some of the best performing ones recently have been based on alternating polyfluorene

copolymers such as, poly{[2,7-(9-(20-ethylhexyl)-9-hexyl- fluorene])-alt-[5,50-(40, 70-di-2-thienyl-20,10,30-benzothiadiazole)]} (PFDTBT) and carbazole based Poly[N-9′-heptadecanyl-2,7-carbazole-alt-5,5-(4′,7′-di-2-thienyl-2′,1′,3′-benzothiadiazole)] (PCDTBT),[33, 34] which due to their deep lying HOMO level gave a very high V_{oc}. Other conjugated polymers have been synthesized having alternating donor-acceptor species, such as dithienogermole (DTG) or dithienosilole (DTS)[35, 36] as the electron donor species with 1,3-dibromo-noctyl-thienopyrrolodione (TPD) as the electron accepting species. These devices have shown PCEs of up to 7.3% in BHJs made in the inverted form. Similarly, alternating thieno[3,4]-thiophene and benzodithiophene units gave us the polymers which currently are the highest performing OPVs such as PTB7 and PCE10.[37, 38] These are low band-gap polymers characterized by high EQE and *Jsc*. By combining it with appropriate acceptors ($PC_{70}BM$) it has been possible to achieve high Voc and fill factors as well giving these devices efficiencies up to 9.4%.[39]

The importance of the acceptor group is thus also paramount in determining the matching of energy levels to give maximum charge collection by reducing the LUMO difference between the donor-acceptor. In turn, a large band-gap between the polymer HOMO and acceptor LUMO ensures maximizing the Voc.[28] Up to now, modified fullerenes have been very successful, with $PC_{60}BM$ being one of the most commonly used acceptors. Its ease in processing due to its good solubility, and electron accepting ability make it a suitable acceptor for BHJ systems.[13] Alternatively, other modified fullerenes have been synthesized the most popular among them being namely ICBA, $PC_{70}BM$. ICBA a bis-adduct has a LUMO level shifted slightly higher than PCBM allowing for larger Voc in those devices. However the light absorption isn't changed much in those cases, which was addressed in the case of $PC_{70}BM$ with greater absorption in the visible range.

Depending on the choice of polymer and thus its energy levels, the appropriate fullerene gives the optimal device performance.

However, as discussed before, factors beyond the electronic properties of the donor and acceptor determine the morphology of the BHJ in the devices and consequently its performance. Thus, with the same materials, the interaction between the polymer and fullerene as well as its subsequent processing and post processing help determine the blend morphology and performance of the device. It is thus important to take those factors into consideration while designing a device with desirable performance.

1.2.2 Polymer-Fullerene Miscibility in BHJs

In applications where fullerenes are blended with polymers (as in BHJ based OPVs), it is necessary to be able to control the interaction between the polymeric matrix and the fullerene molecules in order to control the eventual morphology developed. Troshin et al.,[40] have shown that there is a general dependence of all solar cell parameters (short circuit current, J_{SC}, open circuit voltage, V_{OC}, fill factor, *FF,* and power conversion efficiency η) on the solubility of the fullerene derivative used as an acceptor component in the photoactive layer of an organic solar cell. According to these authors, the best material combinations are those where donor and acceptor components are of similar and sufficiently high solubility in the solvent used for the deposition of the active layer. In order to improve the chemical affinity between the fullerene and the polymer, and ultimately improve the underlying morphology as well as the device efficiency, one strategy has been to functionalize the C_{60} acceptor.[41-46] In a related recent study, it was also shown that thermodynamically stable dispersions of fullerene nanoparticles with a polymer matrix occur for systems where the radius of gyration (R_g) of the polymer is greater than the radius of the

nanoparticle.[47] However, this study does not account for the small solubility limit of C_{60} that is independent of polymer R_g,[48] reinforcing the necessity for further research in this area.

Compelled by the increasing evidence relating fullerene solubility in polymers with solar cell performance, several authors have studied the miscibility and phase diagrams of several P3HT-PCBM blends (Figure 1.5).[49-55] These have included PCBM blends with polythiophenes (P3BT, P3HT, P3DDT),[49-52] with polyphenylene vinylenes (PPVs)[50, 53] and with poly(3-hexylselenothiophene) (P3HS).[54]

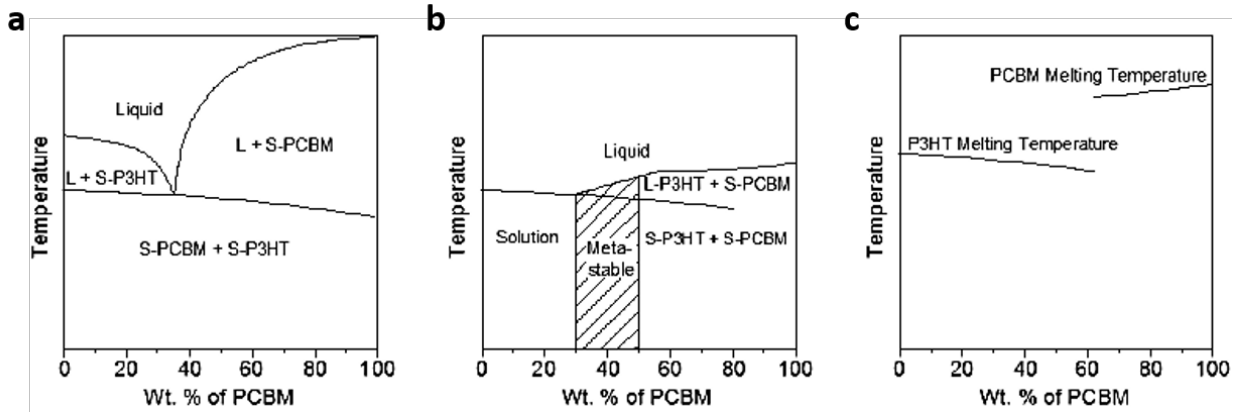

Figure 1.5 Phase diagrams for P3HT-PCBM mixtures showing eutectic like behavior by a) Muller et al. [49] b) Kim et al. [50] and c) Zhao et al. [51]

But although a number of studies have looked into the miscibility behavior of polymer-fullerene mixed systems in significant detail, there's still a great variance in the findings. Within the most popularly studied P3HT-PCBM system, the phase behavior has been described by some as eutectic, [56-58] while others believe it follows a more classical Flory-Huggins phase behavior.[59] The phase diagrams for the blends were determined by different groups using a combination of characterization techniques. Müller et al.,[49] using a combination of DSC, optical microscopy and XRD, studied the phase behavior of PCBM with P3BT, P3HT and P3DDT to show a eutectic like

behavior. Zhao et al.,[51] measured the phase diagram of P3HT:PCBM blends using conventional and modulated temperature DSC (DSC and MTDSC) and investigated PCBM blends with PPV polymers[53] using these same techniques and rapid heat-cool calorimetry (RHC) to determine the P3HT-PCBM blend phase diagram. Kim et al.,[50], using a combination of X-ray diffraction (XRD) and differential scanning calorimetry (DSC), studied the phase behavior of PCBM with P3HT, MDMO-PPV and MEH-PPV and showed it to be eutectic like, and also determined the solubility limits of PCBM in these polymers to be 30, 40 and 50 wt% respectively. These studies have also shown up irregularities in the calculation of miscibility limit of PCBM in P3HT, which vary from 20% [60] to ~42%.[61] This is believed to have arisen from the fact that the crystallinity of the polymer has an effect on the solubility of the fullerene in the mixtures. These have been studied by using P3HT with varying regioregularities, thus having different percentage crystallinity values.[62, 63] The authors showed that under similar annealing conditions, regio-regular P3HT showed much more phase aggregation (larger domains) of pure polymer and fullerene phase in comparison to the regiorandom sample (Figure 1.6). This could be understood in terms of the crystallinity, which is much higher in a regioregular polymer. In comparison thus, the higher amorphous content of regiorandom polymer allows a greater amount of PCBM miscibility and has a higher miscibility limit.

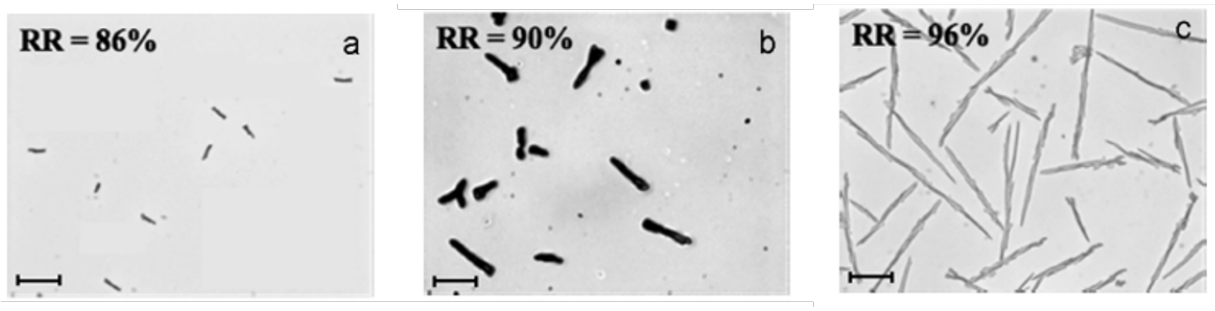

Figure 1.6 Optical microscopy images showing varying amount of PCBM aggregation in a) 86% regioregular P3HT b) 90% regioregular P3HT c) 96% regioregular P3HT (reproduced from reference[62])

Another issue with these studies may be that studying the phase behavior of PCBM: polymer blends using DSC have relied mainly on the tracking of variations of the glass transition temperature (T_g) and on the identification of either one single T_g (one-phase system) or of two different T_gs (two-phase separated system). However, previous studies in PCBM:P3HT blends have shown that experimentally measured glass transition temperatures are subjected to large experimental uncertainties.[51] Furthermore, the measurement of T_g is highly dependent on the measurement technique. According with Zhao et al.,[51] the T_g of the system PCBM:P3HT, as determined using DSC and MTDSC, increases from 12.1 ºC for pure P3HT to 131.2 ºC for pure PCBM. According to Hopkinson et al.,[52] using dynamic mechanical thermal analysis (DMTA), the T_g increases from ~40ºC for pure P3HT to ~70ºC for a PCBM load of 65 wt.% and then drops between 70 and 75 wt.% indicating phase separation. This thus necessitates the determination of a detailed, systematic and more robust method of miscibility study of different analogous polymer-acceptor groups in BHJs and corresponding effect on bulk morphology and device performance.

1.3 EFFECT OF PROCESSING ON ORGANIC SEMICONDUCTORS

It has been seen that not only do the inherent material properties discussed earlier play a role in dictating the resulting device morphology and performance, but processing also have a dominant role.[25] For the PV cell to create charge flow, the photogenerated exciton formed must reach an interface in the polymer-fullerene system before it decays. Consequently, a critical dimension in these systems is the diffusion path length of the excitons, which depends on the materials but is estimated to be of order of 10-20 nm.[64] Therefore forming phase morphology commensurate with these length scales is a vital requirement of heterojunction devices. In addition, the electron and hole created by the dissociation of the exciton at the fullerene-polymer interface must be transported to the electrodes within their respective lifetimes or without recombining with each other. This indicates that a stable interconnected, bicontinuous phase network morphology may be desirable. In these systems, the nanophase morphology will directly affect the charge transport ability.[12] As noted by a number of researchers, although bulk heterojunction PV cells can be prepared very simply by physically blending fullerene-polymer mixtures, variation of the processing parameters can produce very drastic differences in the morphology and correspondingly the device efficiency.[21, 65, 66]

1.3.1 Spin coating of BHJs

As shown in the previous section, the phase diagram of P3HT-PCBM has been predicted to follow something similar to a eutectic behavior. The eutectic composition value in those cases however varies between 35-60% in different studies.[56-58] They used a combination of DSC, XRD and optical microscopy to determine the morphological parameters including the miscibility limit for PCBM in P3HT (~ 30%) [50] In all these cases however, the studies had samples which were

prepared from drop-cast solutions. As discussed in Section 1.3.2, building a bulk heterojunction device involves spin coating a thin film of this polymer-fullerene (donor-acceptor) in between the two electrodes. Thus while studying the thermodynamic behavior of the blends gives us some understanding of these polymer-fullerene mixed systems, the proper understanding of the mixed system within the device structure needs to take into account the kinetic factors arising from the process of spinning.

The effect of the kinetics of solvent drying in the BHJ while spinning has been studied by a number of groups and has seen to have an effect on the morphology of the BHJ.[67-73] This was mainly done either by artificially slow drying the film from a solvent, or by taking a group of solvents of different boiling points and studying their effects. The films could be slow grown either by varying the spin speed while spin coating,[68] the drying rate of the film on the substrate after spinning,[67] or creating an solvent saturated environment for slow drying.[69] With the slow drying of the casting solvent, Vanlaeke et al.[69] showed using both XRD and UV-vis that the resultant slow dried film had enhanced crystallinity of the P3HT polymer and light absorption, which in turn gave better I-V statistics and device performance. Li et al.[67] also observed through UV-vis absorption spectra that the slow grown thin film had a more ordered structure, AFM imaging also showed rougher surfaces for the films, which were also indicative of the possible self-alignment of the chains with time leading to more ordered structures in the film (Figure 1.7). Beside these observations, Campoy-Quiles et al.[68] also used ellipsometry to note the morphological evolution of the fullerene vertical segregation in P3HT-PCBM blends. The fullerene segregation to the top of the film was seen to reduce with slower spin speeds, thus slower drying/growth rates. This is similar to what is observed in the case of thermally annealed thin film. Thus it is believed that the slow drying kinetics using lower spin speeds and higher boiling point solvents such as

chlorobenzene and dichlorobenzene amount to a morphology similar to the thermal or vapor annealing of the sample which give the device a more desired morphology (with more ordered and crystalline regions of the polymer).

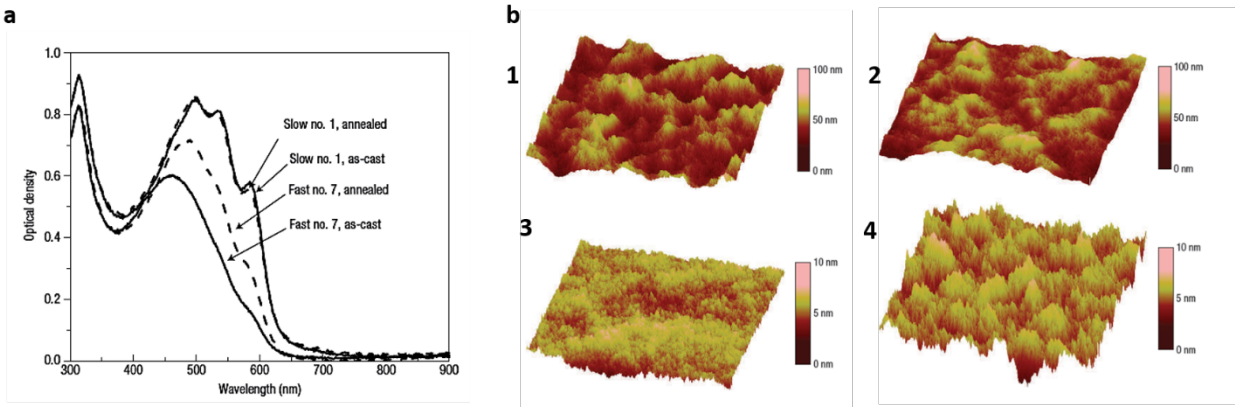

Figure 1.7 Effect of slow annealing shown through a) more ordered structure from UV-vis spectra of slow annealed sample b) AFM images for before and after annealing 1and 2 for slow annealed showing more roughness than 3 and 4 for fast annealed samples (reproduced from reference[67])

1.3.2 Post Processing of Bulk Heterojunctions

Whilst the choice of solvent and spin parameters are important in determining the morphology of the BHJ device, post processing techniques have also seen to have a significant impact on the same. It was observed that by thermal annealing,[16, 18, 74] or solvent annealing[75, 76] one could significantly improve the device efficiency of P3HT-PCBM BHJs by a number of folds and this was a significant step in the development of commercially viable organic solar cells. Heeger et al.[18] used X-ray diffraction (XRD) and AFM to suggest that the thermal annealing process enhances both the crystallinity of the polymer as well as enhances the inter-connection in

the bi-continuous network of polymer and fullerene. In accordance to that, the absorption spectra and EQE spectra of the system was also seen to be enhanced. Chirvase et al. suggested that the red shift in the absorption spectra was borne out of PCBM diffusion out from P3HT matrix leading to greater P3HT ordering [74]. Enhanced charge carrier mobility was also observed upon annealing. The optimal annealing temperature was derived as ~ 140 °C by systematically studying the efficiency and charge carrier mobility with temperature by Kim et al.[70] Others studies determined different optimal temperatures with some suggesting annealing at 155 °C[77] while others at just greater than 110 °C. [78, 79] However the optimal temperature and consequently morphology was shown to be dependent upon the regioregularity of the polymer. Woo et al.[62] showed that P3HT with lower regioregularity required longer annealing times to achieve optimal device efficiencies. Thus differences in regioregularity as well as the annealing times (higher annealing temperature requiring lesser time to be annealed) would account for the differently reported optimal annealing temperature. More recently, Agostinelli et al.[80] used in-situ grazing incidence X-ray diffraction and field-effect transistor mobility measurements to better understand the dynamics of the morphology development on thermal annealing. Initially the annealing leads to a quick polymer crystal growth phase followed by a slower fullerene diffusion in the second. In conjunction, the device efficiency increased till a certain annealing time, followed by saturation at that value (Figure 1.8).

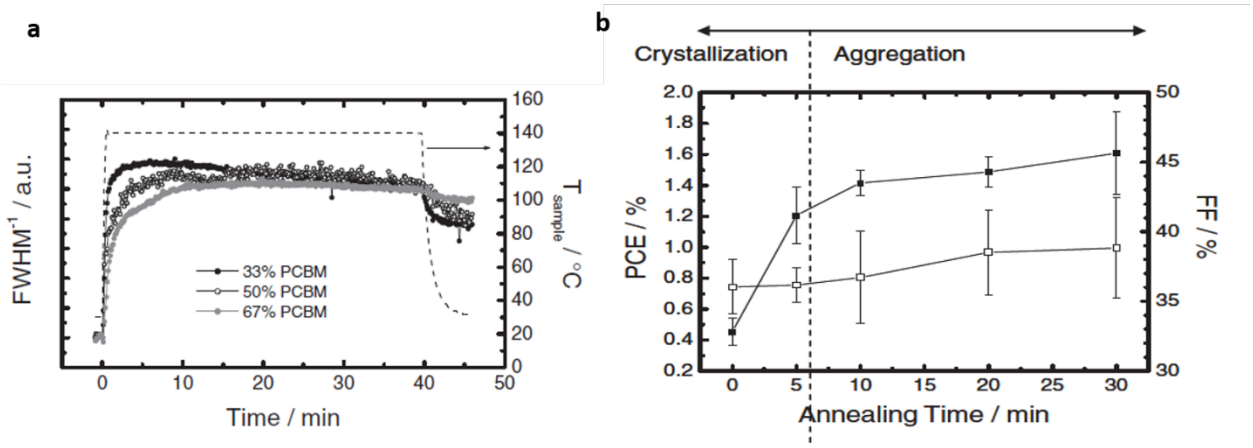

Figure 1.8 Development of P3HT-PCBM (different ratios of PCBM) OPV a) showing full width half max of the P3HT crystal peak decrease (crystal size increase) with annealing time c) PCE and FF of the device increasing with annealing time till a certain value (reproduced from reference[80])

1.4 CHARACTERIZATION OF THIN FILM ORGANIC ELECTRONICS

As discussed in the last few sections, the most efficient form of organic based solar devices to date, consist of donor and acceptor materials mixed together to form what is known as a bulk heterojunction (BHJ). The efficiency of these OPVs have been seen to depend upon a number of factors such as material choice, processing solvent, interfacial effects, processing and annealing conditions, among others. These factors consequently have a direct effect on the morphology of the systems. A better understanding of these effects and their combined implications, would allow us to fully understand structure-property relationships and develop more efficient devices in the future.

1.4.1 Morphological characterization of BHJ OPVs

It is known that the chemical interaction between the polymer and fullerene and as well as with the solvent is critical in determining the morphology of the heterojunction system.[31, 58, 81] Most of the early studies mainly focused on different systems with variations in polymer-fullerene ratio or any chemical changes of one of the species (e.g. side chain of the polymer).[74, 82] However these studies were conducted whilst considering the active layer morphology as an ideal heterogeneous blend throughout the layer.

More recent studies have clearly shown that this picture of the active layer morphology is highly naïve. It has been shown that a bilayer can be effectively converted in to a bulk heterojunction through inter-diffusion of PCBM into P3HT by annealing at 150 °C [83, 84]. During the annealing the P3HT was believed to order initially before the PCBM diffused through the disordered amorphous region of the polymer and the polymer recrystallized with time and gave the heterojunction structure.[83, 85, 86] Earlier studies using techniques such as wide angle X-ray diffraction (WAXD) and TEM on BHJ devices, showed that annealing of the devices has a considerable effect,[18] with recrystallization of the polymer and diffusion of the fullerene occurring through the amorphous regions occurring,[87] and having different implications on the device characteristics.

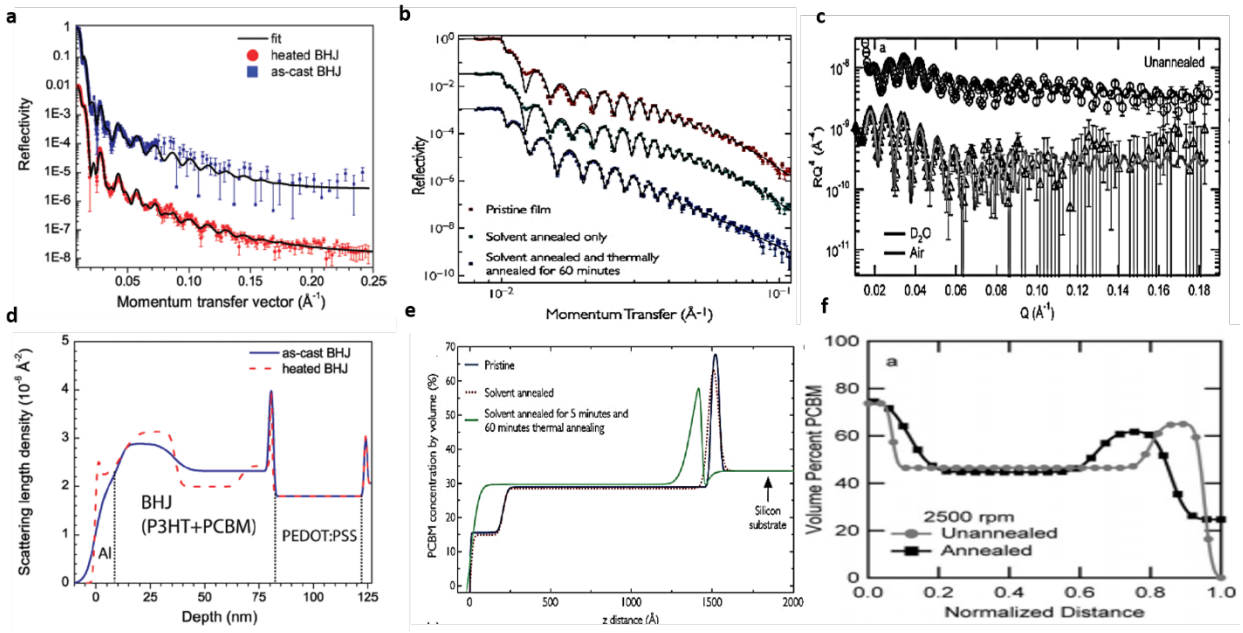

Figure 1.9 Neutron reflectivity profiles and corresponding scattering length densities for before and after annealing P3HT-PCBM BHJ with a)-d) Al electrode on top[88] b)-e) without top electrode[89] c)-f) without electrode on top[90]

While the surface and bulk studies such as AFM, TEM and WAXS do provide information about the morphology, to fully understand the working of the devices, the effect of thin film structure also needed to be considered. Due to the thin and limited quantity of material being studied, indirect measurements of morphology through X-ray and neutron scattering became popular. In addition, the grazing incidence mode could allow for the observation of thin film structures exactly in the device form. Since the bulk heterojunctions layers are thin films of order of 100 nm, at such small thicknesses, the interfacial properties with the bounding electrodes can also play a significant role in affecting both the morphology and consequently the performance of the devices. The morphology that develops in these systems is thus not uniform throughout the thickness of the film and the dependence of this behavior to the device performance is not fully

understood. A number groups have looked and observed a segregation profile through the thickness of the BHJs. Studies on BHJ systems using a number of different techniques (including NEXAFS[91, 92] and TEM[93]) have observed the segregation of PCBM through the thickness of the active layer.

Other groups have conducted recent work on BHJ devices using neutron reflectivity (Figure 1.9). However these have been performed, either in the absence of the top electrode [89, 94] or for just one particular system of P3HT-PCBM.[88] Those studies as well as ones with other semi-crystalline polymer-fullerene systems,[95] have however shown that with NR it is possible to understand not only the bulk behavior, but also the morphological evolution at the interfaces and subsequently the entire device structure. The same study subsequently identified the presence of a polymer enrichment layer at both the top and bottom electrode with the bulk of the active layer having a constant ratio of the polymer and fullerene in both as cast and annealed films. Annealing led to an enrichment of fullerene at the top electrode, which was consequently linked to an improved device performance. The presence of the top electrode is also seen to be crucial in the studies of these systems, as it has been seen that preparation and subsequent annealing of devices before and after placing the top electrode gave sufficiently different interfacial structure and roughness resulting in differing device performances. Devices annealed after the deposition of all the composite layers (including the electrode) produced greater roughness at the BHJ-electrode interface providing additional absorption of light. At the same time, greater vertical segregation through the thickness upon annealing is also seen to give better voltage output because of reduced shunt paths and optimal domains of P3HT-PCBM formed.[96]

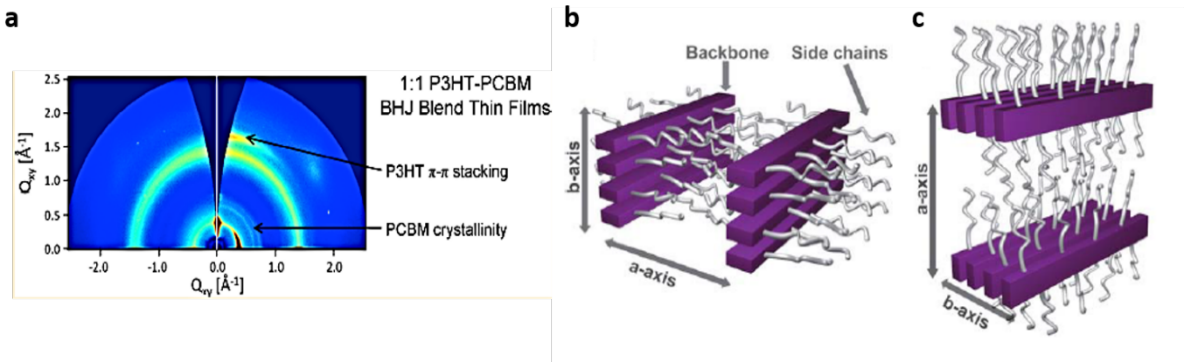

Figure 1.10 a) GIWAXS 2-D profile showing visible peaks for solvent annealed P3HT-PCBM BHJ [32] b)-c) corresponding possible orientations of P3HT, face on (b) and edge on (c)[97]

Besides the vertical segregation profile and diffusion behavior, scattering based techniques have developed into a useful characterization technique to investigate the phase behavior of these systems in detail as well. Use of wide angle X-ray scattering in the grazing incidence mode (GIWAXS) has allowed the determination of the crystal structure and crystallinity of BHJ structures in thin films. Through GIWAXS, crystallinity of the polymer and in turn the device morphology has been shown to be dependent on a number of factors including the regioregularity,[62] solvent used,[98] its concentration[73] and post processing techniques as previously discussed such as thermal[97, 99] and solvent annealing.[32] While improvement in the P3HT crystallinity within minutes of post processing (thermal annealing) was observed previously with regular X-ray diffraction,[18] GIWAXS in addition allowed the determination of the primary orientation of the crystallites in the system. Of the two orientations (Figure 1.10b and c) shown in the figure, the edge on orientation was seen to be the most commonly observable,[80, 97] although Verploegen et al.[32] showed that reorientation of the polymer chains crystals to a more preferable face-on configuration could be achieved by either thermally annealing the system above the P3HT melting point, or solvent annealing it with chloroform (Figure 1.10a). While orientation

information has certainly clarified the crystallographic structure, an added benefit of GIWAXS has been the use of synchrotron X-ray sources in them allowing measurements of in-situ processes. This has been widely utilized to see the effects of the aforementioned annealing conditions on the crystallographic development of the polymer. The time-scales on those measurements were however fairly longer (~ few minutes to hour). More recent in-situ measurements however have been expanded to study faster processes such as in-situ spinning and effect of additives on the morphology. [100-102]

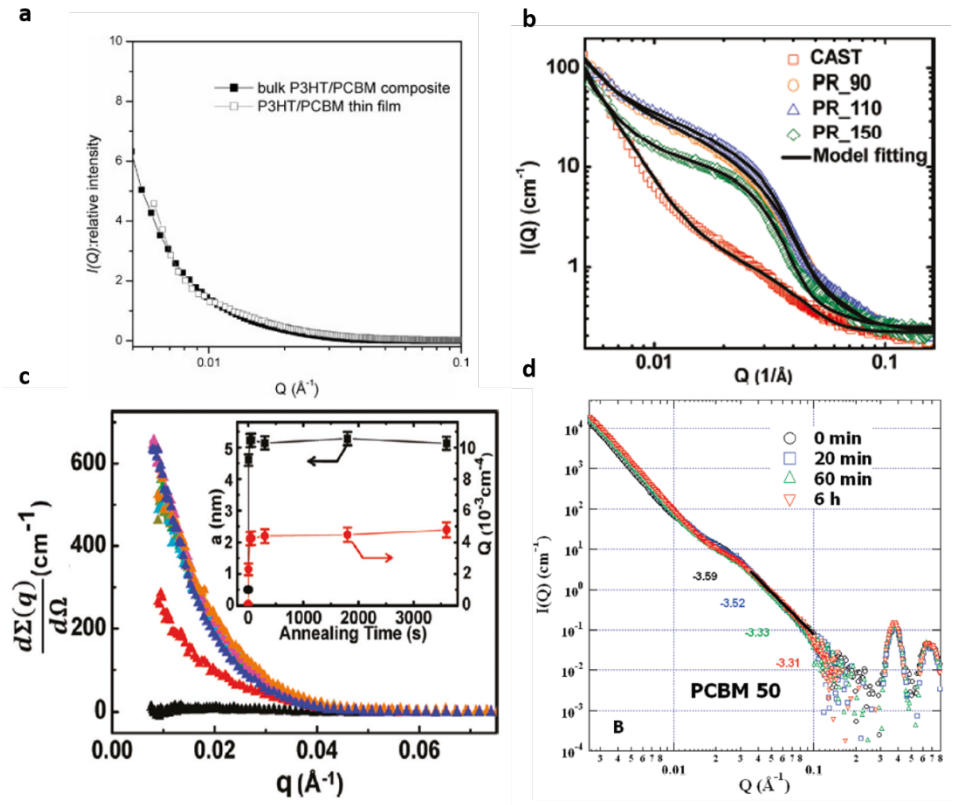

Figure 1.11 Analysis on P3HT PCBM thin films using a) GISAXS and SAXS, showing absence of aggregate structure[103] b) GISAXS showing presence of aggregates at mid q[104] c) SANS showing absence of aggregates[85] d) showing aggregate at mid q.[60]

Although GIWAXS provided us with atomistic level information, larger scaled phases in BHJ devices were limited by the minimum q range of GIWAXS measurements. Thus those structures were studied utilizing scattering at a small incidence angle, in a number of cases (Figure 1.11) using grazing incidence small angle X-ray scattering (GISAXS).[86, 103, 104] Most of the scattering profiles have showed the presence of large scale fullerene (PCBM) aggregates in the other amorphous mixture of P3HT-PCBM, which has been modeled using a hard sphere model with a distribution function (Schultz). On comparing pure P3HT and their blend films with PCBM using in situ GISAXS measurements, Wu et al.[86] also suggested that the process of PCBM aggregation was in competition with the P3HT crystallization. This was in contrast to some of the other studies which suggested the P3HT crystallization being the dominating and primary phase change occurring in blends during formation and annealing.[80, 105] Exact time-scales of the two events are thus still arguable and need clarity.

Although X-ray based scattering techniques have yielded a number of useful results as discussed earlier, neutrons are an ideal source for these polymer-fullerene blends based studies owing to the large neutron contrast between the carbon rich fullerene and comparatively hydrogenated P3AT. This made NR (as mentioned earlier in the discussion of vertical segregation), small angle neutron scattering (SANS) and grazing incidence small angle neutron scattering (GISANS) very useful characterizing techniques for determining phase development in blends (Figure 1.11). In addition, since neutrons are highly penetrating, they could also potentially allow the study of the BHJ layer buried below the top electrodes thus managing to keep the BHJs in full device architecture. A number of studies using SANS have been carried out to look at the large scale phase morphology (1-100 nm) in the BHJ blends.[60, 85, 90, 92] However, owing to its being a transmission mode of characterization, most of the studies were carried out on drop cast blends of

the polymer-fullerene mixtures. Similar to GISAXS measurements, some of the studies observed the presence of PCBM aggregation in the blends,[60, 90] whereas it was absent in some.[92] This dissonance in the observations could most primarily be attributed to the solvent used, which in some cases is dichloromethane, and the others, chlorobenzene. Since the solubility of PCBM varies in these different solvents, one would expect the phase segregation behavior to differ quite a bit as well in the different blends. Thus while these studies did not allow the study of the kinetics involved in the process of BHJ, it gave information about the effects of thermodynamic effects in the formation of the blend films.

Clearly a combination of both through thickness segregation and in-plane phase morphology determine the overall morphology and consequently the device performance. However, further insight into the development of phases with various processing conditions and their specific correlations to device performance remain to be studied.

1.5 LONG TERM STABILITY OF POLYMER FULLERENE BLENDS

1.5.1 Long Term stability studies of BHJ OPVs

As discussed earlier numerous characterization studies have helped derive a substantive understanding of the complex morphology in BHJ device. A significant observation has been that effect of post processing conditions on the controlling the morphology and using it to optimize devices. While methods such as thermal and solvent annealing have been systematically studied to optimize BHJ devices, it was also observed that not properly controlling the post processing could also lead to degradation of the devices. [79, 80, 106] This was attributed to the observed undesirable changes in the morphology. Li et al.[79] found that while P3HT-PCBM based devices showed improved efficiencies with thermal annealing up to a certain temperature (110 °C in this

case), annealing at temperatures beyond those values for prolonged periods led to reduction in the values. AFM images showing lowering of surface roughness with higher annealing temperature and annealing time would have led to lower surface contact with the electrodes leading to lowering of the efficiency (Figure 1.12) Schmidt-Hansberg et al.[106] found that manipulating the slow drying and poor solvents could induce aggregation of the polymer in the solution, leading to better devices, consequently, using fast drying solvents led to poor wetting qualities and low polymer crystallization as seen using GIWAXS. Agostinelli et al.[80] meanwhile carefully studied the effect of the annealing temperature on the morphology with GIWAXS and ellipsometry and observed that initial increase in efficiency could be attributed to increasing P3HT crystallinity, which then stagnated beyond a certain annealing time and led to a plateauing off of the efficiency.

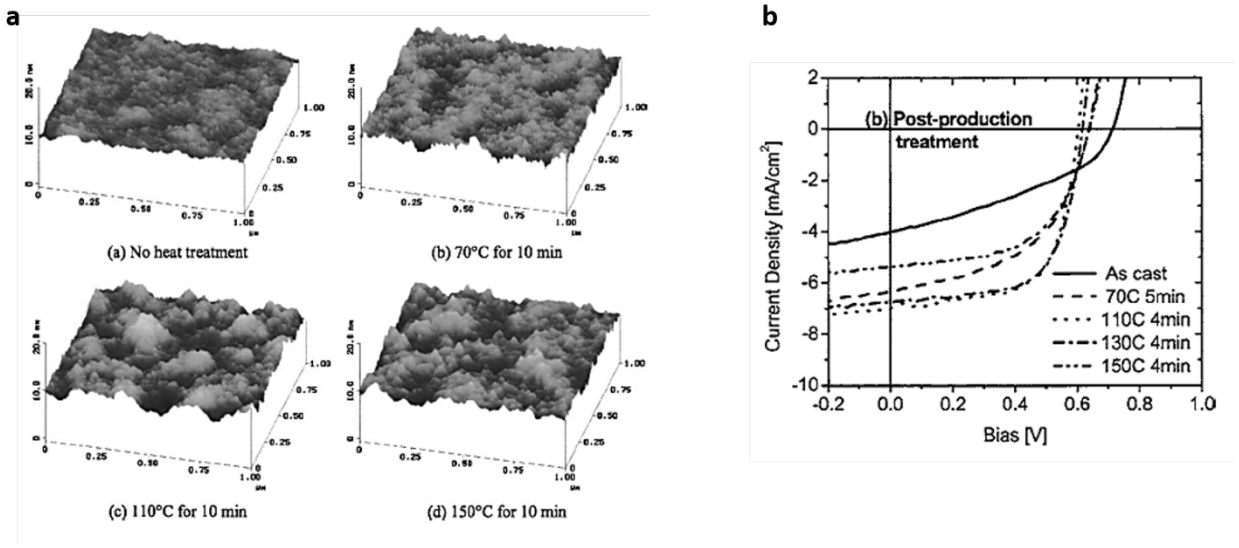

Figure 1.12 a) increase in surface roughness till an optimal annealing temperature (110 °C) followed by decreasing roughness b) corresponding to initial increase in device efficiency followed by decrease (reproduced from reference[79]).

Thus, similar to the changes in the BHJ morphology observed under different processing conditions its modifications over time and changing environments lead to device stability issues. Device stability is an important factor in the determining the price estimate of commercially viable organic solar cells, with Nielsen et al.[107] claiming a need for between 5 to 7 years of lifetime. Although outdoor measurements would be the most accurate estimate of conditions to study device stability measurements, the effect of various factors combined in such conditions make it hard to gain a proper understanding of the cause. Thus stability measurements have been conducted under systems having different controlled parameters.

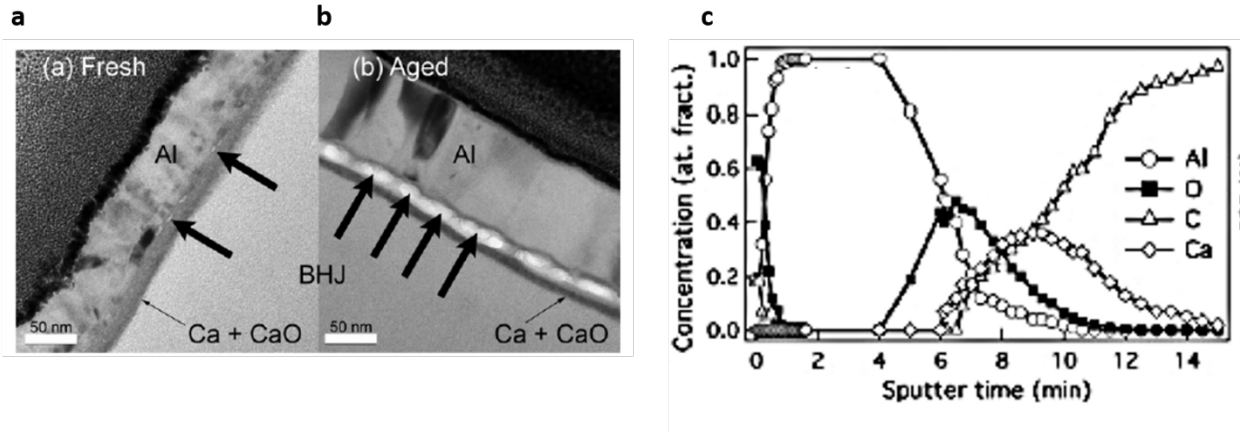

Figure 1.13 Degradation of the aluminum calcium electrode of BHJ in dark by air seen through a)-b) TEM imaging before and after ageingc) Elemental analysis showing presence of oxidized Ca (reproduced from reference[108]).

A number of studies have been conducted under ambient surroundings and illumination with variation of a certain parameter at a time e.g. light intensity, relative humidity etc. Lloyd et al. [108] observed that the main cause of degradation in the case of solar cells stored in dark was the degradation of the metal electrode contact by air, making the choice of the electrode important (Figure 1.13). Some of the major causes of degradation under illuminated settings have been found

to be light induced photo-oxidation of either the transport layer or interface as observed by Rivaton et al.[109] They also noted though that absence of atmospheric oxygen led to an improvement in the lifetimes of the devices, something also observed by other groups.[110, 111] Although the exact mechanism of degradation wasn't clarified in those studies, Tournebize et al.[112] observed recently with the help of UV-vis measurements that the possible cause is the photo-oxidation of the P3HT. Kawano et al.[113] on the other hand observed illumination independent degradation under varying humidity of the measuring conditions, and found the degradation of the PEDOT PSS layer occurring due to water absorption. Number of groups have found other specific causes of photochemical degradation by changing other small parameters Thus, it could be said that under varying conditions present in most ambient surroundings, the solar cells could undergo degradation to effectively reduce their lifetimes.

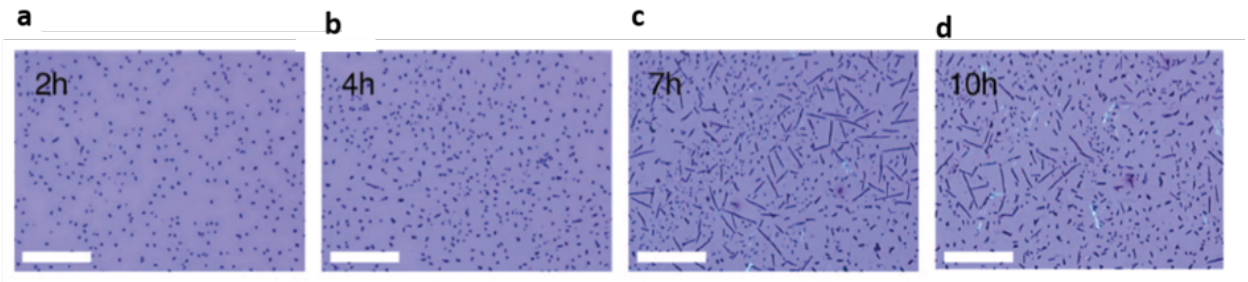

Figure 1.14 Optical microscopy images showing development of needle-like fullerene (PCBM) aggregates from P3HT-PCBM blends with increasing annealing time (reproduced from reference[114]).

While these conditions led to photochemical based degradation of the devices, a number of groups also observed the degradation of devices with thermal effects such as prolonged annealing. [115, 116] Schuller et al. among other groups looked at the degradation behavior with accelerated lifetime measurements. It was observed, that by increasing the temperature of

annealing (from room temperature up to 85 °C), the time scale for degradation could be hastened, though no specific mechanism was ascertained for the degradation. However, time dependent morphological studies at even higher temperatures showed that initial recrystallization of the polymer was followed by aggregation of the fullerene molecules, possibly leading to the eventual breakdown of the device efficiency. [87, 117] Long term effects of thermal annealing were subsequently studied and revealed that P3HT-PCBM aggregation continued for a period of several hours upon annealing, and consequently led to a reduction in the efficiency with time.[62, 114, 118] It was seen that large aggregates of fullerene, visible by optical microscope (Figure 1.14), started occurring within 1-2 hours of annealing at these elevated temperatures (150 °C). These subsequently grew into larger needle like aggregates over several hours. Thus conditioning the devices at near post process annealing temperature, although not representative of the actual environmental conditions did accelerate the rate of fullerene crystal growth and help study the degradation mechanism through the changes in BHJ morphology.

1.5.2 Fullerene Based Acceptors for Long-term Stability of BHJs

The limited solubility of unmodified C_{60} led to the synthesis of new methanofullerene derivatives such as [6,6]-phenyl-C_{60}-butyric methyl ester (PCBM)[119], which were more soluble, as well as more efficient electron acceptors in OPVs. PCBM has since been one of the most popular and widely used acceptor in OPVs.[27, 31, 81] However, as previously noted (in Section 1.5 and 1.6), work done by other groups have shown the active layer of the conjugated polymer-fullerene mixture attains a complex phase behavior as a result of the solution processing and subsequent post processing (annealing) parameters. In addition, optimization of device performance is also often accompanied by annealing the device at temperatures typically well below the melt point of

the polymer or fullerene for short periods of time. However, extended annealing also tends to reduce the device performance and has revealed the change in morphology due to fullerene aggregation as a primary cause of degradation. This annealing is representative of thermal related device stability measurements but at accelerated rates. Thus the control of morphology while processing and over time is a difficult and important issue in optimizing the devices. [120]

To counter the effects of morphological changes, and in particular to prevent or reduce fullerene aggregation, a number of approaches have been implemented including in-situ polymerization of the fullerene,[121, 122] UV assisted oligomerization of the fullerene in the BHJ,[123, 124] solution blending of soluble chemically-derived dimer[125, 126] and even trimer derivatives of PCBM,[9] and introduction of small UV-curable bis-amide cross-linker as an additive to the BHJ layer.[127] The inclusion or formation of these polymerized or multimer fullerenes have typically shown a significant improvement in the long-term stability of the OPV devices under simulated aging. Drees et al. synthesized a glycidol ester modified PCBM molecule, which could be cross-linked in-situ by adding a drop of the initiator $Et_2O.BF_3$ (boron trifluoride diethyl etherate). AFM and TEM measurements showed that while PCBM based films tended to phase segregate upon annealing for prolonged periods at 140 °C, the PCBCG based films remained relatively smooth and uniform. However the current voltage statistics degraded considerably with annealing time, thus hindering its use in long term stability tests. More recently, it was demonstrated that device degradation due to thermal stress could be reduced by photo-induced cross-linking of fullerene in the device, which forms fullerene oligomers and stabilizes the eventual BHJ morphology. In a separate approach to this problem, researchers also synthesized fullerene based dimers, which were soluble in common organic solvents, to be used in BHJ. While Liu et al. directly fabricated the devices with these oligomers and managed to improve device efficiencies long term stability

measurements weren't carried out by the authors. Schroeder et al., however synthesized a similar dumb-bell shaped fullerene dimer, and saw that even though they could only add a fraction of it into devices to keep them efficient, that was sufficient to hinder the crystallization of the remaining PCBM molecules in the device, effectively stabilizing the morphology and improving the long term stability.

While synthesis and application of oligomeric and cross-linked molecules seem a promising approach to controlling the device morphology, most of these multimer fullerenes have either involved lengthy procedures for functionalizing the side groups (to maintain solubility for blends) or lack of control over the cross-linking. This would make reproducibility of devices an issue. On the other hand, a full understanding of the mechanism and kinetics of aggregation inhibition isn't understood yet, which could be the key for development of newer materials giving better control on the morphology.

The ability to control the morphology in the BHJ device can thus be seen as crucial parameter to not only optimizing the device performance but also enhancing the stability and overall lifetime. It is also important to systematically study the morphological development both through the thickness and in the plane of the active layer and correlate it to the device performance. With the use of new oligomeric fullerene derivatives (with good electronic properties) control could be achieved over the diffusion properties of the fullerene in the polymer. This would allow the study of bulk heterojunction in detail as well as predicting ways to achieve stable BHJ phase morphology through device processing conditions. Thus through the next few chapters and purview of the thesis research, a better understanding of the relationship between device architecture, morphology and performance will hopefully be developed.

2 EXPERIMENTAL TECHNIQUES AND METHODOLOGIES

2.1 DENSITY FUNCTIONAL THEORY

Density functional theory is a computational modelling technique used to determine the electronic states or environment of different atoms, molecules etc. in the ground state. This in turn allows the study of interactions between different sets of atoms or molecules, and in our particular case, between fullerenes and polymers. Solubility of C_{60} fullerene in various small molecules and formation of charge transfer states have been widely studied.[128] Recently this has been expanded to studying its interaction with a number of polymers including semiconducting polymers such as polyalkylthiophenes.[129] However, there still needs to be work done in this area to carefully study the effect of the interaction parameters (miscibility etc.) determined from the DFT studies of fullerene-semiconducting polymer systems, and consequently correlate it to the morphological development in the mixture.

As part of the joint DOE funded project with University of Akron and Oakridge National Laboratory, DFT simulations were carried out by Dr. Bobby Sumpter at the Center for Nanophase Material Sciences (CNMS), at ORNL (see Appendix). These were used to determine the binding energy values between different combinations of polyalkylthiophenes and fullerenes. The results were used to determine an estimate of the relative miscibility of the various fullerenes in the polyalkylthiophenes and also help explain the in-plane and out-of-plane phase morphological development in our bulk heterojunction system.

2.2 PREPARATION OF THERMO-CROSS-LINKABLE FULLERENES

2.2.1 Preparation of PCBCB-I

Preparation of a desired thermos-cross-linkable fullerene at device processing temperatures (~150 °C and above) was to be based upon the ability to modify the side chain of the readily available and already popular fullerene, phenyl-C_{60}-butyric acid methyl ester (PCBM). Due to its good miscibility in a variety of solvents, it served as a great starting product. More recently, as discussed earlier, number of groups had utilized the method of modification of the side chain of the PCBM molecule to get desired final products.[44, 119, 130-133] Most of these involved converting the PCBM firstly to its intermediate acid chloride, which subsequently can be substituted by various other groups to give the desired functionality.[44, 119, 130, 131] However, the step to form the acid chloride involves first forming the acid, Phenyl-C_{60}-butyric acid (PCBA). Although poorly soluble in most organic solvents, ortho-dichlorobenzene (o-DCB) could at times be used to carry out esterification reactions directly with PCBA itself.[132, 133]

So the first step involved conversion of PCBM to its acid (PCBA) by standard acid hydrolysis.[119] The acid was subsequently converted to the desired final product PCBCB-I via *N,N′*-dicyclohexylcarbodiimide (DCC) assisted esterification. Details of the reactions are described here.

Table 2.1 Materials for synthesis of PCBA from PCBM via acid hydrolysis

Material	Amount	Mol weight (g/mol)	millimoles
PCBM	500 mg	910.9	0.549
HCl (12 M)	20 ml	36.46	0.549
Acetic Acid	50 ml	60.05	0.832

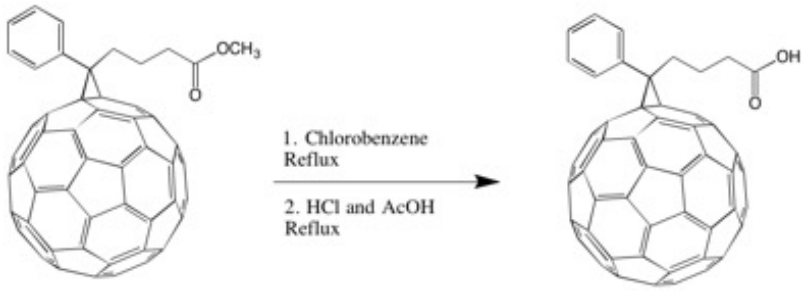

Figure 2.1 Schematic for acid hydrolysis conversion of PCBM to PCBA

For the first part of the synthesis, 500 mg of PCBM was degassed under vacuum for 20 minutes and then purged with N_2 in a 3-necked round-bottom flask. 200 ml of Chlorobenzene was introduced from one of the openings with constant stirring. The solution was kept under constant N_2 flow. It was then brought to the reflux temperature of 135 ^oC and stirred continuously for 3 hours. After 3 hours, the temperature of the solution was brought down. Subsequently, 20 ml of HCl and 50 ml of Acetic acid was introduced through one of the openings using a glass syringe. The temperature was then brought to the reflux temperature of 112 ^oC. The solution was stirred overnight (16 hours) to get the final product.

The final solution obtained was dried in-vacuo to remove most of the solvents. The remaining dry product was first rinsed in methanol for a couple of times and the solvent removed and the sample dried. The dry product was further purified, by dissolving in 3-5 ml of CS_2 and precipitating the solution in methanol. The precipitate was collected and dried to give ~90% yield of the final product, Phenyl-C_{60}-butyric acid (PCBA).

Table 2.2 Materials for synthesis of PCBCB-I from PCBA via acid DCC assisted esterification.

Material	Amount (mg)	Mol mass (g/mol)	millimoles
PCBA	80	896.90	0.09
BCB-OH	16	120.15	0.13
DCC	27	206.32	0.13
DMAP	16	122.17	0.13

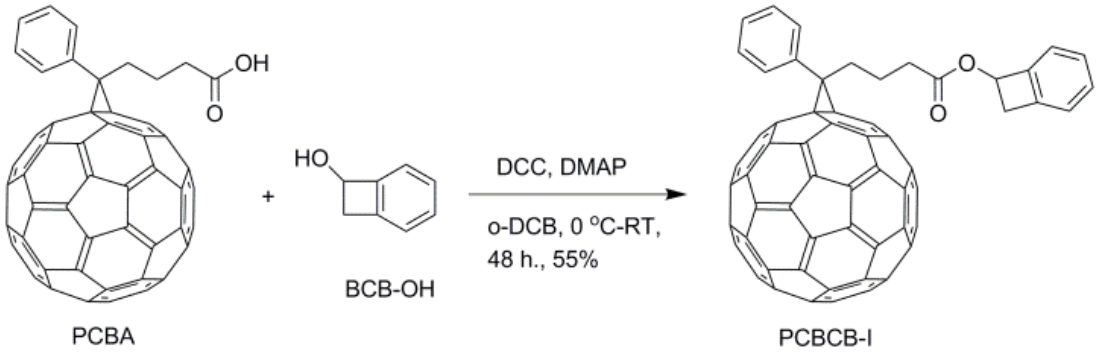

Figure 2.2 Schematic to show preparation of PCBCB-I fullerene from PCBA.

The second step involved the esterification of PCBA with the hydroxyl derivative of benzocyclobutene. Hydroxy-benzocyclobutene (BCB-OH) was synthesized by Karttikay Moudgil in the lab of Dr. Seth Marder, Department of Chemistry, Georgia Institute of Technology (See Appendix). The PCBA was subsequently reacted with BCB-OH under *N*,*N*′-dicyclohexylcarbodiimide (DCC)-assisted esterification conditions in o-dichlorobenzene (oDCB) in order to obtain the desired precursor product phenyl-C_{61}-butyric acid benzocyclobutene ester, (PCBCB-I) (see Scheme 1). 4-Dimethylaminopyridine (DMAP) was also added as a nucleophilic catalyst in the reaction. The choice of solvent was such because of the limited solubility of PBCA in most of the common organic solvents.

The mentioned amount of PCBA (80 mg) was added to a round-bottomed flask and vacuum dried and then purged with N_2. Nitrogen flow was maintained throughout as 30 ml of o-DCB was introduced into the flask whilst constantly stirring. Stirring was continued for a few minutes and then the solution was sonicated for 30 minutes to produce a clear brownish solution. BCB-OH was added to this solution and the solution was allowed to stir while the temperature was brought down to 0 °C using an ice bath. DCC and DMAP were introduced through one of the flask necks when the temperature approached 0 °C. The solution was allowed to stir and kept in the ice bath for 3 hours before being taken out into room temperature. The stirring continued and it was kept as such at room temperature for 1.5 days (around 40 hours). A clear dark brown solution started forming eventually, which was indicative of our final product.

The solution was dried in vacuo, to give our final product (PCBCB-I). PCBCB-I is readily soluble in common organic solvents (including DCM and hexanes), and was purified though column chromatography and characterized by ^{1}H NMR spectroscopy, mass spectrometry and HPLC (by Dr. Raghunath Dasari, see Appendix). Upon purification, 54.5 mg of the final product was obtained to get a final yield of 68.1%.

2.3 SOLUTION CHARACTERIZATION

2.3.1 Cyclic Voltammetry

Cyclic voltammetry measurements was carried out with the help of Dr. Raghunath Dasari, Department of Chemistry, Georgia Institute of Technology. The measurements were carried out under nitrogen in dry deoxygenated 0.1 M tetra-n-butylammonium hexafluorophosphate in dry CH_2Cl_2 using a CH Instruments CHI620D Electrochemical Workstation CHI620D and a conventional three-electrode cell with a glassy carbon working electrode, platinum wire counter

electrode, and an Ag wire coated with AgCl as the pseudo-reference electrode. Potentials were referenced to ferrocenium/ferrocene by using internal ferrocene. Cyclic voltammograms were recorded at a scan rate of 50 mV s^{-1}.

2.3.2 UV-Vis absorption spectroscopy

UV-vis absorption spectra measurements were carried out on a Varian Cary 5E UV-vis-NIR spectrophotometer. The standard wavelength range of 300-800 nm was chosen as the absorption measurements.

Using Beer Lambert's law for absorbance, calibration measurements for the solutions were carried out. The law states that:

$$A = \varepsilon cL \qquad [2.1]$$

Where A is the absorbance, ε is the molar absorptivity of the material, c is the concentration and L is the path length. For a specific material and fixed measuring path length (path length of the quartz cells), the absorbance becomes proportional to the concentration. Thus by measuring the absorbance of a material (absorbance value at the characteristic peak), at different concentrations, one can determine the calibration plot (Figure 2.3).Subsequently, one can derive the concentration of any other unknown solution by using its absorbance value and the calibration plot.

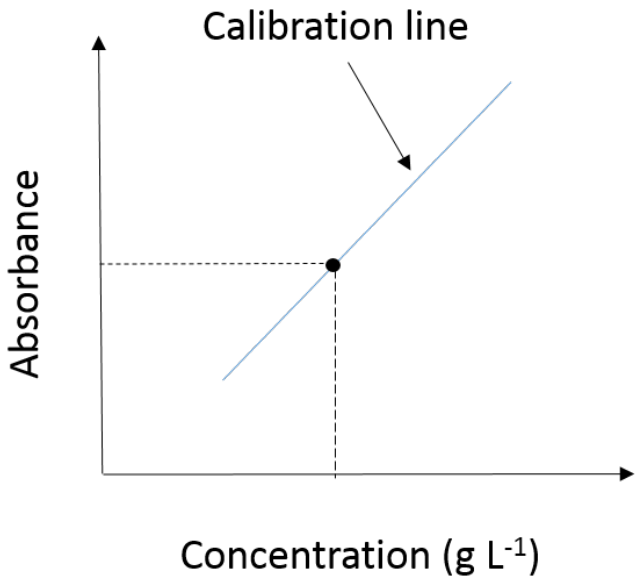

Figure 2.3 Measuring desired concentration value from UV-vis absorbance measurement and a calibration plot

For the calibration measurements in Chapter 6, solution absorption spectra measurements were carried out in quartz crystal glass cells. Solutions were made from SPS grade dichloromethane (DCM) solvent. Maximum absorbance of the calibrant solutions was limited to 0.8 in case of the 0.02 mg/ml solution of PCBCB-I in DCM and minimum to 0.05. For measuring the percentage conversion, thin films (1 mg) annealed at different temperatures and amount of time, were washed with 10 ml of solvent to give the solution to be measured. In case of the absorbance going beyond 0.8, the solution was diluted a further 10 times before measurement. The intensity of the characteristic peak in the measured solution was then matched to the calibrant line to determine the concentration of the fullerene precursor in the solution.

For thin film measurement of absorption spectra, films were spin coated onto pre-cleaned 1 inch by 1 inch glass substrates. For the pure fullerene solutions, a solution of 5 mg/ml in DCM was used and spun at 1500 RPM for 60 seconds to give the desired film on the glass substrate. For

the measurement of the BHJ devices, the solutions were spun from 10 mg/ml in o-DCB on to the glass substrates at a spin speed of 1200 RPM for 50 seconds. All annealing steps were carried out ex-situ in a glove box.

2.4 SCATTERING PRINCIPLES

Scattering is a physical process where an electromagnetic radiation such as visible light, X-ray or a particle e.g. neutron is deviated from its original path upon interaction with the inhomogeneity within the system through which it is passing. Depending on the passing wave or particle, different sort of interactions with the material determine the final scattering profile. So for example, in the case of X-rays, the interaction of the incident X-ray with the electron densities lead to scattering of the wave. Thus the inhomogeneity in electron density of different materials will give us corresponding elastic scattering of X-rays and hence scattering patterns. Once the reflected wave is scattered, it will have constructive interference in certain angles giving us corresponding peaks according to the formula (Bragg's Law)

$$n\lambda = 2dsin(\theta) \qquad [2.2]$$

Thus at large enough values of θ, the repeated atomic structure (e.g. crystal planes) can be studied using X-ray scattering (section 2.4.4). At smaller angles though, it is not possible to distinguish the variation in the electron densities in the repeated atomic structure level, and thus in those cases we get an idea of averaged electron density variation over larger phases (section 2.4.3).

2.4.1 X-ray generation for lab source radiation

X-rays are essentially short wavelength, high energy electromagnetic radiation with wavelengths ranging from 10^{-1} to 10^{-3} nm. X-rays are produced as a product of a number of

different mechanism in our universe including high energy nuclear fission, gravitational forces which give rise to neutron stars, and during growth of matter due to the pull of black holes. For the purpose of characterization however, we need a mechanism which allows us to harness these X-rays. Thus the common method of producing X-rays in a lab is through the use of a Coolidge tube.[134] A modern version of the Coolidge tube is shown in Figure 2.4.

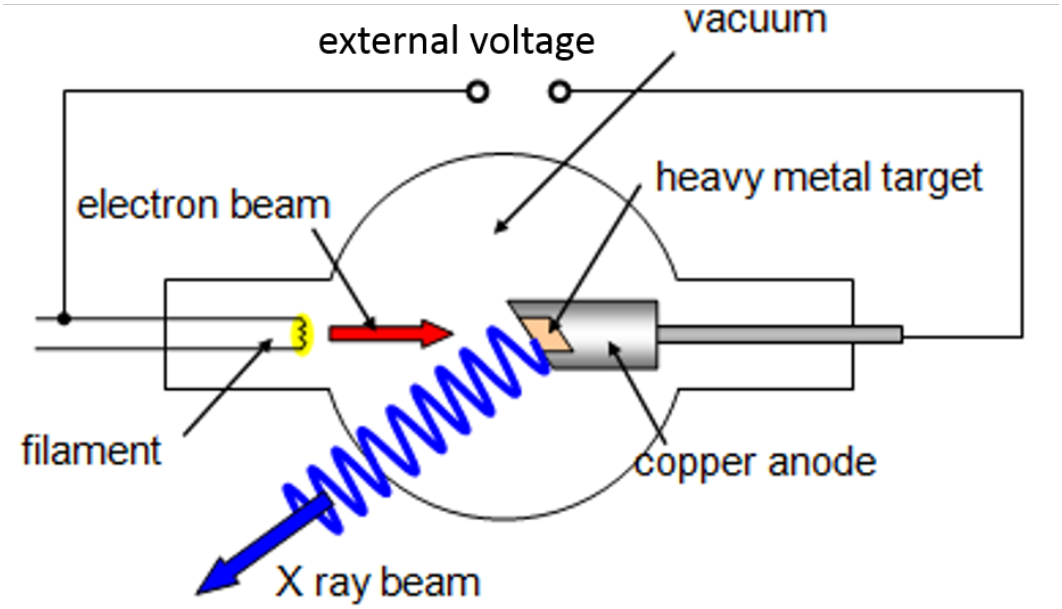

Figure 2.4 Schematic representation of X-ray production using a Coolidge tube (adapted from reference[4])

As we can see, the tube has a heating filament (usually tungsten) which can be heated by applying voltage across it (5-15 V). This leads to thermionic emission of electrons across the tube which is held under vacuum. At the other end of the tube lies a water-cooled target, possibly of a selected material (target) from which we generate the X-rays. Upon the impingement of the electrons onto the target material, the accelerated electrons (from the electron beam) are now slowed down by the electrons in the target due to interaction between them. Consequently, since energy needs to be conserved, the energy lost in the slowing process is released in the form of

radiation. The continuous deceleration of the particle as it approaches leads to a continuous spectrum as shown in Figure 2.5b.

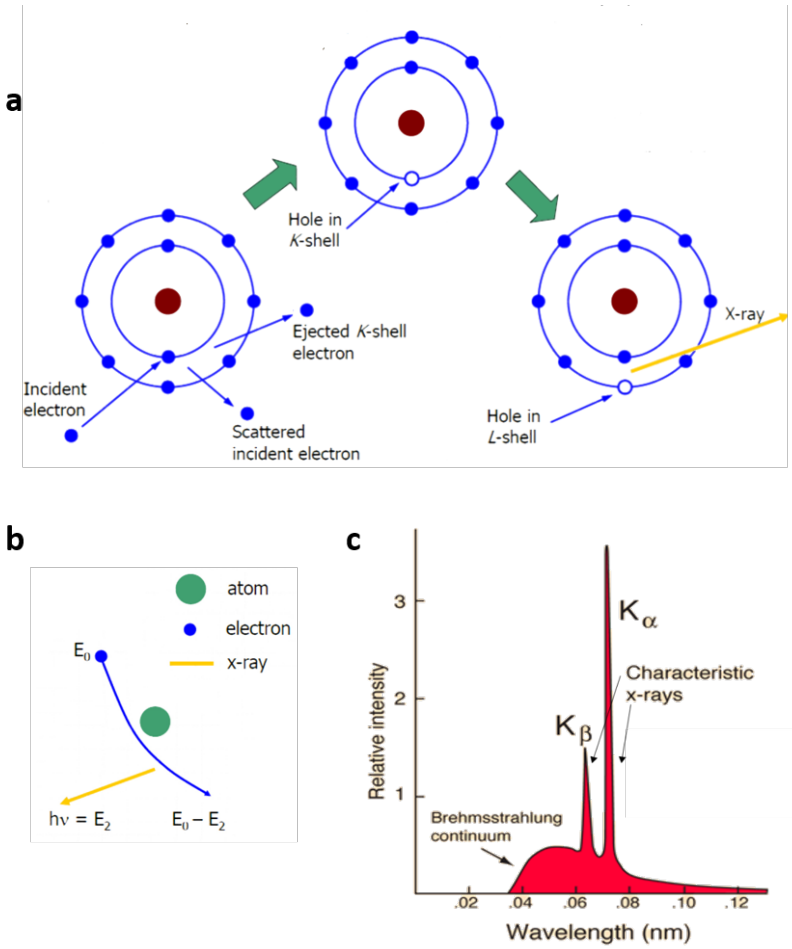

Figure 2.5 Origin of a) characteristic X-ray peaks, b) Brehmsstrahlung spectrum, c)X-ray spectrum depicting continuous Brehmsstrahlung spectrum as well as the characteristic peaks for a Molybdenum target material at 35 kV (adapted from reference[135])

This is known as the Bremsstrahlung spectrum. The characteristic spectrum, discovered by Mosley and Bragg, however occurs when the impinging electron manages to displace an electron from the inner shell of the target materials leading to the formation of a hole. This hole is

subsequently filled by an electron from the outer shell of the target material. Due to that electron going from a higher energy outer shell to a lower energy inner shell, energy is released in the form of radiation at a characteristic wavelength (k_α, Figure 2.5a). These are useful for scattering studies since these now give us a source of radiation at a particular wavelength and energy. There can be a number of characteristic peaks for a given material depending on the orbital level of the hole and the electron which replaces it. Usually $k_{\alpha1}$, $k_{\alpha2}$ are the strongest wavelengths and some common examples of target materials and characteristic wavelengths used in X-ray scattering in house machines are given below:

Table 2.3 Characteristic wavelengths (A) of some commonly used X-ray sources (adapted from various sources)

Element	**K_α**	**K_β**
Cr	2.29	2.08
Fe	1.93	1.75
Cu	1.54	1.39
Mo	0.71	0.63

2.4.2 X-ray and Neutron generation for synchrotron source radiation

Classically, the Larmor formula defines the radiated power (P) associated with an accelerating charged particle:

$$P = \frac{q^2 a^2}{6\pi\varepsilon_0 c^3} \qquad [2.3]$$

in which q is the particle charge, a is the acceleration and ε_0 is the permittivity and c is the speed of light. However, radiation at near relativistic speeds depend upon a relativistic acceleration and the equation gets modified by the incorporation of a factor γ:

$$\gamma = \frac{1}{\sqrt{1 - \frac{v^2}{c^2}}} \qquad [2.4]$$

in which *v* is the particle velocity. Charged particles travelling at such high speeds, when limited to a curved trajectory (of radius r), thus emit electromagnetic radiation according to the formula:

$$P = \frac{q^2 \gamma^4 v^4}{6\pi\varepsilon_0 c^3 r^2} \qquad [2.5]$$

γ can alternately be related to the energy of the charged particle (E_k) by:

$$\gamma - 1 = \frac{E_k}{mc^2} \qquad [2.6]$$

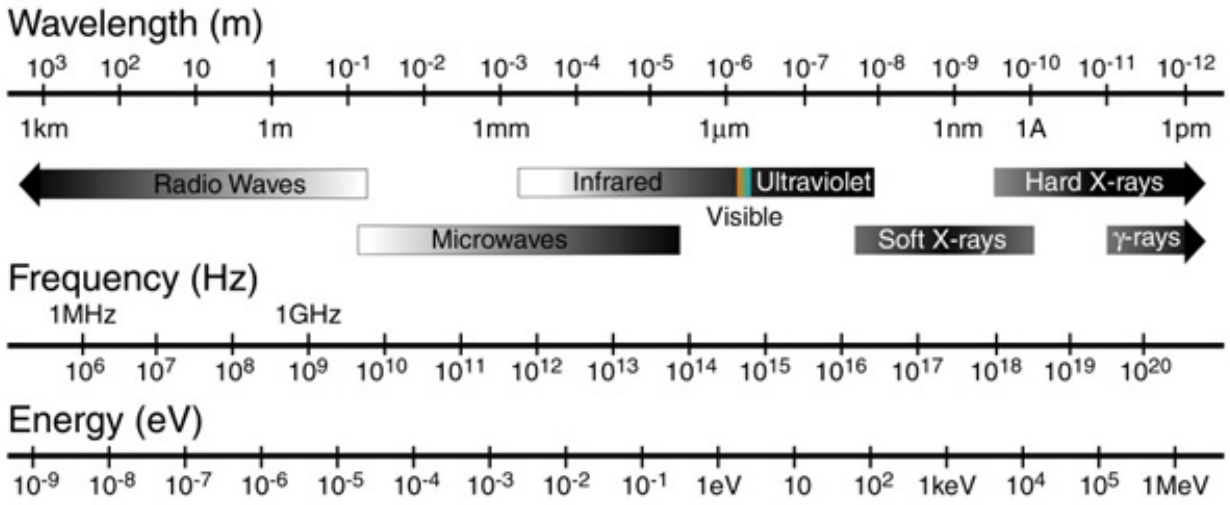

Figure 2.6 Electromagnetic spectrum (reproduced from reference[4])

Thus, X-rays alternatively can be generated from charged particles travelling at relativistic speeds and that the lightest particles (electrons and positrons) would generated the highest intensity beams. Since, the power scales with E_k^4, thus depending on the energy of the accelerating particle, we can get final electromagnetic radiation over a wide variety of wavelength (from infra-red to

hard X-rays, Figure 2.6) Thus we get a source of X-rays which are not only tunable in energy but also has an intensity or brilliance up to 10^{10} times a lab X-ray source.

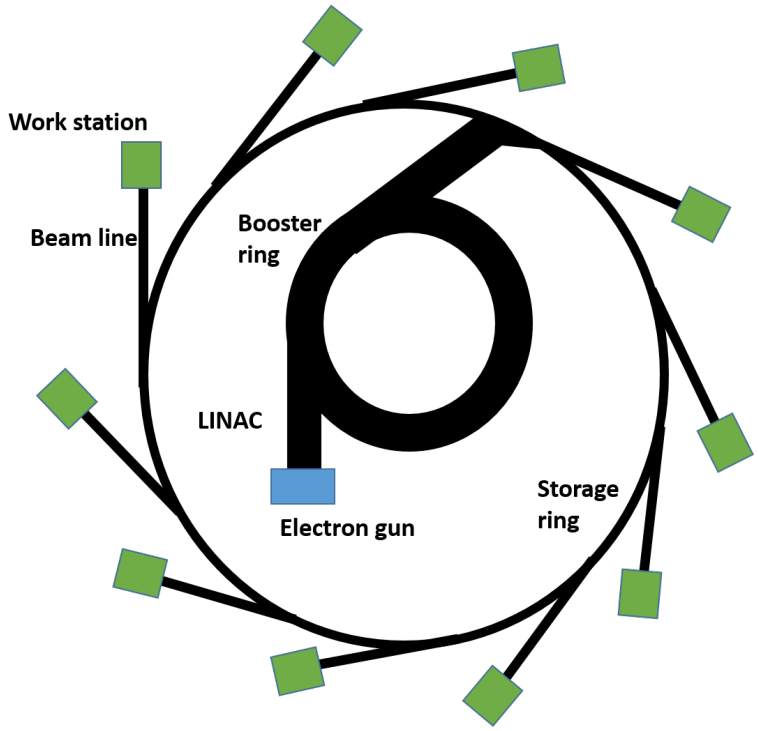

Figure 2.7 Schematic of the top view of a synchrotron light source setup

Due to the high energy of the electrons required, the X-rays in most synchrotrons are produced over a number of steps Figure 2.7. The first step is similar to that of lab X-rays where electrons are produced in an electron gun via thermionic emission of a tungsten cathode. They are subsequently accelerated to energies of around 10 MeV in a linear accelerator. This is done using a series of Radiofrequency cavities operating at high frequencies. Because of this, the radiation is separated into bunches. This is usually followed by further acceleration using boosters (large ring like chamber, ~100 m in circumference) where there are numerous electromagnets to keep the beam inside the synchrotron and a radiofrequency cavity to accelerate the beam further. Upon passing through the booster, the beam finally reaches the storage ring. This is an even larger

circular ring like chamber made of numerous straight section arcs. Each arc has bending magnets to bend the high energy electron beam (at near relativistic speeds) and produce X-rays (synchrotron light) according to the phenomena discussed earlier (Equation 2.5). Individual beam lines are positioned such that they can directly capture the synchrotron light as the incident beam for the scattering measurements. The high energy and high flux synchrotron light beam allows flexibility in studying a number of different materials (including weak scattering materials), as well as in different modes (transmission versus grazing-mode) and considerably reduces the measurement time.

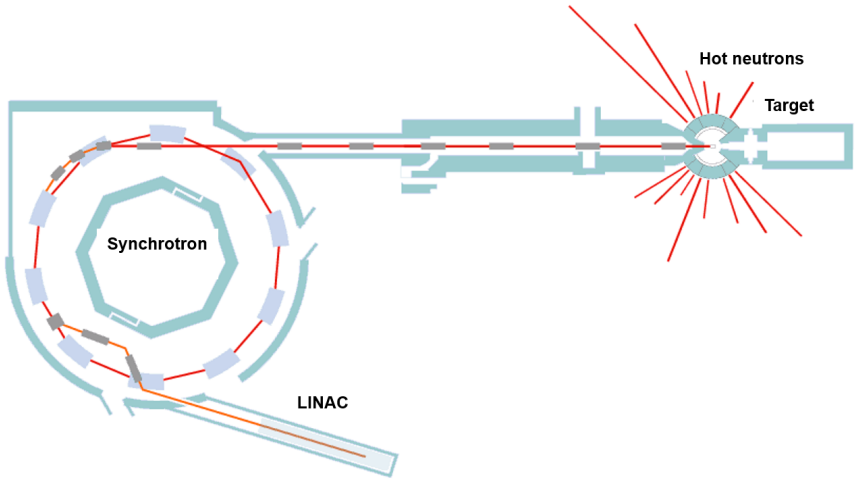

Figure 2.8 Schematic showing the generation of neutrons at a spallation source (adapted from reference[136])

Neutron sources originate from different processes involving the liberation of excess neutron from neutron rich nuclei (e.g. Be, U, Ta, Pb). Few of the specific sources used for scattering purpose include continuous reactors, spallation reactors and pulsed reactors. The source used in our studies (at SNS, Oak Ridge National Lab and SURF, Rutherford Lab) was a spallation source.

In a spallation source, initially a beam of high kinetic energy of H- ions (around 70 MeV at SNS, ORNL) produced using a linear accelerator (Figure 2.8).These are injected into a synchrotron ring to reach even higher energy levels. These beams are passed through a foil which strips them off the electrons leaving behind the protons. These high energy proton beams are then impinged onto target with neutron rich nuclei at a pulse rate of 60 Hz. Around 10-30 neutrons per proton are produced with energies around 1 MeV. These neutrons are then moderated (slowed down using water and some coolant) and directed to the different beam lines for use in different form of scattering experiments. Cold neutrons (slow and of larger wavelength) are better for studies of structure and dynamic studies due to better spatial resolution.

As discussed before, at small incident angles, although it is not possible to study the electronic or other material property variations at an atomic level, an average variation over larger phases can be detected by studying the scattering profile. The principle of this being that scattering of neutron and X-ray occurs through interaction with the nucleus (nuclear scattering) or with the surrounding electron cloud (X-ray scattering). So, if we represent the wavefunction of the incident plane wave as:

$$\psi_i = e^{ikz} \qquad [2.7]$$

in this z is the distance from the scattering object in the propagation direction and k is the wave-number.

2.4.3 Small angle scattering principles (SANS and SAXS)

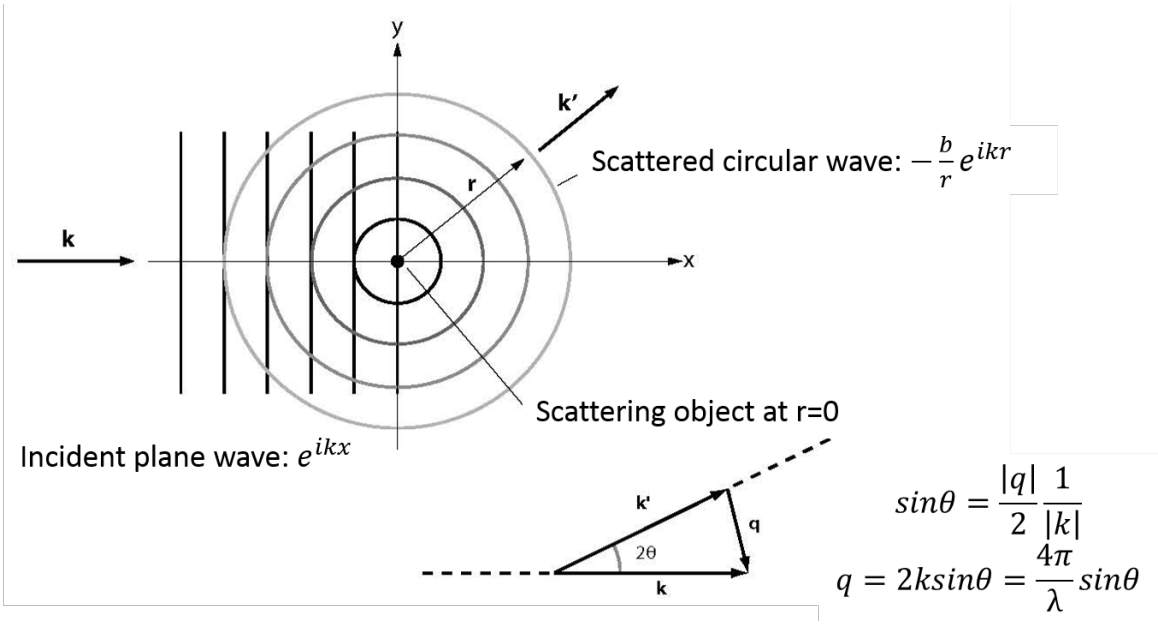

Figure 2.9 Elastic scattering from a point source and the definition of wave-vector q (adapted from reference[137])

Then the scattered wavefunction could then be represented as (assuming the wave is scattered from a point scatterer)[138]:

$$\psi_s = -\frac{b}{r}e^{ikz} \qquad [2.8]$$

where b is called the nuclear or electron scattering length, representative of the interaction of the incident (X-ray or neutron) beam with the corresponding electron cloud or nucleus.[137, 139] The scattering length density is an inherent property of the material. It is different for X-rays and neutrons for the same material. Extrapolating from the case of interaction with a single atom, if we take a three dimensional assembly of atoms, the corresponding scattering wavefunction would be:

$$\psi_s = -\sum_i -\left(\frac{b_i}{r}\right)e^{ikz}e^{iq.r} \qquad [2.9]$$

in which we have a quantity q defined as the scattering vector (from Figure 2.9):

$$q = k - k' = \frac{4\pi}{\lambda sin\theta} \qquad [2.10]$$

k and k' being the incident and scattered wavevectors.

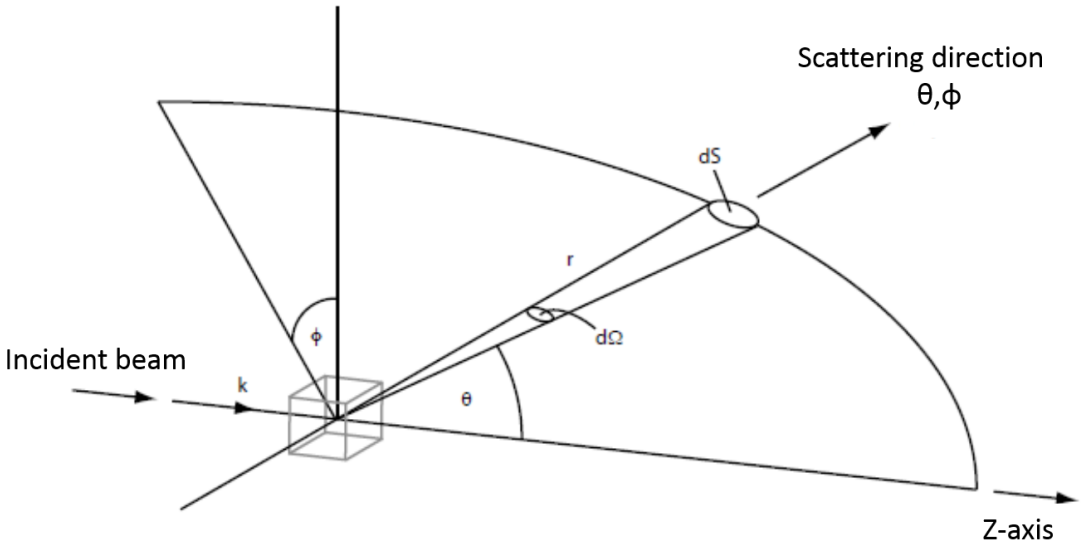

Figure 2.10 Geometry of a scattering experiment (adapted from reference[137])

A small angle scattering experiment usually measures a term called the differential cross-section ($d\sigma/d\Omega$) which is the differential of the scattering cross-section (σ_s) with respect to $d\Omega$ which is a solid angle. Looking at Figure 2.10, we see that this is effectively the measure of the number of scattered X-ray photons/neutrons in a solid angle $d\Omega$ at an angle (θ,Φ), since the scattering cross-section (σ_s) is defined as:

$$\sigma_s = \frac{Total\ number\ of\ scattered\ neutrons\ or\ x-rays\ per\ second}{Number\ of\ incident\ neutrons\ or\ x-rays\ per\ unit\ area\ per\ second}$$

$$\sigma_s = \int \frac{d\sigma}{d\Omega} d\Omega \qquad [2.11]$$

Using the formula for the scattered waves (equation 2.9) and some manipulation, we eventually get the differential scattering cross-section to be:

$$\frac{d\sigma}{d\Omega}(q) = \frac{1}{N}\left|\sum_{i}^{N} b_i\, e^{iqr}\right|^2 \qquad [2.12]$$

This equation however still takes into account the scattering length from each individual atom in the system. In materials characterization, the length scales that are studied are much larger than atoms and it is easier to think in terms of bulk properties. So a quantity called the scattering length density (SLD) 'ρ' is defined for a number of n atoms in a volume V as:

$$\rho = \frac{\sum_i^n b_i}{V} \qquad [2.13]$$

For scattering experiments, the differential scattering cross-section (dσ/dΩ) is normalized by the sample volume (V) to get the macroscopic cross-section (dΣ/dΩ). This can then be calculated (by replacing the summation used in case of atom (equation 2.12) to an integral used for the continuous SLD) as:

$$\frac{d\Sigma}{d\Omega}(q) = \frac{N}{V}\frac{d\sigma}{d\Omega}(q) = \frac{1}{V}\left|\int \rho(r) e^{iqr} dr\right|^2 \qquad [2.14]$$

We thus see that the scattering profile arises out of the inhomogeneity in the distribution of the scattering length in the system and consequently of the material. The integral term is the Fourier transform of the scattering length density distribution. However, since the term is squared, we cannot directly do a reverse Fourier transform of the macroscopic cross-section (dΣ/dΩ) to get the scattering length density profile. This gives rise to the technique of small angle scattering models, which assuming certain composition and distribution and then try to predict the overall profile to match the scattering profile obtained from measurements. Depending on the type of materials, and their distribution, the scattering length density profile may vary giving us different simplified models and equations for calculations and fitting of the dΣ/dΩ profile.

As mentioned earlier, the SLD varies for X-rays and neutron. Also, unlike X-rays where they vary periodically with changing atomic number/number of electrons, the scattering length density for neutrons varies much more randomly. Since the scattering profile is dependent upon the inhomogeneity in the SLDs, this property becomes useful. The scattering length density is quite different even between isotopes as is seen in the case of hydrogen and deuterium. This allows of contrasting between two or more different phases (which might be quite similar) in a system just by incorporating a deuterium instead of hydrogen in a molecule. These principles form the basis of most X-ray and neutron based small and large angle scattering measurements which are discussed in the following sub-sections.

2.4.4 X-ray scattering for bulk characterization (WAXS)

Incident X-rays produced either from lab or synchrotron source may interact with matter in a number of different ways.[140] The X-ray may show no interaction (if they are low energy long wavelength X-rays), get converted to heat, show photoelectric effect, fluorescence, Auger electron production among others. These form the basis for a number of other characterization techniques including X-ray photoelectron spectroscopy (XPS), X-ray fluorescence spectroscopy (XRF), Auger spectroscopy etc.

As discussed earlier in Section 1.4, the interaction of X-rays with matter, specifically with the electron cloud of the material being studied, also leads to coherent scattering. This forms the basis of X-ray scattering and diffraction studies for material characterization. It has also been mentioned earlier, at large enough theta angles, or q values, the fulfilment of Bragg's law (equation 2.2) allows us to look at atomic repeat distances for various materials. This technique is called wide Angle X-ray scattering (WAXS) or wide-angle X-ray diffraction (WAXD). Using incident

X-rays at specific wavelength (either from lab or synchrotron source) and detecting the scattered X-ray on a 2-D or 1-D detector can give us the diffraction pattern for the material commensurate with its atomic crystal structure.

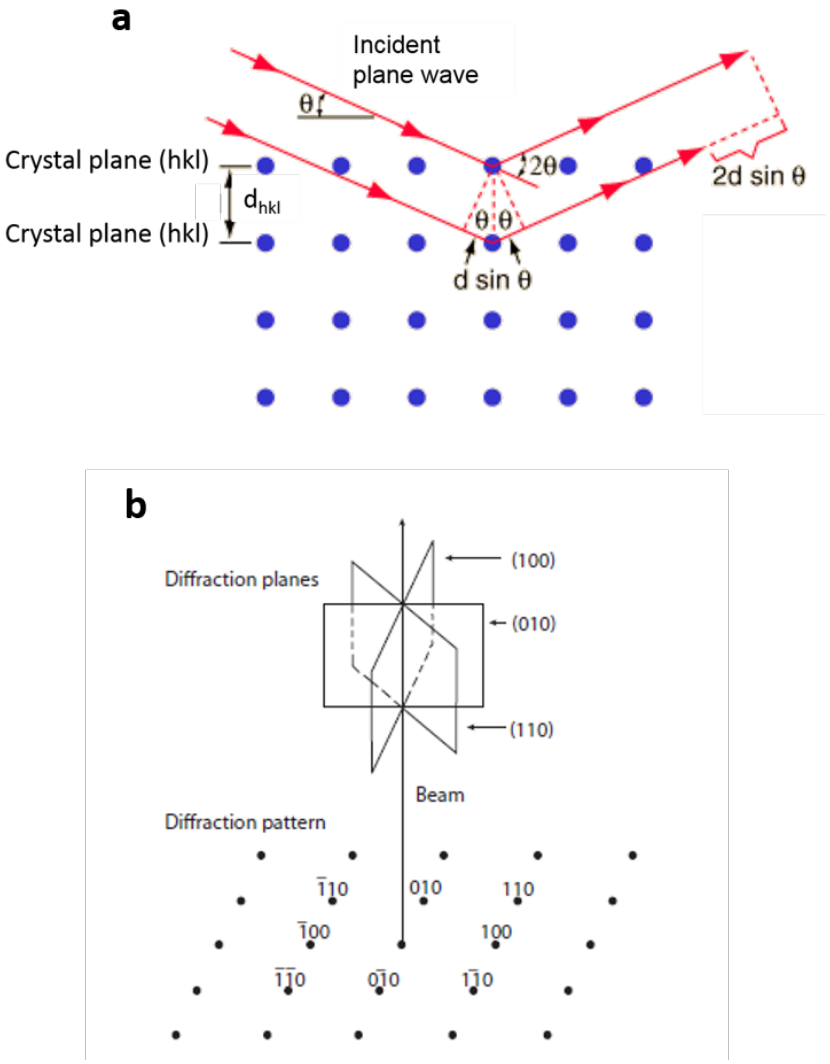

Figure 2.11 a)X-ray diffraction from crystal planes in accordance to Bragg's law (adapted from reference[135]) b) correlation between real space crystal planes and diffraction pattern.

When X-rays reflect from atomic crystal planes (Figure 2.11a), the diffraction is determined according to the Bragg's Law (Equation 2.2). Thus for a specific sample, if the λ is

known and θ is measured from the diffraction pattern, we can determine the d_{hkl} spacing of that specific crystal plane (where <h, k, l> refer to the Miller indices and combine to represent a specific crystal plane such as <100> or <111>). Upon diffraction, a crystal plane is represented by a spot of constructive interference of the scattered X-rays. These diffraction patterns however are not in real space and form an array of diffraction points called the reciprocal lattice. Since, the intensity of the scattered X-ray wave is seen to be a Fourier transform of the electron density distribution, or the lattice distribution of the material. Thus the diffraction pattern is in fact a Fourier transform of the crystal lattice pattern with its spacing being reciprocal to the real space lattice spacing.

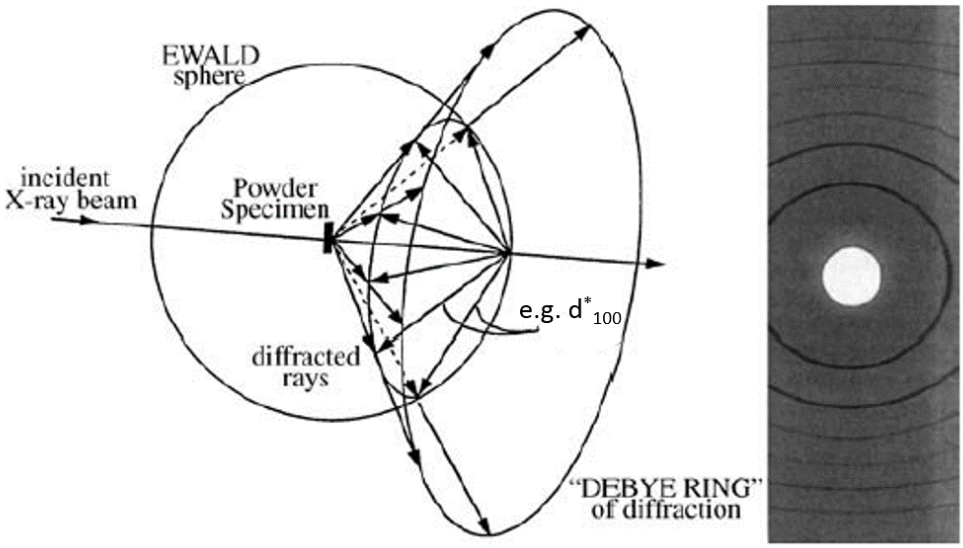

Figure 2.12 Ewald sphere showing the ring pattern obtained by the XRD of a powdered (isotropic) crystal sample in transmission mode (adapted from reference[141]).

Thus to better understand the diffraction pattern, we define a d-spacing (d*) in reciprocal space which is the inverse of the real space d-spacing (d). So we have d* related to the real space in the form:

$$|d^*_{hkl}| = \left|\frac{1}{d_{hkl}}\right| \quad [2.15]$$

$$d^*_{hkl} = ha^* + kb^* + lc^* \quad [2.16]$$

Where a*,b* and c* are the unit vectors in the reciprocal space. Alternatively, the distances in reciprocal space can be expressed in terms of scattering vector q (defined earlier Section 2.4.3) and by using equations 2.2 and 2.10 can be related to d spacing by:

$$d_{hkl} = \frac{2\pi}{q_{hkl}} \quad [2.17]$$

In addition, to better understand formation of diffraction patterns, one can introduce the concept of Ewald sphere (Figure 2.12).[142] The Ewald sphere is a concept used to graphically understand the formation of reciprocal lattices at different theta angles in accordance with Bragg's Law. The Ewald sphere is an imaginary sphere with a radius of λ^{-1}. The center of the sphere represents the position of the crystal to be measured and incident beam is a line which the passes through the center. We see that the intersection of the Ewald sphere with the different diffraction points occur at different 2theta angle (satisfying the conditions for Bragg's law) and each of those represent a lattice plane that has a different diffraction angle. Not all systems are perfectly aligned crystals however. In those cases similarly, the diffraction pattern can be explained by the intersection of the Ewald sphere and the diffracted beams at specific 2theta angles (corresponding to the specific crystal planes). We see the setup for that in Figure 2.12, called the transmission mode. The interaction of a 3-D Ewald sphere with diffracted X-rays in isotropic distributed crystal will give us diffraction rings on our detector. The distance of these rings from the center are representative of their reciprocal d-spacing and can be converted to the actual d-spacing of the crystal planes by inverting it.

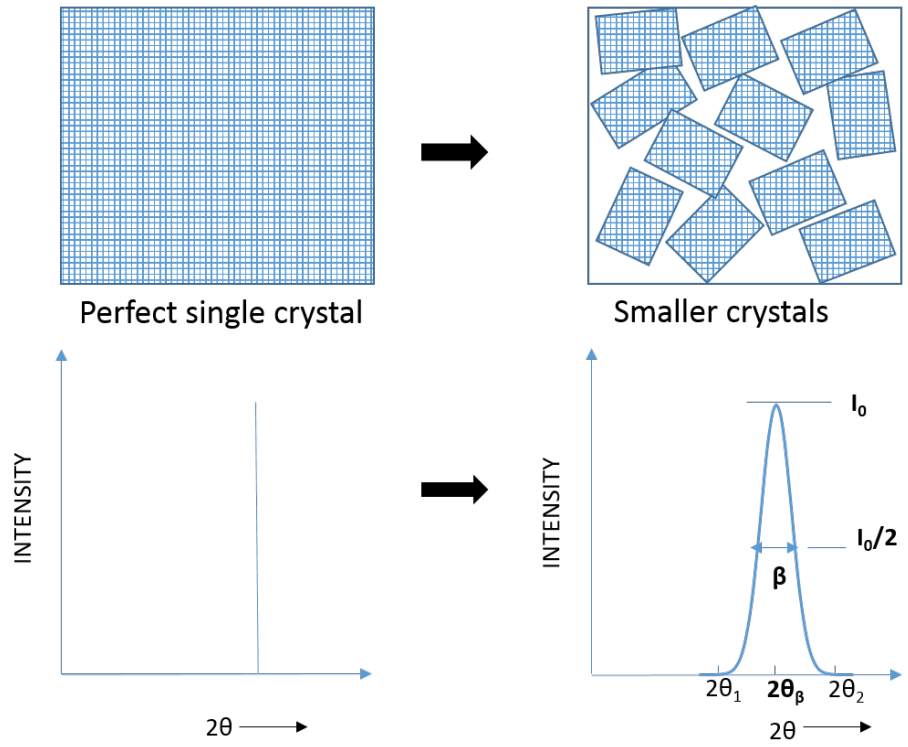

Figure 2.13 Crystal structure and corresponding diffraction peak pattern.

In many cases, as one would expect with samples which aren't perfectly crystalline, the variation from a perfect electron density distribution is translated into a specific width of the crystal diffraction peak (Figure 2.13). Thus the peak is significantly broader than the sharp peak observed in single crystals (ideally width=0 for perfect crystal). Scherrer's equation noted that the peak width is proportional to and can be used to calculate the size of the crystal domains using equation 2.18.[143]

$$\tau = \frac{K\lambda}{\beta cos\theta_\beta} \qquad [2.18]$$

In this equation τ is the mean size of the ordered (crystalline) domains, which may be smaller or equal to the grain size, K is a dimensionless shape factor, with a value close to unity. The shape

factor has a typical value of about 0.9, but varies with the actual shape of the crystallite, λ is the X-ray wavelength, β is the line broadening at half the maximum intensity (FWHM), after subtracting the instrumental line broadening, in radians. This quantity is also sometimes denoted as $\Delta(2\theta)$ and θ_β is the Bragg angle

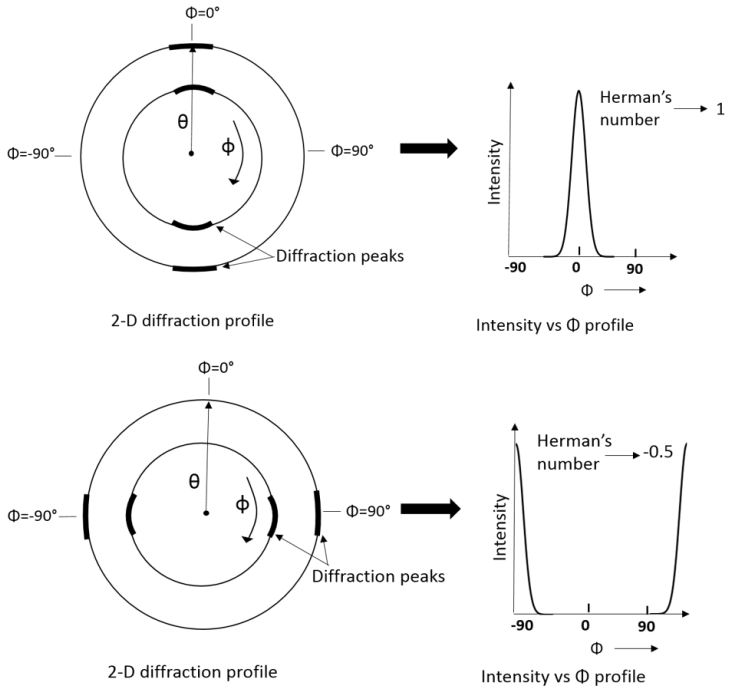

Figure 2.14 Azimuthal integration plots from 2-D diffraction pattern and calculation of Herman's orientation factor from them.

Thus XRD is an important tool for the analysis of the crystal morphology of materials which aren't single crystals or completely crystalline, for e.g. semi-crystalline polymers. In addition to the crystal domain size, the position and intensity of the diffraction peaks could also be used for determination of the crystal orientation in the material with respect to specific directions. The Herman's orientation factor (f_H) was defined to calculate the relative orientation of the crystalline plane towards or perpendicular to an axis using its intensity variation in the azimuthal

direction (angle Φ,Figure 2.14). Setting the selected axis to zero, the intensity is calculated from -90 to 90 degree to get the 1-D integration plot. The Herman's orientation factor (f_H) as a function of the azimuthal angle $'\Phi'$ around the diffraction ring, was calculated using the formula:

$$f_H = \frac{3 < cos^2 \Phi > -1}{2} \qquad [2.19]$$

in which $<\cos^2\Phi>$ is the average cosine squared value for the diffraction ring and is calculated using the following equation:

$$< cos^2 \Phi >= \frac{\sum_{i=0}^{90} I_i cos^2 \Phi_i \sin\Phi_i}{\sum_{i=0}^{90} I_i \sin\Phi_i} \qquad [2.20]$$

f_H ranges between -0.5 and 1; a value of 1 suggesting perfect alignment towards the chosen axis and -0.5 for perfectly perpendicular alignment to the chosen axis. All other alignments give values in between, with the proximity to 1 or -0.5 suggesting the degree of orientation towards those axes. Completely randomly oriented crystals give a Herman's orientation factor of 0

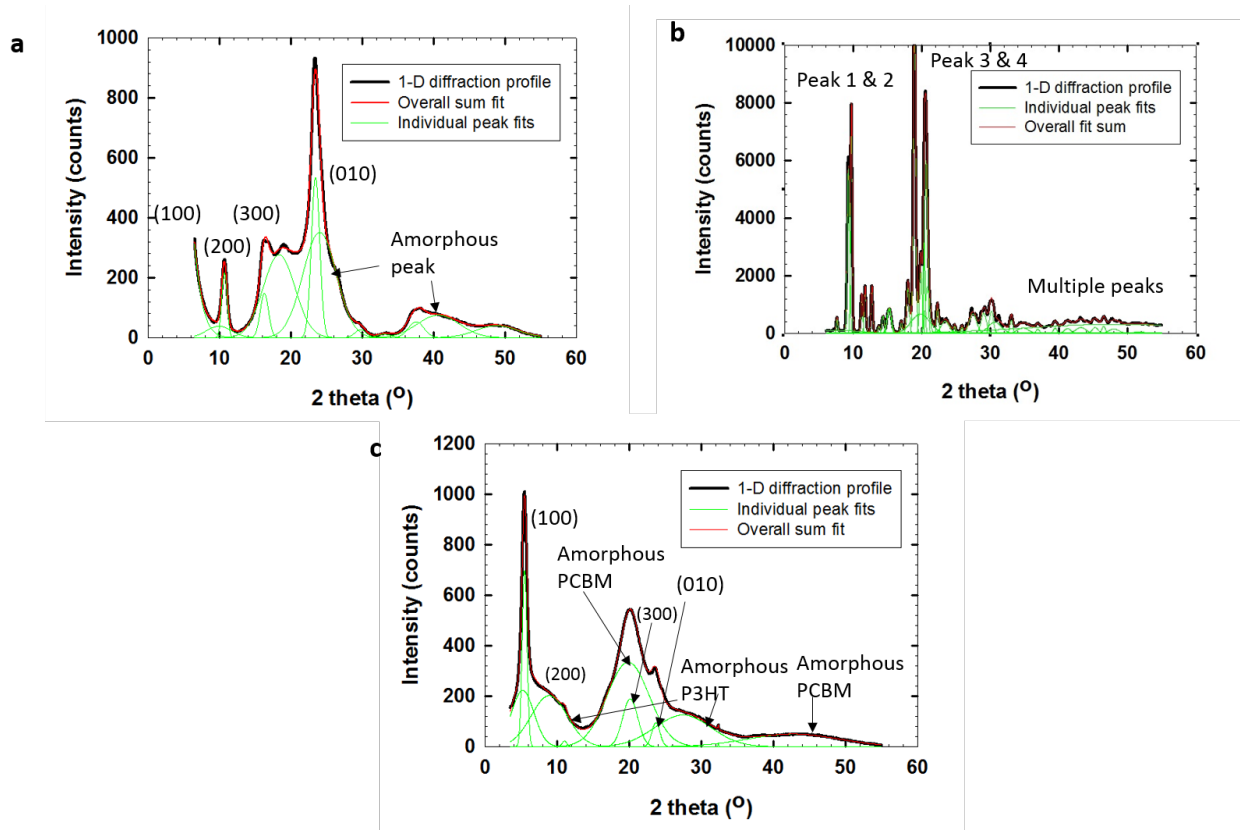

Figure 2.15 WAXS 1-D plots to determine the percentage crystallinity in P3HT-PCBM blends. 1-D plots and fit-peaks for a) pure P3HT film b) pure PCBM film c) P3HT-PCBM blend film

Lastly, in many materials, as is in semi-crystalline polymers, the percentage crystallinity is considerably less than 100%. Thus the percentage crystallinity can be calculated using the peak intensity profile over the entire reciprocal space. If the pattern is symmetric, integration over only half the space is good enough. The integrated intensity with respect to the diffraction angle 2 theta (2θ) gives us a profile which show the characteristic peaks at corresponding characteristic 2θ values for different crystal planes (Figure 2.15). Amorphous regimes in contrast show a broader peak over a longer range of 2θ.

Since X-ray diffraction is mass-dependent (intensity proportional to the amount of material present), thus the relative intensities of the crystalline and amorphous peaks are representative of

the relative content of each. So we can deconvolute the amorphous (broader) peaks from the crystalline (narrow) peaks and taking the area under those curves. This might be a bit complicated for sample blends however.

$$percentage\ crystallinity = \frac{Area\ under\ crystalline\ peaks}{Total\ Area\ under\ peak\ profile} \times 100 \qquad [2.21]$$

So firstly, the peaks in the pure samples (polymer and fullerene) can be identified from their scattering profile. The scattering for each is subtracted for background. In our case, a linear background was taken.[144] We subsequently find the constituent crystalline and amorphous peaks by fitting peaks as well as knowledge of peak positions from literature to use as input parameters in a fitting program (Fityk 0.9.8). A Levenberg-Marquadt least square fitting algorithm is subsequently used to obtain the final peak position and widths and the overall peak summation to match the scattering profile (Figure 2.15a and b).

Using the peak information from the individual samples, the input peaks for the blends are obtained. These undergo a similar fitting procedure as before, to finally derive the individual peak parameters for the blends. The peaks in the blends can be identified as crystalline or amorphous (Figure 2.15c), and can be assigned to the specific component (polymer peaks or fullerene peaks), by comparing with the individual fits (Figure 2.15a and b). To get the values of the amorphous content and crystalline content of the semi-crystalline polymer systems the equation 2.21 thus gets modified as:

$$percentage\ crystallinity\ (polymer) = \frac{Area\ under\ polymer\ crystalline\ peak}{Total\ area\ under\ polymer\ peaks} \qquad [2.22]$$

2.4.5 X-ray scattering for thin film characterization (GIWAXS)

Despite the high brilliance and intensity of synchrotron radiation as well as the great penetration depth of X-rays, scattering experiments of thin films in transmission mode gives us very little scattering information about the thin film surface itself. The reason for this being that most thin films are produced on substrates and are a few orders thinner (~10-200 nm) than the substrate thickness (~0.5 mm). Consequently, in the transmission mode, scattering from the thin film is overshadowed by that of the substrate. To overcome this issue a new mode of scattering was developed known as grazing incidence X-ray scattering (GIXS).[145]

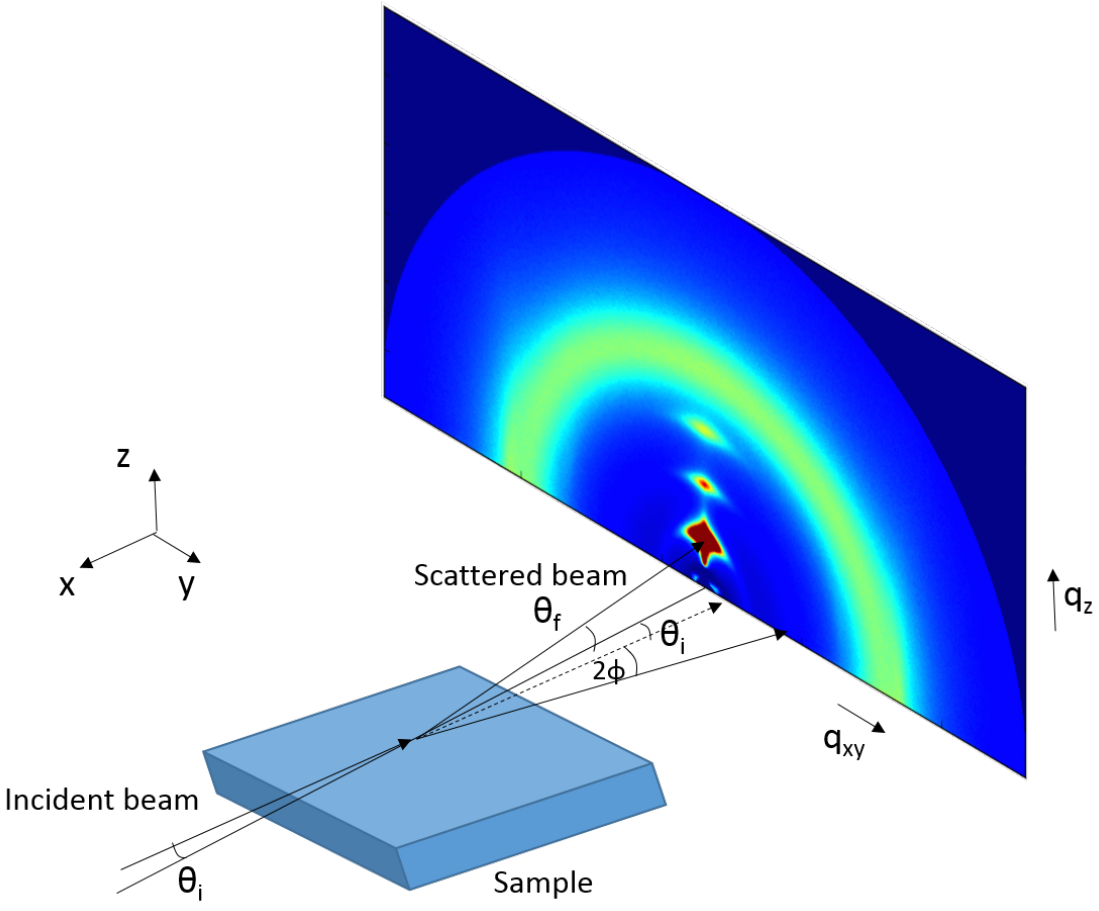

Figure 2.16 GIWAXS setup showing diffraction pattern on a 2-D detector.

A GIWAXS setup is as shown in Figure 2.16.GIWAXS combines the principles of wide angle X-ray scattering (WAXS) and X-ray reflectivity (XRR). At really small angles of incidence (θ_i), the X-ray beams upon entering the thin films, can be totally reflected from the substrate and give us diffraction patterns from the characteristic features in the thin film. Using the principles of XRR, incident X-rays come in near parallel form and get total reflection from the substrate at an angle θ. Using Snell's law and the dependence of the refractive index on the scattering length density, we get the critical angle for total reflection θ_c as:

$$n = 1 - \delta - i\beta \qquad [2.23]$$

$$cos\theta_c = n\,, \theta_c = \sqrt{2\delta}\ for\ small\ incident\ angles$$

Where δ and β are the dispersive and absorptive aspects of the X-ray-matter interaction. By looking at equation 2.23 we see that most materials would have an n<1. Thus by choosing incident angles (θ_i) slightly greater than the critical angle (θ_c) of the polymer but lesser than the critical angle of the substrate, ensures the beam refracts away once it enters the thin film, diffracts from the thin film material and get totally internally reflected at the substrate as in Figure 2.17. The diffracted beam from the thin film is collected onto a 2-d detector as our final diffraction pattern as shown earlier in (Figure 2.16). Peaks and characteristic features on the vertical axis represent crystalline planes which are parallel to the substrate (in-plane) while peaks on the horizontal axis are for crystalline planes which are perpendicular to the substrate (out-of-plane). Thus the integration for a specific peak (crystal plane) along the azimuthal angle can be used to determine the Herman's orientation factor (describe earlier in Section 1.4.4) to determine the orientation of that crystal plane with respect to the in-plane our out-of-plane direction.

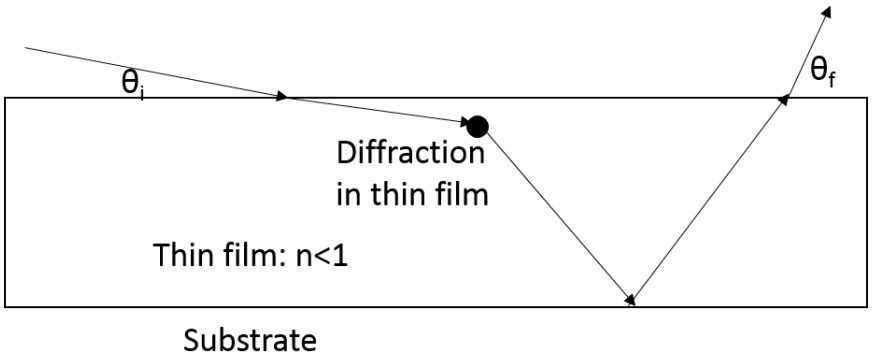

Figure 2.17 Diffraction in thin film from grazing incident X-ray beam.

Once the 2-D intensity profile is obtained in terms of q-space, one can treat it similar to the 2-D WAXS data and also carry out analysis of the crystal d-spacings, domain size and percentage crystallinity as well from the 2-d (I vs q or I vs Φ) integration plot (as discussed earlier in Section 1.4.4).

2.4.6 Neutron scattering for bulk characterization (SANS)

We have described and discussed earlier in equation 2.14, the small angle scattering profile of a sample depends upon the inhomogeneity of the SLDs of the components or the SLD distribution in the system. It is important to note that only the coherent component of $d\Sigma/d\Omega$ (scattering cross-section) contributes to information related to material distribution. Upon further operating on equation 2.14, the scattering profile can be de-convoluted into the effects of the material composition, scattering lengths and spatial arrangements of materials.

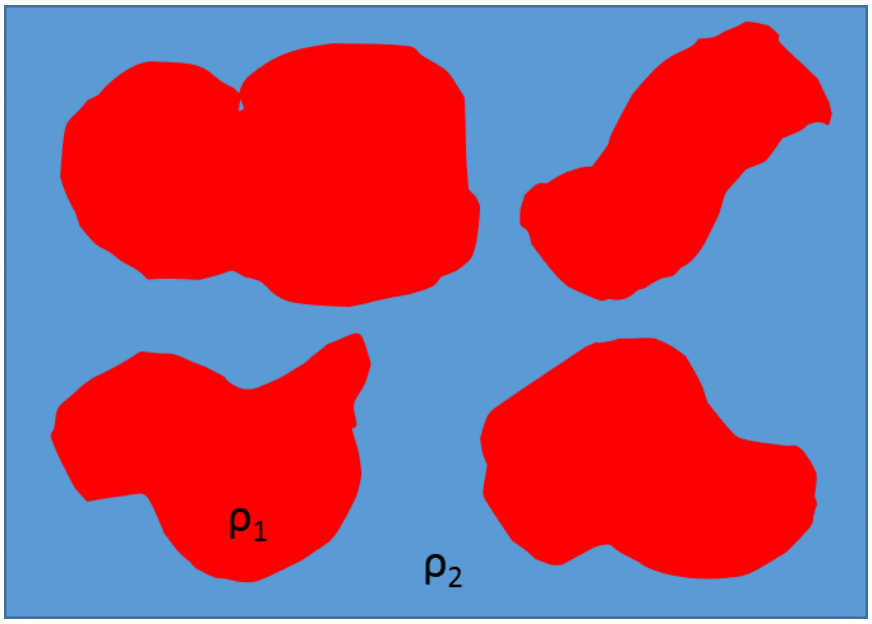

Figure 2.18 Schematic of a two phase system with SLDs ρ_1 and ρ_2.

Considering a simple two phase system, as shown in Figure 2.18, the two phases are assumed to have volumes V_1 and V_2 and SLDs ρ_1 and ρ_2. The scattering cross-section can be taken as a summation of the two components (since it effectively measures the number of scattered particles). It can then be defined as:

$$\frac{d\Sigma}{d\Omega}(q) = \frac{1}{V}\left|\int_{V1}\rho_1(r)e^{iqr}dr_1 + \int_{V2}\rho_2(r)e^{iqr}dr_2\right|^2 \qquad [2.24]$$

Using V_2=V-V_1, it effectively reduces to:

$$\frac{d\Sigma}{d\Omega}(q) = \frac{1}{V}(\rho_1 - \rho_2)^2\left|\int_{V1}e^{iqr}dr_1\right|^2 \qquad [2.25]$$

We thus clearly see that the scattering profile has been separated into effects by the scattering length density, composition which is the term before the integral. The term inside the integral is representative of the various phase shape, size and orientation in material. However the integral term here is squared. This gives rise to Babinet's principle wherein two materials, as

shown in Figure 2.19 will be indistinguishable in terms of the scattering length density profile if the phases are just interchanged between the two regions, since the phase information is lost.

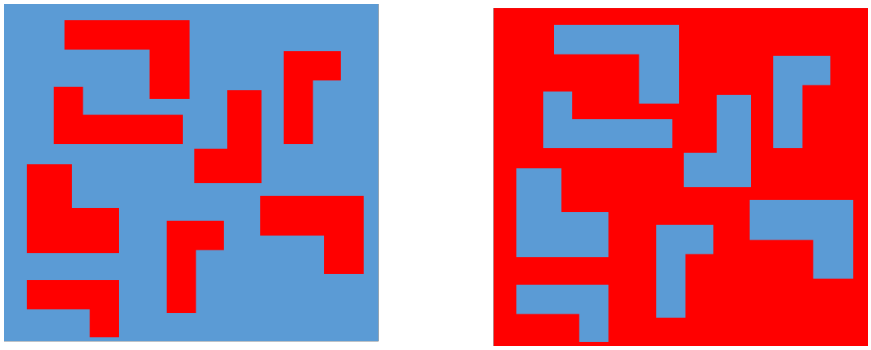

Figure 2.19 Two systems with same structure but with SLDs reversed between the two phases.

So it is important to have some information about the phases e.g. which phase is more than the other in terms of composition, to allow us to obtain a complete information about the correct spatial distribution of the materials as well. As previously mentioned, we will then need to re-calculate the scattering profile using these pre-known information and assumptions and fit it to the measured profile accordingly. The fitting can be done using a number of different complex algorithms with the least-square fitting algorithm being used mostly (using SASVIEW). The correctness of the fit is checked by minimizing the chi-square value of the fit Figure 2.20. To do the analysis of the scattering data, there are two possible approaches.

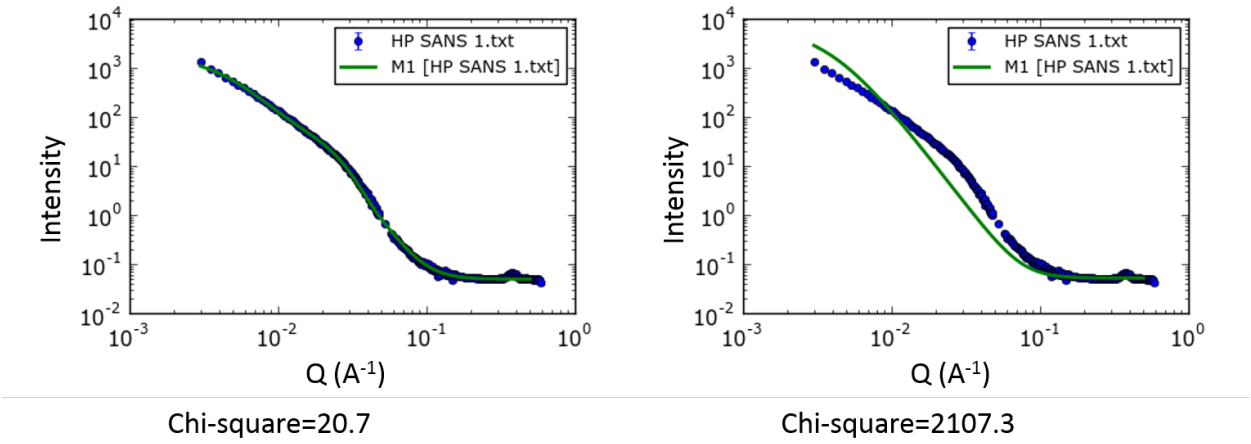

Figure 2.20 Fitting of intensity vs q profile with 2 different models and their corresponding chi-square values.

One can either choose to analyze independent of a model. For e.g. the Porod model assumes, that for very high values of q (where q>>1/dimension of scattering object), the measured scattering intensity I scales as:

$$I(q) \propto q^{-4} \qquad [2.26]$$

Which could eventually give us information about the surface to volume (S/V) ratio of the phases in the material (using a constant term called the invariant Q*):

$$\frac{\pi}{Q * q \to \infty} \lim I(q).q^4 = \frac{S}{V} \qquad [2.27]$$

Using other such analysis techniques such as Guinier analysis, information about phase size, radius of gyration of the scatterer etc. can be found.

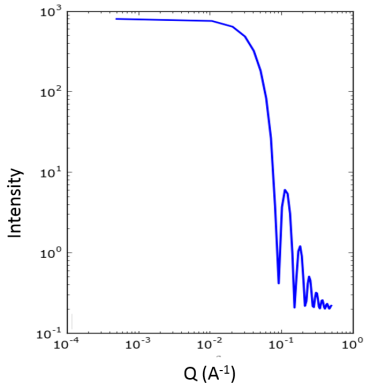

Figure 2.21 Intensity profile for a Sphere model describing spherical particles in a dilute solution with intensity, I(q)= form factor, P(q).

Similarly, one can use specific model systems, assuming a shape and composition of the scattering particles and phases to predict the specific values of their size and distribution using the simplified model equations. The models in these cases reduce the equation for the scattering cross-section as:

$$\frac{d\Sigma}{d\Omega}(q) = \frac{1}{V}(\rho_1 - \rho_2)^2 V^2 P(q) S(q) \qquad [2.28]$$

The integral term essentially separates into P(q) or the form factor, that represents the interference of scattered neutrons from the different scatterers in the same phase while S(q) represents the interference of the scattered neutron from the different phases. If a system is in a dilute solution, it doesn't have inter particulate interaction and hence S(q) = 0. As an example, for a dilute solution of dispersed spheres (radius = r), the structure factor S(q) = 0 and the form factor is given by:

$$P(q) = \left(\frac{3(\sin(qr) - qr\cos(qr))}{qr^3}\right)^2 \qquad [2.29]$$

This eventually gives us a scattering profile such as in Figure 2.21. Thus by selecting the appropriate model (some of which will be discussed later in subsequent chapters and discussions), and some appropriate assumptions of the material compositions, one case generate and fit the scattering profiles. This eventually can give a specific overall picture of the morphological structure in the materials including phase sizes, shapes, composition and distribution.

2.4.7 Neutron scattering for thin film characterization (NR and GISANS)

As seen in the previous section, SANS serves as a very powerful tool to study the overall morphological structure of multi-component material systems. However, as was the issue with the use of X-rays, in case of thin films, there was a need to devise new techniques of measurement to collect enough useful data in the same samples. Thus for the purpose of the thin film analysis, we utilized neutron reflectometry (NR) and grazing incidence small-angle neutron scattering.

NR has only recently been used as a technique to probe surfaces and buried interfaces up to few hundred nanometers deep. In small angle scattering (SANS), we assumed that a neutron is only scattering once while passing through a nucleus. In the case of NR however, at very small critical angles (as seen in X-rays earlier), the neutrons undergo total reflection from smooth surfaces below the thin films, and that assumption is no longer valid (Figure 2.17). According to Snell's law, described earlier for X-rays (Equation 2.23, Section 2.4.5), the critical angle for the reflection (θ_c) is determined by the ratio of the refractive indices for air (n_1) and the film (n_2), with respect to neutrons. The refractive index (n) is related to the scattering length density (ρ) by:

$$n_i = 1 - \frac{\lambda^2 \rho_i}{2\pi} \qquad [2.30]$$

$$\theta_c = \lambda \sqrt{\frac{\rho}{\pi}} \text{ for small incident angle } \theta_i \qquad [2.31]$$

Thus if we take incident beams at angles slightly greater than θ_c, we get specular reflection from the surface. It has been shown that the laws of reflection and refraction apply the same way for neutrons as is in classical optics. So to calculate the reflectivity (R) between two bulk media of refractive indices (n_0 and n_1) we use Fresnel's law to get:

$$R = |r|^2 = \left|\frac{n_0 sin\theta_0 - n_1 sin\theta_1}{n_0 sin\theta_0 + n_1 sin\theta_1}\right| \quad [2.32]$$

This can be extended to the case of a thin film with refractive index n_1, between two bulk materials n_0 and n_2. The reflectivity there comes out to be:

$$R = |r|^2 = \left|\frac{r_{01} + r_{12}e^{2i\beta 1}}{1 + r_{01}r_{12}e^{2i\beta 1}}\right| \quad [2.33]$$

Where r_{ij} is the Fresnel's coefficient for the interface ij and $\beta_i = (2\pi/\lambda).n_i.d.sin\theta_i$. We thus see that the reflectivity is a factor of the refractive index (scattering length density), and the thickness of the layer along with the wavelength of the incident beam and changes with increasing number of layers. To eventually increase this to multilayer systems, we need to define characteristic matrices for each layers which when multiplied together give the overall reflectivity. An initial assumption for this is that all layers are continuous and smooth. To incorporate the presence of interfacial roughness, the Fresnel's coefficients are itself modified with a term that takes into account interfacial width. With this factor, a combination of the scattering length density, interfacial thickness and roughness become the primary parameters which define the final reflectivity profile of a thin film system (Figure 2.22). We thus get information of vertical thickness as well as compositional profile from NR measurements.

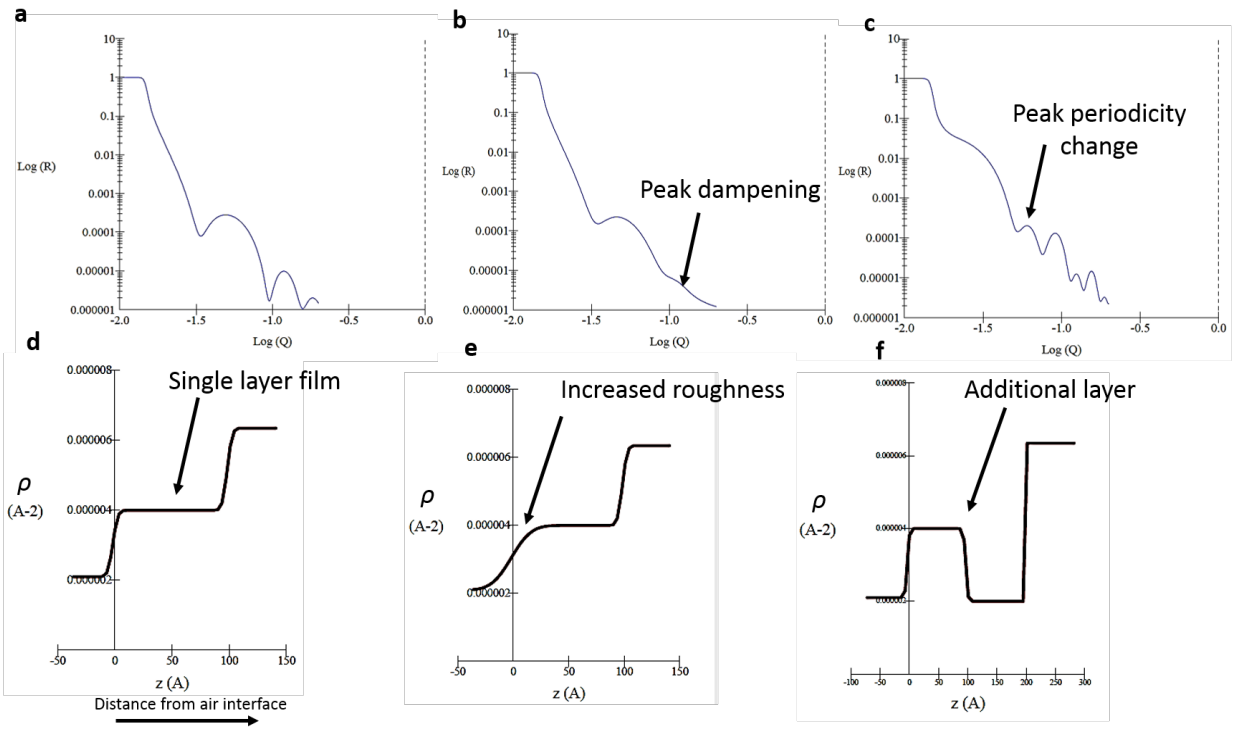

Figure 2.22 Effect of layer roughness and number of layers on the reflectivity profile.

From Figure 2.22 the variation of the reflectivity profile with increasing roughness as well as going from a single to a two layered system can be seen. However, as the number of layers in the system increases beyond 2 layers (and sometimes the total number of layers are also unknown), the reflectivity profile starts becoming even more complicated and the number of unknowns become too many. So, as was in the case with SANS measurements, it is hard to back-calculate and derive the values for the parameters. It thus becomes quite difficult to get an exact match of the reflectivity profile. In such a case, initial guesses need to be made regarding the number of layers and their corresponding three parameters (the SLD, thickness and roughness of each layer). Starting from the least number of layers, iteratively, the parameters are manipulated by different algorithms to give the best fit to the reflectivity profile. This is continued till no considerable change in chi-square (measure of the goodness of the fit to the profile) is observed by increasing

the number of layers or subsequent fitting iteration. Thus with appropriate intial parameters and assumptions the best possible fit to the curve gives us a final specific model (system of parameters and values).

GISANS as a technique is also fairly recent development. We have earlier talked about combining grazing incidence mode with wide-angle X-ray scattering (section 1.4.4) to get GIWAXS from thin films. This gives us information about the crystal structure and morphology in the films. To however look at larger phases and their domain shapes and sizes, we need to use it in the small-angle scattering mode. Grazing incidence small angle scattering would be a natural selection for such studies, However as mentioned earlier, morphological studies using scattering depend upon the SLD contrast between the constituent phases. In the event of low X-ray scattering contrast (as is in the case of polyalkylthiophenes and fullerenes), the contrast of neutron SLD can be utilized. In such a case, GISANS can be used as an appropriate tool for morphological studies.[146] Because of the limited quantity of material (thin film~100 nm), use of synchrotron radiation makes this technique even more viable.[147]

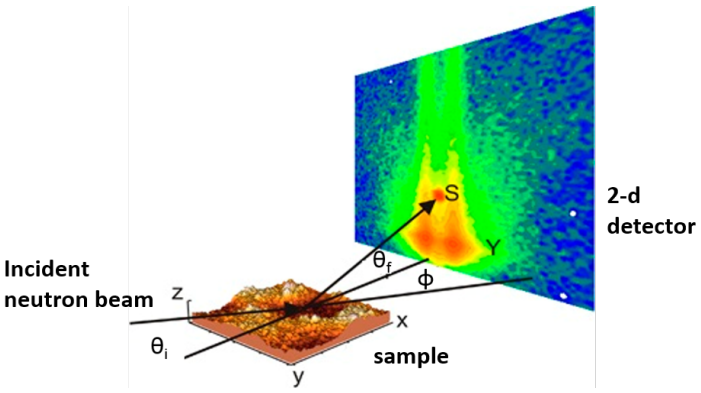

Figure 2.23 GISANS experimental setup (adapted from reference[148]).

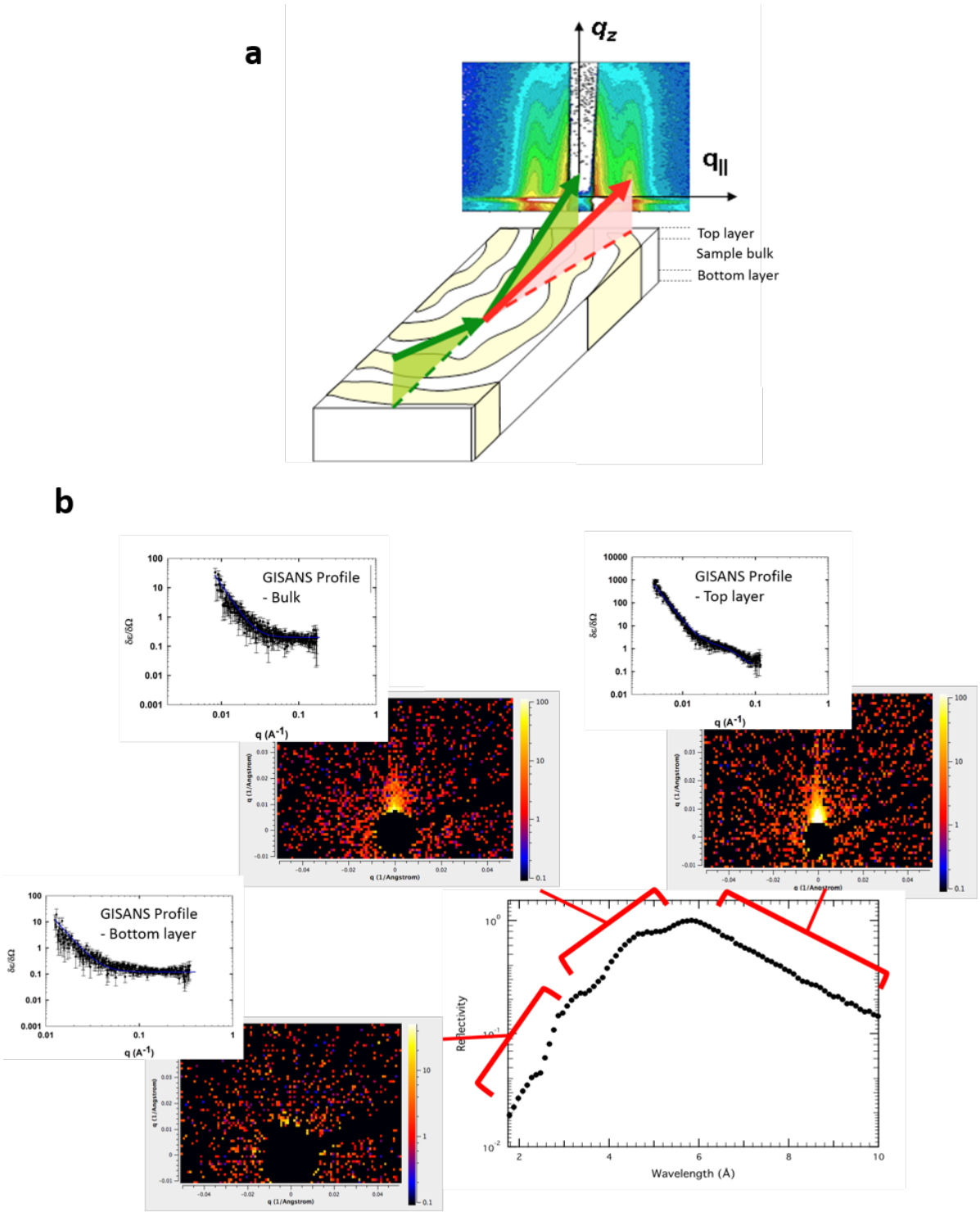

Figure 2.24 a) setup of TOF GISANS measurements (adapted from reference[149]) b) to probe lateral structures at different depths of thin films using different wavelengths of incident neutrons.

The principle of GISANS is quite similar to GIWAXS, wherein the neutron beam hits the thin film sample at a small angle θ_i (Figure 2.23). Instead of the transmission mode however, the beam is used in reflective mode presuming the angle α_i is small enough. The neutron beam then scatters at an angle α_f and at an out of plane angle Φ. A typical GISANS pattern is shown as in Figure 2.24a. For specular reflection we $\theta_i = \theta_f$ and we can measure out-of-plane profiles. Using the off-specular scattering however (at angles Φ), we can also get information about the in-plane structures present. As mentioned earlier in Section 1.4.4, at values of θ_i below the critical angle (θ_c), the beam will tend to reflect completely and this technique can be used to probe the phase structure at the surface. For $\theta_i > \theta_c$, we will obtain refraction and reflection at the interfaces and so this technique can be used to study buried surfaces as well (Figure 2.24).

Alternatively, at a fixed incident angle, GISANS can be combined with time-of-flight (TOF) measurements to give neutron beam of different wavelength ranges which penetrate the sample to different depths.[150-152] This is known as TOF-GISANS, and uses the ability to collect the different wavelength neutron beams scattered as a function of time to get depth information of the lateral structure (Figure 2.24). Another advantage of this technique over X-rays is due to the fact that similar measurement in X-rays would cause inherent radiation damage to the sample. TOF-GISANS have very recently been successfully used to study the depth dependence of scattering in the case of block copolymers.[153, 154] Considering all these advantages, the use of TOF-GISANS was chosen in determining the depth dependence of lateral morphology in our polyalkylthiophene-fullerene mixed systems.

2.5 BULK POLYMER AND FULLERENE CHARACTERIZATION (SCATTERING)

2.5.1 Wide and X-ray scattering (WAXS)

Samples for the WAXS measurements in subsequent studies (Chapter 5) were drop cast films on regular glass cover slips. P3AT (poly-3alkylthiophenes) and a choice of three different fullerene derivatives, C_{60} (fullerene), $PC_{61}BM$, bis-$PC_{61}BM$ were used for the samples. Different combinations of polymer and fullerene were tried to give us nine different blends. Solutions of various polyalkylthiophene and fullerenes were made in o-DCB (20 mg/ml) and stirred overnight at 70 ºC. They were subsequently mixed 1:1 ratio (polymer: fullerene) to give us the desired mixed systems. This was stirred for half a day at the same temperature before drop casting the solution onto the pre-cleaned glass substrates (using deionized water, acetone and isopropanol). The drop cast samples were dried overnight under vacuum after forming a solid film. These films were used for WAXS measurements in the transmission mode.

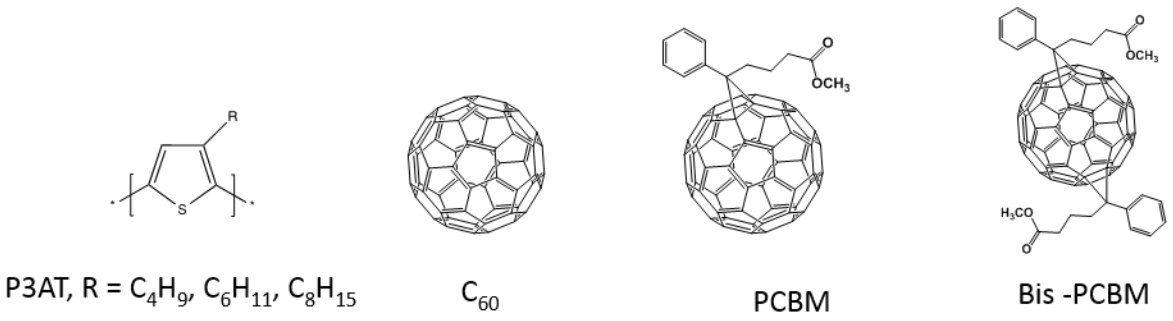

Figure 2.25 Polyalkylthiophenes, C_{60} Fullerene and its derivatives used in the heterojunction blends and devices

WAXS measurements were carried out using the in house X-ray diffraction (XRD) system consisting of a Rigaku Micro Max 002 X-ray generator operated at 45 kV and 0.66 mA and equipped with R-axis VI++ detector. The sample detector distance was 100 mm and the data

collected was analyzed using the software AreaMax v 1.00 to store the 2-D image and also convert it to 1-D integration plots (I vs 2 theta and I vs phi). The 1-D data was subsequently analyzed using softwares MDI Jade to get a 2-column integration plot and Magicplot Pro v 2.5.1 to obtain the peak fitting profile.

The peak fitting was carried out using Gaussian peaks as estimates as described earlier in Section 1.4.4. Peak widths were limited to a 2-theta value of 5° for crystalline peaks for the calculation of percentage crystallinity. Domain size was calculated using Scherrer's Equation, mentioned earlier (Equation 2.2, Section 1.4.4)

2.5.2 Small angle neutron scattering (SANS)

Sample for the amorphous polymer-fullerene blends (Chapter 3) were made from solutions. Blends of the polymers with PCBM were all made by initially dissolving each polymer and the PCBM separately in toluene at concentrations of about 1 wt. %, i.e. well below the solubility limit for each material, and sonicating until dissolved, i.e. typically for a minimum of 20 minutes. Subsequently, the two solutions were mixed to obtain the required ratios of polymer: fullerene. After sonication of the mixed solution for another 20-30 minutes, the blend was precipitated in to an excess of rapidly stirred cold methanol, vacuum filtered using a nylon membrane filter with pore size 0.45 μm (Whatman, cat nº 7404-004) and washed with cold methanol. The solids were then dried in a vacuum until required for the measurements.

Small angle neutron scattering (SANS) data from solid films of the PCBM-amorphous polymer blends (Chapter 3) were acquired on the diffractometer LOQ at the ISIS Facility (Didcot, UK) with the help of Dr. Gabriel Bernardo, Institute of Polymers and Composites, University of Minho.[155] Due to the high carbon to hydrogen content in PCBM, they have a naturally high neutron

scattering density contrast with the hydrogenous polymers, so that no isotropic substitution was required. Data were obtained from samples containing weight fractions of PCBM above and below the critical miscibility limits of the three polymers as determined by DSC analysis. The powders from each sample were pressed into discs in an IR disc press at room temperature using a 2 ton load. No subsequent annealing was undertaken on the samples prior to measurement and therefore the samples reflect the phase structure resulting from the precipitation from solution The samples were prepared to be approximately 1 mm thick, although their exact thickness was measured by micrometer and that value used in the data reduction procedure to ensure proper scaling.

LOQ is a fixed-geometry "white beam" time-of-flight instrument which at 25 Hz utilizes neutrons with wavelengths, λ, between 2 and 10 Å. Data are simultaneously recorded on two, two-dimensional, position-sensitive, neutron detectors, to provide a simultaneous q (the scattering vector, = $4\pi/\lambda \sin \theta/2$, where θ is the scattering angle) range of 0.008−1.6 $Å^{-1}$. Each blend sample and background sample was measured for typically 1 or 2 hours in order to gather data of high statistical precision. Each raw scattering data set was then radially-averaged, corrected for the detector efficiencies, sample transmission and background scattering and converted to scattering cross-section data, i.e. absolute scattering intensity, ($\partial\Sigma/\partial\Omega$ vs q) using the instrument-specific software.[156] The absolute scattering was calibrated using the scattering from a standard sample (a solid blend of hydrogenous and perdeuterated polystyrene) in accordance with established procedures.[157] The data were then fitted to appropriate models using SansView (Version 2.1.1).[158]

SANS measurements of polyalkylthiophene-fullerene mixtures (Chapter 5) were carried out at beam line NGB-30 at NIST Center for Neutron Research (NCNR) with the help of Yimin Mao, National Institute of Standards and Technology (NIST), Gaithersburg. The samples were made similar to the WAXS samples (section 1.5.1) but by drop casting the 1:1(w/w)

polyalkylthiophene: fullerene mixture from o-DCB solution (20mg/ml) onto aluminum foil instead of glass substrate. The films were dried overnight under vacuum before using the SANS measurements in transmission mode. The entire neutron detector system was encapsulated in a 13m-long vacuum chamber. Scattering data covering a Q-range of ~0.003 1/A-0.5 1/A were obtained by combining data collected at three sample-to-detector distances, namely, 1m, 4m, and 13m. The neutron wavelength for 13m and 4m configurations was 6 A, and was 5A for 1m configuration. 0.5" beam size was used for all SANS measurements.

At each configuration, a 'blocked beam' measurement was carried out where a strong neutron absorber, Boron Nitride was inserted to block the incident beam, background due to detector electronic dark count, and other noise from environment was collected. Sample/blank Aluminum foil transmission was measured by taking the ratio of incident beam intensity measured with and without sample. Scattering intensities were normalized using incident beam intensity without sample. Data reduction was done using standard IGOR MACRO written by S. Kline. The final calibrated intensity from 'real' sample was obtained by applying the following formula

$$COR = (SAM - BGD) - [T_{sam}/T_{emp}](EMP - BGD) \quad [2.34]$$

where COR stands for corrected scattering intensity; SAM is total intensity from the sample, including sample cell (the Aluminum foil substrate); EMP is intensity of the empty sample cell (Aluminum foil substrate); BGD is the background collected via 'blocked beam' measurement; T_{sam} and T_{emp} are transmission coefficients for sample (include Aluminum foil substrate) and that of empty cell.

All annealed samples have been annealed ex-situ at 150 °C for 10 min right before SANS measurements. The SANS measurements itself were carried out at ambient temperature. The data was subsequently analyzed using the software SASVIEW inc. (version 2.2.0). Individual models

were chosen from the SASVIEW library and a simple least squares fitting tool was used to obtain the best fit. Single models were used initially to obtain the fitting. Upon further analysis, complex models were devised to try and fit the profile using the sum of two different single models.

2.6 DEVICE FABRICATION AND MEASUREMENT TECHNIQUES

2.6.1 OPVs and thin films for scattering measurements

The bulk heterojunction samples (Chapter 3 and 4) were prepared using P3AT (poly-3alkylthiophenes) and a choice of three different fullerene derivatives, C_{60} (fullerene), $PC_{61}BM$, bis-$PC_{61}BM$ (Figure 2.25). Different combinations of polymer and fullerene were tried to give us nine different heterojunctions.

The solvent chosen was ortho-dichlorobenzene (o-DCB) since it has seen to give better solubility, crystal packing and uniformity in the film thickness in comparison to other solvents such as toluene, and chloroform.[159] Solutions of 0.8% (wt/vol) of all the compounds in o-DCB were prepared and then mixed in 1:1 (polymer: fullerene) ratio.

The bulk heterojunction type solar cells for NR (Chapter 3), GISANS and GIWAXS (Chapter 4) measurements were prepared on silica substrates of 1" by 1". A layer of SiO_2 of ~300 nm thickness had already been pre-deposited on top of the substrate using PECVD. PEDOT: PSS diluted solution (1:6 with water) was used to obtain very thin layers ~ 10nm by spin coating on the oxide layer using water as the solvent using a spin speed of 1200 rpm for 10 sec, followed by 4000 rpm for 60 sec. The layer was subsequently was dried by heating at 150 °C for 20 mins. The BHJ mixtures were then spin coated from the previously prepared solutions directly onto the PEDOT: PSS layer at a speed of 1500 rpm for 40 seconds to give layers in the thickness of ~ (40-50) nm.

The BHJ were finally capped on top by the aluminum (~60nm) cathode layer by thermal evaporation onto the film surface, covering the entire active layer area.

Solar cell devices (Chapter 3) were fabricated on ITO-glass substrates with a square resistance 10 $\Omega \cdot cm^2$. The substrates were initially washed using detergent and rinsed in pure water, followed by ultra-sonication sequentially in acetone and isopropanol. The substrates were dried in oven overnight prior to use. ITO-glass substrates were UV-plasma treated and a ~40nm thick PEDOT: PSS layer was deposited on the substrates. Then BHJ composites were spun cast directly on top of PEDOT: PSS layer in a N_2 filled glove box from pre-prepared solution. Finally, 100 nm of aluminum was thermally evaporated onto the BHJ layers under high vacuum of a minimum of 4×10^{-4} Pa. Pre-annealed BHJs were annealed at 120 °C for 20 minutes before electrode deposition (Ca/Al) and while post-annealed devices were annealed at 150 °C for 10 min after electrode deposition (Al) under N_2 gas.[67]

Solar cell devices with $PC_{61}BM$ electron transport adlayer were made similar to regular ones with the additional step of an extra layer of $PC_{61}BM$ solution (5 mg/mL) spun from a orthogonal solvent (DCM) at 1500 RPM for 30 seconds to give us layers of thickness ~5-10 nm

2.6.2 OPVs and thin films for cross-linkable fullerene related studies

Thin films were prepared for all characterization measurements (optical microscopy, UV-vis measurement, BHJ devices for efficiency measurements and XPS for diffusion measurements), by spin coating solutions from o-dichlorobenzene (o-DCB) onto glass slides. Before use all glass slides were washed with surfactant solution, acetone and isopropanol, consecutively, and after drying the glass surfaces with N_2 gas, were UV-ozone cleaned.

Thin films for GIWAXS, optical microscopy and UV-vis measurement were prepared from different solutions made from pure PCBM and PCBCB-I, and also BHJ blends with P3HT. The P3HT: fullerene ratio in the BHJ layers was kept as 1:1 in all of the films. Films were spun from 20 mg/ml solutions in o-dichlorobenzene solutions (500 RPM for 2 sec followed by 800 RPM for 50 seconds) onto pre-cleaned microscope glass slides (with acetone and isopropanol).

Thin films for OPV device measurements were made on ITO covered glass slides. The slides for OPV devices were pre-cleaned as previously discussed (section 2.6.1). A layer of PEDOT: PSS was first deposited onto the ITO by spin coating a PEDOT: PSS solution (Clevios Al4083 by Heraeus) at 4000 RPM for 45 seconds. Films were subsequently annealed for 10 minutes at 150 ^{o}C in a glove box. The active layer was made of P3HT/fullerene blends in a weight ratio of 1:1, with the fullerene being pure PCBM, PCBCB-I or PCBM: PCBCB-I in a 1:1 ratio. The active layer was spin coated from 20 mg/ml o-DCB solutions (500 RPM for 2 seconds followed by 800 RPM for 50 seconds). All active layer films were annealed at 190 ^{o}C for 10 minutes. Finally a 100 nm Al electrode layer was deposited on to the BHJ using thermal evaporation technique under vacuum. Subsequently, the devices were annealed on a hot plate in the glove box at 150 ^{o}C for varying amounts of time and the OPV efficiency determined using a Keithley's Series 2400 SMU source meter under an AM 1.5 solar spectrum.

Bilayers for the XPS diffusion measurements were made by first spin coating a layer of fullerene (20 mg/ml in o-DCB), onto a glass slide (500 RPM for 2 seconds followed by 800 RPM for 50 seconds). In case of the PCBCB-I film, this was then annealed at 190 ^{o}C for 10 minutes to allow the cross-linking reaction. The P3HT layers were prepared by spinning onto different glass slides that were initially spin coated with PEDOT: PSS. The P3HT polymers were then floated off onto water (to dissolve the PEDOT: PSS and release the P3HT film), which were then transferred

onto the fullerene layer. The resulting bilayer structure was subsequently air dried until no visible water traces remained and then vacuum dried at RT overnight. XPS measurements were performed in the shared user laboratory of the Georgia Tech IEN Organic Cleanroom. The machine used was a Thermo K-alpha XPS. The etching was carried out using a Argon ion source at an energy of 3000 eV, with constant etch time of 20 sec in each etch cycle, i.e. etch time between subsequent measurements.

2.6.3 Space charge limited current devices (SCLC)

SCLC devices and measurements were performed with the help of Jeff Hernandez in Dr. John Reynolds' lab, Department of Chemistry, Georgia Tech. These devices were built on pre-patterned ITO. The pre-patterned slides were ultra-sonicated in sodium dodecyl sulfate and water for 10 minutes, followed by a water rinse. Afterwards, ITO was ultra-sonicated in acetone, then isopropanol for 10 minutes each. ITO was then UV-ozone cleaned for 10 minutes. PEDOT: PSS (Al 4083) was filtered through a 0.45 μm nylon filter and spin coated onto the cleaned ITO at 5000 rpm for 60 seconds. PEDOT: PSS coated devices were then transferred into an Argon filled glovebox and annealed at 120 °C for 15 minutes. Solutions of fullerene with concentrations of 30 mg/mL in chloroform were spin coated onto PEDOT: PSS devices at 1200 rpm for 60 seconds. Subsequently the devices were placed in a thermal evaporator where 1 nm of LiF was deposited, followed by 80 nm of Al. Devices were tested using a Keithley's Series 2400 SMU source meter. Film thicknesses were measured using a Bruker stylus profilometer. The voltage was corrected for built-in voltage (V_{bi}). A value of V_{bi} = 1.4 eV was used and then the data was fitted to the modified Mott-Guerney equation[78] to obtain the value for electron mobilities (using Origin pro):

$$J = \frac{9}{8}\varepsilon_0\varepsilon_r\mu_e\frac{V^2}{L^3} \qquad [2.35]$$

in which J is the current, L is the layer thickness, V is the voltage, ε_o ε_r is the permittivity of the fullerene, and μ_e is the electron mobility.

2.7 THIN FILM POLYMER-FULERENE CHARACTERIZATION (SCATTERING)

2.7.1 Neutron Reflectivity (NR)

Building on the use neutron scattering based characterisation studies, neutron reflectivity provided a technique for indirect measurement of vertical phase composition in complex multi-layer systems as is the case with BHJ based devices. Neutron reflectivity (NR) was performed on the devices of P3AT-fullerene prepared on (2.5×2.5)cm samples using the CRISP and SURF instruments at the ISIS Facility, Rutherford Labs, Oxford, UK and Beamline 4L-B at the Spallation Neutron Source, Oakridge National Lab, TN, USA. The wavelength range was 0.5-6.5A. Reflectivity data were collected over 2 or 3 angles with constant dQ/Q resolution giving a combined *Q*-range from 0.008 - ~0.2 $Å^{-1}$. In comparison to the devices, the samples used here had the electrodes (Al or Al/Ca) completely covering the active layer and were fabricated as discussed in Section 1.6.1.

The raw data was reduced to obtain 'Intensity vs Q' data using the software MANTID and analyzed for fitting using the software RAScal. The fitting program was carried out utilizing alternatively a combination of the Nelder-Mead Simplex Method and the Marquardt-Levenberg method to give us the best fit corresponding to the smallest χ^2 value. Initial predictions for the layer thicknesses were taken from previously conducted profilometry measurements (organic layers) and known controlled thicknesses (metal electrodes from physical vapor deposition). Initial guesses for the scattering length densities (SLDs) of the layers were obtained using the 'SLD calculator' available on the fitting program SASVIEW.

2.7.2 Grazing incidence wide angle X-ray scattering (GIWAXS)

GIWAXS measurements were carried out on beamline 11-3 at the Stanford synchrotron radiation light source (SSRL). The beam was kept at an energy of 13 KeV and the critical angle of measurement was 0.12°. A LaB_6 standard sample was used to calibrate the measurements. The calibrant along with the wavelength and sample-detector distance was used to correct the 2-D image for detector distortion using the software WxDiff (Figure 2.26a). The 2-D images were then reduced to 1-D plots (Intensity vs q and Intensity vs phi, Figure 2.26b and c for subsequent analysis of crystal size, d-spacings, orientation factor and percentage crystallinity as described earlier in (section 2.4.4). Peak fitting for the analysis was done as described earlier (section 2.4.4) using the software MagicPlot Pro.

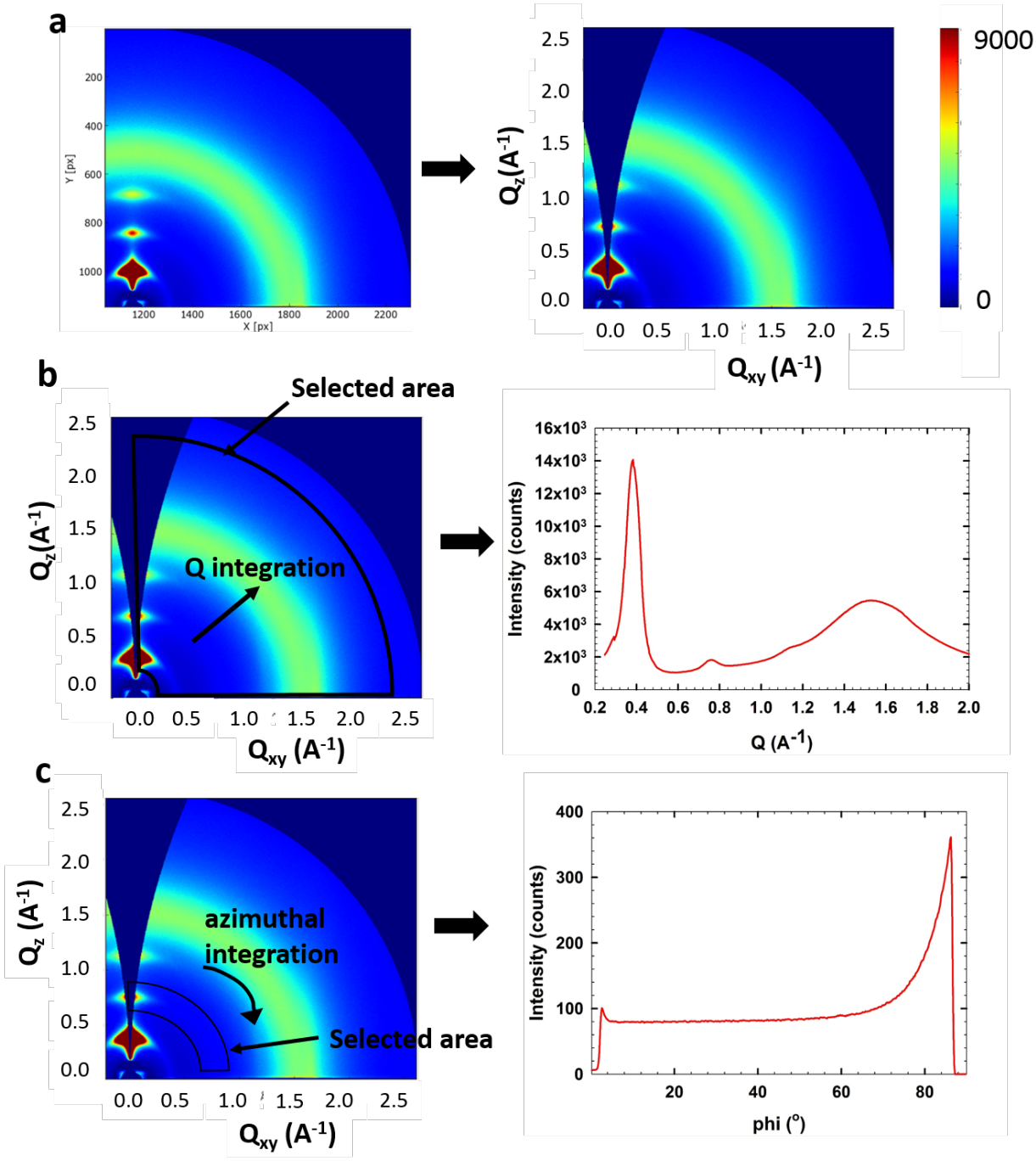

Figure 2.26 GIWAXS image analysis showing a) conversion of 2-D image from detector to corrected intensity vs Qz and Qxy image b) conversion of 2-D image using cake selection into intensity vs q integration plot c) conversion using cake selection into azimuthal integration plot.

2.7.3 Grazing incidence small angle neutron scattering (GISANS)

GISANS measurements were carried out on the SANS2D machine at the ISIS Facility. The measurements were made with the instrument running at an operating at a repetition of 10Hz, giving a wavelength range of 1.75 – 12 Å. Measurements made at fixed incident angle ($\theta = 0.35°$), with the critical edge of the samples occurs at 6 Å. Consequently indirect depth sensitivity is achieved by evaluating the scattering behavior as a function of wavelength above and below this critical wavelength (section 1.4.7, Figure 2.24). The measurement were over three wavelength ranges (1.75-4 Å, 4-6 Å and 6-12 Å) corresponding to the three energy levels of the neutron beam, giving us scattering through the thin film at different depths. Data analysis and fitting using the different models (section 2.4.3 and in later discussions) was carried out using the software package SAVIEW (v 2.2.0).

2.8 OTHER CHARACTERIZATION TECHNIQUES

2.8.1 XPS measurement on thin film BHJs

Besides scattering, X-ray sources can also interact with matter to emit characteristic electrons from atomic orbitals. The characteristic electrons can be of two types, Auger electrons or photoelectrons. These exhibit characteristic energy levels, to be used as a tool for elemental analysis of different materials. An incident X-ray can have sufficient energy to knock off an inner shell electron (e.g. from the K-shell) with a specific kinetic energy.

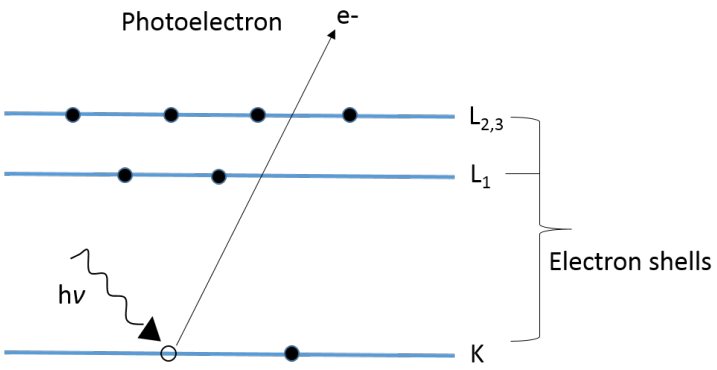

Figure 2.27 Generation of a photoelectron from a X-ray (photon) source.

The kinetic energy (E_{KE}) of the electron can be measured and is related to the energy of the incident X-ray (hν) by:

$$E_{KE} = E_{BE} - h\vartheta - \varphi \qquad [2.35]$$

in which E_{BE} is the photoelectron binding energy, characteristic for each element and φ is the work function of the material (the energy required for an electron to escape a material surface). By using the known value of φ, hν and measuring the E_{KE} using a photodetector, the characteristic binding energy of the photoelectron (E_{BE}) can be determined. The XPS detector eventually collects the list of characteristic binding energy and plots the intensity vs binding energy profile (Figure 2.27). This allows the detection of all the elements and their percentage composition (using the ratio of the area of specific element to the total area) present in the sample.

Depth profiles were obtained by repeated standard XPS measurements followed by sample etching using an Argon ion source. Etching was achieved using an ion source energy of 3000 eV with etch periods of 100s between each measurement. Each etch cycle was found to correspond to the etching of BHJ film thickness of ~8 nm. Due to differences in etching rates, for the same ion source energy, 100s of etching of Al resulted in film thickness changes of only 2 nm. Thermo

Scientific Avantage Data System software was used to determine the concentration of different elements.

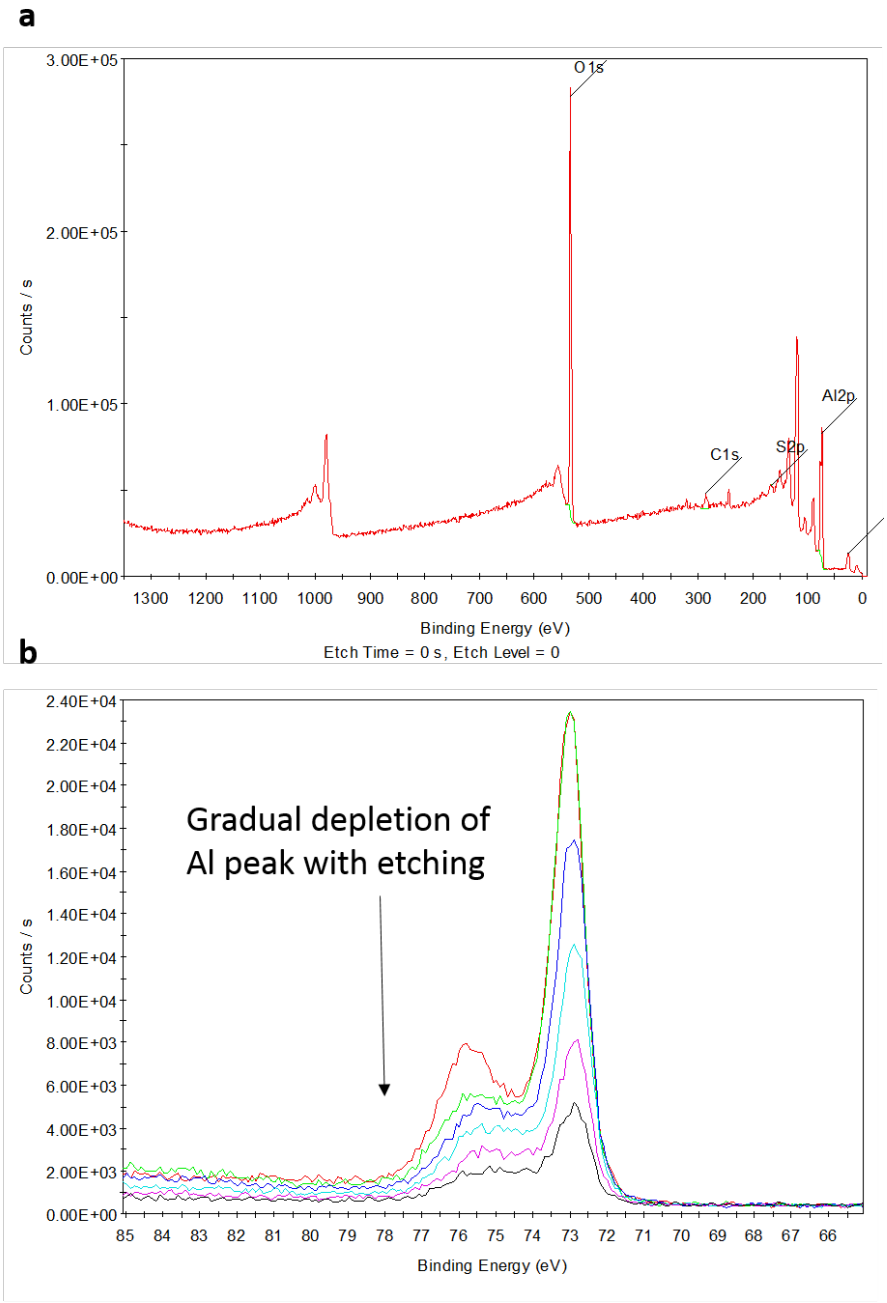

Figure 2.28 XPS measurement in etching mode of a P3HT-PCBM BHJ device a) the survey scan showing all the peaks at the Al/BHJ interface b) gradual decrease of Al peak on etching.

XPS measurements were performed in the shared user laboratory of the Georgia Tech IEN Organic Cleanroom. The machine used was a Thermo K-alpha XPS, with an X-ray source.

The percentage composition of the different elements present was subsequently analyzed and provided by the software. Consequently, using the molecular weights of the constituent materials, and the percentage composition of the characteristic element (e.g. sulfur in P3HT), the percentage composition of that material was determined at different etch depths. Pure polymer and fullerenes were etched initially to compare the etch rates. The absence of Al while etching from the top signaled the beginning of active layer. Similarly, the shifting of the S peak signaled the occurrence of PEDOT: PSS. This allows the determination of the top and bottom interfaces. The gradual disappearance of these peaks (instead of a sudden dip, Figure 2.28b) suggest an interfacial width which is representative of the interface roughness seen in the NR measurements as well.

2.8.2 Differential scanning calorimetry (DSC)

Differential scanning calorimetry is a technique used to study the thermal transitions in polymers upon heating. Thermal transitions may be of the first order (involving latent heat) such as polymer melting (T_m), recrystallization (T_c). It can also detect second order phase transitions such as glass transition of polymers, (T_g).

The apparatus is set up as shown in Figure 2.29a. In the typical design, two pans sit on a pair of identical platforms, connected to a furnace with a common heat flow path. One of them is the reference pan which is empty. The other pan is the one where a pre-measured amount of the polymer is taken. Both the pans are sealed from the top with lids. Once the pans are placed and the chamber for the pans is closed, the required environment is maintained, e.g. N2 gas for an inert

environment. The computer program 'TA universal analysis' is then used to set up a procedure for carrying out the heating and cooling cycle(s) in order to obtain the thermal transition profile.

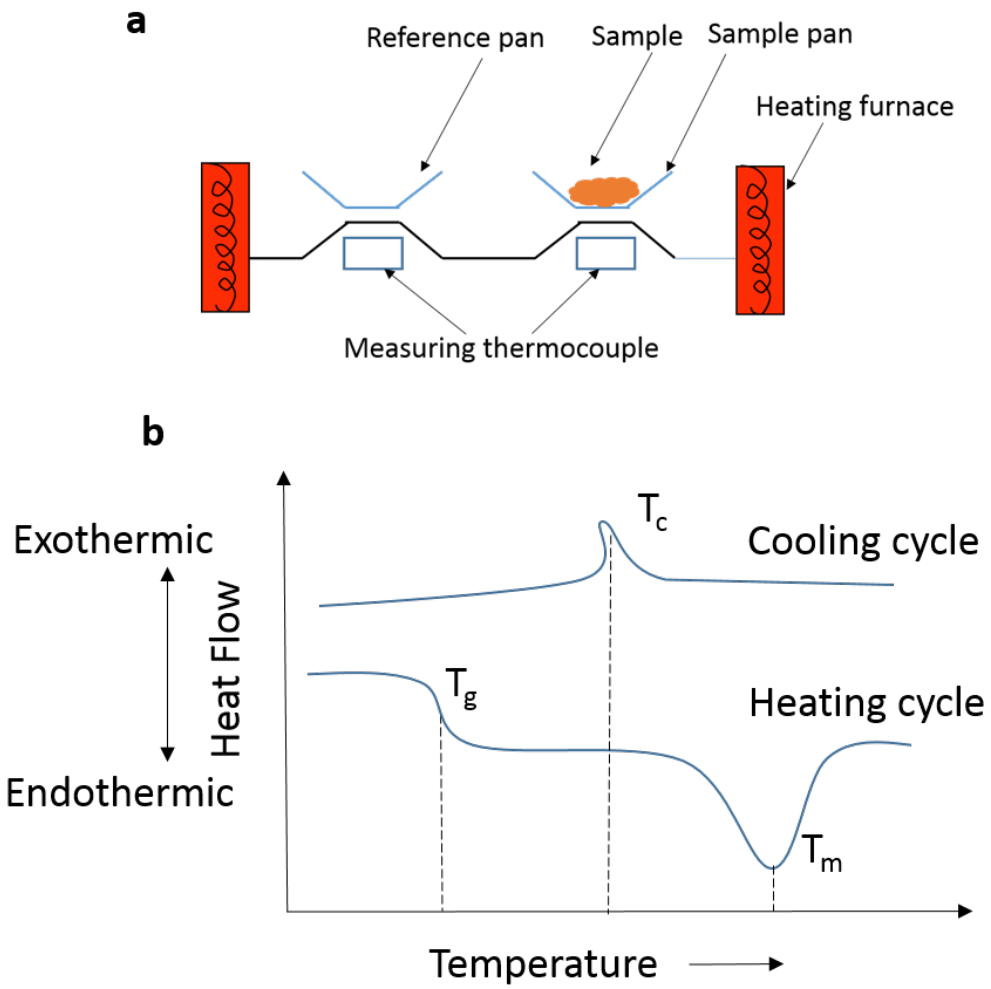

Figure 2.29 a) Schematic for a typical setup of a DSC machine b) a DSC heat flow profile showing a heating cycle with Tg-glass transition, Tc-crystallization and Tm- melting peaks.

Upon running the procedure, both the pans are heated at the same pre-determined rate (usually between 5-10 °C/minute). The DSC measures the difference in the heat flow between the two pans. This remains at a constant value with increasing temperature until the material encounters a phase transition wherein the heat flow rate changes to a different slope. This is due

to the extra heat being absorbed or released during the phase transition. A typical profile with the possible thermal transitions is shown in Figure 2.29b. By looking at the peak position, the onset of the respective thermal transitions can be predicted. The Tg and Tm both show endothermic phase transitions during the heating cycle while recrystallization shows exothermic transition during the cooling cycle. In addition to these phase transitions, a temperature initiated chemical reaction, such as a thermo-cross-linking reaction would also show an exothermic peak owing to the release of energy during the heating cycle.

Utilizing these features of the DSC, the machine was used to determine a number of different parameters for the polymers. DSC measurements of all blends and pure compounds were made in standard mode on a TA Instruments Q200. Argon with a flux of about 50 mL min^{-1} was used as a purge gas. For all of the studies conducted, the heating rate was chosen as 10 C/min. Samples were equilibrated at a low temperature initially (~-50 C) and to look at phase transitions, the second heating/cooling cycles were considered. The first cycle was used to remove any thermal history of the sample. For detecting the exothermic peak related to thermos cross-linking, the first heating cycle itself was considered.

In the miscibility studies of the polymer fullerene systems (Chapter 3), the different mixtures were taken in Aluminum hermetic pans and heated from 20 to 300 C to get a look at the melting temperature peaks of the fullerene. By looking at different weight ratios of the polymer: fullerene, the miscibility of the fullerene in the polymer could be predicted as the weight ratio where the fullerene Tm first appears. Thermal transition peaks (and their areas) were analyzed using the TA universal analysis software.

DSC analysis of the PCBCB-I cross-linkable fullerene precursor (Chapter 6) was carried out using hermetically sealed Al pans from a start temperature of -50 ^{o}C up to 300 ^{o}C at a heating

rate of 10 °C /min. Similar measurement was carried out using the films made from PCBCB-I, BCB-OH, PCBM and other mixtures of these. The final thermal transition profile was analyzed using TA universal analysis software.

2.8.3 Profilometry

Profilometry is a technique used to measure the surface profile. The profilometer gives us an estimate of the layer thickness and roughness being measured. It is a mechanical method, wherein the movement of a stylus on a surface registers the variations in the surface profile. This is known as the contact-mode profilometer. Newer profilometers are developing non-contact mode such as laser triangulation, confocal microscopy etc. The profilometer used in these studies was a Bruker Dektak XT.

2.8.4 Atomic force microscopy

Atomic force microscopy (AFM) is a technique used to study the surface of materials by scanning using a solid probe. Specifically, it uses the near-field forces between the tip of the probe and surface atoms to generate a signal which eventually derives the surface morphology of the material.

The operating modes of an AFM can be mainly divided into static and dynamic modes. In the static mode the probe, which is a cantilever, scans over the sample to be imaged. The cantilever touches the surface physically and gets deflected whilst moving through the varying topography on the surface Figure 2.30a.

The samples in these studies were measured in the dynamic mode. In the dynamic mode, the cantilever moves with a certain frequency while scanning over the sample (Figure 2.30b). The

interaction with the sample causes change in the amplitude of oscillation according to the surface topology and sends signals to the feedback loop which tried to maintain a certain value of amplitude.

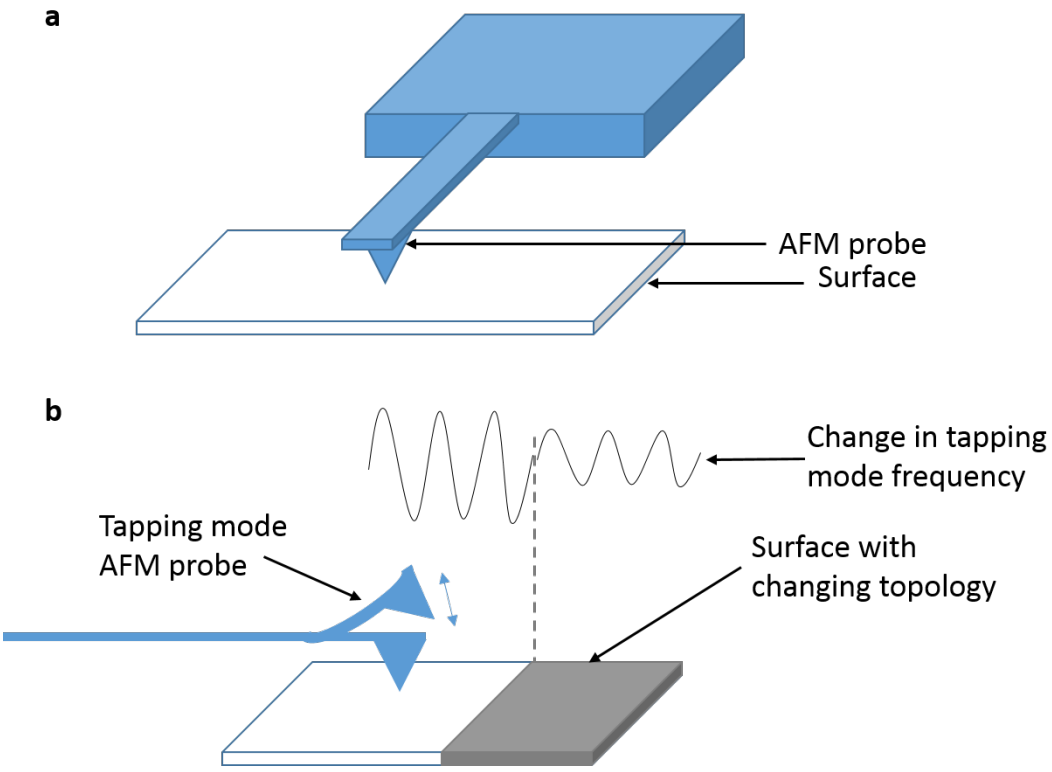

Figure 2.30 a) Schematic showing an AFM surface probe scanning a surface. b) tapping mode AFM showing the changing frequency with change in surface topology of the material.

Thus an image of the surface profile from the signal is obtained. This is also known as the tapping mode and can avoid sample damage unlike the contact mode. In addition, depending upon the type of forces causing the deflection, it can be used to determine the chemical and physical properties of the surface as well. By monitoring the phase lag between the probe oscillation and the signal, the phase changes on the surface could be detected. Thus using the software Nanoscope

Analysis v 1.40, information about the surface roughness as well as phase dimensions can be obtained.

2.8.5 Optical Microscopy

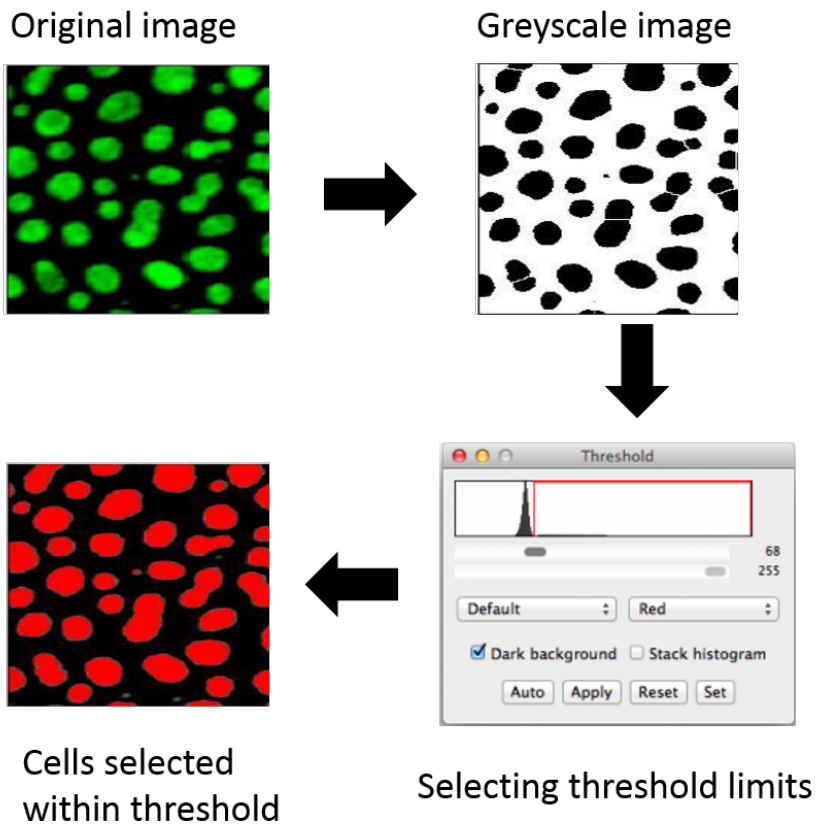

Figure 2.31 Procedure for deriving crystal size and area using cell calculation in ImageJ.

Optical microscopy was used to observe large scale aggregation in thin film OPVs. The optical microscope used for our studies (Chapter 6), was an Olympus BX51 with a 20x zoom lens. The samples for the optical microscopy were prepared on regular glass substrates as discussed in Section 2.6.2.

Analysis of the images collected from the microscope was conducted using the software ImageJ v 1.48. To calculate the area of the PCBM crystallites available, the image was first converted to a greyscale image (Figure 2.31). The cells (areas of crystallite formation) can now be counted in two ways. In the manual counting method, first select open up the threshold tab. A profile as seen in Figure 2.31 and the selected region of the profile is chosen in a way to make sure intensity of the cell areas will lie in that threshold value. Following this, the ROI manager was opened from the tools section. Following this, the peak options was selected from the main window and each individual cell in the image could be selected by clicking on it. The cell area and mean length get added to the ROI manager and the information is stored. All the selected cells can be seen (red area in Figure 2.31). Finally, in the end, a mean of their average length as well as the sum of the area can be calculated to get the mean crystal size and total crystalline area.

Alternately in the automatic counting method, instead of opening the ROI manger, the analyze measurements option was first opened and the boxes for total cell area and average cell size were selected. The option for 'analyze particle' is then selected, where some parameters for the basis of cell selection are set (like whether holes in selected area should be considered etc.). Running the analyze particle tool finally shows us the image with the selected cells (similarly colored red as before) and the relevant information (cell total area and cell average dimension) that was selected. Both the methods were compared and shown to give similar results for out method so automatic counting method was used since it is faster.

3 MORPHOLOGICAL STUDIES OF AMORPHOUS POLYMER-FULLERENE MIXTURES

Since their discovery, fullerenes have been widely studied and are finding increasing application in numerous technological areas, including in stateof-the-art polymer photovoltaic devices (OPVs). Following its discovery, pristine fullerene C_{60} was quickly implemented as an electron acceptor in polymer photovoltaic research.[160, 161] However, as discussed before (section 1.4.3), C_{60} is poorly soluble in most common organic solvents, and poorly miscible in conjugated polymer matrices, limiting its ability to be incorporated in commercial products. An important breakthrough in polymer photovoltaic devices was achieved when pristine fullerene C_{60} was replaced by its highly soluble derivative PCBM ([6,6]-phenyl C_{61}-butyric acid methyl ester).[162]

At present, there is a race to develop novel conjugated polymers (electron donors) that can further improve the efficiency of polymer solar cells. PCBM remains the most popular electron acceptor material for organic solar cells, although there are question marks over just how chemically compatible PCBM is with the huge diversity of donor polymers. The frequently observed poor device performance, when testing new polymers with PCBM, might be partially related to a chemical incompatibility between the polymer and PCBM. Furthermore, it has been recently recognized that the solubility of a fullerene derivative strongly affects the morphology of its composite with poly(3-hexylthiophene) (P3HT), which is commonly used as active material in bulk heterojunction organic solar cells. Troshin et al.,[40] have shown that there is a general dependence of all solar cell parameters (short circuit current, J_{sc}, open circuit voltage, V_{oc}, fill factor, FF, and power conversion efficiency η) on the solubility of the fullerene derivative used as

an acceptor component in the photoactive layer of an organic solar cell. According to these authors, the best material combinations are those where donor and acceptor components are of similar and sufficiently high solubility in the solvent used for the deposition of the active layer. In order to improve the chemical affinity between the fullerene and the polymer, and ultimately improve the underlying morphology as well as the device efficiency, one strategy has been to functionalize the C_{60} or C_{70} donor.[41-46] A different strategy has been to alter the pendant groups in the polythiophene acceptor.[49] For all these reasons, there is a need for a greater fundamental understanding of the interactions between the fullerene derivatives and the polymers.

Previous studies on the phase behavior of PCBM: polymer blends using differential scanning calorimetry (DSC) have relied mainly on the tracking of variations of the glass transition temperature (T_g) and on the identification of either one single T_g (one-phase system) or of two different T_gs (two-phase separated system). However, previous studies in PCBM:P3HT blends have shown that experimentally measured glass transition temperatures are subjected to large experimental uncertainties.[51] Furthermore, the measurement of T_g is highly dependent on the measurement technique. According to Zhao et al.,[51] the T_g of the system PCBM:P3HT, as determined using DSC and modulated temperature DSC (MTDSC), increases from 12.1 ºC for pure P3HT to 131.2 ºC for pure PCBM. According to Hopkinson et al.,[52] using dynamic mechanical thermal analysis (DMTA), the T_g increases from ~40ºC for pure P3HT to ~70ºC for a PCBM load of 65 wt.%. The T_g then drops for a higher PCBM loading of between 70 and 75 wt.% indicating phase separation.

This work is a preliminary part of the studies on conjugated polymer fullerene systems discussed in the subsequent chapters.[163] It specifically focuses on the study of the phase behavior of PCBM blends with amorphous polymers of different aromaticity, namely polystyrene (PS, with

1 aromatic ring), poly(2-vinyl- naphthalene) (P2NN, with 2 fused aromatic rings) and poly(9-vinyl-phenanthrene) (P9VPh, with 3 fused aromatic rings). The ultimate goal is to understand how aromaticity affects the miscibility of PCBM. By comparison with a previous study on pristine C_{60} in PS, P2VN and P9VPh,[164] the aim is also to understand the effect of the PCBM pendant group on the PCBM miscibility.

3.1 MISCIBILITY LIMITS OF POLYMER FULLERENE MIXTURES

In order to estimate the value of PCBM miscibility in different amorphous polymers DSC measurements were undertaken. Figure 3.1 shows DSC thermograms of blends of PCBM with three different vinyl polymers: PS, P2VN and P9VPh, over a wide composition range. All three pure polymers are amorphous, thus neither melting nor crystallization can be seen on their corresponding thermograms. Pure PCBM is semicrystalline and shows two melting peaks with the main peak at higher temperature and the smaller peak at lower temperature, in agreement with literature.[49, 51, 165] This is possibly due to the possible existence of the PCBM in two different crystal forms as has been observed by Ripens et al while crystallizing PCBM out of two different solvents.[166] No confirmation of this has been observed yet while casting from a single solution. Therefore, for all the PCBM: polymer blends with different compositions, both the crystallization and melting can be attributed to PCBM.

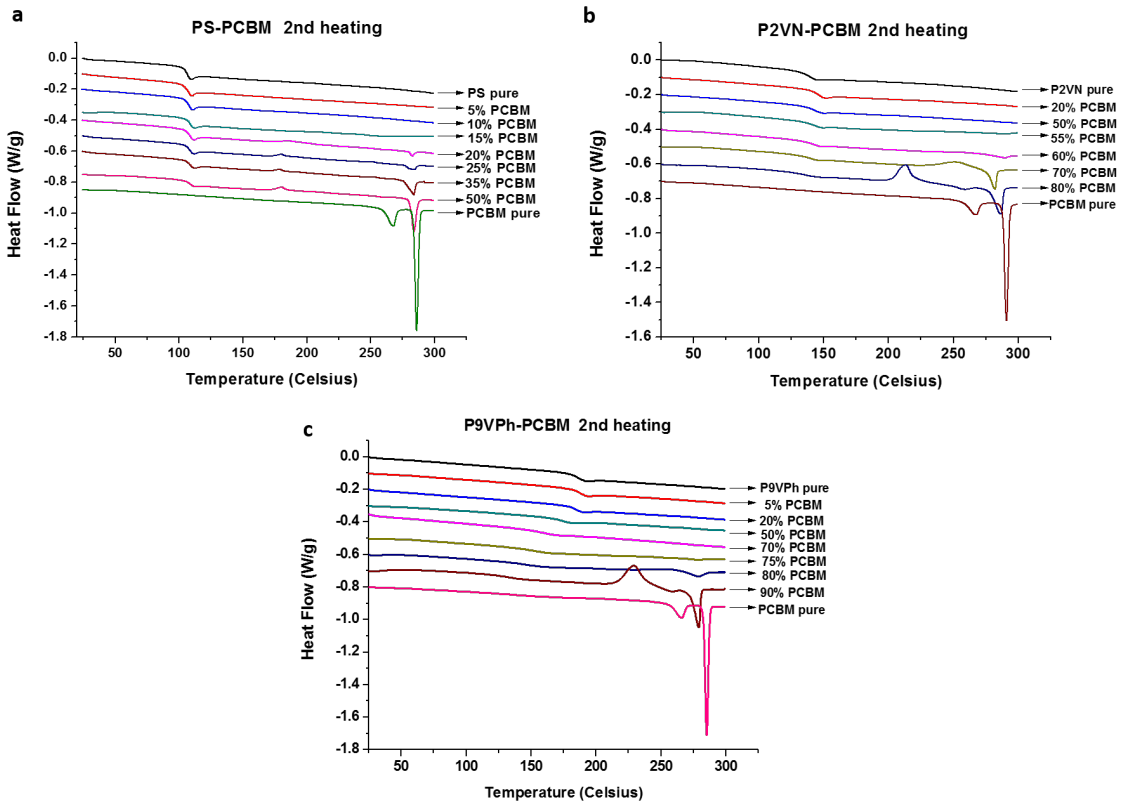

Figure 3.1 DSC thermograms of a) PS-PCBM, b) P2VN-PCBM and c) P9VPh-PCBM blends, as a function of PCBM concentration. DSC traces have been translated vertically for clarity.

For all these systems the polymer glass transition temperatures are clearly visible (Figure 3.1). For the PS blends, the PS glass transition temperature increases only slightly with the increase in PCBM load. For the P2VN blends, the T_g increases by ~10 degrees, up to 20 wt. % PCBM load but then decreases at higher PCBM loads returning to T_g values very similar to the values of the pure polymer. For the P9VPh blends the T_g remains approximately constant up to 20 wt. % loading, but then decreases considerably at higher PCBM loads.

These observations, for all the systems, contrast with previous observations in blends of PCBM with conjugated polymers (namely P3HT) in which much larger variations in T_g (from 12.1ºC for pure P3HT to 131.2ºC for pure PCBM) have been observed.[51]

With increased concentration of polymer in the blend, the crystallinity of PCBM decreases significantly. As shown in Figure 3.1 a cold crystallization peak appears in the second heating for all the blends above a critical weight fraction of PCBM as well as in pure PCBM. They are however absent at the lower concentrations of PCBM inclusion and can be attributed to complete dissolution of PCBM in the amorphous polymer. It is thus assumed that the appearance of this cold crystallization peak together with the PCBM melt peak is indicative of the formation of pure phases of PCBM. For the PS blends, the cold crystallization peak appears at ~180 ºC and together with the observation of a PCBM melt peak at ~266 ºC. The melt peaks decrease in area as the PCBM content is decreased and disappears at a critical value of PCBM between 15 and 20 wt.%. This indicates a miscibility limit between 15-20% for PCBM in the PS blends. For the P2VN-PCBM blends whilst the first observable cold crystallization peak is very broad for 70 wt. % PCBM blends the peak is not even observable in the 60 wt. % PCBM blends. This indicates that the critical miscibility is between 60 and 70 wt. % PCBM. Similarly, for the P9VPh blends the cold crystallization peak is only observed in the blends of greater than 90 wt. % PCBM, but a broad melt peak appears at 80 wt% PCBM loading suggesting a miscibility limit of between 75 and 80 wt.% PCBM loading.

Table 3.1 Area under PCBM melting peaks, A_{melt} (J/g), determined from DSC measurements as a function of weight percentage of PCBM, x (wt. %).

PS + *x*.PCBM		P2VN + *x*.PCBM		P9VPh + *x*.PCBM	
x **(wt.%)**	A_{melt} **(J/g)**	***x*** **(wt.%)**	A_{melt} **(J/g)**	***x*** **(wt.%)**	A_{melt} **(J/g)**
20	0.603	60	1.212	75	0.352
25	1.385	80	6.713	80	2.464
35	3.190	100	13.850	90	7.735
50	5.404	-	-	100	13.850
100	13.850	-	-	-	-

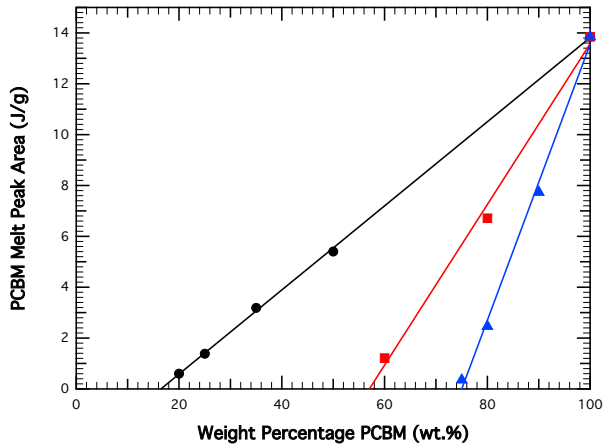

Figure 3.2 Area under the PCBM DSC determined melting peaks for PS (●), P2VN (■) and P9VPh (▲) blends as a function of PCBM content. Solid lines are linear fits to the data.

A better measure of the limit of miscibility of PCBM in each of the polymers was established by determining the areas under the PCBM melt peak and plotting as a function of PCBM. Therefore, the limit of miscibility is defined as the point at which no pure crystalline PCBM phases are observed in the system. The extracted values of peak areas are given in Table 3.1, and plotted in Figure 3.2.

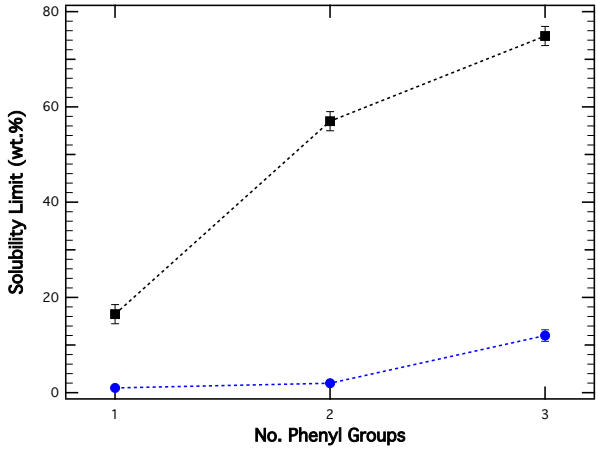

Figure 3.3 Solubility limit of PCBM (■) compared to C_{60} (●) for PS, P2VN and P9VPh. Data for C_{60} miscibility are from taken from reference [164] for comparison

Using the value for pure PCBM and extrapolating the values of peak area for each of these polymer blends to a zero peak area, the values of the miscibility limit of PCBM in the three polymers can be determined. Using this approach PCBM miscibility limits of 16.5 wt. % in PS, 57.0 wt.% in P2VN and 74.9 wt.% in P9VPh were obtained. These values are considerably higher than previous results obtained for solubility of C_{60} in the same polymers,[164] as shown in Figure 3.3. The interaction between the vinyl polymers and C_{60} was seen to be largely associated with van der Waals interactions of the phenyl side groups with the phenyl side groups. Therefore, the increasing number of side-chain phenyl groups lends to increased interaction (and binding energy) with the C_{60} molecules. It is believed the presence of the ligand in PCBM on the fullerene cage introduces an even stronger interaction with the phenyl side groups on the polymer, thus increasing the miscibility limit of PCBM in these polymers. Such a solvating effect has been seen for PCBM in organic solvents through DFT calculations.[167]

3.2 EFFECT OF FULLERENE CONCENTRATION ON PHASE MORPHOLOGY

To understand the effect of the nature of the side group on the phase behaviour of the polymer-fullerene blends, SANS measurements were used to investigate the effect on phase behavior with increasing PCBM content.[168] As discussed earlier (Section 2.4.5) the magnitude of the scattering cross-section (intensity) in SANS is proportional to the number, size and 'visibility' (contrast) of the scattering entities in a sample, whilst the q-dependence of the cross-section is related to their shape and local arrangement.

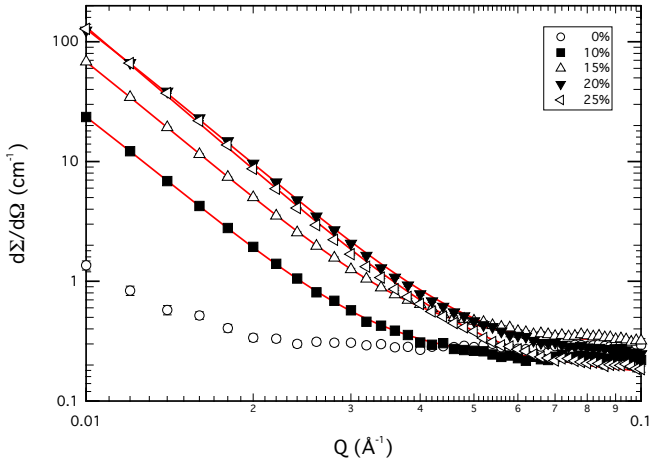

Figure 3.4 Radially averaged 1D absolute small angle scattering intensity as a function of scattering vector for PS-PCBM blends at 0 (○), 10 (■), 15 (△), 20 (▼) and 25 (◁) % PCBM content. The solid lines represent fits to the data using the DB model (Equation 3.1).

The SANS data for the three polymers with PCBM mixtures, along with their fits are shown in Figure 3.4. For these, the scattering shows similar behavior, displaying an increase in intensity with decreasing q. This indicates that neutrons are being scattered from relatively large characteristic length scales (of the order $2\pi/q$). The scattering in the pure polymers show a different

q-dependence compared to the blends and results from density fluctuations in the sample. The scattering is therefore weaker than the blends because the neutron scattering contrast between the regions of varying density is smaller in the pure polymers. The different q-dependence in the blends indicates that the scattering primarily arises from the presence of PCBM as well as any change in the local arrangement of the PS that the PCBM molecules impose. This is further confirmed by the observation that the intensity increases with increasing PCBM volume fraction, ϕ_{PCBM}. At values of ϕ_{PCBM} above the DSC determined miscibility limit (Figure 3.4) the scattering intensity does not increase at low-q.

A simple power law fit to the low-q data shows that in all but the pure polymer samples the intensity decays with a power law relationship proportional to $q^{-\alpha}$, with α between 3.2 and 3.6. A value of α=4 corresponds to completely smooth interfaces between the constituent phases while α=3 suggests the phases being fractal with rough edges. The values of α (closer to 3) suggest that the underlying morphology of the samples is fractal and composed of distinct regions delineated by rough boundaries. With this in mind, the data was initially fitted to a scattering law variously called the Debye-Bueche (DB) or Debye-Anderson-Brumberger model.

This has the form:[169, 170]

$$\frac{d\Sigma}{d\Omega}(\mathrm{q}) = \frac{c_{DB}}{(1+(q\xi)^2)^2} + b \qquad [3.1]$$

where $c_{DB} \propto (\Delta\rho)^2$ is a scaling factor ($\Delta\rho$ is the neutron scattering length density difference between the phases) and b is the background intensity that includes both instrumental and sample specific factors related to predominantly the incoherent scattering from the sample.

Table 3.2 Scaling factors and correlation lengths for vinyl polymer-PCBM blends determined from the DAB model (equation 3.1) fits to the SANS data.

PS+PCBM			P2VN+PCBM			P9VPh+PCBM		
ϕ_{PCBM}	c_{DB}	ξ (Å)	ϕ_{PCBM}	c_{DB}	ξ (Å)	ϕ_{PCBM}	c_{DB}	ξ (Å)
0.10	8.8×10^{-5}	309.7 ± 15.2	0.20	1.62×10^{-4}	112.3 ± 0.7	0.05	3.2×10^{-5}	175.2 ± 3.5
0.15	2.8×10^{-4}	360.7 ± 12.7	0.55	5.9×10^{-4}	273.6 ± 3.4	0.20	5.5×10^{-4}	216 ± 20.0
0.20	4.7×10^{-4}	298.3 ± 5.0	0.60	6.8×10^{-4}	449.4 ± 15.6	0.70	2.7×10^{-4}	138.1 ± 0.5
0.25	1.1×10^{-3}	839.9 ± 100.0	0.70	8.1×10^{-4}	427.9 ± 12.1	0.80	2.5×10^{-4}	151.4 ± 0.7

Table 3.3 Mass fractal dimensions, and fractal cut-off lengths determined using MF model fits (Equation 3.2) to the SANS data assuming a primary particle radius of 5 Å.

PS+PCBM			P2VN+PCBM			P9VPh+PCBM		
ϕ_{PCBM}	D_m	ζ (Å)	ϕ_{PCBM}	D_m	ζ (Å)	ϕ_{PCBM}	D_m	ζ (Å)
0.10	3.01 ± 0.01	271.9 ± 22.1	0.20	2.98 ± 0.01	117.5 ± 1.8	0.05	2.99 ± 0.01	180.9 ± 9.4
0.15	3.01 ± 0.01	271.4 ± 1.3	0.55	3.02 ± 0.02	219.3 ± 3.7	0.20	3.04 ± 0.01	476.9 ± 432.5
0.20	3.02 ± 0.01	222.2 ± 0.7	0.60	3.01 ± 0.02	318.9 ± 11.5	0.70	3.12 ± 0.03	105.4 ± 0.6
0.30	3.04 ± 0.01	277.5 ± 7.5	0.70	3.00 ± 0.01	448.4 ± 26.9	0.80	3.08 ± 0.02	125.6 ± 0.9

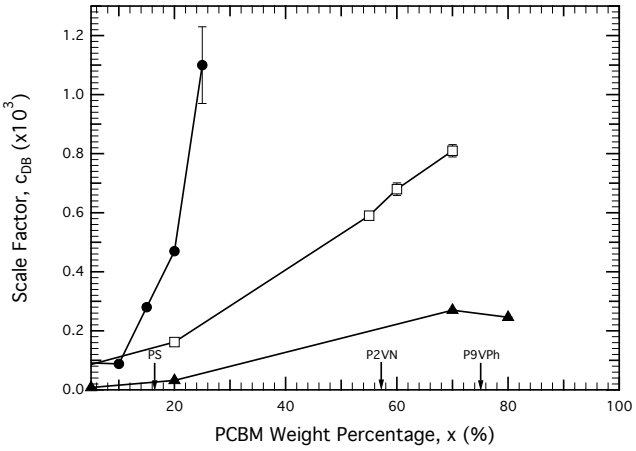

Figure 3.5 Plot of DAB-model scale factor (derived using fits to from Equation 3.1), as a function of PCBM concentration for PS (●), P2VN (□) and P9VPh (▲). The arrows indicate the miscibility limit determined by DSC from crystalline-peak area analysis.

This model assumes that the coherent part of the scattering arises from two randomly distributed phases characterized by a single average density correlation length, ξ; essentially the average separation between the phases. From Figure 3.4 the DB model is seen to be an adequate description of the data at all concentrations for all three polymers. The values obtained from the fitting for c_{DB} and ξ using Equation 3.1 are given in Table 3.2.

A weakness with using DB analysis is that it is a shape-independent model and in that respect provides rather limited system specific information. However, it is known that the system may be more than simply two-phase, particularly since the presence of PCBM 'clusters' in the blends have been advocated by other researchers. A more sophisticated model would combine the scattering from a fractal morphology with that from particulate clusters, and this is the basis of the Mass-Fractal (MF) model.

This defines the scattering in terms of fractal aggregates consisting of spherical primary particles of radius R, such that:[171]

$$\frac{d\Sigma}{d\Omega}(q) = c_{MF}\frac{3[\sin(qR)^2 - (qR)^2\cos(qR)^2]}{(qR)^6} \times \frac{\Gamma(D_m-1)\zeta^{(D_m-1)}}{[1+(q\zeta)^2]^{\frac{(D_m-1)}{2}}} \cdot \frac{\sin[(D_m-1)\,tan^{-1}(q\zeta)]}{q} + b \qquad [3.2]$$

where D_m is the mass fractal dimension, ζ is the fractal cut-off length, and c_{MF} is a scale factor that is also proportional to $(\Delta\rho)^2$. The MF model is, however, extremely sensitive to these three parameters if they are fitted as independent variables. Given the suspected presence of PCBM aggregates the data was fitted using Equation 3.2 assuming a fixed value of $R = 5$ Å, *i.e.* the approximate equivalent spherical radius for a PCBM molecule. Using this assumption the MF model also gives equally good fits to the SANS data. The derived parameters are shown in Table 3.3.

Clearly, both the DB and MF fitting models suggest that for all three polymers at all compositions above and below the miscibility limit (determined from the DSC measurements) the blends are composed of two phase morphologies. This behavior indicates that the systems are not at equilibrium, as may be anticipated from the sample preparation method for the SANS samples. The question remains about what the apparent phases are composed of and consequently what are the origins of the observed concentration dependent changes seen in the scattering data. A route to understand this is behavior is to explore the behavior of the fitting parameters more deeply.

From fits to the DB model it is seen that for all three polymers the value of L is reasonably large (hundreds of Ångstrom). This result is mirrored by the results from the MF model. The values of ζ are broadly comparable to the ξ values and generally reflect the same changes with PCBM content, although there are no clear systematic changes in the values of ξ or ζ with increasing

ϕ_{PCBM} from either model fit. However, as shown in Figure 3.5, the variation in DAB scaling factor (c_{DB}) for all the polymer systems shows clear non-linear increases with PCBM concentration.

Similar increases in the scale factor (c_{MF}) are also observed from fits to the MF model (Equation 3.2). The largest values of c_{DB} are seen in the PS system and are smallest for the P9VPh system. Since c_{DB} is proportional to the scattering length density difference between phases it is clear that at these maximum values greater mixing in the systems is observed in the P9VPh compared to P2VN, which in turn is more miscible than the PS system. This is consistent with the values of L, which are smaller in the P9VPh system at 70-80% PCBM loading than they are in the P2VN system. For the PS-PCBM system there is a distinct upturn in the c_{DB} at a PCBM concentration that is consistent with the miscibility limit determined by the DSC crystalline-peak area disappearance. At these concentrations pure PCBM crystals are observed in the system (as determined by DSC), so that the upturn in c_{DB} is associated with formation of PCBM crystals and PS-rich (PCBM depleted) domains forming above this critical concentration. Although c_{DB} increases for the P2VN and P9VPh system with increasing PCBM concentration there is no apparent faster increase observed above the critical values determined by DSC. This is presumably because of the difference in miscibility of PCBM in these two polymers compared to PS, so that even though PCBM-phases are formed the degree of PCBM in the remaining matrix of the system remains high.

From the mass fractal fits, it is seen that the fractal dimension values are all approximately 3 for all three polymers at all concentrations. The scattering behavior from fractals follows a q^{-D_m} scattering dependence for q < ζ^{-1}, and changes to q^{D_m-6} for q > ζ^{-1}.[171] Given the values of ζ (Table 3.3) from the fitting results where $D_m \sim 3$ a q^{-3} scattering dependence may be observed. This is consistent with the observed scattering power law dependence where a $q^{-3.2}$ to $q^{-3.6}$ behavior

was obtained. This indicates that at the length scales being observed, the interfaces between the phases are rough and may partly explain the apparent concentration independence of the phase correlation lengths.

3.3 SUMMARY – PHASE MORPHOLOGY OF AMORPHOUS POLYMER-FULLERENE MIXTURES

The miscibility limit of PCBM in vinyl polymer matrices with different aromaticities were investigated by means of DSC and SANS. Using DSC, the miscibility limit of PCBM in these polymers as defined by the loss of any crystallinity of the PCBM was found to increase non-linearly with the number of aromatic moieties in the side chain with 16.5 wt. % in PS (1 aromatic ring), 57.0 wt.% in P2VN (2-fused aromatic rings) and 74.9 wt.% in P9VPh (3-fused aromatic rings). The increase in miscibility may be attributed to increased van der Waals interactions between the phenyl side chains and the PCBM molecules. The increase is however non-linear and a possible explanation for this could be the curvature of the higher order aromatic side chains make it even more conformal to the fullerene enhancing its interaction with it, as seen by Campbell et al.[164] in studies with C_{60}. PCBM however has considerably higher miscibility that the corresponding C_{60}-polymer blends. One reason for this could be that PCBM itself is inherently more soluble in the solvents being used (toluene) than C_{60}.[172, 173] Consequently, the molecules are more intercalated in the solution state than C60 and in turn tend to be more easily included in the amorphous region of the polymer upon solvent drying. Alternately, as suggested before, the greater interaction of the phenyl group on the side chain with the aromatic side chains of the polymer could allow it to solubilize more in the polymer and give higher miscibility limits, unlike C_{60} where the interaction is only possible with the fullerene cage.[174]

Below this miscibility limit a two-phase morphology is determined in all three polymer-PCBM blends at all concentrations. The phase domain sizes were not found to show strong dependence on the concentration and were either approximately constant or increased slightly for each polymer. In addition, the domains were found to have rough boundaries indicating the phases were intermixed and not distinctly phase separated. The scattering length density difference between the phases was strongly dependent on the concentration for each polymer system. Even at the lowest concentration of PCBM in each polymer, distinct two-phase domain structures are observed. The difference in the concentration of the PCBM between the two phases is very low. As the overall PCBM content increases in the blend, the concentration difference of the PCBM between the two phases becomes more distinct. This is shown most dramatically for the PS-PCBM system where there is a distinct increase in the PCBM concentration difference in the phase-domains above the critical miscibility limit as determined by DSC. At a high concentration, DSC measurements indicate the presence of pure PCBM crystals in all the blends, with the remaining phase depleted of PCBM. The variation in miscibility of PCBM in the three polymers as determined by the DSC results is clearly reflected in the difference in the scattering length density values at the highest PCBM content samples measured. In this case PS demonstrates the greatest degree of partitioning of PCBM between the two phases so that when pure PCBM domains are present there is the least amount of PCBM remaining in the other phase. The opposite is true for the P9VPh system where, in comparison a large amount of PCBM is found in the remaining phase. In either case though, the DAB model was derived to be an appropriate model to describe phase morphology of the different amorphous polymer-fullerene systems. At the higher concentrations, it forms a more accurate representation of such mixtures and can be used as the basis for the future

studies on the morphology of semiconducting polymers (semicrystalline) and fullerene based mixtures for BHJ based OPVs.

4 MORPHOLOGICAL STUDIES OF CONJUGATED POLYMER-FULLERENE BHJ DEVICES PART 1: OUT-OF-PLANE MORPHOLOGY

The studies on the miscibility of PCBM with a series of amorphous polymers in the previous chapters helped in better understanding the morphology development and phase behavior of blends of fullerene based small molecules in polymers. This understanding was used as a basis for proceeding on to morphological studies of blends of the semi-crystalline conjugated polymers and fullerenes which form bulk heterojunction (BHJ) type organic photovoltaic (OPV) devices.

4.1 DEVICE PERFORMANCE AND SEGREGATION PROFILES IN OPVS

Nanoscale BHJ systems, typically consisting of fullerenes dispersed in conjugated polymers as the active component, have been actively studied over the last decade in order to produce high performance OPV devices. A significant role in the device efficiency is played by the active layer morphology, but despite considerable study, a full understanding of the exact role that morphology plays, and therefore a definitive method to produce and control an ideal morphology, is missing. In order to understand the phase behavior in these devices, a number of advanced characterization techniques have been used including neutron reflection, together with grazing incidence X-ray and neutron scattering, and X-ray photoelectron spectroscopy (XPS) to determine the morphology of the BHJ active layer in functional devices. Model bulk heterojunction (BHJ) films based on mixtures of poly(3-alkylthiophene)s (P3AT), with three different fullerenes (C_{60}, PCBM and bis-PCBM), have been studied, which provides variations in crystallinity and miscibility within the BHJ. In studying the behavior of these OPV devices,

possible correlations between the observed morphology within the BHJ layer and the device performance metrics were shown, i.e. the short-circuit current (J_{SC}), fill factor (FF), open-circuit voltage (V_{OC}) and overall power conversion efficiency (PCE), η.

Using these model systems, the effect of thermal annealing on the BHJ morphology through the film thickness as a function of varying polythiophene-fullerene mixtures and different electron transport layer interface were determined.

4.1.1 Device Characteristics in the OPVs

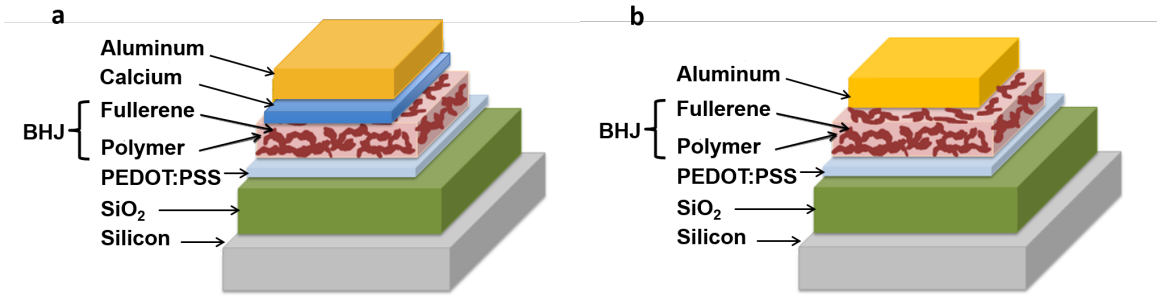

Figure 4.1 Layers in the bulk heterojunction structure for scattering experiments having polymer-fullerene mixed active layer (polyalkylthiophenes with modified fullerenes) a) with Ca electrode b) without Ca electrode.

(Note: SiO_2/Silicon was replaced by ITO/Glass for the device measurements.)

The bulk heterojunction samples were prepared using three different P3AT (poly-3alkylthiophenes) and a choice of three different fullerene derivatives, C_{60} (fullerene), PCBM, bis-PCBM (Figure 4.2). Different combinations of polymer and fullerene were used to give 9 different heterojunctions. Solutions of 0.8% (wt/vol) of all the compounds in O-DCB were prepared and then mixed in 1:1 (polymer: fullerene) ratio.

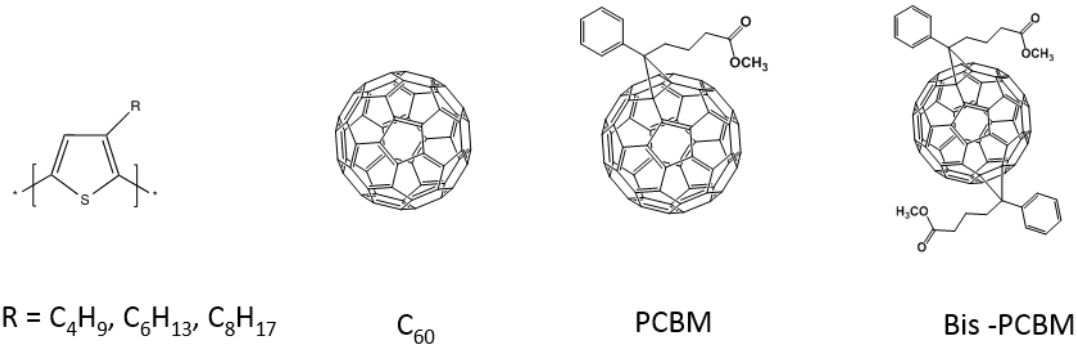

Figure 4.2 Polyalkylthiophene, C_{60} fullerene and its derivatives used in the heterojunction devices.

Bulk heterojunction devices (ratio 1:1), shown schematically in Figure 4.1, were prepared from these solutions as discussed in the experimental Section 2.6.1 and the dark and light current-voltage statistics were measured using a Keithley's Series 2400 SMU source meter under an AM 1.5 solar spectrum.. Devices were measured both pre- and post-annealed relative to Ca/Al or Al electrode deposition at temperatures optimized previously in literature[67] (Pre anneal – 120 °C for 10 minutes before electrode deposition and Post anneal – 150 °C for 10 minutes after electrode deposition, experimental Section 2.6.1 for further details). As seen in Table 4.1 and 4.2, devices without the Ca layer performed better with annealing post Al layer deposition (post-anneal), whereas devices with the Ca-add layer performed better with only pre-annealing before the Ca/Al deposition (pre-anneal), and these devices were used for further morphological studies using the characterization techniques mentioned earlier.

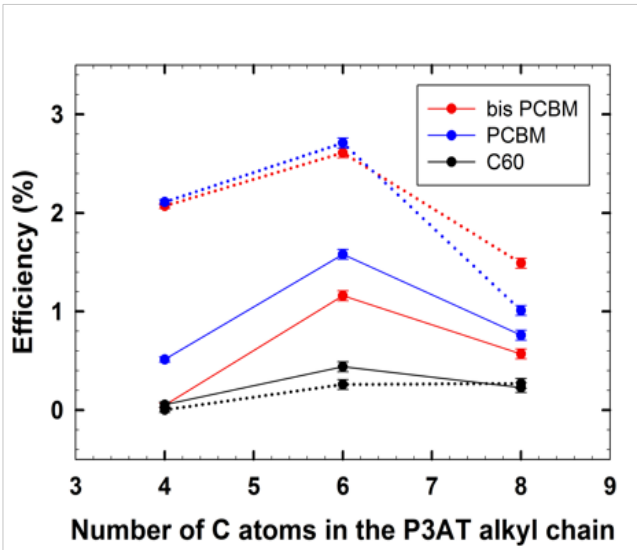

Figure 4.3 Power conversion efficiency values, for the different devices with Ca (dashed) and without Ca (solid line).

Table 4.1 Device parameters for the optimally performing annealed BHJ systems with Al electrode.

Device	V_{OC} **(V)**	J_{SC} **(mA/cm^2)**	**FF (%)**	**PCE (%)**
P3BT:C_{60}	0.37±0.01	0.39±0.019	29.24±0.585	0.04±0.001
P3BT:PCBM	0.49±0.01	2.6±0.13	39.97±0.799	0.51±0.010
P3BT:bis-PCBM	0.57±0.01	0.37±0.018	38.29±0.765	0.06±0.001
P3HT:C_{60}	0.35±0.007	5.13±0.256	24.71±0.494	0.44±0.009
P3HT:PCBM	0.45±0.009	7.03±0.352	49.41±0.988	1.58±0.031
P3HT:bis-PCBM	0.66±0.013	4.07±0.203	43.35±0.867	1.16±0.023
P3OT:C_{60}	0.33±0.006	2.43±0.122	28.31±0.566	0.23±0.004
P3OT:PCBM	0.45±0.009	3.79±0.189	44.46±0.889	0.76±0.015
P3OT:bis-PCBM	0.66±0.013	2.19±0.109	39.62±0.792	0.57±0.011

Table 4.2 Device parameters for the optimally performing annealed BHJ systems with Ca/Al electrode.

Device	V_{OC} (V)	J_{SC} (mA/cm^2)	FF (%)	PCE (%)
P3BT:C_{60}	0.1±0.002	0.006±0.01	23.7±0.47	0.002±0.01
P3BT:PCBM	0.56±0.001	6.50±0.13	58.1±1.0	2.11±0.02
P3BT:bis-PCBM	0.69±0.006	5.66±0.15	52.9±0.8	2.07±0.05
P3HT:C_{60}	0.6±0.012	1.32±0.066	32.6±0.65	0.26±0.01
P3HT:PCBM	0.60±0.001	7.53±0.34	59.6±1.0	2.71±0.08
P3HT:bis-PCBM	0.72±0.001	6.42±0.25	56.3±0.6	2.61±0.13
P3OT:C_{60}	0.45±0.009	1.52±0.07	39.4±0.79	0.27±0.005
P3OT:PCBM	0.55±0.006	3.30±0.15	55.2±3.2	1.01±0.10
P3OT:bis-PCBM	0.70±0.023	3.91±0.39	54.0±1.5	1.49±0.22

From the measured J-V curves the J_{sc}, V_{oc} and the Fill Factor were extracted (using the in-house software designed by Marcin Kielar) for the different devices and reported in Table 4.1 and 4.2. For the devices made with and without the Ca add layer, a larger V_{OC} is observed for BHJ containing bis-PCBM than its counterparts with PCBM, both exhibiting larger V_{OC} than C_{60}, which is in good agreement with other reports in the literature.[27, 175] On comparing devices made with the same fullerene electron acceptor, the J_{sc} values followed the trend of J_{sc} (P3HT) > J_{sc} (P3BT) ~ J_{sc} (P3OT), i.e. P3HT based devices facilitates the highest amount of charge collection at the electrodes. Since the absorption characteristics of these polymer systems have been seen to be not so different previously,[176] a considerable factor for the trend in the *Jsc* could be the morphology of P3HT facilitating charge transport and collection more efficiently. The *FF* of the devices was maximum for the case of P3HT (P3HT>P3OT>P3BT) with any fullerene, and similarly for any polymer the trend observed was PCBM>bis PCBM>C_{60}. The presence of the Ca add-layer

produced higher FF values in almost all systems compared to Al only devices, the exceptions being for two of the C_{60} containing devices. From the J_{sc}, V_{oc} and FF values the device power conversion efficiency (PCE), was calculated from $PCE = (V_{oc} J_{sc} FF)/I_o$, where I_o is the incident light intensity. The values obtained are given in Tables 4.1 and 4.2 and shown plotted against the number of carbons in the P3AT alkyl side chain in Figure 4.3c. It is seen that devices containing P3HT-PCBM as the BHJ gave the best device efficiencies among all the P3AT-PCBM based devices, as has been well known in literature.[153, 177] Interestingly, on post-annealing, the devices showed some improvement in the performance when there is no Ca add-layer, whereas the devices made with Ca showed no improvement or even a reduction in the PCE even in the case of P3HT-PCBM. This could be associated with Ca diffusion into the active layer or oxidation of the electrode on annealing after the deposition, producing a reduction in the short circuit current. [178, 179]

4.1.2 DFT simulations

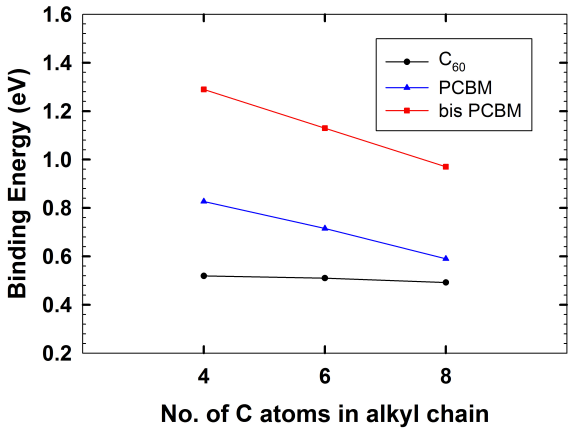

Figure 4.4 Binding Energy vs alkyl chain length of the polyalkylthiphene for the different mixtures

DFT simulations were carried by Dr. Bobby G Sumpter at the Oak Ridge National Laboratory, on the combinations of the 9 different oligoalkylthiophenes-fullerene pairs to give the binding energy values for the combinations. This helped us determine the miscibility of the fullerene in the polymer in each case (see Appendix). These measurements were part of the joint DOE project, contract No. DE-FG02-10ER4779 of which Dr. Sumpter was a part of.

The result of these measurements showed that the binding energy, E_b, decreased with increasing side chain length (Figure 4.4), giving the highest E_b value for the P3BT-bis-PCBM combination, whilst also suggesting that the solubility of the fullerenes in the polyalkylthiophene follow the trend bis-PCBM>PCBM>C_{60}. So the trend for the fullerene miscibility increases as one increases the side chains on the fullerene. This is also witnessed in the previous chapter for PCBM in miscibility in amorphous fullerenes wich were seen to be significantly more than known C_{60} miscibility in those fullerenes.

4.1.3 Neutron Reflectivity Measurement and Depth Profile

Neutron reflectivity (NR) was performed on the devices of P3AT-fullerene prepared on (2.5×2.5)cm samples using the CRISP and SURF instruments at the ISIS Facility, UK. Reflectivity data were collected over 2 or 3 angles with constant angular resolution giving a combined *Q*-range from 0.008 - ~0.2 $Å^{-1}$. A representative set of NR data and the associated fits to the data together with the corresponding scattering length density profiles are shown in Figure 4.5.

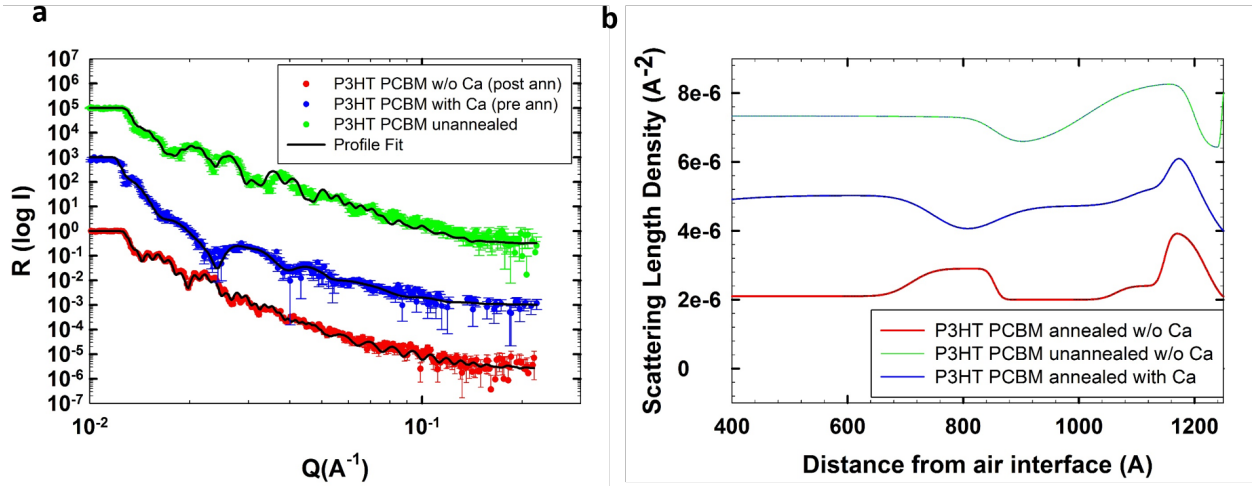

Figure 4.5 a) Neutron reflectivity plots (Reflectivity vs momentum transfer) for pre- and post-annealed P3HT- PCBM devices b) SLD profile through the layers in the heterojunction device, for pre- and post-annealed P3HT-PCBM systems. (Active layer starts ~600 Å from air interface)

Figure 4.5a shows reflectivity versus momentum transfer (Q) plots for devices containing BHJs made of P3HT-PCBM and compares the pre-annealed, post-annealed and unannealed samples. The data were fitted using RASCal software (developed at ISIS) to determine the corresponding scattering length density for the sample from which the distribution of the polymer and fullerene in the heterojunction layer between the two electrodes is shown in Figure 4.5b. It is immediately clear from the NR data that the BHJ cannot be fitted as a single homogeneous layer. The simplest model that both adequately fits the data and is consistent with all the devices measured is to consider the BHJ layer to be composed of three layers of varying thicknesses and scattering length densities. Models with more layers also fitted the data equally well, but the significance of the additional parameters these models include cannot be justified, and therefore a simpler three-layer model is used in the following discussions.

With the values of the scattering length density (SLD) from the fits, the values of the volume fraction of fullerene ϕ_f in the three different sub-layers were calculated using Equation

4.1, by assuming that the heterojunction layer is a binary mixture of polymer and fullerene and thus the component scattering length densities were additive.

$$\rho_h = \phi_p \rho_p + \phi_f \rho_f \quad [4.1]$$

Here ϕ_i and ρ_i are the volume fraction and the scattering length density of the material i, where the subscripts h, p and f refer to the heterojunction, polymer, and fullerene, respectively. The SLD values of fullerenes are significantly higher than polyalkylthiophenes, for instance for PCBM, ρ_f = 4.34×10^{-6} A^{-2} and for P3HT, ρ_p = 0.74×10^{-6} A^{-2}. All theoretically calculated SLD values (used as initial guess parameters in fitting) are tabulated in Table 4.3. In addition, the theoretical values for the surface energy and Hansen's solubility parameter of the BHJ components were calculated. These are solubility parameters for interaction between polymer and fullerene and not their solubilities in solvents as has been already reported by Machui et al.[173] The surface energies (γ) were estimated using the Parachor equations and adding up the Parachor contributions (P_s) of their constituent atomic and structural groups[1] and the molecular volume (V) in cm^3/mol.

$$\gamma = \left(\frac{P_S}{V}\right)^4 \quad [4.2]$$

Hansen solubility parameters (δ) were calculated using the constituent terms of atomic dispersive interactions (δ_D), permanent dipole molecular interactions (δ_P) and molecular hydrogen bonding interactions (δ_H) and the equation:

$$\delta^2 = (\delta_D)^2 + (\delta_H)^2 + (\delta_P)^2 \quad [4.3]$$

[1] from *Properties of Polymers*, D.W. Van Krevelen, Elsevier, Fourth Edition, 2009

Table 4.3 Calculated values of Scattering Length Density (SLD), surface energy (γ) from the Parachor equation and Hansen solubility parameter (δ) for the different components of the BHJ.

Material	**Scattering Length Density ($Å^{-2}$)**	**Surface Energy(γ) (mN/m^2)**	**Solubility Parameter (δ) ($MP_a^{1/2}$)**
P3BT	0.93E-06	28.70	20.77
P3HT	0.79 E-06	21.87	20.83
P3OT	0.59E-06	34.45	20.71
C_{60}	5.73 E-06	40.11	19.82
PCBM	4.34 E-06	38.30	19.86
Bis PCBM	3.5 E-06	37.16	19.89
PEDOT : PSS	1.14 E-06	-	-
SiO2	3.4 E-06	-	-
Al	2.08 E-06	-	-
Si	2.07 E-06	-	-
Ca	1.09E-06	-	-

Using the SLD profile obtained and calculating ϕ_f from Equation 4.1, the percentage-segregated volume of the fullerene through the depth of the BHJ was determined which included the excess volume of fullerene segregated at the interfaces (given by the hatched area in Figure 4.6, Equation 4.4). As mentioned earlier, plots were derived for the *PCE* values of the same devices from the device measurements (Figure 4.3) to obtain correlations between device parameters and the morphological data from the NR measurement.

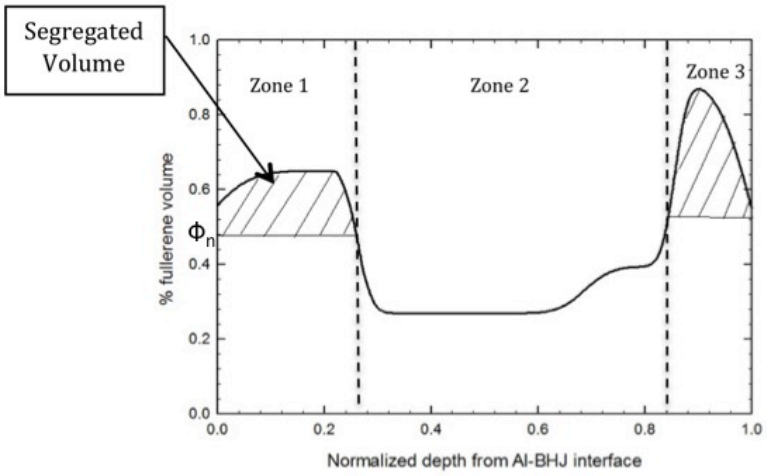

Figure 4.6 Segregated volume fraction of fullerene through normalized depth of post annealed P3HT-PCBM BHJ.

$$\textit{Excess Segregated Fullerene (\%)} = 100 \int_{z=z_i}^{z_n} [f(z) - \emptyset_n]\, dz \qquad [4.4]$$

Even before annealing, 3 distinct layers are observed in the heterojunction, a layer of fullerene enrichment near the PEDOT:PSS, a layer of fullerene depletion in the middle and a layer of fullerene depletion near the aluminum cathode as seen in the profile of the unannealed sample (green line in Figure 4.5b). Upon annealing, it is seen that the fullerene enriched layers and consequently the depleted layers become further enriched and depleted respectively, compared to the pre-annealed films (red and blue lines in Figure 4.5b). The interface between the BHJ and aluminum layers is also seen to broaden in the devices, which is consistent with studies by other groups. [88, 92] This suggests that either the Al deposition process induces a significant degree of intermixing or more probably, Al has diffused into the bulk heterojunction layer during annealing. In order to interpret the SLD data at the electrode interfaces and convert to volume fraction of the individual BHJ components a number of assumptions were made. Firstly, the region from midpoints of the BHJ interfaces with the Al on one extreme and underlying PEDOT:PSS at the

other was defined as the total BHJ film thickness . In addition the heterojunction near the interface was treated as only a two-component system. It is important to note was that in previous studies on BHJ segregation profiles [88, 92, 95, 96], the fullerene-enriched layer was considerably sharp (5 nm), compared to the samples used in this study, where it is slightly more prominent (~10-15nm), which in turn would affect the device properties substantially. Studies on a different donor-acceptor system [180] have suggested that the formation of a fullerene enrichment at the bottom electrode, depends not only on the surface energy but also on the thickness of the film and amount of polymer being spun. Thus for a thinner film with, the fullerene would be a considerably larger fraction of the thickness as is in this case compared to previous studies.

Given the three-layer model from the profile fit, the BHJ was thus divided into three zones (see Figure 4.7). Defining the interfacial region near the aluminum surface as Zone 1, an enrichment of fullerene is seen in this zone during post-annealing together with an increase in roughness at the Al/BHJ interface possibly due to diffusion of aluminum into the BHJ. By contrast, polymer enrichment near the Al or Ca surface is observed in the pre-annealed or unannealed devices. From the SLD values obtained in the fits, the percentage of excess fullerene (percentage greater than the 50% as is expected in 1:1 composition) in Zone 1 can be determined (Equation 4.4) and for the post-annealed samples this is seen to increase from around 2.3% in the case of C_{60} as the fullerene, to nearly 20 % in the case of bis-PCBM in P3HT based devices(Table 4.4). Similar increases are seen in devices made from P3BT and P3OT as well. The thickness of Zone 1 thus remains mostly the same before and after annealing for different samples (~ 7-9 nm) but content-wise changes from a fullerene-depleted region to a fullerene enhanced region in the case of the post-annealed samples. The depletion however still remains in the case of pre annealed samples (with Ca), albeit the width of the depletion region isn't as pronounced as in the case of

unannealed devices. The region near the PEDOT:PSS interface is defined as Zone 3. In this zone, an increase in SLD is observed in both the pre- and post-annealed cases, indicating fullerene enrichment in all systems. The amount of fullerene in this zone is seen to decrease with increasing functionality as C_{60}>PCBM>bis-PCBM (see Table 4.4 and 4.5). However, the thickness of Zone 3 varies considerably between the fullerenes, as seen in Table 4.5. Consequently, to allow comparisons of the segregation, a normalized percentage segregated volume of the fullerene is used (Equation 4.4, Table 4.4 and 4.5). Owing to the enrichment of fullerene at both the electrode interfaces in post-annealed samples, it is depleted from between these regions, i.e. in Zone 2, leading to an enrichment of the P3AT. The three layered model proposed is thus shown here schematically.

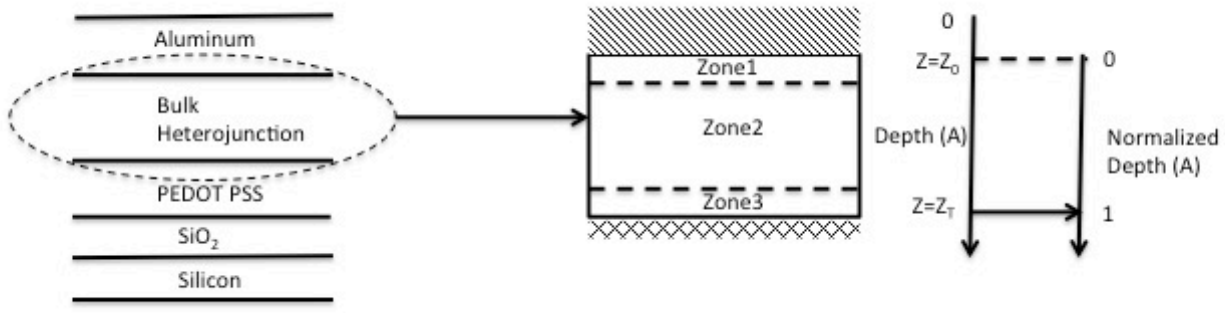

Figure 4.7 Three layered proposed structure of heterojunction.

4.1.4 XPS measurements and Depth Profile

To corroborate the segregation behavior in the active layer in the two different device configurations i.e. with and without Ca, XPS depth profile measurements were conducted on devices that were exactly the same as for the NR measurements. Depth profiles were obtained by repeated standard XPS measurements, followed by sample etching using an Argon ion source. Etching was achieved using an ion source energy of 3000 eV with etch periods of 100s between

each measurement. Each etch cycle was found to correspond to the etching of BHJ film thickness of ~8 nm. Due to differences in etching rates, for the same ion source energy, 100s of etching of Al resulted in film thickness changes of only 2 nm. Using sulfur as a critical marker of the P3AT, the depth dependency of S was used to establish the relative levels of polymer and fullerene through the BHJ film. Based on the average atomic percent content of sulfur (S) equal to 4.1% in a homogeneous 50:50 P3HT-PCBM mixture[181], the segregation behavior of P3AT and consequently the fullerene in the BHJ layer can be determined. A plot of the S content as a function of etch depth through an Al/P3HT-PCBM/PEDOT:PSS system is shown in Figure 4.8. Sulfur from PEDOT:PSS is expected at the bottom electrode, but the S peak is distinctly present at 168 eV in contrast to the S in P3HT which is at 163 eV (Figure 4.8b). Thus the S from P3HT can be distinguished and quantified throughout the etch depth. For the pre-annealed sample, as with the results from the NR, it is clear that the P3HT is not uniformly distributed through the film thickness. The S content at the bottom interface (PEDOT PSS – BHJ) in both the cases is seen to be around 1.8% which would correspond to ~25% of P3HT at that interface and consequently 75% of PCBM. At the other interface (Cathode-BHJ) however, the pre-annealed case shows a fullerene enrichment, corresponding to 5% S content, or ~60% P3HT or a depletion of PCBM (40%). The post-annealed samples at this interface though, show a S content of around 3.2% corresponding to 40% P3HT or 60% PCBM (fullerene enriched).

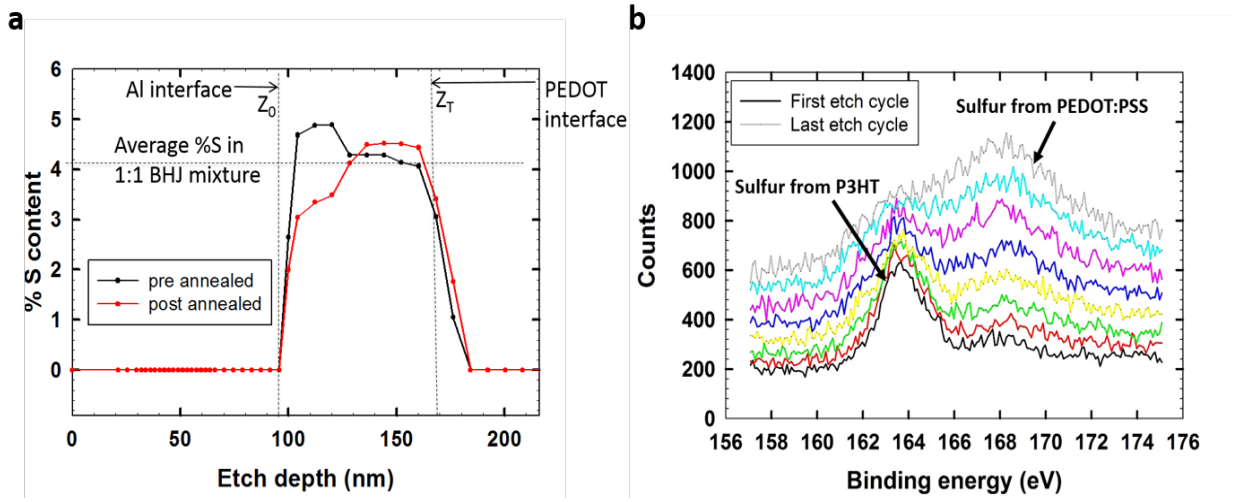

Figure 4.8 a) Atomic percent of S as a function of XPS depth profiling through P3HT-PCBM based device structure, pre- and post-annealed b) S peaks from P3HT and PEDOT:PSS.

4.2 MULTI-LAYERED STRUCTURES IN THIN FILM OPV

As determined through the NR and XPS measurements, the active layer in the BHJ devices could be modeled as comprising of 3 zones or layers. Analysis of the data gave us a depth composition profile which was subsequently quantified and tabulated, zone by zone. (Table 4.4 and 4.5)

Table 4.4 Values of depletion layer width, and fullerene composition percentage in the depletion layer and fullerene rich layer in Post Annealed BHJ w/o Ca.

Post Annealing	**P3HT-C_{60}**	**P3BT-C_{60}**	**P3OT-C_{60}**
Width Zone 1(Å)	123	115	123
Width Zone 3(Å)	63	52	54
Excess Segregated Fullerene Zone 1 (%)	2.9	0.1	1.3
Excess Segregated Fullerene Zone3 (%)	5.7	10.1	6.1
Roughness Zone 3 (Å)	7.4	15.7	10.2
Fullerene Zone 2 (%)	41.1	45.1	38.3
Post Annealing	**P3HT-PCBM**	**P3BT-PCBM**	**P3OT- PCBM**
Width Zone 1(Å)	144	145	143
Width Zone 3(Å)	72	81	78
Excess Segregated Fullerene Zone1 (%)	7.8	5.1	6.1
Excess Segregated Fullerene Zone3 (%)	4.4	4.92	4.9
Roughness Zone 3 (Å)	5	8.1	5.3
Fullerene Zone 2 (%)	34.2	39.4	34.4
Post Annealing	**P3HT-bis PCBM**	**P3BT-bis PCBM**	**P3OT-bis PCBM**
Width Zone 1(Å)	88	99	99
Width Zone 3(Å)	73	76	60
Excess Segregated Fullerene Zone 1 (%)	20.5	13.4	17.1
Excess Segregated Fullerene Zone3 (%)	5.3	10.6	6.2
Roughness Zone 3 (Å)	5.2	6.3	5.5
Fullerene Zone 2 (%)	28.2	30.5	29.4

Table 4.5 Values of depletion layer width, and fullerene composition percentage in the fullerene rich layer in Pre Annealed BHJ with Ca.

Pre Annealing	**P3HT-C_{60}**	**P3BT-C_{60}**	**P3OT-C_{60}**
Width Zone 1(Å)	63	65	53
Width Zone 3(Å)	140	172	142
Excess Segregated Fullerene Zone 3 (%)	12.4	15.2	12.75
Roughness Zone 3 (A)	7.1	8.4	7.2
Fullerene Zone 2 (%)	45.2	43.1	47.3
Pre Annealing	**P3HT-PCBM**	**P3BT-PCBM**	**P3OT- PCBM**
Width Zone 1(Å)	161	165	153
Width Zone 3(Å)	52	51	58
Excess Segregated Fullerene Zone 3 (%)	6.5	6.80	6.92
Roughness Zone 3 (A)	5.1	5.7	5.9
Fullerene Zone 2 (%)	48.7	45.2	48.3
Pre Annealing	**P3HT-bis PCBM**	**P3BT-bis PCBM**	**P3OT-bis PCBM**
Width Zone 1(Å)	86	75	80
Width Zone 3(Å)	90	110	95
Excess Segregated Fullerene Zone 3 (%)	7.3	9.5	7.8
Roughness Zone 3 (A)	6.2	7.4	6.5
Fullerene Zone 2 (%)	47.5	44.2	48.1

4.2.1 Zone 1 (Near Cathode) in the Active Layer

As seen in Figure 4.5b, in the post-annealed BHJ samples, a fullerene-enriched layer is observed at the BHJ/Al interface. This is consistent with observations made previously using NEXAFS and DSIMS measurements[92] as well as neutron reflectivity for the case of P3HT/PCBM.[88, 182] Other results have observed fullerene depletion at the BHJ top interface when studied without an electrode,[86] which is consistent with the behavior of the current pre-annealed devices with a BHJ-Ca interface. There is thus a clear indication of the importance of the sequence of electrode deposition and annealing which affects the segregation profile in these devices. This behavior can be rationalized by considering the surface energies of the different materials. Since

the surface energy of P3HT (Γ = 26.9 mJ m^{-2}) is lower than that for PCBM (Γ = 37.8 mJ m^{-2}) [183] in the absence of a capping layer, P3HT would preferentially segregate to the air interface, as seen in the unannealed and pre-annealed samples. Aluminum however has a higher surface energy (Γ = 1143 mJ m^{-2})[184] than both the polymer and fullerene and thus causes the fullerene to preferentially segregate towards it when post-annealed after the electrode deposition. Similar values were theoretically calculated for the other polymer and fullerenes (Table 4.3) thus explaining the presence of the electron accepting fullerene near the cathode which in turn is expected to enhance the efficiency of the device.

4.2.2 Zone 3 (Near Anode) in the Active Layer

In Zone 3, fullerene segregation is observed near the PEDOT: PSS interface in all the devices, both with or without Ca (Figure 4.5b, red and blue line). The segregated fullerene volume is a bit more prominent in pre-annealed devices (with Ca) than in post-annealed (without Ca). Compared to the unannealed, a considerable amount of fullerene, after annealing (both pre and post) is seen to shift towards the Al electrode, but the concentration of fullerene is still considerably enhanced near the PEDOT: PSS interface.

Before annealing, the devices have segregated fullerene in Zone 3 (Figure 4.5b, green line), which has been attributed to the fact that fullerenes are less soluble in the o-DCB than polymers. Consequently, during evaporation of the solvent during spin coating, the fullerene comes out of the solution first on the bottom substrate.(See Table 4.3 for Hansen solubility parameters)[185] Upon annealing the fullerene moves to the Al/BHJ interface, much more easily for P3OT than the other polymers. This movement is also much more pronounced for the case of post-annealing where fullerene movement is also driven by Al/BHJ interfacial surface energy effects, than just thermal

effects (of annealing) in case of pre-annealed samples where the top interface is absent during annealing. Despite the movement of the fullerene, a thin layer of fullerene still remains on this interface after annealing, due to the matching of the PEDOT PSS surface energy (72.88 mJ/m^2) [186] to the higher surface energy of the fullerene, as compared to the polymer. When the fill factor and the segregated fullerene in Zone 3 (Tables 4.4 and 4.5) are compared to each other, a correlation (discussed later in Section 4.3.3) between these parameters is observed in both device types, i.e. with and without Ca (see Figure 4.10). This correlation of a reduction in FF with increasing fullerene segregation at the PEDOT:PSS interface is consequently stronger for the post-annealed devices/without Ca (Figure 4.10a). This behavior indicates that excess fullerene in the vicinity of the PEDOT:PSS hole transport layer inhibits hole transport and is discussed later in depth.

4.2.3 Zone 2 (Bulk) in the Active Layer

In Zone 2, as is expected, a bulk phase of mostly homogenous polymer-fullerene composition was seen. On performing mass balance of the polymer and fullerene in the active layer, it is observed that this composition in this zone is not quite 1:1, owing to the fullerene enrichment at the two electrodes in the case of post-annealed with Al electrode. The fullerene composition in those cases vary ~35% in Zone 2 (Table 4.4). In contrast, the bulk composition in the pre-annealed devices with Ca/Al electrode showed a fullerene composition ~ 45% (Table 4.5) and thus closer to the overall 1:1 composition. The V_{oc} of a device depends directly on the energy bandgap between the constituent polymer and fullerene, presuming an equal composition of both.[28] The fill factor of a system in turn depends on the effective charge transport, shunts etc. Thus the homogenous mixture ~1:1 composition leads to not only a higher V_{oc} but also better charge

transport in the bulk leading to higher fill factors (Table 4.1 and 4.2) in the case of pre annealed with Ca/Al electrode.

4.3 STRUCTURE – DEVICE PERFORMANCE CORRELATIONS IN THIN FILM OPVS

4.3.1 Through Thickness Morphological Variation

As introduced earlier in this chapter, both the morphological and device measurements were made in full device configuration as shown in Figure 4.1 which allowed a direct comparison between the segregation profile and device characteristics measured. Devices were built both with and without a calcium electron transport layer. The Ca not only affects the work function of the electrode, but due to differences in surface energies, also affects the interaction with the BHJ. At the same time, to quantify the segregation and obtain a depth profile with around nanoscale resolution, neutron reflectivity (NR) and XPS were used in the current study of these BHJ systems.

The efficiency of a heterojunction is defined by its power conversion efficiency (PCE), which is dependent upon the J_{sc}, V_{oc} and the fill factor (FF) of the devices. The short circuit current, J_{sc}, is the current density produced in an unbiased system based on absorption of a particular part of the solar spectrum by the semiconductor. It is determined from a measure of the charge generation, diffusion and collection of the light generated current[187]. However, it also depends on a number of external factors such as the material, optical property, exposure area as well as parameters influenced by morphology, such as charge carrier mobility and probability of charge collection, among other things. The open circuit voltage, V_{oc}, depends mainly upon the HOMO of the donor and LUMO of the acceptor used and on recombination losses[28]. Thus an important component in determining and optimizing is the right choice of bandgap between the polymer

(donor) and fullerene (acceptor). Both these factors though are heavily influenced by the morphological state of the active layer. The FF in turn is related to the ratio of the maximum power output to the product of J_{sc} and V_{oc}. Therefore, any morphology that cause electronic losses through recombination or resistance (shunts, series resistance) would adversely affect the FF.[188]

Based on the through-thickness composition profile shown schematically in Fig. 5, it may be anticipated that fullerene enrichment in Zone 1 would assist in electron transport to the aluminum electrode, thus increasing the J_{sc}. On the other hand, fullerene present in Zone 3 near the PEDOT:PSS, as seen in devices with both Al and Al/Ca electrodes, might prevent efficient charge transport to the PEDOT:PSS leading to recombination losses and consequently adversely affecting the FF. This three-layered composition profile suggested by the NR studies was also confirmed in the XPS studies by tracking the S content through the film thickness of the BHJ. Keeping all this in mind, the trends from the quantitative data obtained for the phase segregation profile and device measurements were collated and used to derive possible correlations between them

4.3.2 Interfacial effects at the Aluminum-BHJ interface

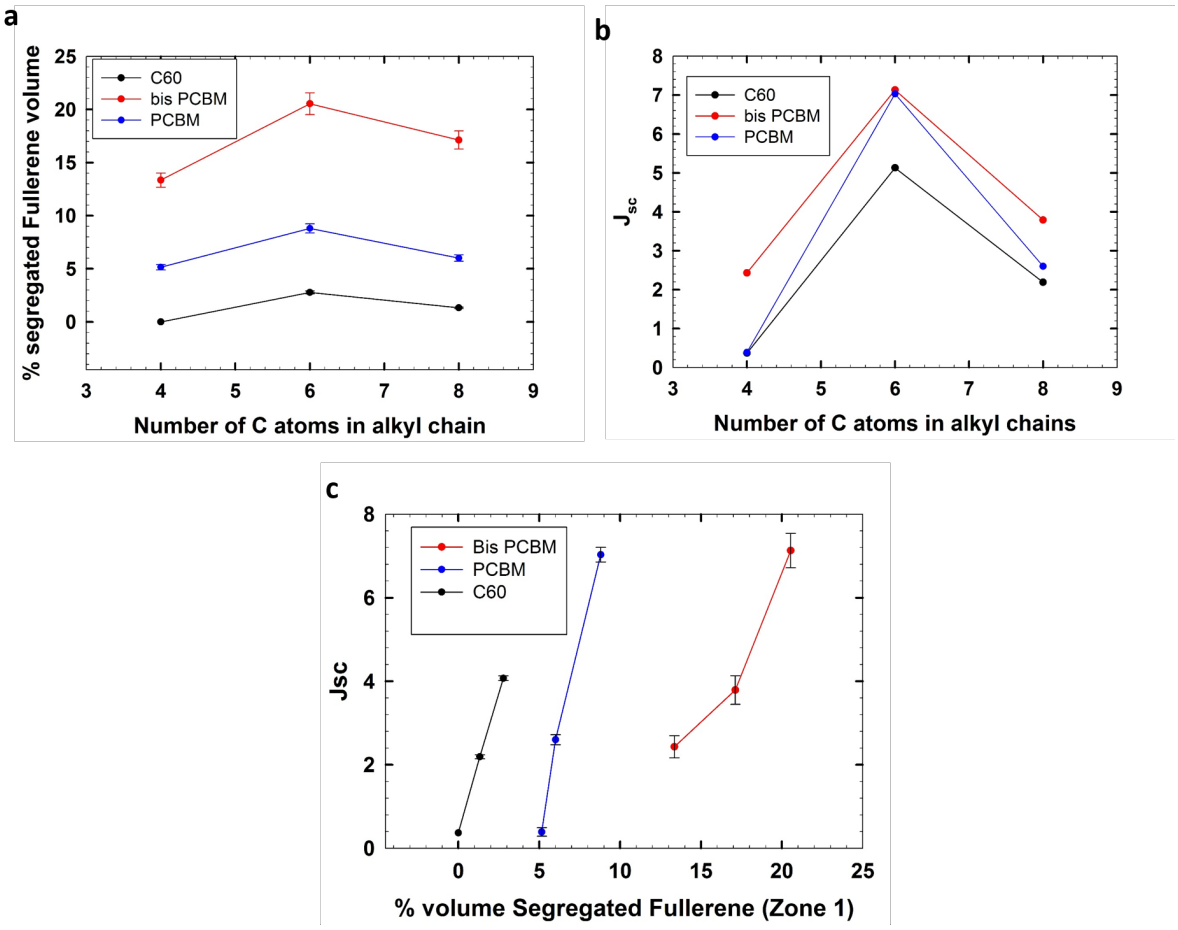

Figure 4.9 a) Volume of segregated fullerenes in Zone 1 and b) J_{sc} , vs no. of C atoms in alkyl chain, c) correlation between segregated volume of fullerene and J_{sc} in the annealed devices.

As seen in Figure 4.5b, in the post-annealed BHJ samples, a fullerene-enriched layer is observed at the BHJ/Al interface. This is consistent with observations made previously using NEXAFS and DSIMS measurements[92] as well as neutron reflectivity for the case of P3HT/PCBM.[88, 182] Other results have observed fullerene depletion at the BHJ top interface when studied without an electrode,[86] which is consistent with the behavior of the current pre-annealed devices with a BHJ-Ca interface. This clearly indicates the importance of the sequence of electrode

deposition and annealing on the segregation profile in these devices. This behavior can be rationalized by considering the surface energies of the different materials. Since the surface energy of P3HT (Γ = 26.9 mJ m^{-2}) is lower than that for PCBM (Γ = 37.8 mJ m^{-2}) [183] in the absence of a capping layer, P3HT would preferentially segregate to the vacuum interface, as seen in the unannealed and pre-annealed samples. Aluminum however has a higher surface energy (Γ = 1143 mJ m^{-2})[184] than both the polymer and fullerene and thus causes the fullerene to preferentially segregate towards it when post-annealed after the electrode deposition. Similar values were theoretically calculated for the other polymer and fullerenes (Table 4.3) thus explaining the presence of the electron accepting fullerene near the cathode which in turn is expected to enhance the efficiency of the device.

The pre-annealed samples (Figure 4.5b, green line) show excess of fullerene towards the bottom and polymer excess towards the top initially (due to the polymers lower surface energy). As postulated by other groups previously[60, 68] the diffusion of fullerene occurs through the amorphous domains of the poly(alkyl thiophene)s during annealing. Solubility between the polymer and fullerene can be estimated from interaction (binding) energies between the polymer-fullerene pairs as have been seen through the DFT measurements. According to the initial DFT simulations conducted on the oligomer-fullerene pairs (see Figure 4.4), P3BT is expected to have the greatest miscibility with the fullerenes presumably due to the short alkyl-chains not sterically hindering backbone interactions with the fullerene. This should cause the larger amount of fullerene miscibility in the polymer and thus greater movement through the polymer amorphous region (and segregated amount) towards the top of the active layer for shorter side chain polymers (P3BT>P3HT>P3OT). Consequently, larger side chains (P3OT>P3HT>P3BT) lead to lower polymer crystallinity (Figure 4.7), allowing easier diffusion of fullerenes on annealing and lead to

phase segregation of the polymer-fullerene through the bulk of the material [176]. The polymer crystallinity, combined with effect of surface energy at the electrode interface, drives the fullerene to move towards the surface and explains the greater segregation of the fullerenes to Zone 1 on post-annealing. A mix of these three counteracting, thermodynamic (miscibility, surface energy) and kinetic (diffusion) factors thus ensures that the optimal phase separation of fullerene occurs in the P3HT:electron acceptor active layer near the cathode (Figure 4.5b, red line) which in turn facilitates electron transport and improves the efficiency.

Plots of both the J_{sc} and segregated volume of fullerene in Zone 1 versus the number of C atoms in the P3AT alkyl chain are shown in Figure 4.9(*a*) and (b). The amount of segregation for all the three fullerenes is seen to be maximum in devices with P3HT (Figure 4.9a). At the same time, the highest J_{sc} observed when comparing the polymer is also with P3HT for any of the fullerenes. This behavior can be better understood when directly comparing fullerene segregation in Zone 1 against the J_{sc} in these devices as shown in Figure 4.9(c). In this plot it is clear that there is a linear dependence between segregated amounts of fullerene at the Al-BHJ interface and the device $J_{sc.}$

4.3.3 Interfacial effects at the PEDOT: PSS – BHJ interface

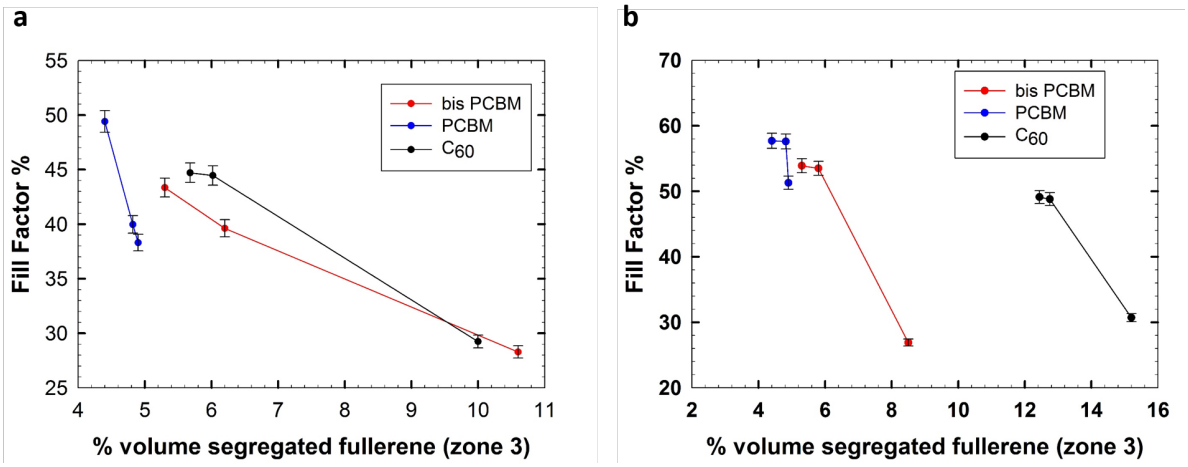

Figure 4.10 Fill Factor vs segregated volume of fullerene in Zone 3 (*a*) without and (*b*) with Ca layer

In Zone 3 however, fullerene segregation is observed near the PEDOT:PSS interface (Figure 4.5b, red and blue line) in all the devices, both with or without Ca. The segregated fullerene volume is a bit more prominent in pre-annealed devices than in post-annealed (Figure 4.5b). Compared to the unannealed, a considerable amount of fullerene, after annealing (both pre and post) is seen to shift towards the Al electrode, but the concentration of fullerene is still considerably enhanced near the PEDOT:PSS interface.

The fullerene rich content and layer thickness in Zone 3 is a maximum in BHJ devices with P3BT (see Table 4.4 and 4.5), which is inversely proportional to the change in device performance (as seen Figure 4.3). This again implies, as discussed for zone 1, that the length of side chain affects is affecting the degree of fullerene segregation, and the amount of fullerene segregated to the PEDOT:PSS interface can possibly be used to predict changes in device performance. Before annealing, the devices have segregated fullerene in Zone 3 (Figure 4.5b, green line), which has been attributed to the fact that fullerenes are more soluble in the o-DCB than in the polymers.[40] Consequently, during evaporation of the solvent during spin coating, due to the nature of solvent

drying, the fullerene stays in the solution near the bottom of the substrate till it dries up.[189] (See Table 4.3 for Hansen solubility parameters)[185] Upon annealing the fullerene moves to the Al/BHJ interface, much more easily for P3OT than the other polymers. This movement is also much more pronounced for the case of post-annealing where fullerene movement is also driven by Al/BHJ interfacial surface energy effects, than just thermal effects (of annealing) in case of pre-annealed samples where the top interface is absent during annealing. Despite the movement of the fullerene, a thin layer of fullerene still remains on this interface after annealing, due to the matching of the PEDOT PSS surface energy (72.88 mJ/m^2) [186] to the higher surface energy of the fullerene, as compared to the polymer. When the fill factor and the segregated fullerene in Zone 3 (Tables 4.4 and 4.5) are compared to each other, a correlation between these parameters is observed in both device types, i.e. with and without Ca (see Figure 4.10). This correlation of a reduction in FF with increasing fullerene segregation at the PEDOT:PSS interface is seen to be stronger for the post-annealed devices/without Ca (Figure 4.10a). The behavior strongly indicates that excess fullerene in the vicinity of the PEDOT:PSS hole transport layer inhibits hole transport.

Even though the excess fullerene content at this interface for P3HT and P3OT showed marginal differences (~ 6.5 and 6.9 % respectively for the PCBM based devices, Table 4.5) the fill factor is the highest for the P3HT-fullerene systems (compared to the other two polymers). This suggests that other factors such as the morphological structure of the fullerene polymer system at the interface might also be of importance. Hole transport that should occur through the polymer, would be affected by the nature of the environment the polymers see, both locally i.e. cyrstallinity, and macroscopically, i.e. phase behavior. Excess fullerene segregtion at the PEDOT PSS interface that adversely affects continuity of polymer phases and thereby hole transport would consequently be inhibited and lead to reduction in the fill factor.

In addition, studies on the interfacial effects on device performance have to take into consideration the interfacial roughness. In the P3BT-C_{60} heterojunctions, in addition to fullerene segregation, the roughness of the P3BT-C_{60} at the PEDOT:PSS interface is extremely high[190] and a smooth enough heterojunction film of the same is difficult to obtain. Heterojunction film roughnesses for all the devices, obtained from NR measurements, are thus seen to adversely affect the fill factor considerably and lead to the lower of device performance (Table 4.4 and 4.5). The roughness of the film can be attributed to the low miscibility (leading to phase segregation) of C_{60} in P3BT and the solvent discussed later through GIWAXS measurements (section 6.3.2). Miscibility thus plays an important role in the film formation and its roughness, consequently affecting the fill factor and device performance

4.3.4 Annealing Effects on Segregation

It has been determined that for thin BHJ films, as in the current work (~80 nm), the J_{sc} is very low compared to P3HT-PCBM systems that have optimized thicker films.[191] It was seen that device efficiency improved after post-annealing in the absence of Ca, whereas post-annealing had a detrimental effect on the efficiency in the presence of a Ca layer. The effect the presence of Ca at the Al cathode interface after post-annealing has been observed previously, and was explained by the small Ca atoms diffusing into the active layer [192] or Ca oxidation [178], during annealing, causing a reduction in the efficiency of the device.

On annealing, recrystallization of the polymer occurs whilst simultaneously causing phase segregation within the active layer.[193] The enhanced polymer crystallinity leads to increased hole mobility and hence increases J_{sc}.[18, 67] In addition, when the samples are post-annealed with the electrode in place, the increased segregation of fullerene to the Al interface due to surface energy

differences, as discussed earlier, also enhances the J_{sc}. In this study, because the BHJ films are slightly thinner than the convention, the device properties are even more likely to be dominated by the interfacial effects, where the relative proportion of segregated volume fraction compared to the overall BHJ layer thickness will be large. This will therefore cause a bigger increase in J_{sc} compared to thicker films.

4.3.5 Fullerene adlayer

To test the hypothesis that fullerene enrichment has a significant effect on device behavior and specifically the J_{sc}, P3HT-PCBM devices with and without Ca were prepared with an additional PCBM layer deliberately deposited between the BHJ and the Ca/Al interface. The additional layer was placed so that it would serve as an electron transport layer at the BHJ-cathode interface, and thus enhance the charge collection and consequently the J_{sc}. The presence of a pure PCBM layer on the top was confirmed by an XPS measurement, to detect the absence of sulfur at the top layer (Figure 4.11). For both device types, a distinct improvement in J_{sc} was observed (see Table 4.6), with a 20% improvement seen for Ca/Al containing devices compared to 8% improvement for devices without Ca. The difference in improvement is possibly because the pre-annealed devices (without an adlayer) didn't start off with a fullerene-enriched layer and so the addition of an extra fullerene layer acted as an electron transport layer for the device. By comparison the post-annealed devices already had a segregated fullerene layer as the cathode, and so the added layer wasn't as effective in enhancing its J_{sc}. The fact that the J_{sc} of the pre-annealed with Ca device was already higher (before addition of an adlayer) suggests that other factors besides fullerene segregation also play an important part in the charge collection and J_{sc}. These results support the hypothesis that the fullerene segregation to the device cathode directly affects

the short circuit current and consequently provides design strategies for improving device performance.

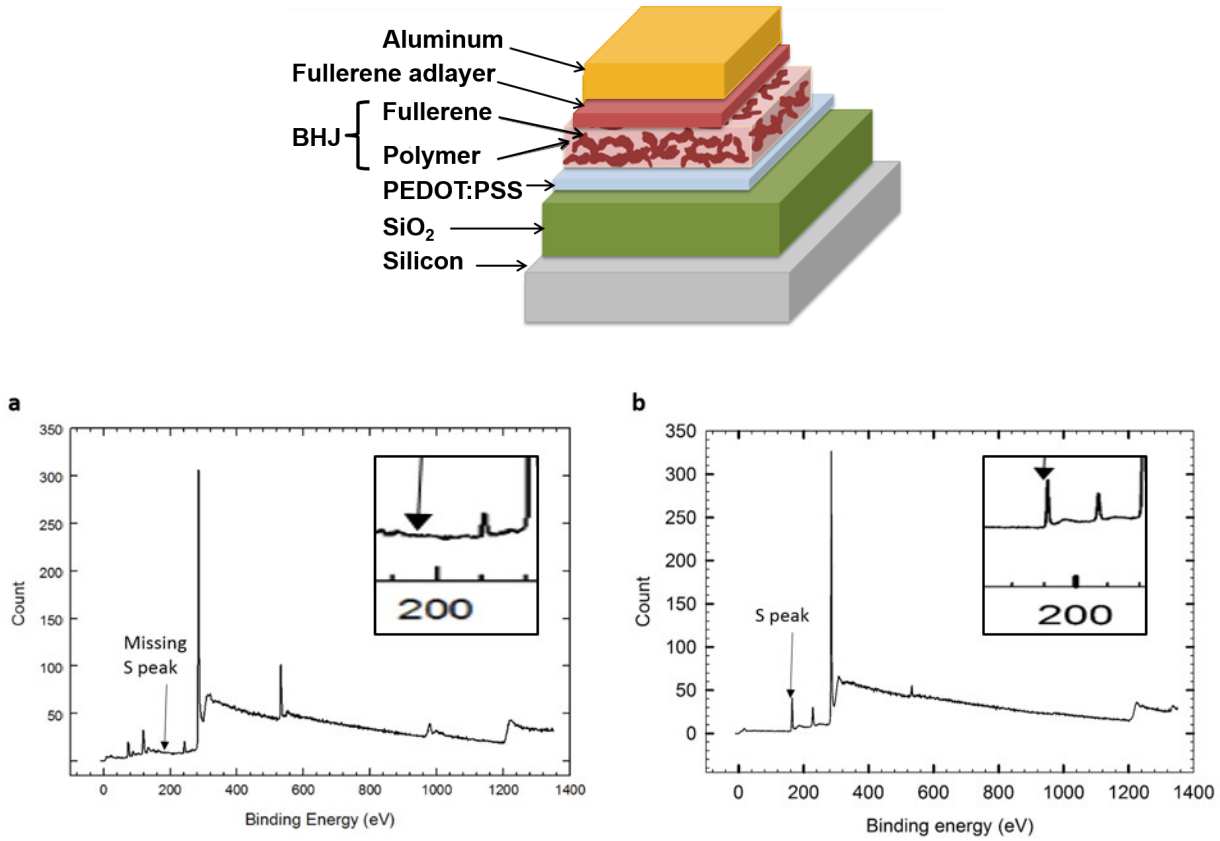

Figure 4.11 a) Schematic of BHJ device with fullerene adlayer deposited between the BHJ and top electrode. XPS profile for b) PCBM adlayer of P3HT-PCBM BHJ and c) P3HT-PCBM BHJ without an adlayer on top, showing the position of the sulfur peak (inset shows zoomed in region for sulfur peak. Peaks at 285.1 eV and 531.3 eV are for carbon and oxygen respectively).

Table 4.6 Effect of fullerene adlayer on *Jsc* of P3HT-PCBM devices, with and without Ca

Sample Type	**w/o add layer (mA/cm^2)**	**with add layer (mA/cm^2)**
w/o Ca	5.1	5.9
with Ca	5.5	7.1

4.4 SUMMARY

Neutron reflectivity and XPS measurements show that the bulk heterojunction in OPVs is not homogeneous through its thickness but can be considered to be stratified into three zones, with fullerenes predominantly segregated at the two electrode interfaces leaving the central layer of the film polymer-rich. The segregation of the fullerene in the different P3AT-fullerene devices was correlated to the device performance values through either the J_{sc} or FF parameters. The degree of interfacial segregation of the fullerenes is a balance in wetting behavior (surface energy differences), polymer-fullerene miscibility and fullerene mobility through the polymer. Differences in polymer-fullerene solubility ensures less roughness of the interface of films at the top electrode initially, while upon annealing also allows for greater segregation of fullerenes towards the cathode and away from the anode. Greater fullerene segregation at the cathode promotes better electron transport and thus improves the J_{sc} and consequently device performance. The fullerene at the anodic interface should have the opposing effect in terms of promoting charge recombination, thus reducing the fill factor and consequently, hindering efficient device performance. The significance of fullerene segregation to the cathode by deliberately building devices with a fullerene adlayer at the cathode was demonstrated, which increased the device performance with an improvement in the J_{sc} of ~ 20%. This may in part also be stemming for improved absorbance of the films and that needs to be confirmed with IPCE measurements. However with the addition of the adlayer, we had already exceeded the optimal amount of fullerene (1:1 ratio with P3HT) for maximum absorbance, it is believed to be less likely to be a factor.

The morphology of the BHJ thus is complex and these results suggest that it is also important to subsequently study not only the lateral structure, but its depth dependency as well. GISANS and GIWAXS was used to study depth dependent phase morphology along with polymer

crystal orientation, and domain size, for the same series of BHJ devices. A combination of the two studies could then be used to derive a unified morphological structure in the BHJ.

5 MORPHOLOGICAL STUDIES OF CONJUGATED POLYMER-FULLERENE BHJ DEVICES PART 2: IN-PLANE MORPHOLOGY

Following the studies out-of-plane morphology of the polyalkylthiophene-fullerene based devices, it was inferred that the segregation profile was possibly leading to effects in the device performance. However, as has been discussed previously, the phase morphology of the device components (polymer-fullerene) would also complement the segregation effects witnessed in influencing the device performance. Thus, the same systematic study was carried out on the set of polymer-fullerene systems as previously used. Starting from the bulk materials to the eventually thin film devices, X-ray and neutron scattering techniques were used to determine the morphological structures. Starting from shape, size and orientation of nanoscale crystals to the shape, size and composition of the mesoscale phases, scattering techniques provided an easy non-destructive way of studying the morphology over a long range of length scale. This made it an ideal choice for the subsequent studies.

Studies on the pure polymer and fullerene powders as well as drop cast films for the different polyalkylthiophene-fullerene mixtures (see Section 2.5.1, 2.5.2) were carried out using WAXS and SANS. Subsequently, thin film devices of the same materials were made (see Section 2.6.1) and studied using GIWAXS and GISANS. By choosing the q range from small to wide angle, one can cover the morphological features of the entire length scale of interest for these studies.

5.1 WAXS MEASUREMENTS OF PURE POLYMER, FULLERENE AND MIXTURES

Powder wide angle X-ray scattering (WAXS) experiments were carried out, firstly on pure polyalkylthiophene and fullerene derivatives to get the values of their crystallinity, crystal plane spacings, and crystal domain sizes. The 1-D intensity vs *q* integration plots are displayed in Figure 3.1 and the values tabulated in Table 5.1. The samples were made from annealed drop cast films (see experimental Section 2.5.1). As expected, the crystal spacing (d_{100}) increased with increasing in length of side chain for the polyalkylthiophenes (Table 5.1). In the same time, the percentage crystallinity increased with decreasing side chain length. P3BT had the highest crystalline component in all polymer-fullerene combinations. This could be explained by the fact that shorter side chains provide less hindrance for packing of backbones leading to larger overall crystallinity.[194] However, upon calculating the domain sizes it was seen that the largest domains were formed by the polyoctylthiophene-based systems. This has been previously studied and attributed to the fact that side chains assist in the ordering of the polyalkylthiophenes and the ordering goes up with increasing in side-chain length.[195, 196] While overall crystallinity is largest in P3BT, the domain sizes are largest in P3OT. In the case of fullerenes, a similar pattern is visible, with bis-PCBM-based systems being considerably less crystalline than PCBM which, in turn, is less crystalline than C_{60}. This can be explained owing to the fact that bis-PCBM has been seen to be the most soluble fullerene in polymers and consequently, would have the least amount of phase separated polymer and fullerene crystal domains and the maximum amount of amorphous mixture of polymer and fullerene. This aspect is studied subsequently, in detail, through SANS measurements in the bulk films (drop cast) and in the thin films (spin coated) through GIWAXS and GISANS measurements.

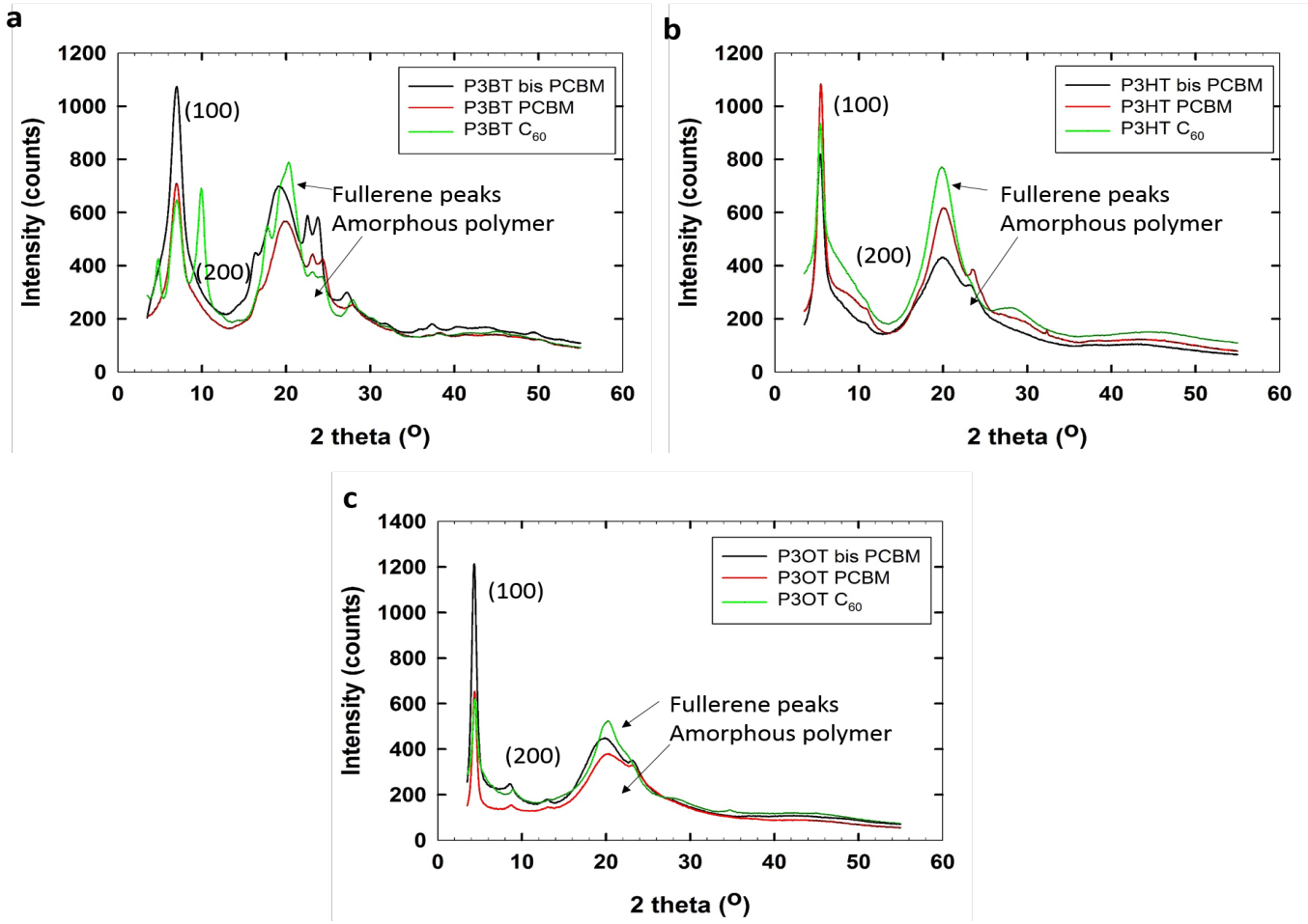

Figure 5.1 WAXS 1D integration profiles (I vs q) for a) P3BT b) P3HT c) P3OT with different fullerenes.

Table 5.1 Values of d_{100}, percentage crystallinity of the polymer and domain size of the polymer crystals in the different polymer-fullerene drop cast blends (all post annealed).

Sample Name	D_{100} plane (Å)	Crystallinity (%)	Domain size (Å)
P3BT-C_{60}	13.33±0.11	38.35±0.96	145.12±2.35
P3BT-PCBM	13.56±0.15	35.11±0.90	140.3±2.20
P3BT-bisPCBM	13.64±0.21	37.24±0.80	135.51±2.06
P3HT-C_{60}	16.52±.07	32.57±1.05	168.63±1.05
P3HT-PCBM	16.63±0.12	32.32±0.96	171.46±2.14
P3HT-bisPCBM	16.34±0.15	31.21±0.74	172.77±3.18
P3OT-C_{60}	20.14±0.09	25.84±0.55	221.61±2.64
P3OT-PCBM	20.16±0.18	26.61±0.63	221.15±2.63
P3OT-bisPCBM	20.51±0.09	26.88±0.66	223.54±2.70

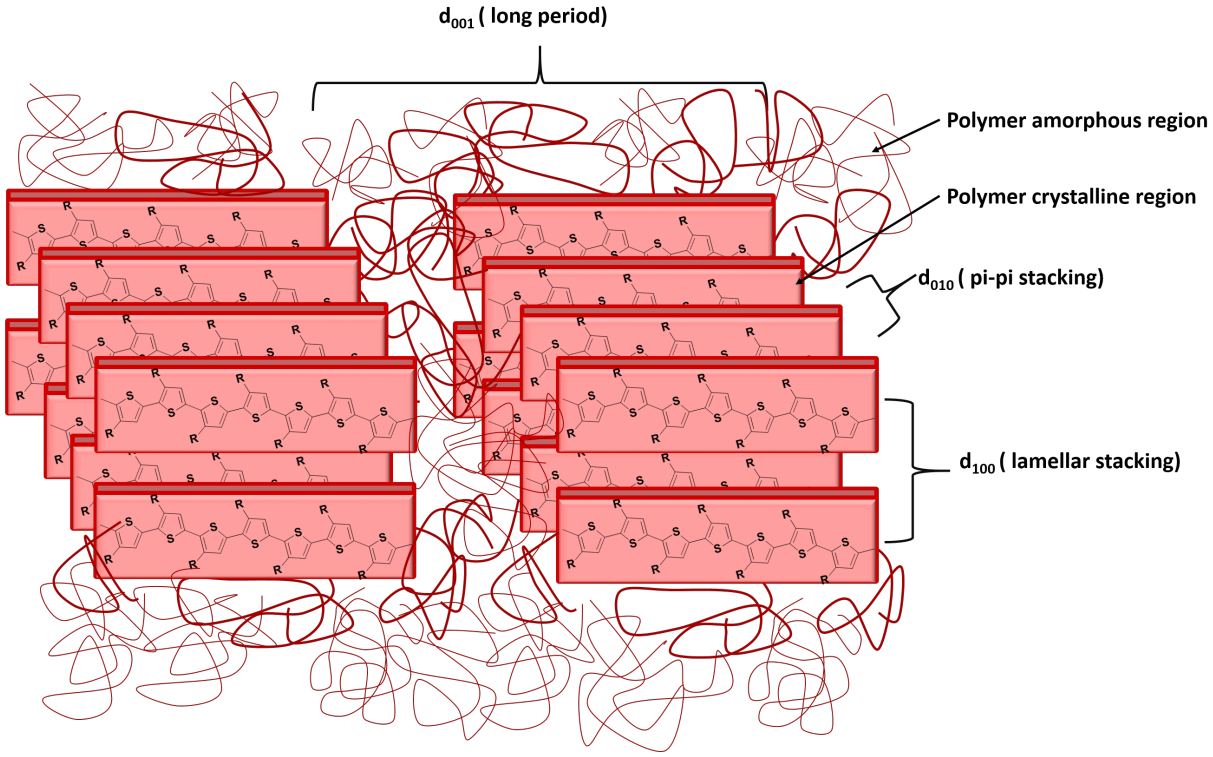

Figure 5.2 crystalline morphology of polyalkylthiophene polymers.

5.2 SANS MEASUREMENT OF BULK POLYMER-FULLERENE MIXTURES

Following the WAXS measurements where information about the crystal morphology of polymer-fullerene mixtures in bulk was obtained, SANS measurements were used to look at the large-scale phase morphology. SANS measurements were carried out on drop-cast films from polyalkylthiophene-fullerene mixtures as described in Section 2.5.2. A representative SANS measurement is shown in Figure 5.3. It can be seen that by analyzing the different sections of the q regimes, one can obtain morphological information about different length scales, and specifically, in this case, of multiple phases in blends. Since q is a unit in reciprocal space (described earlier in Section 2.4.3), the low-q regime was used to effectively study large phases and domains of ~100 nm and above. The measurement of scattering at low-q thus gave information of any large-scale phase segregation. The medium-q regime gave information about the formation of smaller phases ~10 nm or less. This could give information about smaller phases segregating out of those large phases. The high-q regime can be used to identify even smaller morphological structures, like lower order peaks from crystal planes (100). Individual shape independent models to fit these regimes were tried and eventually used in combination to derive the overall structure by fitting with a combined model. All 1D integration plots for scattering cross-section (a measure of the scattered neutrons, Section 2.5.1) versus q are plotted in Figure 5.4 and used for subsequent analyses.

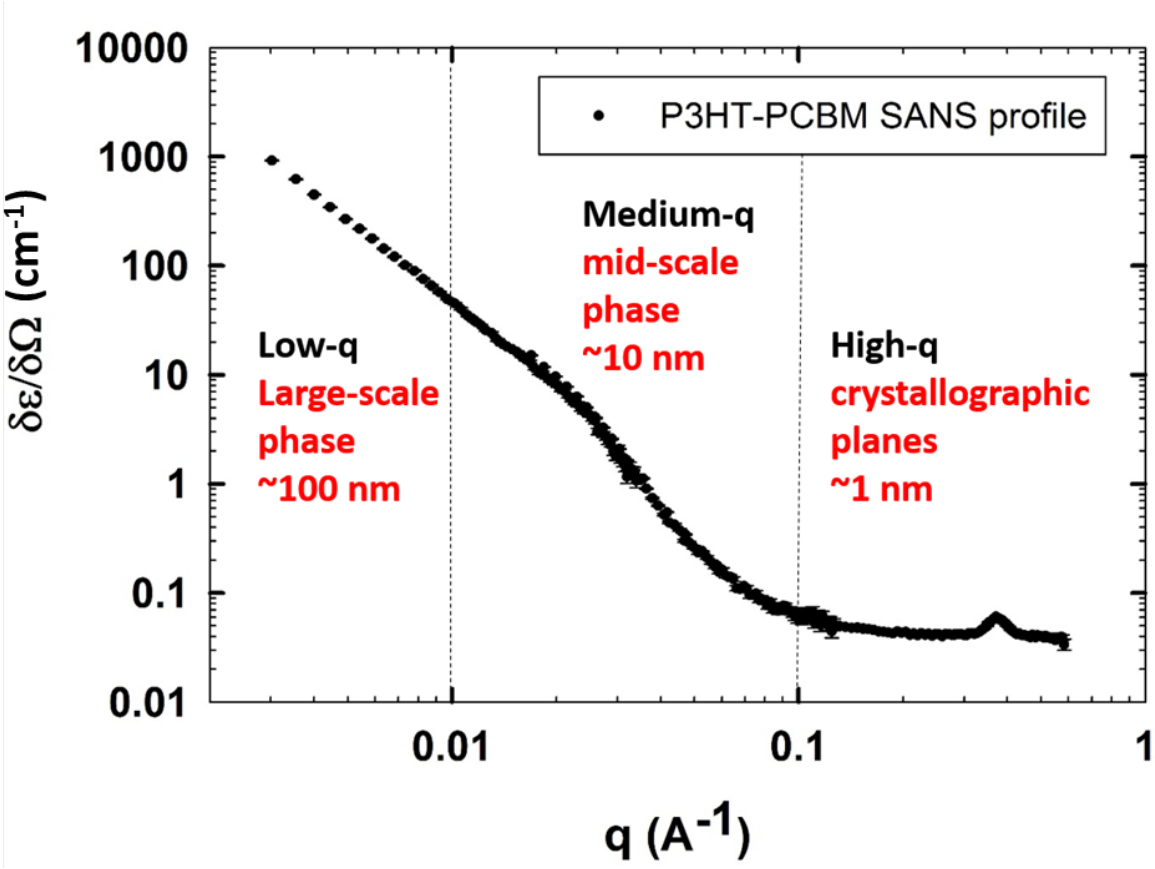

Figure 5.3 Representative SANS profile (P3HT-PCBM) depicting the different q-regimes (black) and corresponding phase information (red).

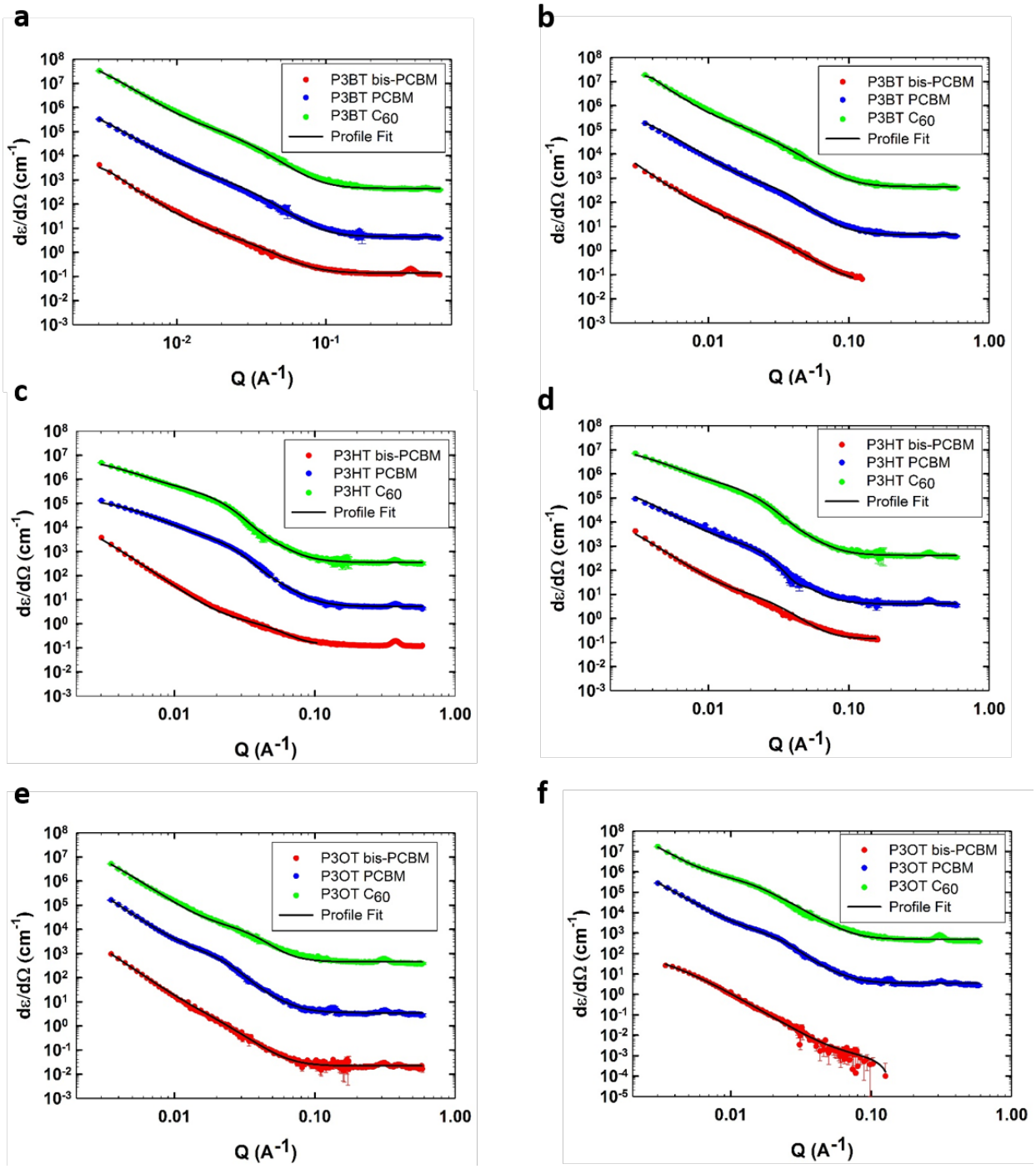

Figure 5.4 SANS profile showing scattering cross-section (dε/dΩ) vs q for unannealed and annealed a-b) P3BT fullerene mixtures c-d) P3HT fullerene mixtures e-f) P3OT fullerene mixtures along with plot fits.

5.2.1 Analysis of high-q regime

Initial analysis was conducted on the high q- regimes ($q>0.1A^{-1}$). As is shown in Figure 5.4 (zoomed-in regions in Figure 5.5), most of the samples showed a characteristic peak in this region (except for the bis-PCBM-based samples which did not go to high enough q value for the annealed samples). Peaks were visible for the profiles both before and after annealing (Figure 5.4). The values of the polymer crystal spacing obtained from the peaks were tabulated (Table 5.2). These peaks were seen to be consistent with the peak for the polymer crystals obtained from the WAXS measurement of the same drop cast films (Table 5.1). However, no further development of any fullerene peak in this regime was observed. This suggested polymer crystals formed in the film but that the process of annealing was not causing any fullerene crystallization to interfere with the formation of the polymer crystals.

Table 5.2 d_{100} values from high-q SANS measurements

Sample Name	**d_{100} plane (Å)**
P3BT-C_{60}	12.81±0.11
P3BT-PCBM	13.05±0.18
P3BT-bisPCBM	13.09±0.12
P3HT-C_{60}	16.55±0.12
P3HT-PCBM	16.50±0.16
P3HT-bisPCBM	16.59±0.10
P3OT-C_{60}	19.87±0.16
P3OT-PCBM	19.93±0.21
P3OT-bisPCBM	20.16±0.15

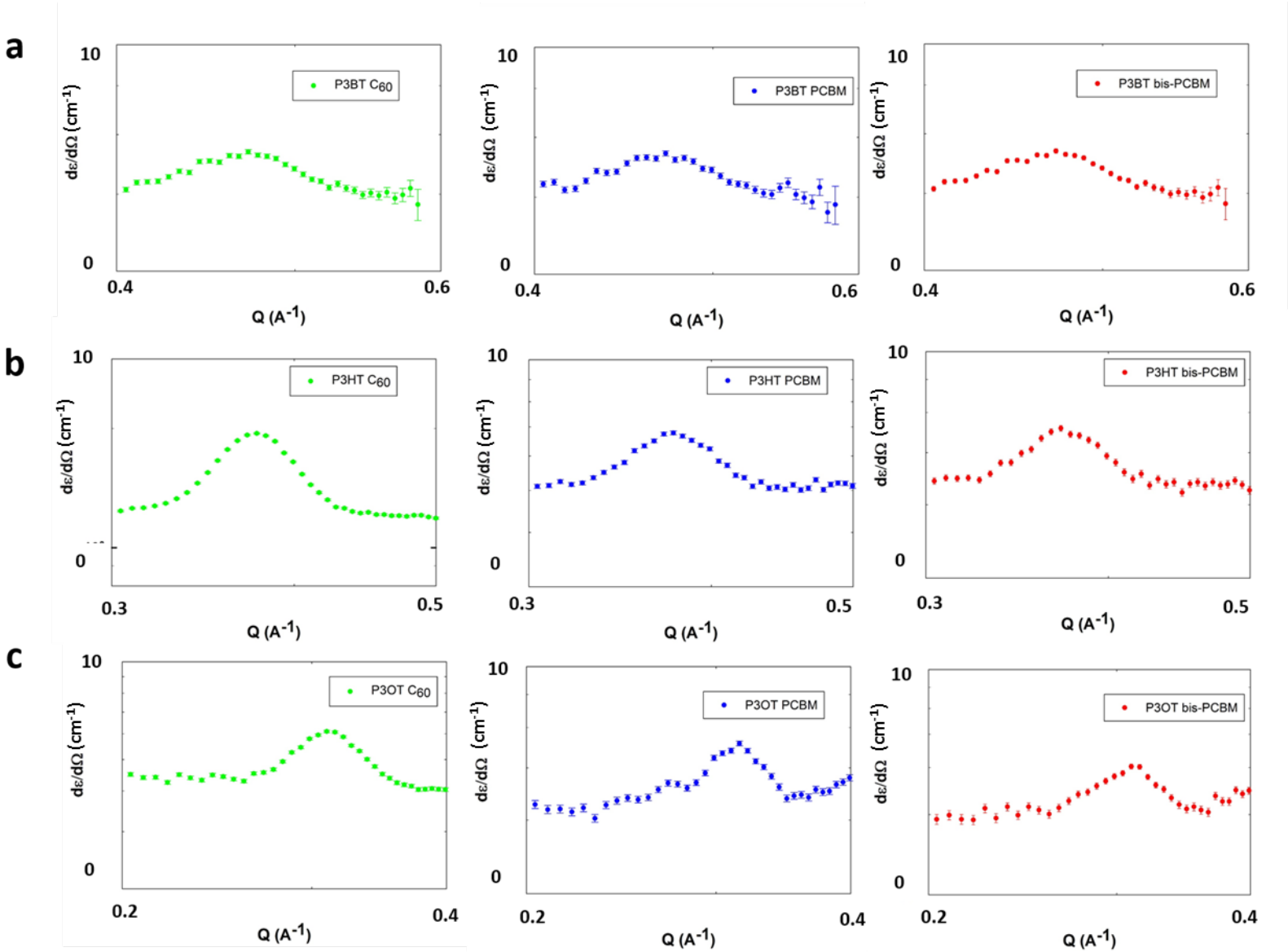

Figure 5.5 High-q peaks for the different combinations of fullerenes with polymers a) P3BT b) P3HT c) P3OT

5.2.2 Analysis of medium and low-q regime

The WAXS and SANS high-q measurement did not show a considerable growth in the percentage crystallinity of the polymer upon annealing or any significant change in the polymer crystal domain size after annealing. This could be attributed to the fact that significant crystallization of the polymers had already taken place in the slow drying process of drop-casting from high boiling point solvent (o-DCB).[55] However, looking at the medium-q regime of the SANS measurement further development of the characteristic features at the low and medium q-regimes upon annealing could be seen (Figure 5.6). Thus, a quantitative study of this regime through SANS was used to provide a better understanding of other phase developments in these blends beside the pure polymer crystal phase.

The increase in the scattering signal in the low q regime suggested further development of a large mixed phase and the appearance of a characteristic feature (bump in the plot) in the mid-q regime and also indicates enhancement of a smaller scale region from the amorphous phase on annealing. These changes are much more subtle or prominent in other cases depending upon the contrast between the different phases (SLDs of the polymer and fullerene) and the characteristic feature lengths.

The combination of studying the different q-regimes suggests a change in the phase composition in the amorphous region along with an increase in polymer crystallinity (seen from the WAXS measurement). Similar studies with SANS[60, 85, 90, 92] and SAXS/GISAXS[86, 103, 104] by other groups have observed such morphological development in the P3HT-PCBM blend thin films. Thus, overall, these systems possibly consist of at least three regions: a polymer crystalline region, a larger amorphous region (possibly polymer rich) and a smaller region born out of fullerene

immiscible in the amorphous polymer. The varying sizes and composition of these phases depend on the constituent materials and their interaction. These were then studied further by analyzing the SANS data with various fits in the different q-regimes.

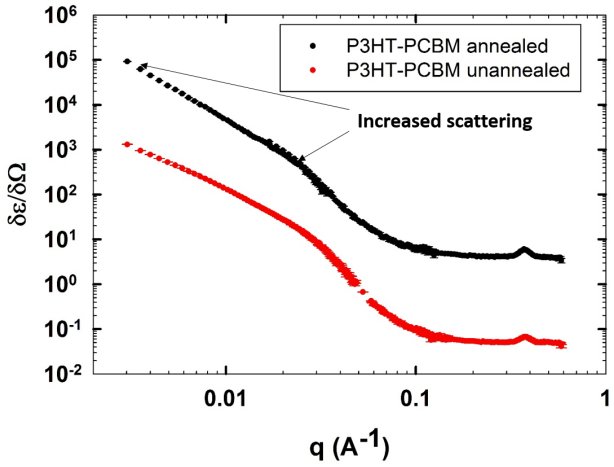

Figure 5.6 Comparison of low and medium q scattering between unannealed and annealed polymer- fullerene mixtures.

5.2.3 Porod analysis

To study the interfacial structure of the polymer crystal and the mixed amorphous phase in the BHJ, Porod analysis was carried out in the medium to high q regime. Porod's law is for scattering at values of q where q>>1/d (d being the size of the scattering object) if there are sharp boundaries between the phases of the system. For medium and high q regime (q > 0.01 A^{-1}) Porod analysis can be used. The law states that at large q:

$$I\,(q) = \; q\alpha \qquad [5.1]$$

$$\frac{\pi}{q_{inv}} . \lim_{q\to\infty} (I(q).q^4) = \frac{S}{V} \qquad [5.2]$$

$$q_{inv} = \frac{1}{2\pi^2} \int_0^\infty q^2 . I(q) dq \qquad [5.3]$$

in which $\alpha = 6\text{-}D_s$, D_s being the surface fractal dimension. A value of $\alpha = 4$ defines sharp interfacial boundary between the phases in the system while values closer to $\alpha = 3$ suggest fractal surfaces of the phases with a certain roughness attributed to them (Figure 5.7). Samples showed a decrease in the power law exponent in all the cases after annealing (Table 5.3) which leads to increase in the fractal dimension D_s. This suggests an increase in roughness of the interfacial area upon annealing.

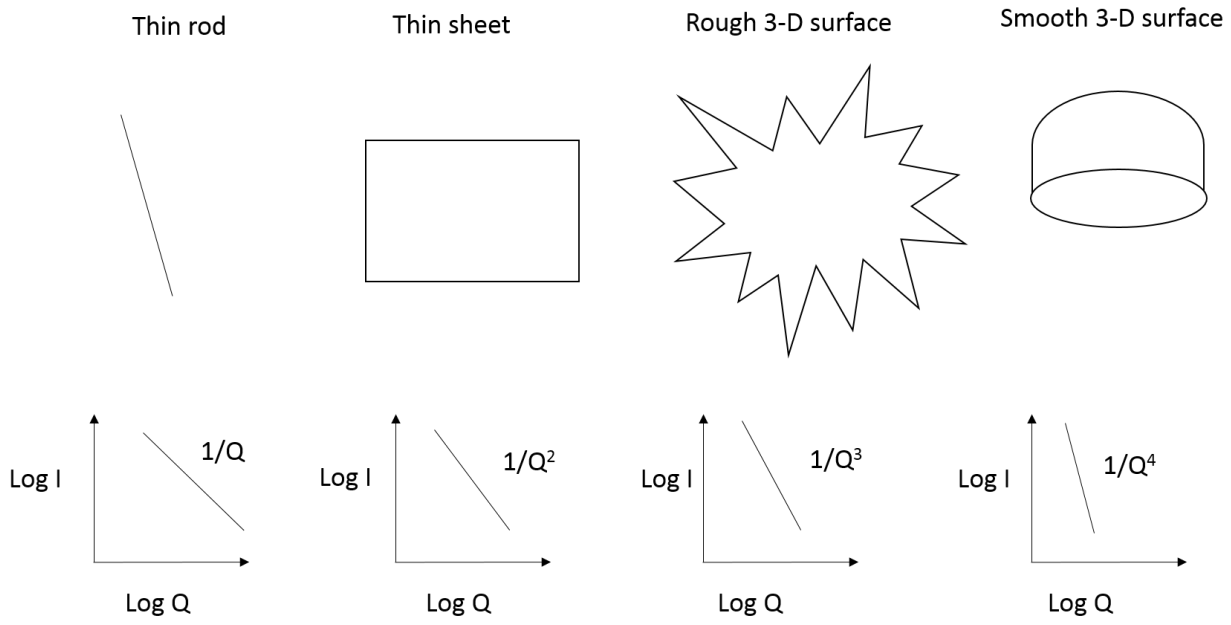

Figure 5.7 Variation of the Porod exponent with the type of scattering surface.

Most of the samples show an initial value of $\alpha \sim 3.5$ which decreases to $\alpha \sim 3$. WAXS measurements show an increase in the domain size of the polymers without a great change in the percentage crystallinity. This suggests no significant increase in the interface between the polymer crystals and the amorphous polymer regime. On the other hand, annealing quite clearly leads to enhancement of the peak in the mid-q regime. The length scale suggests a possible fullerene rich domain, born out of immiscible fullerene in the amorphous polymer rich region. This aspect is

studied later in the model fitting (Section 3.2.6). Thus, initially, the Porod analysis is possibly dominated by the polymer crystal-polymer rich amorphous phase interface. Upon annealing, new phases are formed (possibly fullerene rich), whose interface with the amorphous phase dominates the Power Law behavior.

Looking at the trend of the Porod constant (α) for the blends of different fullerenes mixed with thesame polymer, $\alpha_{bisPCBM} > \alpha_{PCBM} > \alpha_{C60}$. In comparison, the trend established previously (using DFT calculations, Section 4.1.2, appendix) suggests fullerene miscibility in the polyalkylthiophenes follows the trend of bis-PCBM>PCBM>C_{60}. Hence, in mixtures, there would sharper edges between the polymer crystals and polymer rich amorphous phase in the case of bis-PCBM, whereas there would be rougher interfaces formed between immiscible C_{60} rich phases and polymer amorphous phase giving the trend mentioned earlier. Comparison between the polymers shows P3OT has the highest amount of amorphous content, leading to the most amount of miscible fullerene in the polymer amorphous region. Consequently, it is dominated by the sharp interface with the polymer crystals rather than the rough interface between that and immiscible fullerene rich region, as in the case of P3BT.

It is also observed that from the Porod analysis one can determine the 'Surface to Volume' ratio (S/V) which gives an estimate of the size of the phases (Equation 5.2). The ratio is inversely proportional to the size. An increase in ratio suggest reduction in the size of the phases or formation of newer surfaces. To calculate the S/V ratio however, the value of q_{inv} (scattering invariant) is needed. Porod derived this ratio to be a constant (Equation 5.3), which is significant as it suggests the total scattering from a sample is always a constant, for a given composition of that material (irrespective of the phase structures in the system). From Equation 5.1, one can see that the Porod plot (Iq^4 vs q), will be a horizontal line whose asymptotic limit at high q ($q \to \infty$) gives us the

value proportional S/V. This value also includes q_{inv}, which even though is constant for the sample before and after annealing (since the total composition isn't changing),it is different for the different mixtures. Thus this value only can be used for comparison of the S/V ratio between the samples before and after annealing. The value of S/V ratio was seen to increase (Table 5.3) upon annealing suggesting formation of newer surface area. This is consistent with the Porod analysis which suggests an increase in roughness of the interfacial area upon annealing. This mostly comes from the rough interface between the new fullerene-rich phase formed from the polymer rich amorphous phase (studied later in the overall model fitting of the profile Section 6.2.6)

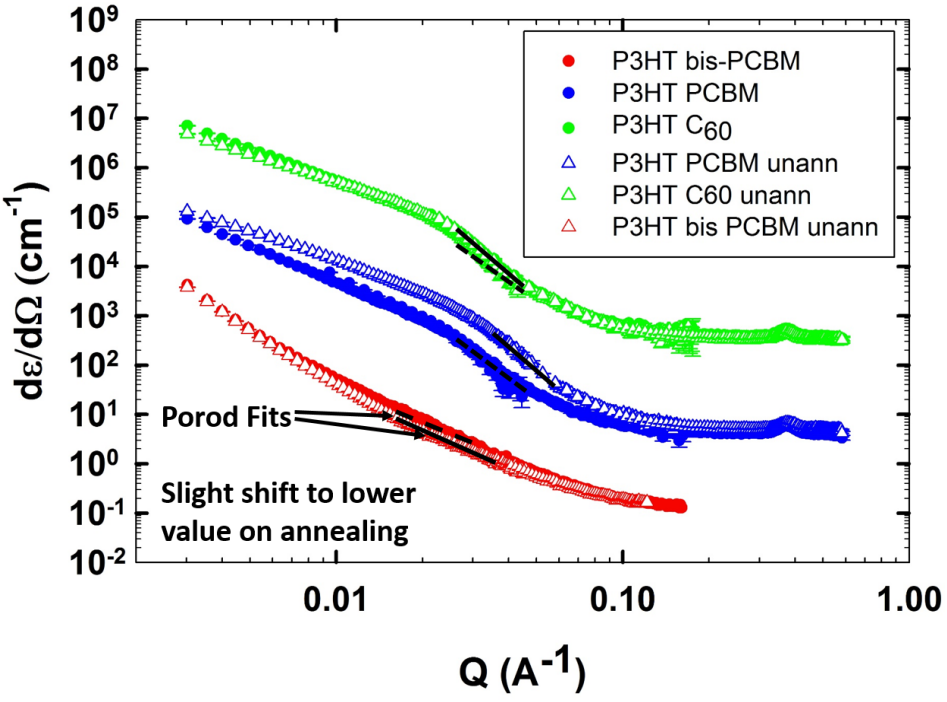

Figure 5.8 Porod fits (solid lines for unannealed samples and dashed lines for annealed samples) over the mid-q regime for unannealed and annealed polymer-fullerene combinations.

Table 5.3 Porod exponent (m) and surface to volume ratio (Q_{inv} * S/V) using Power Law Fits (ann – annealed).

Sample	**m**	**Q_{inv} * (S/V) ($Å^{-1}$)**
P3BT C_{60}	3.31±0.15	0.04±0.002
P3BT C_{60} ann	2.98±0.14	0.05±0.003
P3BT PCBM	3.5±0.17	0.012±0.001
P3BT PCBM ann	2.98±0.14	0.014±0.001
P3BT bis-PCBM	3.26±0.12	0.012±0.002
P3BT bis-PCBM ann	3.2±0.24	0.008±0.001
P3HT C_{60}	3.5±0.17	0.03±0.002
P3HT C_{60} ann	3.16±0.15	0.04±0.002
P3HT PCBM	3.52±0.17	0.01±0.00
P3HT PCBM ann	3.28±0.13	0.012±0.001
P3HT bis-PCBM	3.62±0.12	0.012±0.001
P3HT bis-PCBM ann	3.45±0.11	0.015±0.001
P3OT C_{60}	3.44±0.15	0.05±0.002
P3OT C_{60} ann	2.95±0.14	0.08±0.001
P3OT PCBM	3.72±0.18	0.01±0.001
P3OT PCBM ann	3.34±0.16	0.03±0.002
P3OT bis-PCBM	3.75±0.14	0.009±0.00
P3OT bis-PCBM ann	3.53±0.17	0.021±0.001

5.2.4 Lorentzian Peaks

A qualitative look at the 'I vs q' profile showed an increase in the intensity at low q with annealing (Figure 5.6). This can be attributed to the enhancement of a large-scale phase separation (corresponding to low q). Consequently, Lorentzian peak analysis can be carried out in the low-q regime to look at the domain sizes for both the long and short polymer crystal repeat distance. The short repeat distance is representative of the polymer crystal plane repeat distance. The long crystal

repeat distance (Figure 5.2) is representative of the distance between one crystalline regime and the next. The short repeat distance was already studied in the high-q regime analysis and WAXS measurements (section 5.1 and 5.2.1, respectively). Analyzing the long-crystal repeat distance, it shows an increase upon annealing. This can be attributed to increasing polymer crystal domain sizes on annealing, as seen earlier in the WAXS measurements (section 5.1). Comparison between the different polymers (Table 5.4), P3OT has the largest long-crystal repeat distance, correlated to the crystal domain size P3OT>P3HT>P3BT. Also, as seen in the WAXS experiments, the amorphous content in the polymers increases as P3OT>P3HT>P3BT. Thus, the size of the combined polymer crystal + amorphous chains is a possible explanation for the largest repeat in P3OT. It was also previously noted that the long order in P3HT did not change substantially from a very low content of fullerene to 50% fullerene, suggesting that the fullerenes crystals were not incorporated between the crystal chains in the direction of the long order.[60] This is also confirmed by the insignificant difference of the length scales on annealing or with different fullerenes in the blend system for the same polymer (Figure 5.9b). On annealing however, the peaks become even more diffused, possibly due to formation of more pure fullerene regions which interfere with the contrast (gives rise to the peak intensity) between the polymer crystal and amorphous phases.

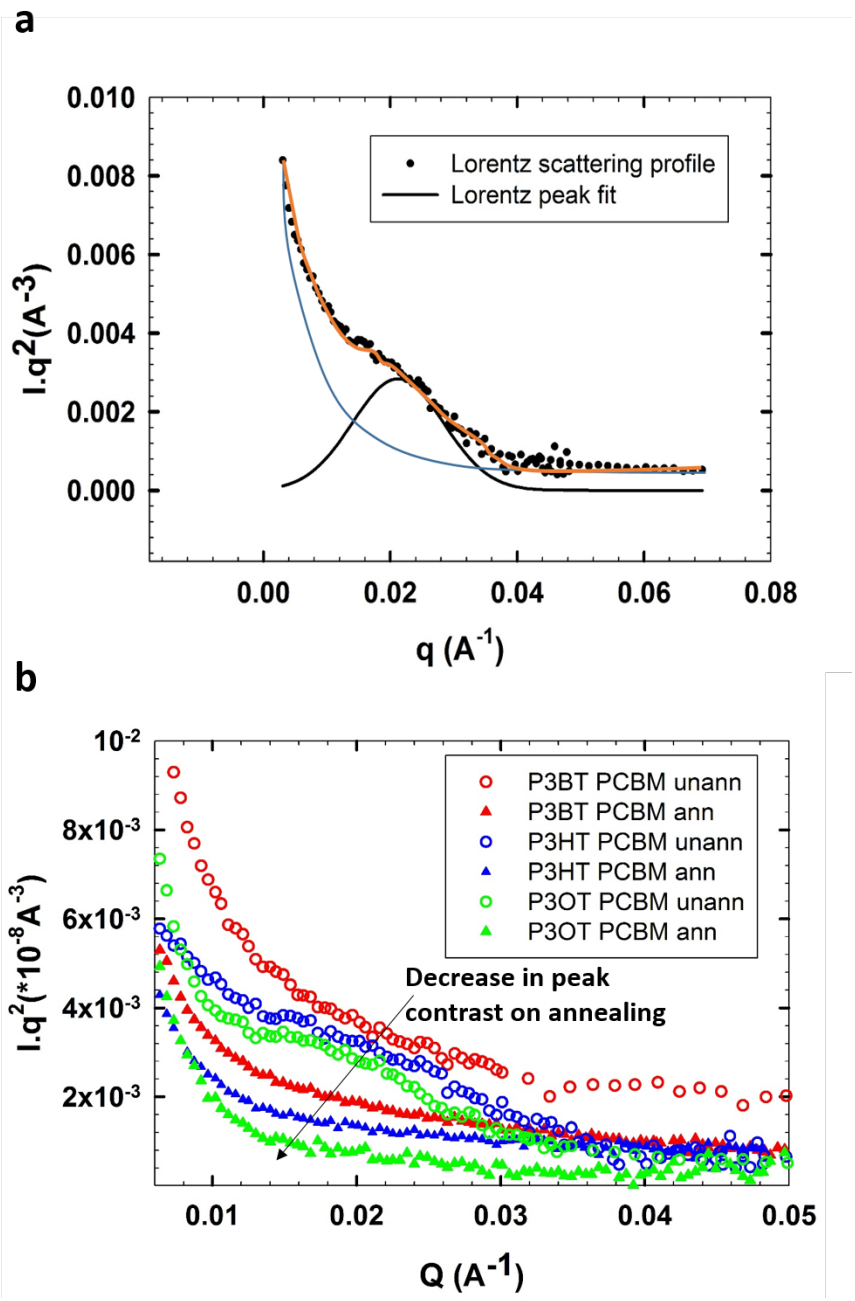

Figure 5.9 a) Typical Lorentz peak and fit (blue line – background) b) Lorentz scattering profile and peak fit for P3AT-PCBM annealed (P3AT-PCBM ann) sample and P3AT-PCBM unannealed samples (P3AT-PCBM unann).

Table 5.4 Polymer long-order period from low-q Lorentzian fits of the SANS profile (ann – annealed)

Sample	**Long-order period size (Å)**
P3BT C_{60}	228.28±14.56
P3BT C_{60} ann	235.7±16.71
P3BT PCBM	214.05±16.28
P3BT PCBM ann	249.6±18.99
P3BT bis-PCBM	218.66±10.9
P3BT bis-PCBM ann	228.01±23.4
P3HT C_{60}	277.02±15.14
P3HT C_{60} ann	292.24±25.84
P3HT PCBM	267.52±12.55
P3HT PCBM ann	272.35±19.44
P3HT bis-PCBM	287.25±18.36
P3HT bis-PCBM ann	298.41±24.92
P3OT C_{60}	377.3±27.54
P3OT C_{60} ann	396.45±25.92
P3OT PCBM	367.59±17.35
P3OT PCBM ann	392.96±33.85
P3OT bis-PCBM	346.76±22.33
P3OT bis-PCBM ann	356.21±32.82

5.2.5 Debye Bueche Fits

To further corroborate the model whether the increase in intensity at low q could be attributed to a large-scale amorphous phase, the Debye-Bueche analysis was carried out. The dimensions of the phase can be obtained by fitting the scattering curve to the Debye-Bueche equation mentioned earlier (see Section 3.2):

$$I(q) = \frac{C_{DB}}{(1 + q^2\xi^2)^2} \quad [5.4]$$

Where ξ is the correlation length of the large amorphous phase, C_{DB} is the prefactor related to the volume fraction Φ and contrast factor $\Delta\rho^2$ as:

$$C_{DB} = 8\pi\Delta\rho^2\Phi\xi^3 \quad [5.5]$$

By plotting $I(q)^{-1/2}$ vs q^2, the correlation length from the slope can be obtained. A representative plot along with the fits is shown in Figure 5.10a. The correlation length is characteristic of the large-scale phases that were predicted to form in the amorphous region of the active layer. It is effectively the length of a crystalline + amorphous regime Figure 5.10c. Debye Bueche analysis in similar P3HT-PCBM-based drop-cast films have been carried out by other groups [60, 92] giving correlation lengths of the order of ~200 nm. Yet, they were prepared from a different solvent. The solvent used here, DCB is notably not only a better solvent for both polymer and fullerene but also it has a higher boiling point. One thus expects the drop cast film to have a greater amount of time to form polymer crystals and that is evident from the long-crystal repeat distance calculated previously. This ensures that the amorphous content and consequently the correlation length of the amorphous section could be smaller in this case. Comparing the correlation lengths (ξ) among the different polymers (Table 5.5), the decreasing trend observed is of P3OT>P3HT>P3BT. This is inversely related to the percentage crystallinity of the polymers, which follows the opposite trend.

Comparison of the correlation lengths (ξ) between the blends of the different fullerenes, before annealing, show a decreasing trend of bis PCBM>PCBM>C_{60}. Upon annealing, the trend is reversed, as shown by the increasing slope of the same sample on annealing in Figure 5.10b. This may be born out of the fact that now, the newly formed or enhanced (to be discussed in Section 5.2.6) fullerene rich domains from the amorphous phases are contributing to the correlation length even more, and the segregation of these phases follow the order C_{60}>PCBM> bis PCBM. Keeping this in mind, suitable models can be chosen to fit the overall scattering profile in the subsequent section.

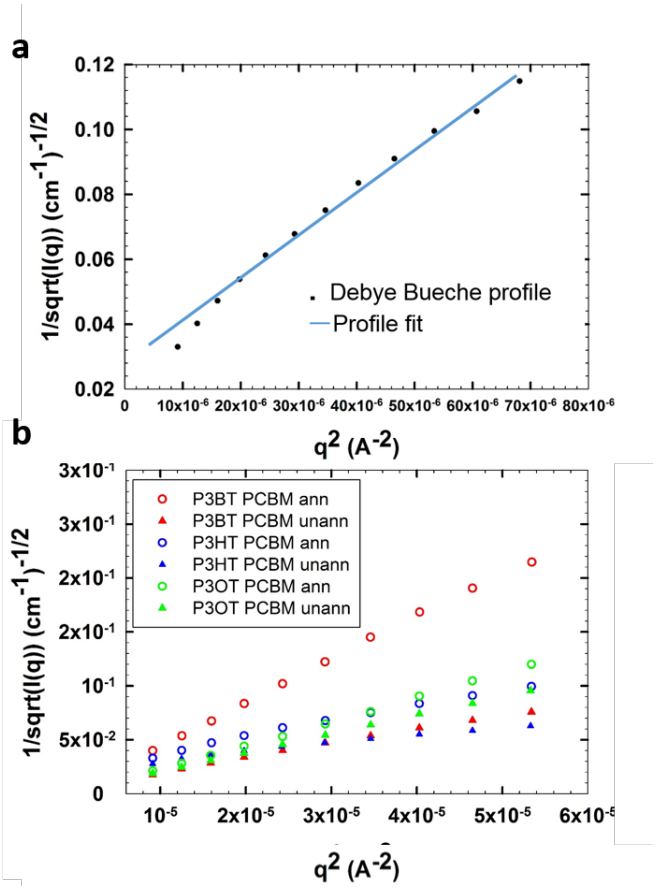

Figure 5.10. a) Debye Bueche fit for P3HT PCBM annealed b) Debye Bueche plots for different polymer-fullerene combinations, before and after annealing.

Table 5.5 Debye- Bueche Fits for low-q SANS measurements

(ann – annealed, unann-unannealed).

Sample	**Dimension (Å)**
P3BT C_{60}	1802.36±16.05
P3BT C_{60} ann	2692.65±33.85
P3BT PCBM	1676.73±19.53
P3BT PCBM ann	2265.25±21.3
P3BT bis-PCBM	1715.52±12.25
P3BT bis-PCBM ann	2214.24±16.53
P3HT C_{60}	1994.31±19.88
P3HT C_{60} ann	2218.23±32.36
P3HT PCBM	1768.7±5.37
P3HT PCBM ann	1928.87±6.58
P3HT bis-PCBM	1840.12±2.42
P3HT bis-PCBM ann	1984.04±8.71
P3OT C_{60}	2185.41±23.71
P3OT C_{60} ann	2438.79±36.77
P3OT PCBM	1744.23±14.88
P3OT PCBM ann	1918.21±18.36
P3OT bis-PCBM	1810.66±7.63
P3OT bis-PCBM ann	1961.54±12.37

5.2.6 Overall model fitting for SANS profile

The different analysis techniques over the entire q regime gave us an estimate of the various phases present and their possible length scales in the polymer-fullerene mixture. Due to the SANS data being at absolute intensity, the intensity plot was fitted to various shape dependent or independent model, through which the exact overall morphological structure was determined. A schematic of the general parameters of the phases and their corresponding generated scattering

pattern is shown in Figure 5.11. Previous models and the knowledge of the phases present in similar systems in literature were initially implemented in the data fitting.

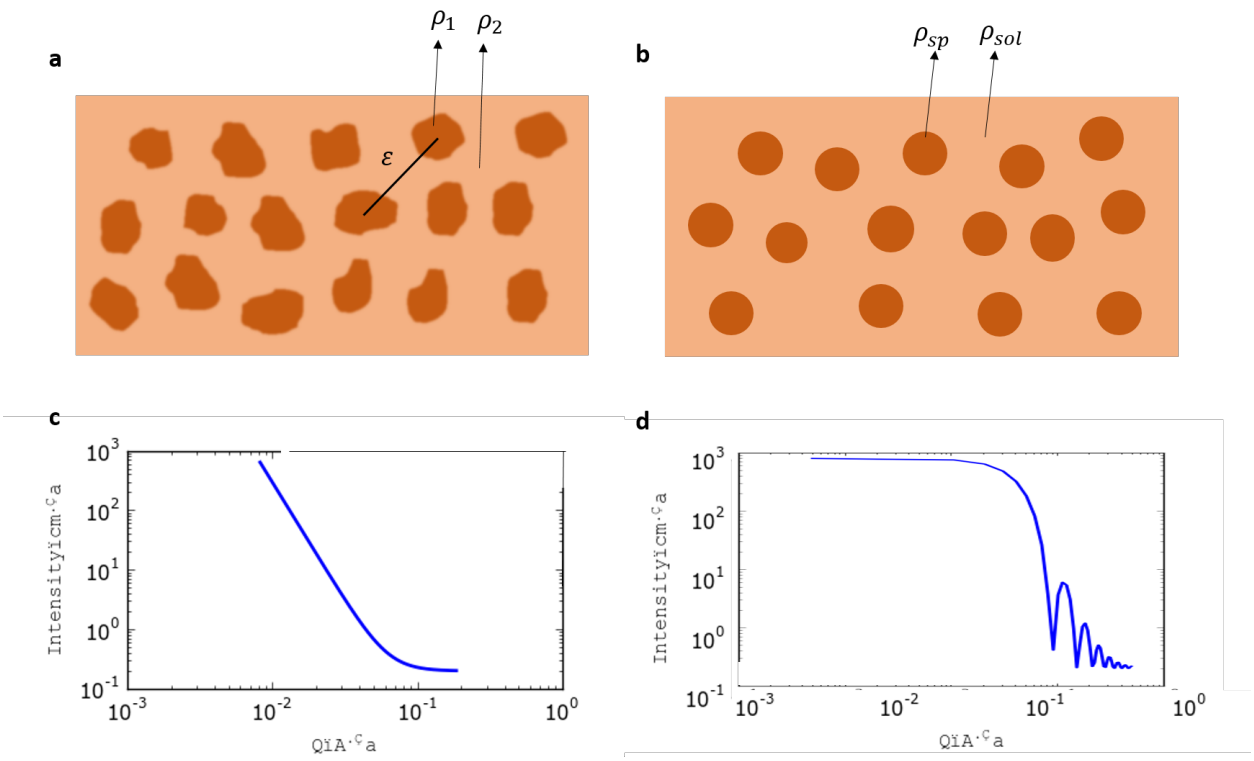

Figure 5.11 Schematic representation of a) shape independent 2 phase system where ξ is the correlation length, ρ_1 and ρ_2 are the SLD of the two phases b) shape dependent (in this case hard sphere) 2 phase system with r_1 representing the sphere radius and ρ_{sp} and ρ_{sol} representing the sphere and solvent SLD and their corresponding scattering profiles c) and d).

First was the Teubner-Strey model (Teubner-Strey, 1987). This model was devised to represent the structure of micellar systems. The scattering patterns of these systems were characterized by peak which represents the inter-micellar interactions. The scattering cross-section for this model is given by:

$$\frac{d\Sigma(q)}{d\Omega} = \Phi\Delta\rho^2 \frac{\left(\frac{8\pi}{\xi}\right)}{\left(\frac{a_2}{c_2} + \frac{c_1}{c_2}q^2 + q^4\right)} \quad [5.6]$$

Were the parameters a_1, c_1 and c_2 are defined by:

$$\frac{a_2}{c_2} = \frac{\left(1 + \left(\frac{2\pi\xi}{d}\right)^2\right)^2}{\xi^4} \quad [5.7]$$

$$\frac{c_1}{c_2} = \frac{\left(-2\xi^2\left(\frac{2\pi\xi}{d}\right)^2 + 2\xi^2\right)}{\xi^4} \quad [5.8]$$

Here ξ is a correlation length and d is a d-spacing (characteristic of the domain size), Φ is the volume fraction and $\Delta\rho^2$ is the contrast factor (difference between the scattering length densities of the two components).

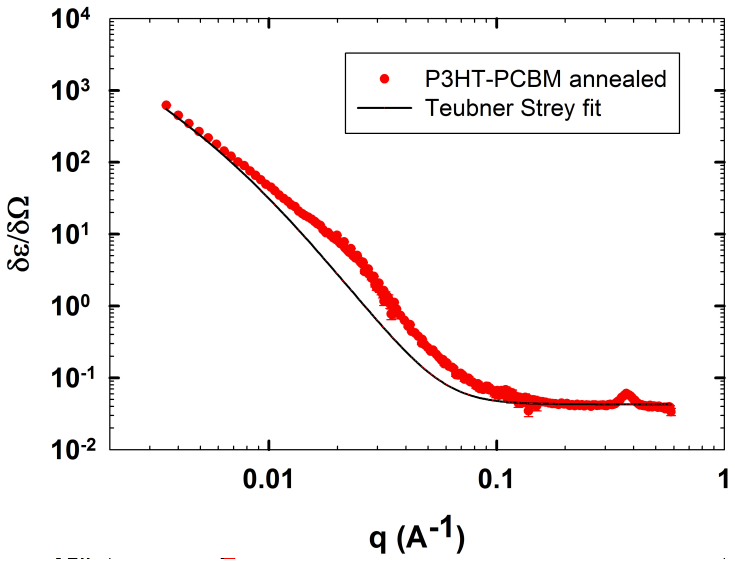

Figure 5.12 Teubner Strey fit for P3HT-PCBM scattering profile.

Fitting one of the SANS profile with the shape independent Teubner-Strey model (Figure 5.12) however showed a good fit over the mid q regime, but couldn't account for the increase in

scattering intensity at the lower q regime. It thus seems that the micellar domain structure isn't sufficient to also fit the large scale phase domains originating in these systems.

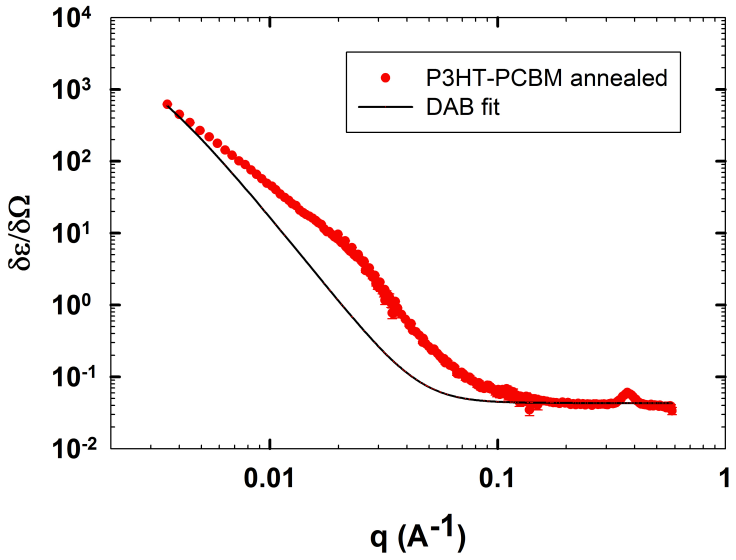

Figure 5.13 DAB model fit for P3HT PCBM scattering profile.

Subsequently another shape independent model, the DAB (Debye-Anderson-Brumberger) model was tried. This model is used to calculate scattering from randomly distributed two phase system. In this case, this would be the crystalline polymer and amorphous phase. The two-phase system is characterized by a single length scale, in this case the correlation length. This is the average spacing between the phases 1 and 2. One of the main assumptions in this model is that the interfaces between the surfaces of the two phases are smooth and they exhibit Porod behavior at large q values. The scattering cross-section of the DAB model is given by:

$$\frac{d\Sigma(q)}{d\Omega} = \frac{C_{DB}}{(1 + (q\xi)^2)^2} \qquad [5.9]$$

in which ξ is the correlation length in Å and C_{DB} is the prefactor defined by:

$$C_{DB} = 8\pi(\Delta\rho)^2\Phi_1\Phi_2 \qquad [5.10]$$

The scale factor, C_{DB} is an independent fitting parameter, but in the DAB model is related to the volume fraction of the two phases Φ_1 and Φ_2 and the contrast $\Delta\rho^2$ (difference between the two SLDs). A representative fit with the DAB model is shown in Figure 5.13. As suggested in the definition of the DAB model, it works well for fitting the profile which represents two phases with a sharp edge. It thus works well for fitting the low-q regime which possibly represents the spacing between the polymer crystal and polymer rich amorphous region. However, the appearance of the characteristic peak at the mid-q regime could not be fitted using the single DAB model.

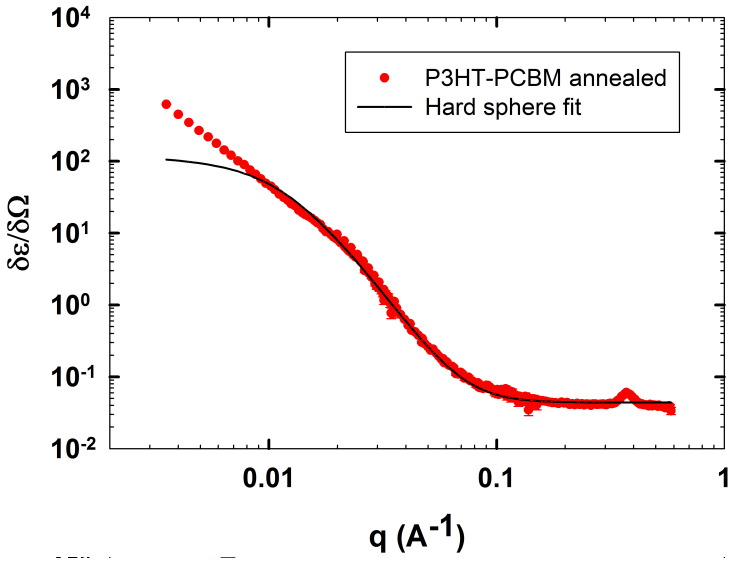

Figure 5.14 Hard sphere model fit for P3HT-PCBM scattering profile.

Lastly, the hard sphere model was tried. The hard sphere model has also been used previously to define the fullerene crystal formation from the polymer rich amorphous regime. The hard sphere model has been used before to define fullerene aggregates in solutions using SAXS.[104] The form factor for the hard sphere model is defined by

$$F = \frac{A}{V}\left(\frac{3V(\Delta\rho)(\sin(qr) - qrcos(qr))}{(qr)^3}\right)^2 \qquad [5.11]$$

where A is the scale factor, r is the hard sphere radius, and V is the volume of the spheres. A quick fit of this model did not yield good results. It was suggested that the spheres are possibly polydisperse. A Schulz distribution was used to take into account the polydispersity of the hard spheres because a similar model has been used previously with similar studies.[90, 104] The scattering cross-section in such a case then becomes:

$$\frac{d\Sigma(q)}{d\Omega} = \Phi V(\rho)^2 \left(\int_0^\infty F_i(q, r_i) f(r_i) dr_i + \iint_0^\infty F_i(q, r_i) F_j(q, r_j) H_{ij}(q, r_i r_j) f(r_i) f(r_j) dr_i dr_j \right) \quad [5.12]$$

where f(r) is the Schulz distribution function and $H(q,r_i,r_j)$ is the pair structure function which takes into account the interaction between the hard spheres. The polydispersity p is calculated by:

$$p = \frac{a}{R} \quad [5.13]$$

where a^2 is the variance of the Schulz distribution and R is the mean radius of the hard spheres. This addition did give us better fits for the data for the mid-q regime which were missing from the DAB model (Figure 5.14) but did not satisfactorily cover the low q scattering intensity. Thus the hard sphere model was not a satisfactory single model to explain the complete phase morphology of the system either.

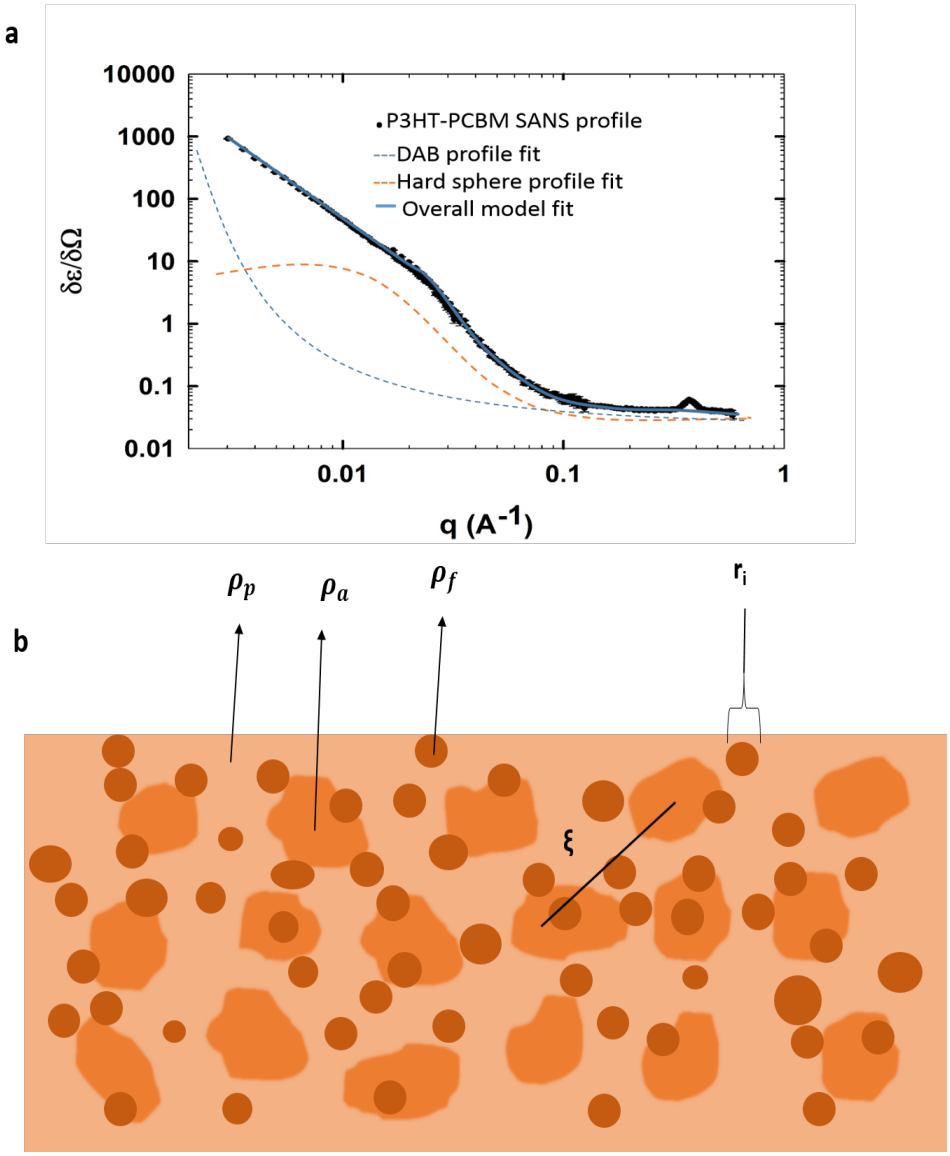

Figure 5.15 a) Combined DAB + Hard sphere models to give an overall fitting model b) Schematic showing the overall morphological structure in the blends where ρ_a, ρ_p and ρ_f are the SLD of the amorphous mixed phase, polymer crystal and fullerene hard sphere phases, r_i is the radius of the hard sphere and ξ is the DAB correlation length.

Taking into account all these individual fits, it was surmised that no single model could fit the entire q-regime and thus could not describe the complete phase morphology of the system.

Consequently, there were definitely more than two phases in all the systems that, in combination, showed the characteristic scattering pattern from the SANS measurement. Thus a combination of two of the models were decided to be used to help describing the overall morphology of this system (Figure 5.15a). Proceeding from the previous analysis (in the low-and mid-q regimes) and studies conducted in literature using GISAXS and SANS, a combination of two models was thought to be suitable for fitting the scattering data over the entire q regime.[90, 104] The DAB model has quite often been used to describe two phases of polymer-nanoparticle mixtures with varying compositions and thus could be chosen as a base for describing the large scale phases (visible at the low-q regime). The hard-sphere model, in turn, gave us a good fit for the characteristic peak in the mid-q regime. A combination of the two models gave us a good fit for the overall scattering pattern (Figure 5.15a). The same combined model was then extrapolated to the other polymer-fullerene systems as well and consistently showed good fits. The combined model intensity could be represented as a sum of the pre-defined DAB (1st term on the right side) and hard sphere models (2nd and 3rd terms):

$$\frac{d\Sigma(q)}{d\Omega} = \frac{C_{DB}}{(1+(q\xi)^2)^2} + \Phi V(\rho)^2 \left(\int_0^\infty F_i(q,r_i) f(r_i) dr_i + \iint_0^\infty F_i(q,r_i) F_j(q,r_j) H_{ij}(q,r_i r_j) f(r_i) f(r_j) dr_i dr_j \right) \quad [5.14]$$

Firstly, for the different polymers, the correlation lengths for the large phase (originating from the low-q data) determined were ~100 nm corroborating the correlation lengths from the Debye-Bueche fits. The pre factor C_{DB} (Equation 5.5 for DAB model given previously) can be used to derive the scattering contrast Δρ between the constituent materials as well as the volume

fraction of the fullerene in the mixed phase. Since the SLD for pure polymer and fullerene could be computed (and have been shown earlier in Table 4.3), thus the scattering contrast could give a good estimate of the composition of the large phase. The SLD contrast values were also tabulated (Table 5.6) and it was noticeable that the large phases (corresponding to the DAB correlation length ξ) predominantly comprised of polymer with a minimal amount of fullerene. According to the previous Debye Bueche fits (section 5.2.5) and from literature [60, 92, 104] this can be attributed to an amorphous phase of fullerene intermixed in the polymer. In addition, ξ decreases in the order P3OT>P3HT>P3BT, in the same order as that of polymer crystallinity. This suggests the polymer with the greatest amorphous content will consequently have the most amount of fullerene in a mixed phase, giving the largest correlation lengths. This phase also contains a minor component of fullerene as well, the amount of which is limited by the solubility limit of the fullerene in the polymer. This may be estimated using column 4, with the volume fraction of fullerene spheres (aggregated fullerenes) being maximum in case of least amount of fullerene-polymer mixing. However, it may be noted that the values do not differ by a significant amount before annealing though the difference becomes a bit more pronounced on annealing due to further fullerene forming hard sphere aggregations.

Moving onto the mid-q range, the hard sphere model gives dimensions ~1-10 nm. Since the characteristic peak for the polymer crystal is already observed at higher q, this region could possibly be fullerene enriched. This is indeed confirmed by the SLD values for this phase observed from the fits (and compared to SLD values for fullerenes Table 4.3, Chapter 3). The pre-factor 'A' from the hard sphere model fit (Equation 5.11) gives the values of the volume fraction of the hard sphere, their average radius and the SLD. The SLD comparison to the theoretically calculated value of fullerenes confirms the hypothesis of the hard spheres being primarily fullerene.

Comparing the size of the fullerene hard spheres though (Table 5.6) it is seen that C60>PCBM>bis PCBM in terms of hard sphere size as well as the volume fraction of the fullerene spheres. This can be understood in terms of the polymer?: fullerene miscibility limits in the drop cast blend samples. Due to the absence of other kinetic factors owing to the slow evaporation mechanism as well as absence of interfaces, the miscibility seems to be the dominating factor in the morphological developments of these films. Thus, a fullerene with lower miscibility in the polymer would have lesser composition in the amorphous polymer region and a greater composition in the formation of fullerene rich hard spheres. Upon annealing, this behavior is further enhanced with fullerene volume fraction in amorphous polymer ($\Delta\rho$ in Table 5.6) going down and fullerene volume fraction in hard sphere going up suggesting that this is a more thermodynamically favorable state for the fullerenes.

Table 5.6 Parameters from DAB + Hard sphere model fitting for the different polyalkylthiophene-fullerene combinations.

Sample	**Hard sphere Radius r (Å)**	**Correlation Length ξ (Å**	**Vol Fraction of Fullerene spheres**	**Δρ from the DAB model**
P3BT C_{60}	24.34±0.41	1600.23±18.04	17.62	2.00E-06
P3BT C_{60} ann	40.41±1.21	1650.00±19.42	20.08	1.88E-06
P3BT PCBM	21.57±0.21	1500.1±10.01	14.03	1.83E-06
P3BT PCBM ann	35.55±0.71	1771.14±13.42	17.03	1.66E-06
P3BT bis-PCBM	20.12±0.44	1654.23±12.25	13.52	1.13E-06
P3BT bis-PCBM ann	32.25±0.95	1712.22±16.53	17.66	0.94E-06
P3HT C_{60}	35.57±0.71	1700.12±20.15	12.04	1.6E-06
P3HT C_{60} ann	87.49±1.15	1740.2±20.8	14.30	1.36E-06
P3HT PCBM	45.53±0.91	1600.45±6.01	11.62	1.21E-06
P3HT PCBM ann	70.20±1.40	1831.51±8.02	12.11	1.12E-06
P3HT bis-PCBM	32.23±0.25	1810.42±8.76	10.13	0.96E-06
P3HT bis-PCBM ann	40.21±0.51	1870.21±10.32	11.87	0.91E-06
P3OT C_{60}	48.91±0.98	2300.11±26.02	11.05	1.41E-06
P3OT C_{60} ann	85.84±1.71	2403.40±32.1	14.66	8.15E-07
P3OT PCBM	40.59±1.41	2000.24±20	10.51	1.11E-06
P3OT PCBM ann	70.59±1.44	2031.53±20.63	11.47	0.84E-06
P3OT bis-PCBM	39.31±1.15	1853.32±13.31	9.91	0.83E-06
P3OT bis-PCBM ann	45.23±1.38	2023.1±14.52	11.41	0.67E-06

5.3 THIN FILM SMALL-SCALE DOMAIN STRUCTURE STUDIES

The device performance is expected to depend on the molecular crystallography in these different zones within the active layers, and parameters including the amount of crystallinity, crystal domain size and orientation. GIWAXS was used to determine the in- and out-of-plane crystallography of the BHJ layer within the devices in full device configuration. Representative 2D GIWAXS patterns are shown in Figure 5.16(b) and (c), where characteristic (*h00*) (h=1,2,3, etc) peaks corresponding to the polymer chain crystal planes and (*0k0*) (k=1,2,3) peaks corresponding to the polymer π-π stacking crystal planes are labeled. The *d*-spacing for the polymer crystal stacking (d_{h00}) and π-π stacking (d_{0k0}) are calculated from the peak positions (Table 5.7). Using Scherrer's equation (section 2.4.4) and the (*100*) reflection as reference, corresponding domain sizes for the crystals were determined (Table 5.7). The crystallinity of the polymer was calculated (Table 5.9) while the Herman's orientation parameter, f_H, was obtained (see Section 2.4.4) to give a value for the orientation of the *(100)* plane (see Table 5.8). For a comparison of the crystal orientations in the various devices and its effect on the device performance, a ratio of the edge-on to face-on contribution from the azimuthal angle integration plot was calculated (Figure 5.16). Crystals with an orientation of $\varphi = 90°$ are considered to be oriented edge-on whilst those at $\varphi = 0°$ have face-on crystal orientation. The areas under these respective curves and their ratios were calculated and plotted vs the J_{sc}. (Figure 5.20)

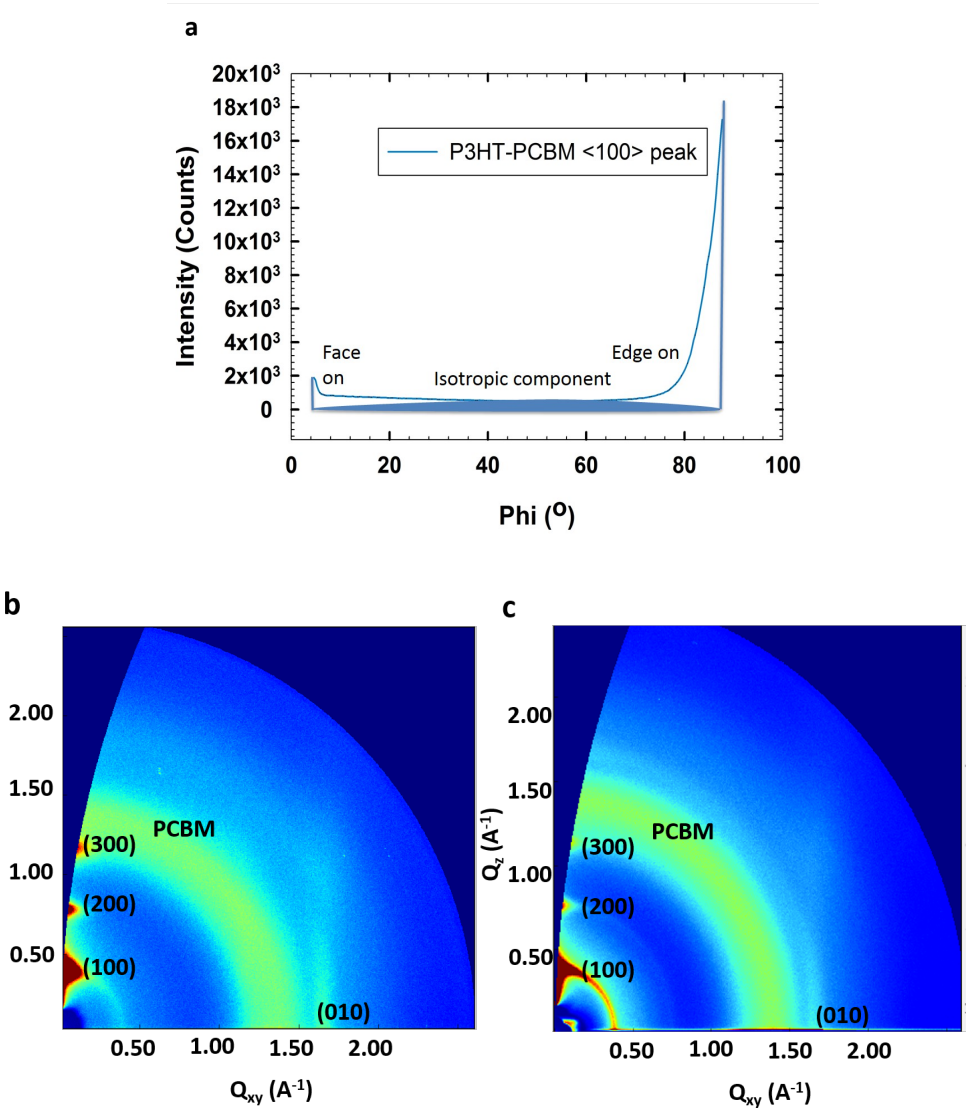

Figure 5.16 a) Azimuthal scan for <100> plane obtained from P3HT-PCBM GIWAXS pattern. GIWAXS patterns for b) unannealed and c) annealed P3HT PCBM showing increased crystallinity and characteristic <h00> and <0k0> peaks.

5.3.1 Crystal spacing and domain sizes

The 2D images of GIWAXS results qualitatively show changes in the crystal orientation, crystal domain size, and an increase in the crystallinity in the different systems upon annealing (Figure 5.18).

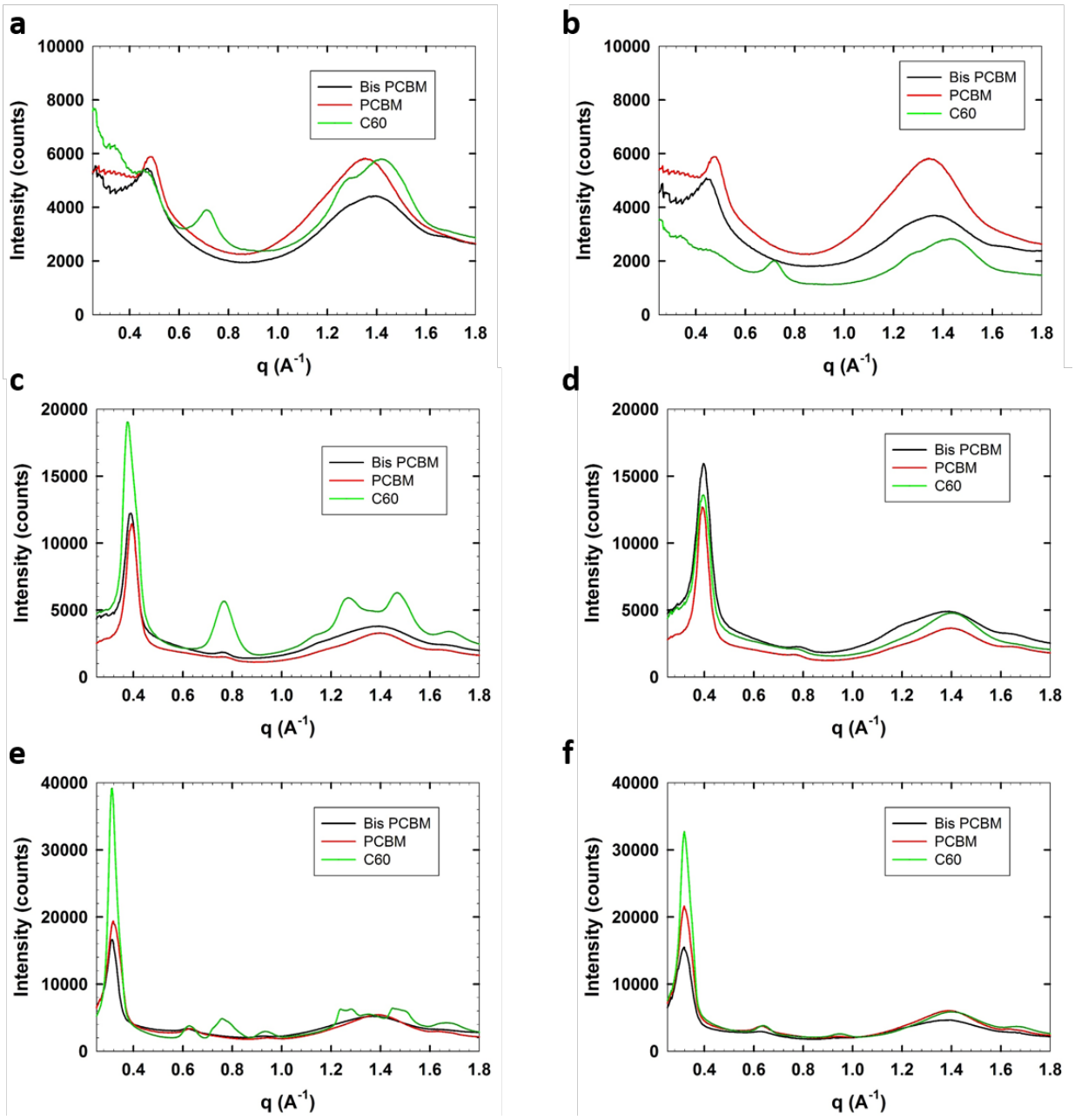

Figure 5.17 1D integration plots (Intensity vs q) for GIWAXS measurements of thin films of different fullerenes mixed with a) P3BT b) P3HT c) P3OT unannealed and their corresponding annealed samples d) - f).

Increasing crystalline domain size and orientation of the crystals, upon annealing, both have an influence on J_{sc}. The Scherrer equation was used in the determination of size of particles of polymer crystals in the thin films from the GIWAXS patterns as described earlier in Section 2.4.4.

The closer the domain size approaches the exciton diffusion length (typically ~8-10 nm in these materials [197]), the higher is the probability that the excitons formed would diffuse to an interface and dissociate rather than recombine. In this domain size range the system is expected to produce the maximum charge generation as is also seen in the devices (Figure 5.19).

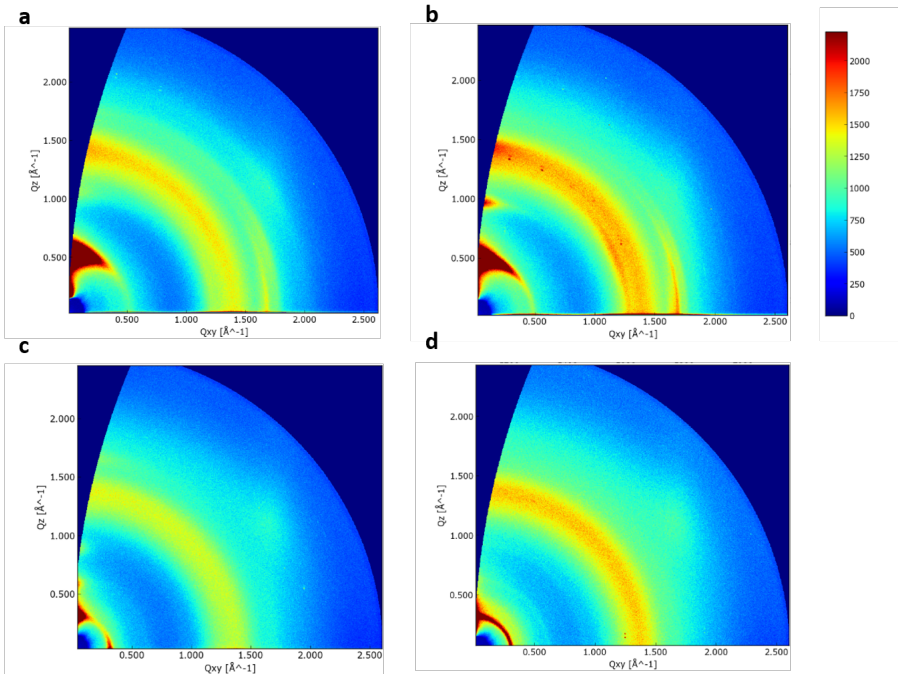

Figure 5.18 2D GIWAXS images for different P3AT- PCBM systems a) unannealed P3BT-PCBM b) annealed P3BT-PCBM c) unannealed P3OT-PCBM and d) annealed P3OT-PCBM.

The d-spacing for (100) crystal planes and the pi-pi stacking planes were calculating using the peak positions of the crystals planes and then converting from q-space to real space.

The value for the d-spacing was given by:

$$d_{hkl} = \frac{2\pi}{q} \qquad [5.15]$$

Where d_{hkl} is the d-spacing value for the crystal plane (hkl).

Table 5.7 d-spacing for (100) polymer crystal planes and (010) π-π stacking.

Sample Name	d_{100} plane (Å)	d_{010} plane (Å)
P3BT-C_{60}	13.1±0.07	3.71±0.08
P3BT-PCBM	12.69±0.06	3.65±0.06
P3BT-bisPCBM	13.1±0.06	3.65±0.09
P3HT-C_{60}	16.2±0.08	3.71±0.07
P3HT-PCBM	15.96±0.08	3.75±0.08
P3HT-bisPCBM	16.15±0.08	3.72±0.06
P3OT-C_{60}	19.85±0.09	3.72±0.09
P3OT-PCBM	19.63±0.08	3.72±0.07
P3OT-bisPCBM	20.01±0.08	3.66±0.09

The d-spacing values for the polymer crystals obtained were as expected with the polyalkylthiophene with larger side chains showing greater d-spacing of the (100) planes. The spacing of the π-π crystal repeat planes however did not vary much within all the samples. The crystal orientation suggests that these crystal planes are parallel to the polymer backbone plane (Figure 5.2) and are not affected by the length of the side chains. One could thus surmise that the π-π overlap in these cases are mostly similar and the corresponding d-spacing would not have such an impact on the electronic properties of these polymer-based BHJs.

At the same time, orientation of the crystals with a face-on orientation relative to the substrate would be conducive to charge transport and thus a larger face-on contribution of crystals correlates to a better charge generation and hence an increase in J_{sc}. Thus it is seen that P3HT,

(Figure 5.20) which shows the smallest edge-on to face-on ratio (consequently maximum amount of face-on orientation) in these devices, resulting in the highest J_{sc}. This correlation is more strongly valid for the case where there is limited large-scale phase separation occurring in the active layer. Phase separation usually is not prevalent in pre-annealed samples, but it might develop in post-annealed samples due to the high boiling point solvent used (o-dichlorobenzene), which would evaporate slowly and over time promote fullerene aggregation. This is especially true in the case of devices made with C_{60} fullerene (Figure 5.22a and b), where the active layer has large fullerene aggregates (~10 nm) in the bulk that are phase separated due to poor miscibility with the polymers. Due to the reduced miscibility (based on the binding energy calculation values, Section 4.2.1), C_{60} devices would consequently also have the least amount of molecularly dispersed fullerene in the amorphous polymer regions, which reduce efficient charge separation in the device (exciton separation occurring at the polymer-fullerene interfaces). Limited miscibility of fullerenes also causes device roughness at the interface (seen in table 4.4 and 4.5, Section 4.2) and these effects, combined, could be adversely affecting the J_{sc} and PCE as seen in C_{60}-based devices described earlier in Chapter 4.

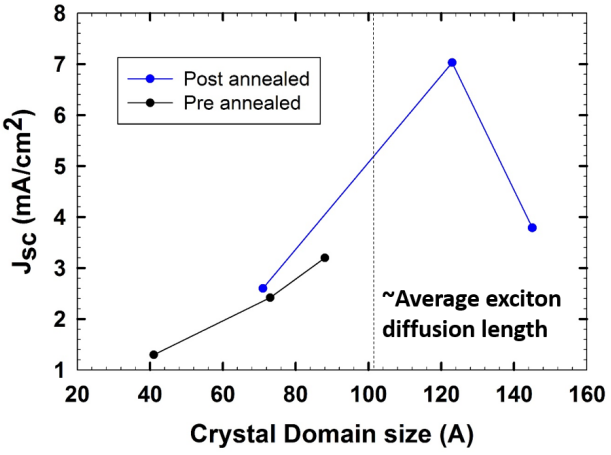

Figure 5.19 Correlation of crystal domain size with J_{sc} for P3AT –PCBM devices.

5.3.2 Crystalline Morphology and Orientation

As mentioned earlier, besides the crystal spacing and domain sizes, the orientation of the crystals are influential in affecting the electronic properties of these polymer-fullerene mixed systems. A measure of crystalline orientation, the Herman's orientation factor, was described previously (section 2.4.4). The Herman's orientation factor for the polymer (100) crystal planes was calculated and tabulated (Table 5.8). f_H ranges between -0.5 and 1; 1 corresponding to the peak being completely in the out of plane direction and thus suggesting a primarily edge on orientation and -0.5 thus corresponding to the lamellar peak being in plane giving us a face on orientation.

Table 5.8 f_H values for different devices, before and after annealing.

Sample Name	Unannealed	Annealed
P3BT-C_{60}	0.72	0.76
P3BT-PCBM	0.92	0.90
P3BT-bisPCBM	0.86	0.88
P3HT-C_{60}	0.63	0.60
P3HT-PCBM	0.62	0.63
P3HT-bisPCBM	0.74	0.73
P3OT-C_{60}	0.66	0.66
P3OT-PCBM	0.74	0.79
P3OT-bisPCBM	0.78	0.77

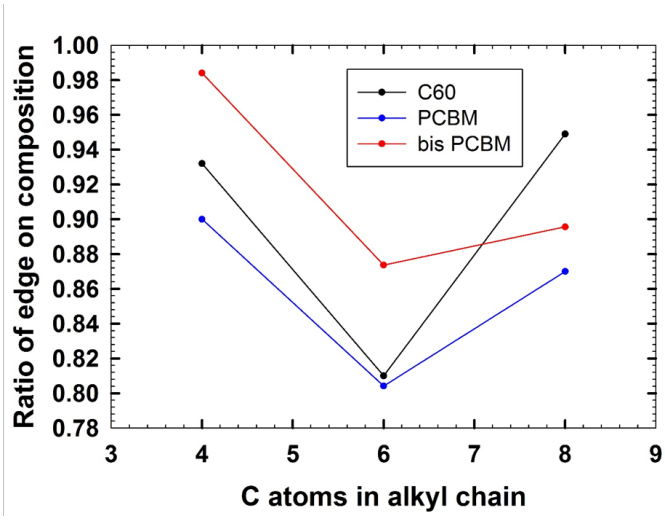

Figure 5.20 Variation of edge-on composition of <100> crystal plane for P3AT-Fullerene samples.

The Herman's orientation factor quantifies the degree of orientation of the polymer crystals. This would however be only attributed to the orientation of one of the components (edge-on or face-on) at a time. Because the electron transport in the different directions of the crystal vary, to easily compare the effect of orientation to the device performance, the ratio of the two orientation components was found as described earlier is Section 5.3 (edge-on and face-on, Figure 5.16). One expects the orientation of the crystals with a face-on orientation relative to the substrate would be conducive to charge transport and thus a larger face-on contribution of crystals correlates to a better charge generation and hence an increase in J_{sc}. Thus, P3HT, (Figure 5.20) which shows the smallest edge-on to face-on ratio (consequently maximum amount of face on orientation) in these devices, shows the highest J_{sc}. This correlation will be more strongly valid for the case where there is not any large-scale phase separation occurring in the active layer since that would inhibit charge separation itself.

Crystallinity itself has been studied extensively and it is suggested that larger amount of interpenetrating crystalline phases would also facilitate the easy hole transport to the electrodes.[78] With this is mind, the percentage crystallinity for the polymer in the different samples was calculated (Table 5.9). Polymer crystallinity was evaluated by the methods discussed earlier (See experimental Section 2.4.4). A correlation between the percentage crystallinity to the *Jsc* values measured earlier (Figure 5.21) was obtained as well. Although no direct correlation between the two could be obtained, most P3HT and P3OT-based devices showed values of *Jsc* which increased within a range of increasing crystallinity (dotted lines Figure 5.21). In contrast though, P3BT based devices gave us points which were clear outliers and most definitely suggested that there are other parameters, more significantly affecting the *Jsc*. This is substantiated in the earlier studies through Chapter 3 as well as in this chapter. Thus unlike the all-encompassing value of percentage crystallinity in the entire film, more nuanced parameters such as amount of segregation, crystal domain size as well as crystal orientation are better suited for such device-performance correlations.

One such reason for the inconsistency of crystallinity being a determinant of good electronic properties is phase separation. Phase separation usually is not prevalent in pre-annealed samples, but it might develop in post-annealed samples due to the high boiling point solvent used (o-dichlorobenzene), which would evaporate slowly and over time promote fullerene aggregation. This is especially true in the case of devices made with C_{60} fullerene (Figure 5.22a and b), where the active layer has large fullerene aggregates (~10 nm) in the bulk that are phase segregated due to poor miscibility with the polymers. Due to the reduced miscibility (based on the binding energy calculation values, Section 4.2.1), C_{60} devices would consequently also have the least amount of molecularly dispersed fullerene in the amorphous polymer regions, which reduce efficient charge separation in the device (exciton separation occurring at the polymer-fullerene interfaces). Limited

miscibility of fullerenes also causes device roughness at the interface (also seen in the roughness values, (Section 4.2) and these effects, combined, could be adversely affecting the J_{sc} and PCE as seen in C_{60} based devices in (Chapter 4).

Table 5.9 Polymer crystallinity values for different devices, before and after annealing.

Sample Name	Unannealed	Annealed
P3BT-C_{60}	30.12	31.3
P3BT-PCBM	32.41	36.1
P3BT-bisPCBM	24.15	26.9
P3HT-C_{60}	21.84	23.8
P3HT-PCBM	24.73	26.2
P3HT-bisPCBM	22.31	23.4
P3OT-C_{60}	18.66	20.1
P3OT-PCBM	23.61	24.5
P3OT-bisPCBM	16.82	17.20

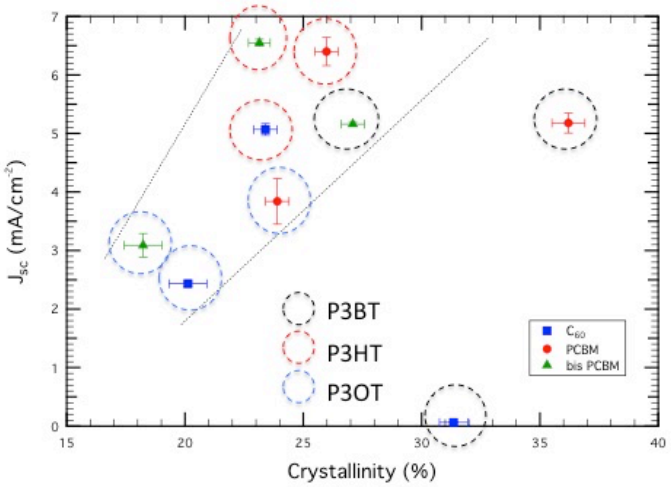

Figure 5.21 Percentage crystallinity vs Jsc plot for different P3AT-Fullerene devices.

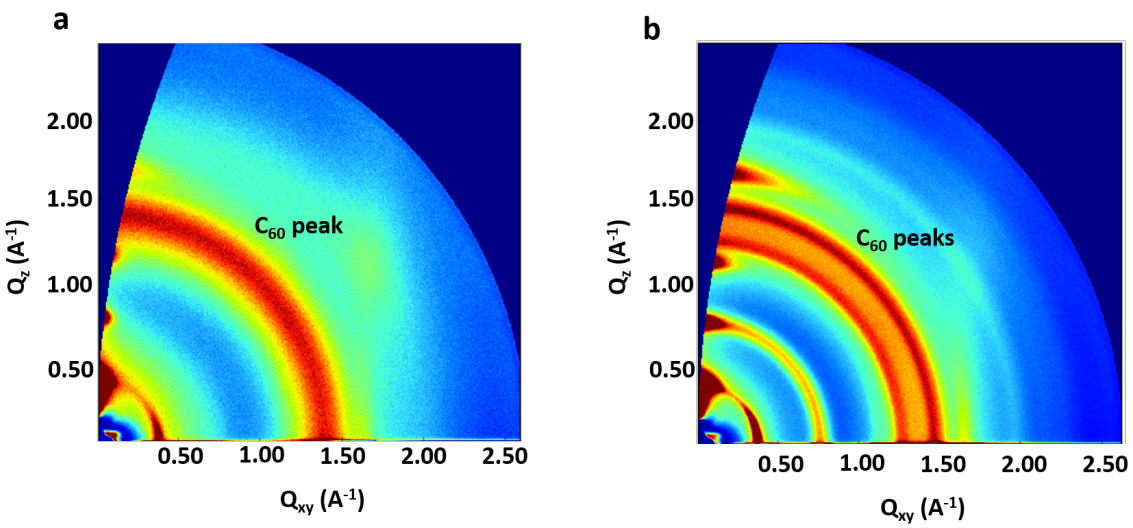

Figure 5.22 GIWAXS pattern for a) pre- and b) post-annealedP3HT C60 showing fullerene aggregation leading to phase separation.

5.4 THIN FILM LARGE-SCALE DOMAIN STRUCTURE STUDIES

Following on from the GIWAXS measurements to study the small-scale morphological structure in the thin films, GISANS measurements were used to obtain information about the larger phase structure in the thin films and help develop an understanding of the overall lateral phase morphology of the thin film BHJ systems. Based on the SANS analysis (Section 3.2.6) of the drop cast films, a combined DAB + hard sphere model was introduced. This was seen to best describe the three phases present in the drop cast polymer-fullerene mixtures. Using the models studied before as a template (Section 3.2), the study was expanded to the phase morphology of the thin film active layer in the BHJ devices. The thin films were made from the combination of P3HT with the three fullerenes used previously by the procedure discussed previously (Section 2.6.1). Also, as previously explained (Section 2.4.7), the GISANS measurements were divided into three wavelength ranges (corresponding to different energy levels). By utilizing these wavelength ranges

(correspondingly neutrons beams of different energy levels) scattering information from the regions near the Al/BHJ interface, bulk BHJ interface, BHJ/PEDOT: PSS interface could be obtained (Figure 5.23). A quick look at the three scattering patterns shows them to be qualitatively different. The inherent difference in the scattering pattern in the three regions qualitatively suggests the possibility of different phase morphology. Thus the three regions were studied separately and fitted with appropriate SANS models to get an estimate of the phase morphology variations in them.

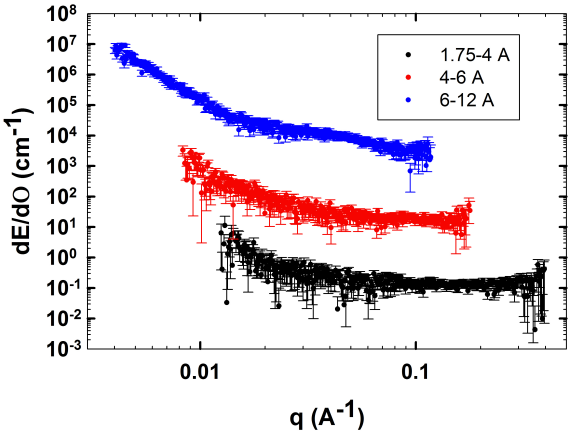

Figure 5.23 GISANS profiles for P3HT:-$PC_{61}BM$ devices measured at different wavelength ranges (offset on the y-axis for easier viewing).

5.4.1 Morphological Structure in Zone 1 (Near Cathode) in the Active Layer

The scattering for the shortest wavelength range (6-12 A) penetrated the BHJ the least and gave information about the region near the top interface (Zone 1 or Al/BHJ layer) qualitatively showed a profile similar to the post annealed SANS profiles for the polymer-fullerene drop cast films (Figure 5.3). A high scattering intensity at low q and characteristic peak at the mid-q region suggested that a similar model could be used for both. Thus the previously discussed DAB+Hard sphere model (Section 3.2.6) was chosen to fit to the measured profile. The fit for the profile

(Figure 5.24) showed good correlation and definitely the lowest variance compared to other models which were tried on the same. Thus, as shown before, using the fitting parameters, information regarding the hard sphere and amorphous polymer phase size and composition was obtained (Table 5.10).

In terms of the correlation length, corresponding to the amorphous polymer-fullerene mixed regime, the trend of the domain size was similar to that seen in the drop cast equivalent of the same films (Table 5.6, Section 5.2.6). The correlation length was larger in bis-PCBM>PCBM>C_{60} (Table 5.10). This could be attributed to once again their respective trend of solubility in P3HT, which in turn ensured a bigger domain size. The correlation lengths itself were however larger in the thin films compared to the drop cast films. Combined with the WAXS, GIWAXS measurements, a possible reasoning for this could be that in the slow developing drop-cast film, more time is available for the polymer in the films to crystallize. In turn, the polymer (P3HT) crystal size in the drop cast films in much larger than in the thin film. In turn, despite the post annealing of these materials, the amorphous content of polymers is more in thin films, lending to larger regions of amorphous mixed polymer-fullerene phases.

In contrast to the SANS measurement however, the fullerene composition and hard sphere size is the largest in the case of bis-PCBM>PCBM>C_{60}. It is important to note that the SANS measurement and model fit (Section 3.2.6) is representative of the entire drop-cast film, while in contrast this section is representative of only the near-top layer of the BHJ. As discussed previously in Chapter 2, there is fullerene segregation towards the electrode, driven by the electrode surface energy. The trend seen here is similar to that observed in Section 2.6. A possible explanation could be the mechanism through which the fullerene segregation develops in the BHJ. It can be hypothesized that to lower the interfacial energy of the Al/BHJ interface, upon annealing, the

fullerene moves through the amorphous portion of the polymer, creating a fullerene rich layer near the top electrode. Previous studies on bilayer have also shown that the rapid movement of fullerene into polyalkylthiophene occurs through the amorphous regime of the polymer.[85] Thus larger the solubility of the fullerene in the amorphous polymer, easier it is for the fullerene to move to the top. Thus a combination of kinetic and thermodynamic effect in a more equitable measure determine the phase morphology in this this regime despite they being structurally similar.

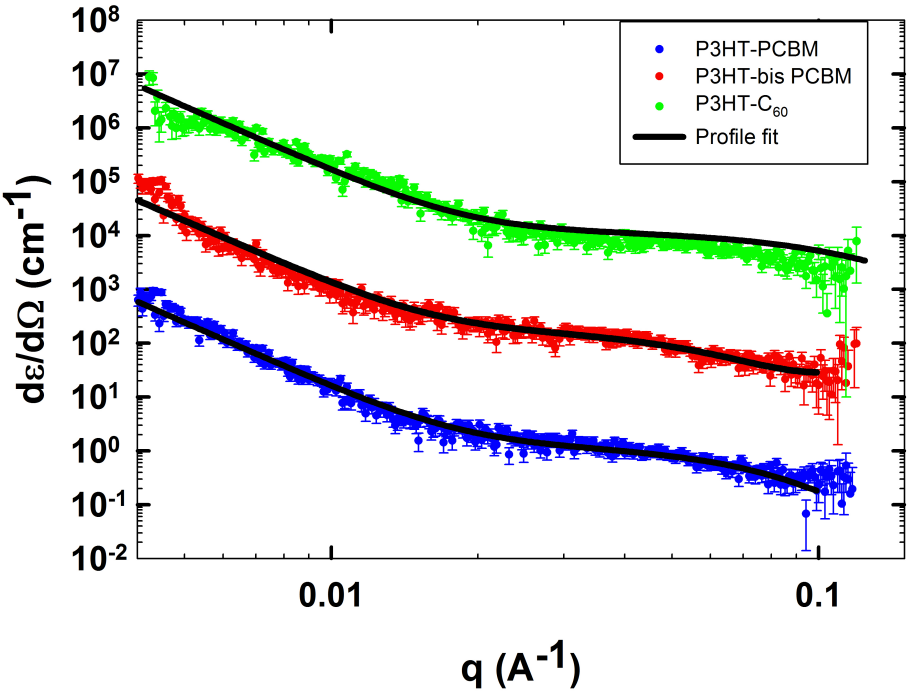

Figure 5.24 GISANS profile and fit for scattering from near Al/BHJ interface (Zone 1).

Table 5.10 Morphological parameters obtained from DAB model fit of SANS profile (Zone 1)

Sample	Hard sphere Radius (A)	Correlation Length. ξ (A)	%Fullerene (from spheres)	% Fullerene in Amorphous
P3HT-C_{60}	30.74±1.15	2000.32±20.8	21.31	15.12
P3HT-PCBM	45.11±1.4	2151.21±12.03	26.65	26.33
P3HT-bis PCBM	50.23±1.31	2400.45±15.21	34.43	28.24

5.4.2 Morphological Structure in Zone 2 (Bulk) in the Active Layer

Compared to the scattering from top Al/BHJ layer (Zone 1), the scattering in bulk BHJ (Zone 2) showed absence of the characteristic peak at the mid-q region (Figure 5.25). Since this inherently corresponds to the hard sphere component of the model, it made sense to fit these profiles first with just the single DAB model (Section 3.2.6). This indeed gave us accurate fits with values of correlation lengths that suggested the phase domain sizes in this region (bulk BHJ). Looking at the contrast values from these fits suggested the presence of polymer rich phases with some fullerene mixed in it. Thus this region was similar to the other amorphous polymer-fullerene regions seen previously (Section 3.2.6, 3.4.1) This also suggested that the overall fullerene content in this region was not high enough for the fullerene to segregate out and form fullerene-based hard spheres, a feature of Zone 1. It may be noted that we do see some possible features at the medium q value for P3HT-C_{60} sample which might possibly coming from some small hard spheres. If we look back to Section 3.2.6, devices with C_{60} had the highest concentration of fullerene in Zone 2 ~40-45% compared to other devices, owing to the fact that it diffuses the least to the top electrode. With the solubility of C_{60} being lesser than 20%, one would expect the fullerene to segregate out. However, since the feature observed here is not as prominent as large as the hard spheres obtained

from the measurement of zone 1, this possibly suggests that not just a fullerene excess, but a minimum amount of excess fullerene is required before it starts forming hard spheres. And all this once again held in line with the previously determined overview of the vertical phase segregation profile in BHJs, wherein it was suggested that Zone 2 is a polymer rich phase (fullerene depleted phase). So having a depleted amount of fullerene ensure it can almost entirely be soluble in the amorphous polymer.

The correlation lengths itself were comparatively larger than those in Zone 1, possibly because of the formation of larger amorphous domains in the absence of segregated hard spheres. The lengths quantitatively are quite similar and the contrast in the phases gives rise to information of the phase composition. From the contrast it is possible to suggest that the amount of fullerene in the system is again determined by the solubility limit of the fullerene. However, in this case, that factor is balanced out by the fact that there is fullerene movement away from the Zone 2 to Zone 1 (towards the top electrode Al). These two contrasting factors in combination decide the final fullerene composition in the amorphous polymer in this zone.

The scale factor in turn, is directly proportional to the volume fraction of the fullerene and SLD contrast between the amorphous mixed and pure crystalline phases in the system (Equation 5.9 and 5.10). Thus to corroborate the model fit with the NR profile hypothesized (Chapter 4), the fullerene composition in Zone 2 was used (Table 4.4) to calculate the expected $\Delta\rho$ in Zone 2 and compared to the $\Delta\rho$ value obtained from the SANS fits. The two phases in this region were assumed to be pure polymer crystalline phase and a phase of polymer-fullerene mixture. The SLD of the two phases was calculated using the fullerene composition values in Table 4.4, SLD values in Table 4.3 and equation 4.1. The difference of ρ between the two phases gave us $\Delta\rho$. The $\Delta\rho$ values calculated from the NR measurement were then compared to that obtained by the GISANS

fitting, in Table 5.11. The values seem to be quite close to each other, though the GISANS experimental values slightly under-predicts the one obtained from the NR measurements. This could possibly be because the region being covered by the SANS measurement is not necessarily the exact region of Zone 2 (in terms of depth range), but in fact might include some components of Zone 1 or 3 as well. Since the fullerene distribution is not uniform through the thickness as has been already established, this would have thrown off the prediction of the SLD contrast and fullerene volume fraction (and thus the scale factor), by a bit.

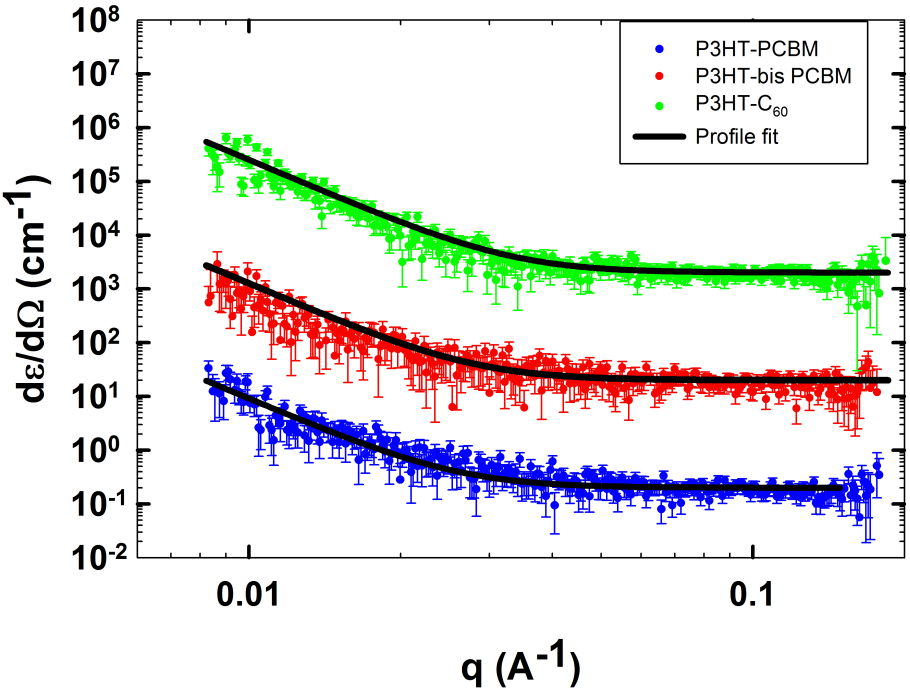

Figure 5.25 GISANS profile and fit for scattering from bulk BHJ (Zone 2).

Table 5.11 Morphological parameters obtained from DAB model fit of SANS profile (Zone 2)

Sample	Correlation Length. ξ (A)	$\Delta\rho_{SANS}$	$\Delta\rho_{NR}$
P3HT-C_{60}	2300.32±16.54	0.81E-06	0.87E-06
P3HT-PCBM	2631.23±32.11	0.65E-06	0.71E-06
P3HT-bis PCBM	2812.42±25.23	0.46E-06	0.52E-06

5.4.3 Morphological Structure in Zone 3 (Near Anode) in the Active Layer

The third wavelength range (1.75-4 A) produced the largest energy neutron beams and consequently penetrated the BHJ the most, giving us morphological information from the lowermost regions of the BHJ (BHJ/PEDOT: PSS interface). Looking at the model fitting of this profile (Figure 5.26), it is qualitatively seen to more closely resemble that from Zone 2 more than the profile from Zone 1. Thus, the same DAB model (see Section 3.2.6) was used to fit the scattering profile (Figure 5.26) and gave good correlation between the fit and measured plot. The variance of the fit was not subsequently improved on adding of an additional hard sphere model (as it did before when we used the combined models) and so the DAB model was adjudged to be suitable to represent the phase morphology in this Zone.

An issue with this measurement however was that the data collected, was inherently low in quality due to large noise signal and consequently had larger errors than all other GISANS measurements. A better technique of measuring the scattering from the bottom surface would ensure this problem can be avoided. That would allow to further study the morphology of Zone 3 in detail and confirm the various hypotheses made previously.

As was in the case of the measurement of Zone 2 (section 4.4.2), the scale factor from the experimental fits (section 4.2.6, DAB model) was used to calculate Δρ (SLD contrast), and

compared to calculated Δρ using the fullerene composition values derived from NR measurements (Table 4.4). The SLD contrast here also (Table 5.12), were comparable, though not exactly matching, with the reasoning for the dissonance between the two value being the same as that for Zone 2, ie. the exact area being probed by the GISANS measurement and region defined as Zone 3 in the NR measurements would not be exactly similar. The lack of information over the exact thickness range measured through the high energy neutron beams (1.75-4 A), might be the cause of small discrepancy between the NR and SANS values for the scale factor. The DAB model however fit the profiles well and the parameters showed a trend we expected to suggest that the phase morphology predicted by us is consistent.

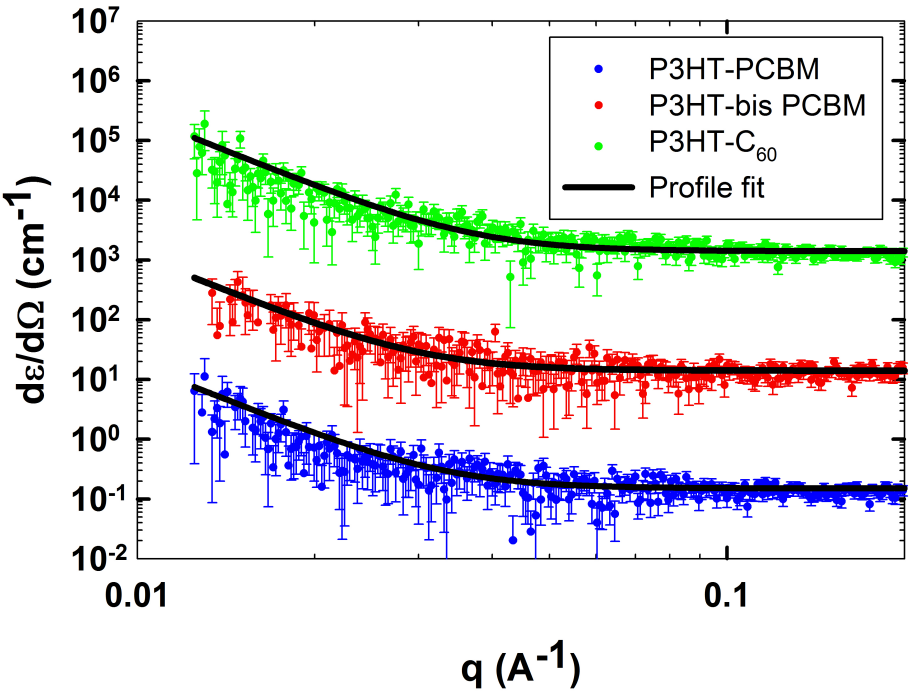

Figure 5.26 GISANS profile and fit for scattering from bulk BHJ (Zone 3).

Table 5.12 Morphological parameters obtained from DAB model fit of SANS profile (Zone 3).

Sample	Correlation Length. ξ (A)	$\Delta\rho_{SANS}$	$\Delta\rho_{NR}$
P3HT-C_{60}	2231.35±14.23	2.24e-06	2.49e-06
P3HT-PCBM	2421.43±12.01	1.81e-06	1.94e-06
P3HT-bis PCBM	2844.32±32.21	1.34e-06	1.59e-06

5.5 SUMMARY - OVERALL MORPHOLOGICAL STRUCTURE IN THIN FILM BHJs

Taking the previously studied vertical segregation (Chapter 3), lateral (in-plane) morphology, crystal structure and orientation (Chapter 4) into consideration, a possible overall morphological structure in the active layer for post-annealed BHJ devices is proposed. From the NR measurements, a through-thickness profile of fullerene segregation at the interfaces was obtained and the GIWAXS measurement suggests multiple phases in the system including regions of crystalline polymers, fullerene dispersed in amorphous polymer phases and phase segregated excess fullerene. The lateral morphology can be understood from the GISANS measurements at three different wavelength ranges (Figure 5.23) corresponding to three different depth scales corresponding ie. Al/active layer interface (Zone 1), intermediary bulk zone (Zone 2) and the active layer/PEDOT:PSS interface (Zone 3). From the fitting of the data from the three wavelength ranges, it is seen that a characteristic domain size of ~6 nm were seen in Zone 1 together with larger domains that are >200 nm (Figure 5.24 and Figure 5.25). The smaller domains are considered to be in the right size range to be ideal for exciton diffusion and dissociation, in addition to providing the channels transporting the electronic charges the Al electrode. The SLD values for the fit suggest

the smaller domains to be in the shape of hard sphere based on pure fullerene and the larger domains consisting of a mixture of fullerene and polymer. This explains the excess fullerene content and its strong correlation to the J_{sc} in this region. In Zone 2 (Figure 5.25), the small domains (pure fullerene) are absent and only the single larger phase (mixture of amorphous polymer-fullerene) structures are found, suggesting the absence of fullerene enrichment and phase segregation in this region. Given the average compositions through the film thickness determined previously from the NR measurements (Chapter 4), these domains are thought to be polymer-rich phases. Similarly in Zone 3 (Figure 5.26) although the Q-range is limited, there is no suggestion of smaller domains in this region and only scattering consistent with large-scale (>200 nm) domain structures is observed. In this region though these large-scale domains must be assumed to be fullerene-rich since the values of SLD contrast obtained from SANS is similar to that obtained from the calculated values of NR parameters in Chapter 4 (which calculated fullerene to be in excess).

Thus for the overall morphological structure (Figure 5.27), it is theorized that the active layer contains mainly a dispersion of segregated fullerene in polymer or domains of pure polymer crystals and fullerene with some regions of fullerene molecularly dispersed in amorphous polymer.[177] Taking into consideration the depth-dependent GISANS experiments, Zone 1 would have distinct fullerene domains (hard spheres) since it is in excess, and some small amount of fullerene dispersed in the amorphous phases of the polymer. GIWAXS experiments confirmed that these large phases of polymer-fullerene amorphous blends would be present along with polymer crystallites. The bulk region (Zone 2), having a more homogenous composition (with slight polymer excess) would thus have only the polymer crystallites and similar polymer-fullerene amorphous mixtures characterized by large domain sizes. The depleted amounts of fullerene would

allow the complete miscibility of most of the fullerene in this region into the amorphous polymer. For the last Zone (Zone 3), even though GISANS analysis is not definitive, the available data allows us to predict that similar large domains of amorphous polymer-fullerene mixtures would be seen. Here however, the SLD contrast suggests a region with greater fullerene content than in the other regimes. Given the limited Q-range of GISANS data in this region, limits the ability to fully fit and characterize this profile. With the use of one of the previously used models (DAB), a region of possibly fullerene excess can be predicted, mainly consisting of large domains of fullerene agglomeration interspersed with amorphous polymer. Further investigation of this regime through both direct (imaging techniques like SEM, TEM) and indirect techniques (GISANS) would further elucidate the overall morphology of thin film BHJs and help understand and design better BHJ architectures.

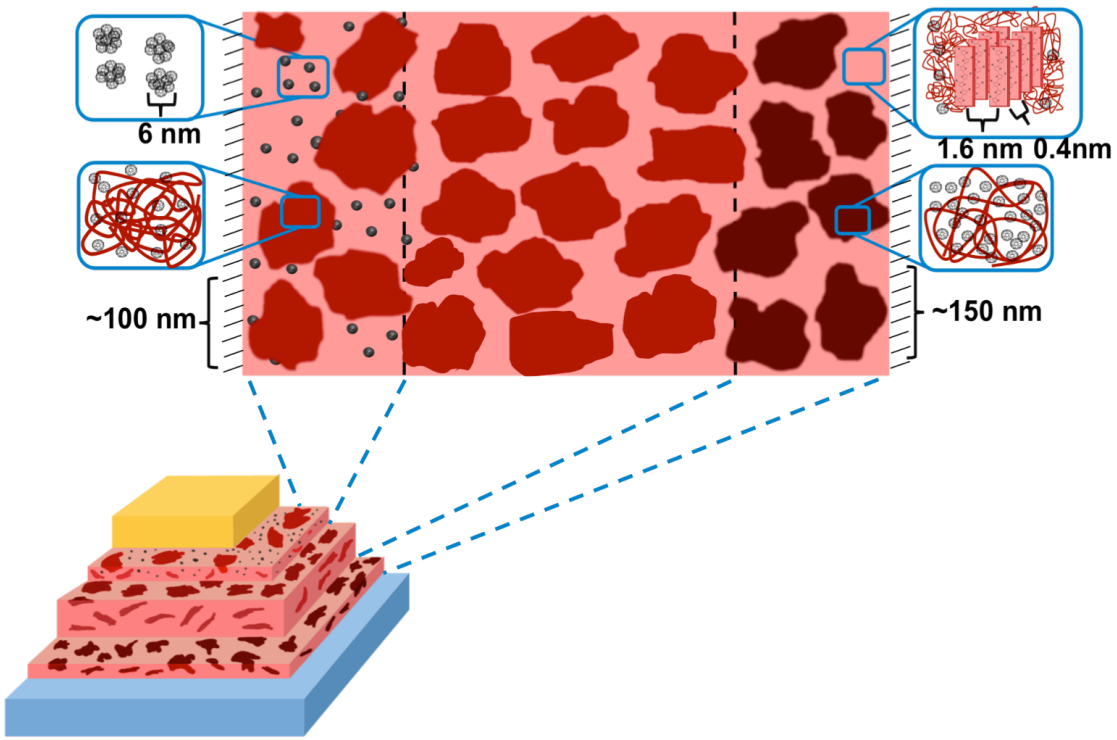

Figure 5.27 Overall morphological structure of the BHJ in OPV devices

6 THERMO-CROSS-LINKABLE FULLERENE BASED BHJ DEVICES

Synthesis of new methanofullerene derivatives such as [6,6]-phenyl-C_{60}-butyric methyl ester (PCBM)[119], which were more soluble, as well as more efficient electron acceptors in OPVs have been an area of extensive study in the OPVs as well. As seen in the device characterization experiments shown in the previous chapters, the active layer i.e. the bulk hereterojunction (BHJ) layer of the conjugated polymer-fullerene mixture attains a complex phase behavior as a result of the solution processing and subsequent thermal annealing. When blended, and subsequently subjected to high temperature for a long period of time, poly(3-thiophene) (P3HT) and PCBM fullerene tends to phase segregate leading to large scale fullerene- and P3HT-rich phases that cause a detrimental effect on the device efficiency as well as its long-term stability.[120]

In addition, within the bulk-heterojunction, fullerene enriched layers are observed near the anode and cathode and consequently fullerene depletion (polymer enrichment) in the middle layer (Chapter 3). Concurrently, the interfaces between the BHJ and the electrodes are diffused. It is thus important to systematically further study the correlation of fullerene-polymer segregation in the active layer to the device performance.

Optimization of device performance is also often accompanied by annealing the device at temperatures typically well below the melt point of the polymer or fullerene for short periods of time. However, extended annealing also tends to reduce the device performance. [79, 80, 106] This annealing directly affects the phase morphology of the polymer and fullerene blend in the BHJ. Previous studies on bilayer devices have shown that an initially pure layer of PCBM will diffuse through a pure P3HT layer within a few minutes when annealed at 150 ^{o}C.[85] Since the annealing

temperature is well below T_m of the polymer or fullerene, but above the T_g of the polymer, diffusion of the fullerene has to be occurring through the mobile amorphous phase of polymer. This consequently leads to fullerene aggregation at elevated temperatures leading to significant degradation in device performance. Keeping these factors in mind, it is thus important to be able to understand and eventually control the morphological development of the bulk heterojunction system.

Thus an approach was developed to design oligomeric fullerene derivatives (with good electronic properties) with the aim of controlling the diffusion of fullerene through the polymer. This would allow systematic studies of the bulk heterojunction as well as achieve a more stable desired BHJ phase morphology through various device processing conditions.

A two-step procedure was developed for obtaining a fullerene with a cross-linkable benzocyclobutene moiety, which is thermally cross-linked in-situ. Benzocyclobutene is often used as a thermal cross-linking group, and undergoes dimerization *via* a o-quinodimethane reactive intermediate in the presence of heat.[198, 199] A thermal cross-linking strategy was chosen because unlike the final cross-linked fullerene, its monomeric fullerene precursor is readily soluble, which allows us to use established processing conditions to fabricate the devices. Thus the cross-linked fullerene could be used to study the fullerene diffusion and aggregation behavior in bulk-heterojunction devices using P3HT as a donor in BHJs. The devices with cross-linked fullerene show extremely good stability against thermal induced degradation, and device performance was correlated with the observed morphological behavior. Through these studies hopefully a better understanding of the relationship between device architecture, morphology and performance can be drawn.

6.1 SYNTHESIS AND CHARACTERIZATION OF PCBCB-I PRECURSOR

Synthesis of PCBM with a BCB thermal cross-linker was carried out as shown in Figure 6.1. The starting materials of [6,6]-phenyl-C_{60}-butyric acid (PCBA), synthesized from commercially sourced PCBM (American Dye Source, inc.), and the 1-hydroxy benzocyclobutene (BCB-OH) were both synthesized following reported procedures (see Section 2.2.1 for details).[119, 200, 201] The PCBA was subsequently reacted with BCB-OH under *N*,*N*′-dicyclohexylcarbodiimide (DCC)-assisted esterification conditions in ortho-dichlorobenzene (o-DCB) in order to obtain the desired precursor product phenyl-C_{61}-butyric acid benzocyclobutene ester, (PCBCB-I) (see Scheme 1). PCBCB-I, which is readily soluble in common organic solvents, was purified though column chromatography and characterized by ^{1}H NMR spectroscopy (section 6.1.1), high-performance liquid chromatography (HPLC, Section 6.1.1) and mass spectrometry (section 6.1.3).

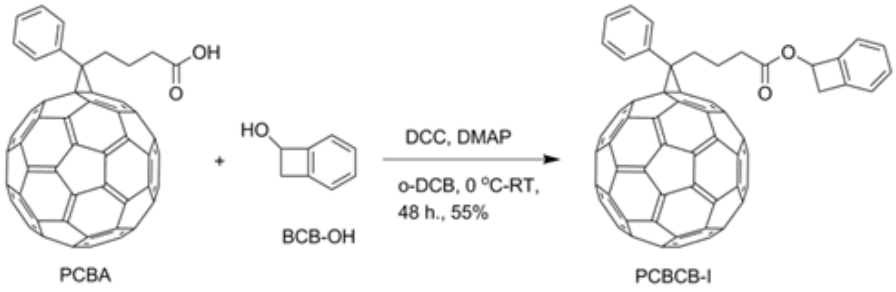

Figure 6.1 Synthesis of PCBCB from PCBA.

The fullerene cross-linked product ((PCBCB)$_n$) was formed in-situ from the purified PCBCB-I *via* thermal annealing. Mass spectral analysis of annealed PCBCB-1 film showed the formation of fullerene dimer along with monomeric fullerene and other decomposition products (see Section 6.1.2). However, although formation of higher oligomeric and polymeric products may be possible, but they were not observed in the mass spectral analysis, suggesting (PCBCB)$_n$,

where n = 2 is the major product. Due to insolubility of the final cross-linked products, further structural characterization could not be carried out. However, results of thermally annealing different combinations of the precursor (PCBCB-I), PCBM and the BCB compounds and previous studies on these materials in literature [199, 201-203] lead us to suggest the possible reaction pathways for the formation of the final cross-linked fullerene products (i.e. $(PCBCB)_n$)

6.1.1 1H NMR and HPLC Characterization

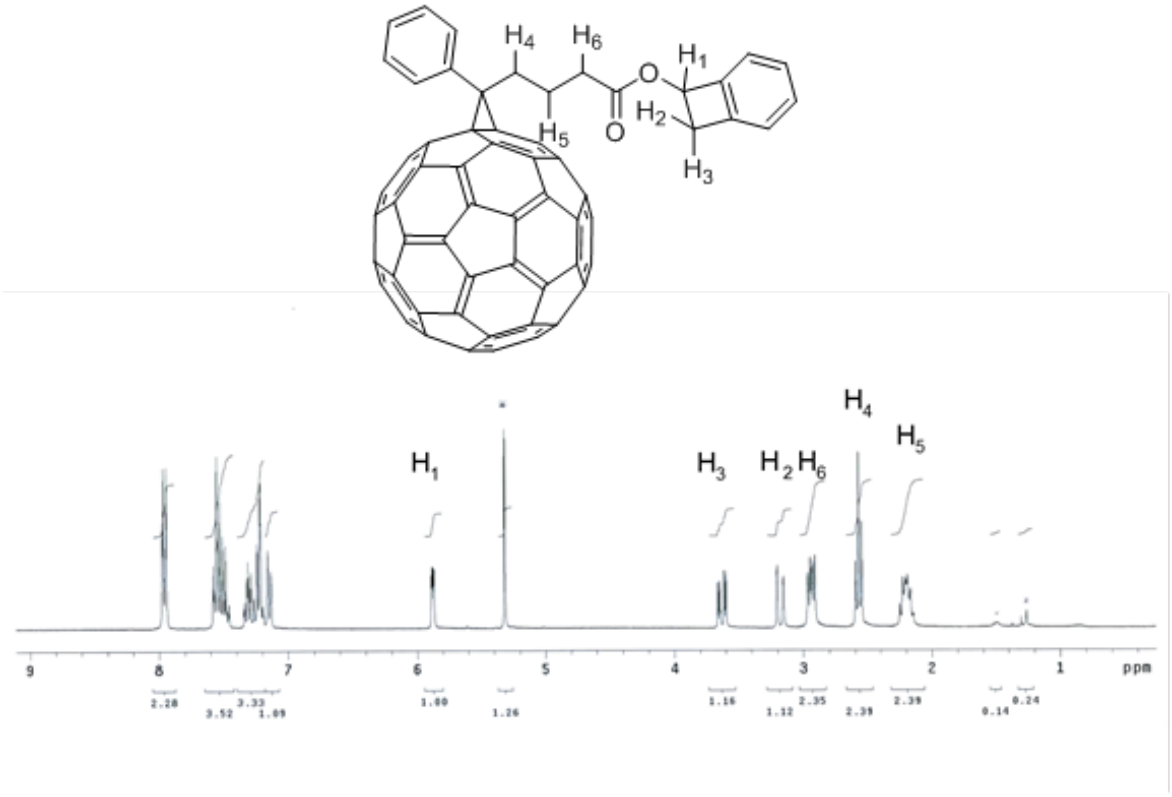

Figure 6.2 ^{1}H NMR spectrum of PCBCB-I in CD_2Cl_2.

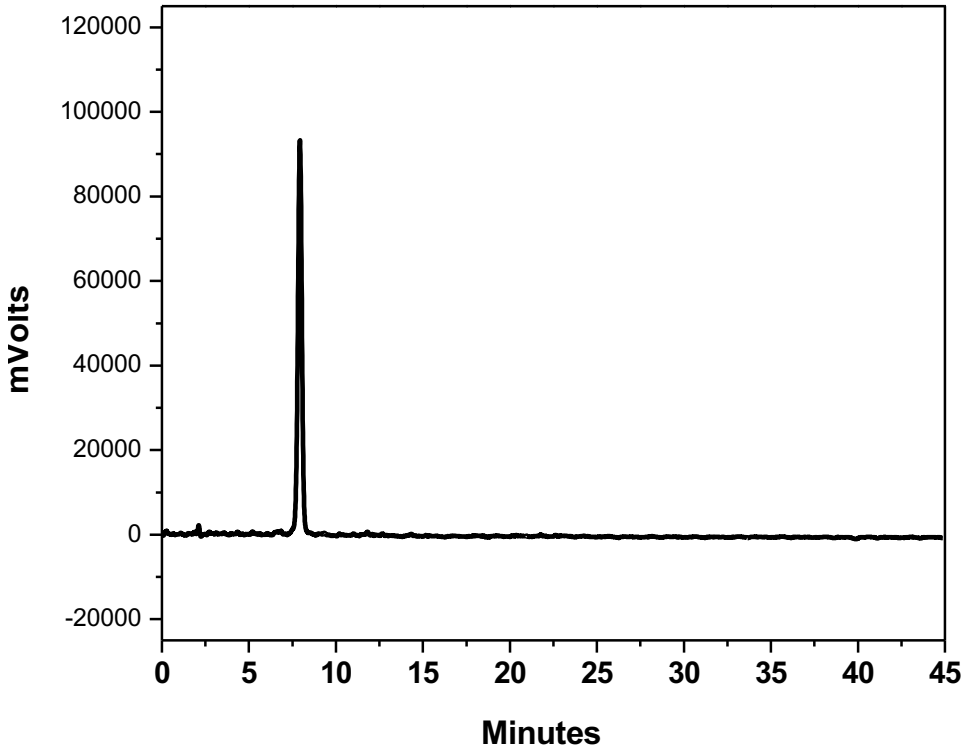

Figure 6.3 HPLC trace of PCBCB-I in THF/MeOH (40:60 v/v) showing pure sample

PCBCB-I was synthesized as shown in scheme 1. The crude product collected was purified through column chromatography (silica, 50:50 v/v CH_2Cl_2/hexanes) to yield PCBCB-I (0.049 g, 55%).[1]H NMR was carried out in CD_2Cl_2 with the help of Dr. Raghunath Dasari (Department of Chemistry, Georgia Tech) to obtain the characteristic peaks expected for a BCB group being attached to the fullerene. (Figure 6.2). ^{1}H NMR (CD_2Cl_2, 300 MHz) δ 7.97-7.94 (m, 2H), 7.58-7.44 (m, 3H), 7.34-7.19 (m, 3H), 7.14 (d, J = 7.2 Hz, 1H), 5.88 (dd, J = 4.5, 2.1 Hz, 1H), 3.62 (dd, J = 14.4, 4.5 Hz, 1H), 3.19 (dm, J = 14.2, 1H), 2.97-2.91 (m, 2H), 2.57 (t, J = 7.2 Hz, 2H), 2.49-2.14 (m, 2H).

6.1.2 Thermo Cross-linking of PCBCB-I Precursor

DSC analysis of the PCBCB-I was carried out using hermetically sealed Al pans from a start temperature of -20 ºC up to 300 ºC at a heating rate of 10 °C /min. The heating and cooling cycles are shown in Figure 6.4a. The first cycle showed a strong exothermic peak, beginning at ~150 ºC, indicative of an exothermic chemical reaction, associated with the cross-linking reaction of BCB moieties. This is in good agreement with previously observed cross-linking temperatures also measured by DSC for other BCB-based thermally induced cross-linked reactions.[199]

To select a suitable temperature for cross-linking reaction in the thin film devices, UV-vis absorption spectra was obtained for films annealed at different temperatures from 150 °C to 210 °C (see Section 2.2). To confirm complete cross-linking reaction of the PCBCB-I precursor at the chosen temperature of 190 °C, DSC analysis of the precursor was conducted by heating it up to a temperature of 190 °C and holding it for 1

0 minutes before cooling it back to -50 C (starting point). This cycle showed the onset of an exothermic peak during the heating cycle (Figure 6.4b). In the second cycle, the sample was heated up to 300 °C as before and the absence of the exothermic peak characteristic of the chemical reaction (cross-linking), suggested that the reaction had mostly occurred already at 190°C.

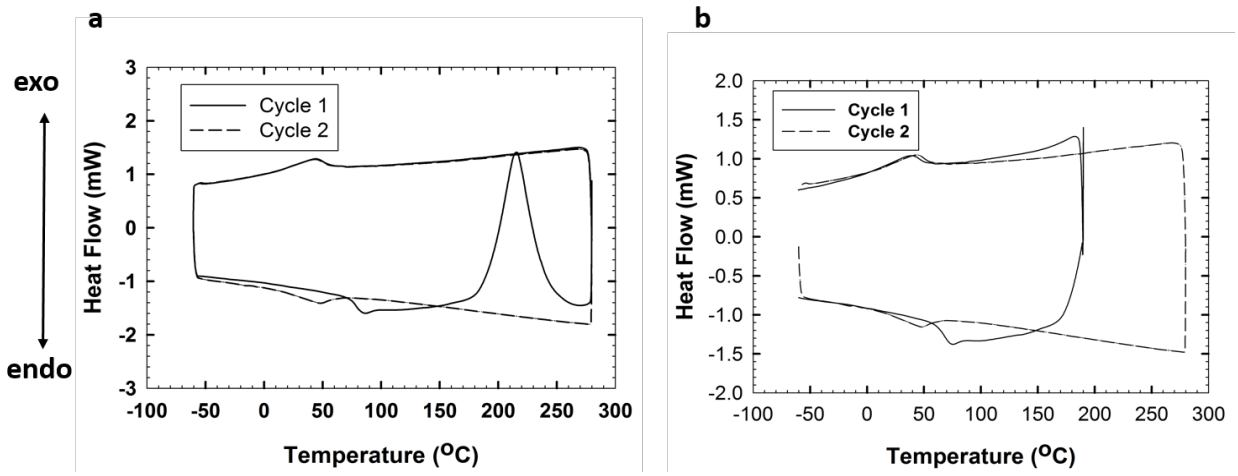

Figure 6.4 DSC measurement to observe a) cross-linking reaction of PCBCB-I b) controlled heating of PCBCB-I at 190 °C for 10 min.

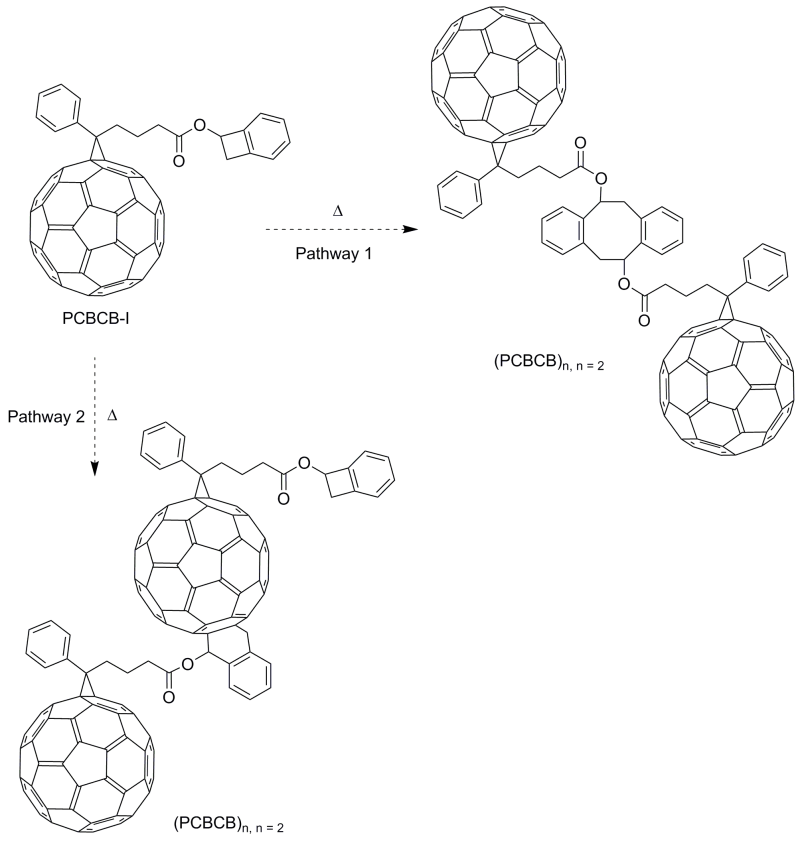

Figure 6.5 Possible pathways for cross-linking of PCBCB-I.

The thermal cross-linking of PCBCB-1 is anticipated to occur through two possible pathways (Figure 6.5). One is based on the formation of quinodimethane intermediate and subsequently coupling to yield fullerene dimer.[199] Also, cycloaddition of quinodimethane intermediate with fullerenes has been observed in the literature as shown in pathway 2.[203]

6.1.3 Mass Spectrometry Results

MALDI measurements were carried out in the negative ion mode on an ABI QSTAR-XL of hybrid Q-TOF machine by David Bostwick at the Bioanalytical and mass spectrometry core facility, Georgia institute of technology. The precursor, PCBCB-I was obtained was clearly isolated and the visible peak was seen at 999.14 m/z (Figure 6.6a). The cross-linked fullerene was obtained by drop casting a film made from the (5mg/ml) solution of PCBCB-I in DCM and then annealing it at 190 °C for 10 mins (as was the standard procedure chosen later for carrying out all the cross-linking reactions). In addition to the peaks previously visible, an additional peak is obtained at 1998.4 m/z, representative of the dimer peak (Figure 6.6b). Absence of other higher molecular weight peaks suggested that formation of other oligomers were unlikely though could possibly be present if they were not as ionizable as the monomeric and dimeric species.

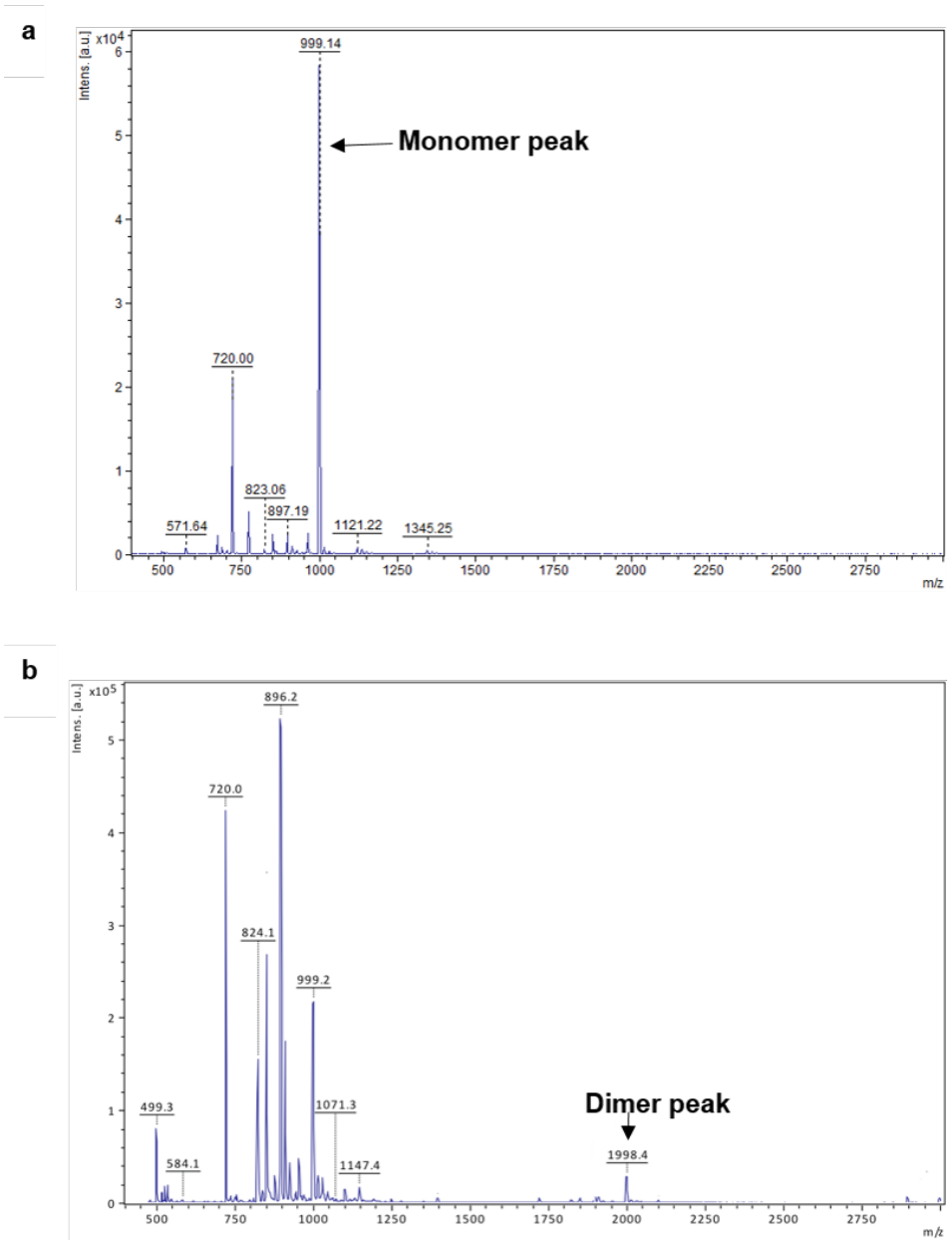

Figure 6.6 MALDI spectrum showing a) PCBCB-I (m/z 999.14) from precursor and b) $(PCBCB)_n$ (m/z 1998.4) from thermo-cross-linked film, along with other fragments of the products.

6.2 OPTICAL STUDIES OF PCBCB-I PRECURSOR

6.2.1 UV-Vis spectra analysis

Absorption spectra of the cross-linked fullerene and PCBM in thin films were measured, before and after annealing at different temperatures (150, 190 and 230 °C) for 10 mins. While PCBM showed no significant changes post annealing (Figure 6.7b), PCBCB-I showed a distinct reduction in the peak intensity at 360 nm, indicative of a change in the packing of the system beginning as low at 150 °C (possibly associated with onset of the cross-linking reaction as indicated by the DSC measurements, Table 6.1). Subsequent annealing of the PCBCB-I at higher temperatures did not make significant changes to the UV behavior beyond those observed at 190°C, (see Figure 6.7a), suggesting that all or the majority of the changes in the structure had already occurred at 190 °C and cross-linking percentage estimated to be close to 100% (see Section 6.3.1). Thus this was the temperature used subsequently for carrying out the cross-linking in thin films.

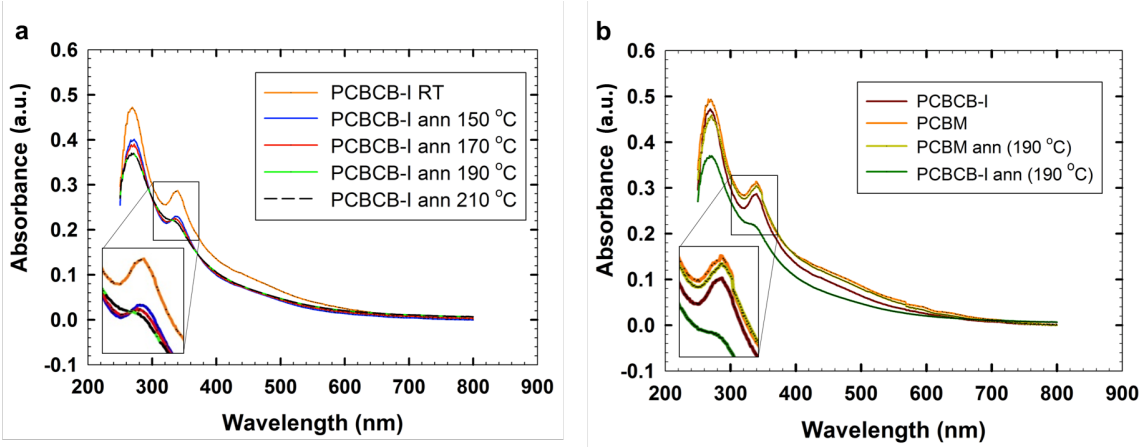

Figure 6.7 UV-Vis absorption spectra of, a) PCBCB-I annealed at different temperatures b) pre- and post-annealed PCBCB-I and PCBM (insets show the zoomed in areas inside the box).

6.2.2 Cyclic Voltammetry measurements

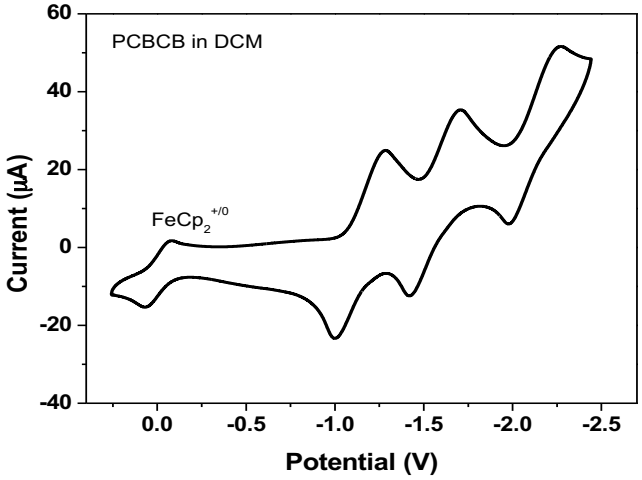

Figure 6.8 Cyclic voltammogram of PCBCB in CH_2Cl_2.

Cyclic voltammetry (CV) measurements were performed using an EG&G Princeton Applied Research model 273A potentiostat-galvanostat. The electrochemical cell was setup using a Ag/Ag+ electrode as the reference, a platinum flag or coil as the counter electrode, and a 0.1 M solution of tetra *n*butylammonium hexafluophosphate (TBAPF6) in acetonitrile was used as the electrolyte. The working electrode consisted of a thin film of PCBCB-I drop-casted from a 1 mg/mL DCM solution onto a platinum disk electrode (0.02 cm2). The calibration was done by measuring the oxidation potential of the ferrocene/ferrocenium (Fc/Fc+) couple dissolved in the electrolyte solution versus the Ag/Ag+ reference. The scans gave us a reduction potential at -1.14 V for the PCBCB-I precursor material (Figure 6.8). It was thus seen to be comparable to the reduction potential of the PCBM which was found to be at -1.11 V and one would thus expect the precursor to have a similar LUMO energy level. CV measurement however couldn't be carried out on the final cross-linked product due to its insolubility in most organic solvents. It would however not be expected to change much since the cross-linking reaction is only affecting the side chain in

the cross-linking reaction. However, in the event that the cross-linking is directly affecting the fullerene ring, there would be a modification in the frontier energy levels thus leading to a change in the CV.

6.3 OPTICAL STUDIES OF PCBCB-II

6.3.1 UV-Vis spectra analysis

To determine the degree of cross-linking of the PCBCB-I precursor on annealing, UV-Vis spectra analysis was used. A calibration plot of the precursor was first determined using absorption measurements of solutions of different concentration (0.02, 0.01, 0.001 mg/ml) in DCM (Figure 6.9a). Subsequently, drop cast films from the PCBCB-I precursor (1mg) in DCM (1 ml) were deposited on glass substrates and annealed for varying amounts of time. The films were subsequently washed with 1 ml of DCM each and sonicated to dissolve the non-cross-linked part of the film. These 1 ml solutions were twice diluted to 10 times their volume to bring the concentration within the range of the calibration value. The absorption spectra for those were then obtained (Figure 6.9b) and the intensity of the characteristic peak at λ_{max}=330 nm was obtained. The calibration plot was then used to determine the remaining concentration of the precursor in the annealed films (by measuring the intensity of the characteristic peaks in the solutions). This in turn determined the percentage conversion into the cross-linked product $(PCBCB)_n$ (Figure 6.9c, Table 6.1). Annealing at 120 C for 10 minutes (not shown here), all of the film was washed off leaving behind no insoluble cross-linked product. On the other end though, it could be seen that beyond annealing at 190 C for 10 min, the percentage conversion increased minimally, suggesting that possibly the full conversion had taken place. The amount of conversion however was still not exactly 100%, which could possibly have arisen due to the fact that the film wasn't smooth and

continuous everywhere, leading to areas where it was impossible for the precursor to encounter another molecule, and thus leaving behind some unreacted precursor. In addition, by varying the annealing temperature the percentage conversion to the cross-linked fullerene could be varied, giving us a mechanism to control the degree of cross-linking in the fullerene. The increase isn't linear with temperature either so further studies can be carried out to fine-tune the thermal processing control of cross-linking.

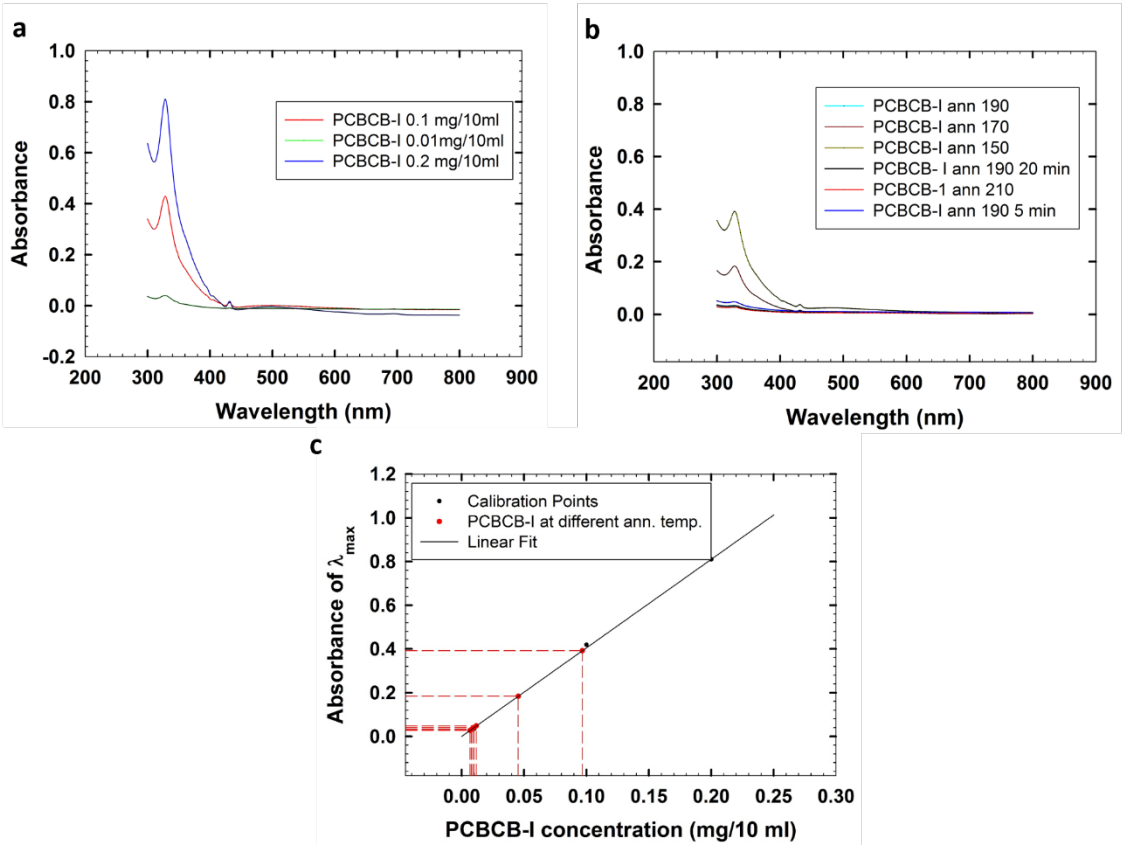

Figure 6.9 Absorption spectra of a) varying concentrations of PCBCB-I in DCM b) residual precursor from annealed samples of PCBCB-I at different temperatures (time =10 min unless otherwise mentioned) c) Calculation of percentage cross-link conversion of PCBCB-I to $(PCBCB)_n$ using a calibration plot

Table 6.1 Percentage conversion of PCBCB-I at different annealing temperatures.

Sample	% conversion
Annealed 150 °C 10 min	52.69
Annealed 170 °C 10 min	95.46
Annealed 190 °C 10 min	99.11
Annealed 210 °C 10 min	99.33
Annealed 190 °C 5 min	98.83
Annealed 190 °C 20 min	99.21

6.3.2 Fullerene-polymer diffusion behavior

An important part of controlling the morphology of BHJ systems is control of the diffusion of the fullerene through the polymer. Thus diffusion behavior of the $(PCBCB)_n$ fullerene into P3HT was compared to that of PCBM. Upon preparing bilayers of the fullerenes and P3HT (see experimental) the sulfur content through the BHJ film thickness was determined using XPS measurements at various depths into the film as a function of the annealing time. The various depths were accessed by etching the film with an Ar gun for varying lengths of time. The samples were measured as unannealed bilayers and also after annealing for different amounts of time at 150 $^{\circ}$C. In the pristine samples the two-layer structure is defined by a sharp but finite interface between the P3HT upper layer and the underlying fullerene. Diffusion of the fullerene through the polymer is characterized by loss of the initial interface to give a uniform distribution of the S through the film thickness (Figure 6.10).). In a 1:1 ratio of the P3HT: fullerene the calculated S content in a homogeneous blend would be 4 (atomic) %, a value which both films prepared

with PCBM and $(PCBCB)_n$ obtained after sufficient annealing times. PCBM has been known to diffuse quickly through the amorphous regions and the grain boundaries of P3HT upon various annealing conditions.[83, 85, 204] Thus in the PCBM system (Figure 6.10a), a homogeneous film composition was observed very quickly within 1 minute of annealing at 150 °C, which is consistent with previously reported studies.[85] By comparison, the $(PCBCB)_n$ (Figure 6.10b), shows negligible diffusion into P3HT for the first 15 minutes of annealing, although a homogeneous composition occurs at some time between 15 and 30 minutes annealing. This clearly shows that the diffusion rate of the $(PCBCB)_n$ that is at least an order of magnitude slower than PCBM.

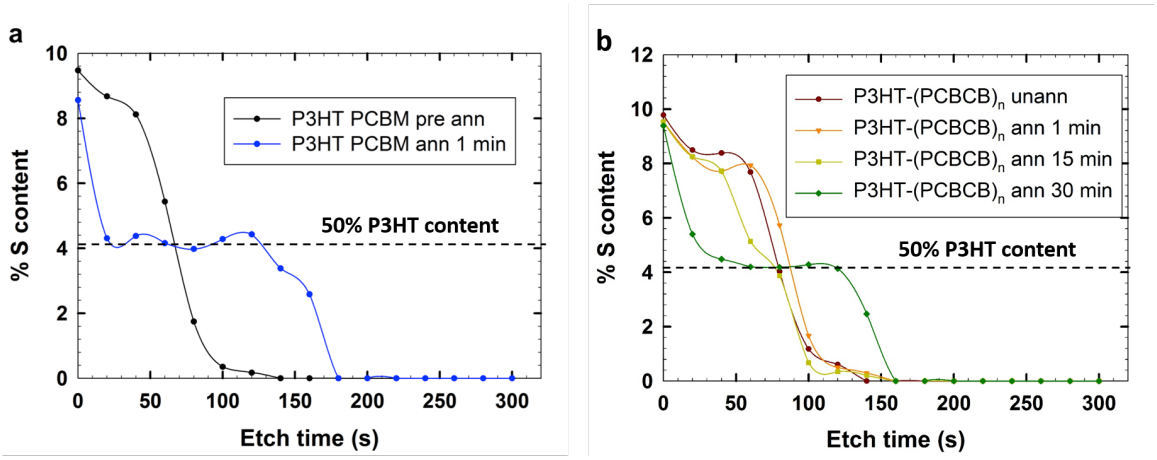

Figure 6.10 Percentage S content through as a function of etch time, annealing at 150 °C for different amounts of time for (a) P3HT-PCBM bilayer and (b) P3HT-$(PCBCB)_n$ bilayer.

6.4 DEVICE CHARACTERIZATION AND LONG TERM THERMAL STABILITY OF BHJS

To fully characterize the electronic behavior of the cross-linked fullerene based bulk heterojunctions, the electron mobility and device efficiencies were obtained and compared to

regulation PCBM based devices. As discussed previously, the effect of cross-linking on the long term stability of the devices was also subsequently studied and possible explanations were derived using GIWAXS and optical microscopy measurements.

6.4.1 Electron Mobility using Space Charge Limiting Current Devices

The electron mobility values of the fullerenes were determined from space charge limited current (SCLC) measurements (see Figure 6.11, results in Table 6.2). These measurements showed that compared to PCBM the PCBCB-I precursor has a slightly lower, but comparable electron mobility values. The electron mobility value for PCBCB-I though does increases significantly upon the cross-linking reaction once the $(PCBCB)_n$ is formed. To get a better understanding and possible explanation of this enhancement, GIWAXS measurements to determine the crystal structures were carried out and are discussed later (see Section 3.4.3).

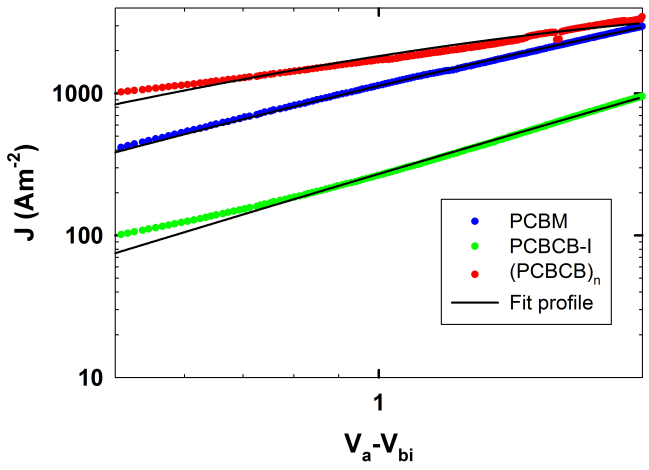

Figure 6.11 Electron mobility (SCLC) measurements and fits for PCBM, PCBCB-I and $(PCBCB)_n$.

Table 6.2 Electron mobility values (SCLC) for the different fullerenes (thickness - 210nm).

Material	μ (cm^2/Vs)
PCBM	$9.1\pm1.0 \times 10^{-4}$
PCBCB-I	$1.3\pm0.3 \times 10^{-4}$
$(PCBCB)_n$	$5.9\pm1.8 \times 10^{-3}$

6.4.2 BHJ Device Efficiencies and Thermal Stability Measurements

Given the acceptable values of electron mobility and similar LUMO energy levels for the PCBM and $(PCBCB)_n$, BHJ devices were made with these materials as acceptors. The devices were annealed for 10 minutes each at 190 ºC to allow for the cross-linking of PCBCB-I to occur following the spin coating of the active layer and before the aluminum electrode deposition. No observable change in morphology was seen through AFM imaging before and after annealing (see Appendix). In addition, the PCBM and $(PCBCB)_n$ based devices showed comparable efficiencies as made, with the cross-linked fullerene showing only a slightly reduced initial efficiency.

These devices were subsequently annealed at 150 ºC for increasing periods of time (up to 48 hours or 2880 minutes) and the device efficiencies measured at regular intervals. It was observed that the P3HT-PCBM based samples degrade substantially within 1 hour of annealing, and very quickly thereafter show only 40% their initial efficiency, as seen previously in a number of other studies (Figure 6.12).[79, 132, 179, 205] By comparison, the devices where the acceptor was a 1:1 ratio PCBM: $(PCBCB)_n$ blend or pure $(PCBCB)_n$ initially showed a slight increase and then a stable value of the device efficiency. More importantly neither of the devices containing $(PCBCB)_n$ showed any effective degradation in the device efficiency (compared to its initial device efficiency) even when annealed for up to 48 hours at elevated temperatures.

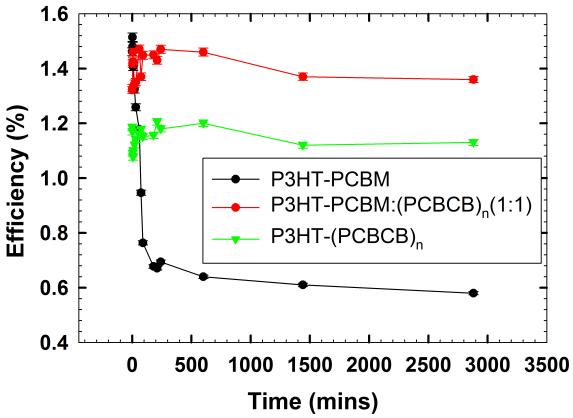

Figure 6.12 Device efficiency as function of annealing time for P3HT-fullerene BHJs where the fullerenes are PCBM (black), 1:1 PCBM: $(PCBCB)_n$ blend (red) and $(PCBCB)_n$ (green)

6.4.3 Fullerene crystal and aggregation growth

2-D GIWAXS patterns and subsequent integration plots of PCBCB-I and $(PCBCB)_n$ showed an increase in the crystalline behavior upon formation of the cross-linked fullerene from the precursor, with the peak widths becoming visibly narrower (Figure 6.13c, Table 6.3 showing the full-width half max of the characteristic peak at q= 1.41 A^{-1}). Peak fitting consequently also gave us the value of the spacing between the fullerene groups, which for the cross-linked system was reduced, but minimally so. Thus even though some sign of increasing crystallinity is seen upon cross-linking from the GIWAXS measurement, it can't be said be said with surety that it is the dominating cause for the increase in electron mobility observed in Section 6.4.1.

To study the effect of temperature on fullerene crystallization, GIWAXS measurements were carried out on the thin films of PCBM and $(PCBCB)_n$ annealed for different amounts of time. 2-D images of the fullerenes showed differences before and after annealing (Figure 6.13). In the case of PCBM, upon post annealing, distinct crystalline peaks of the fullerenes from possible re-crystallization and subsequent large-scale aggregation, had replaced the initial amorphous halos.

In contrast, the GIWAXS image for the annealed $(PCBCB)_n$ films did not show a significant change in the crystalline behavior suggesting a tendency not to re-crystallize even after prolonged annealing at elevated temperatures (150 $^{\circ}$C, Figure 6.13).

The crystallization kinetics were measured using optical microscopy (see Section 2.8.5) and the BHJs with fullerenes in different ratios (pure PCBM, PCBM: $(PCBCB)_n$ in 1:1 ratio and pure $(PCBCB)_n$) were compared. During annealing of the P3HT-PCBM sample, formation of a large number of macroscopic-sized crystallites is observed (Figure 6.14). These crystals are believed to be aggregates of fullerene as described before in literature and indicated by the GIWAXS results of the prolonged annealed PCBM thin films (Figure 6.13b).[68] This aggregation behavior and large-scale crystallization of fullerenes has been shown to lead to the breakdown of the polymer-fullerene based BHJ device efficiency under high temperature over time, and explains the loss in device efficiency in this system.[79, 120, 206] When the PCBM is partly or completely replaced by $(PCBCB)_n$ as the acceptor the number density of fullerene crystallites formed was observed to decrease with increasing amount of $(PCBCB)_n$ in the system (Figure 6.15a). This suggests that the $(PCBCB)_n$ actively inhibits the aggregation and crystallization of the PCBM molecules. This is assisted by the order of magnitude lower diffusion rate of $(PCBCB)_n$ in the P3HT compared to the PCBM. This diffusion rate inhibits rapid mobility and hence reduces aggregation of the fullerenes in the system leading to higher lifetimes of the devices even under elevated temperatures.

Simultaneously, by analyzing the crystallite size as a function of annealing time (Figure 6.15b) and fitting using the Avrami equation (Equation 6.1) the fullerene crystallization growth rate in the active layers were obtained. The Avrami equation takes the form:

$$\alpha(t) = 1 - \exp\left[-(kt)^n\right] \qquad [6.1]$$

Where α(t) is the volume (or in our case area of the crystal at time t), k is the rate constant and n is the Avrami exponent. By measuring the change in crystal dimension over a period of time (minimum 3 data points), the data can be fitted to the curve mentioned in equation 6.1 to give us the two variables, k and n (Table 6.4).

Since pure $(PCBCB)_n$ based devices barely showed any visible aggregation (as also observed in the GIWAXS measurements) Avrami analysis was not possible in this case. However, the calculated Avrami exponents in the systems containing pure PCBM, PCBM: $(PCBCB)_n$ (3:1) and (1:1) showed values close to 2 suggesting a 2-dimensional growth (Table 6.4). At the same time the rate constant calculated for the crystal growth was, as anticipated, significantly lower when the cross-linked fullerene was introduced as an acceptor, compared to pure PCBM, consistent with our hypothesis that introduction of a cross-linked fullerene is inhibiting the rate of growth of the PCBM crystals. In addition, significant reduction in the rate occurred with addition of just 25% $(PCBCB)_n$ suggesting a minimal amount of the cross-linkable fullerene could eventually be calculated and added to PCBM to hinder the aggregation. Thus the reduction in crystal growth and aggregation arises from the introduction of the $(PCBCB)_n$ as a slow diffusing aggregation inhibiting agent.

Table 6.3 Full width half max (FWHM) values and d-spacing for the characteristic peaks from GIWAXS analysis.

Sample	**FWHM(A^{-1})**	**d-spacing (A)**
PCBM	0.28	4.56
PCBCB-I	0.35	4.52
$(PCBCB)_n$	0.26	4.51

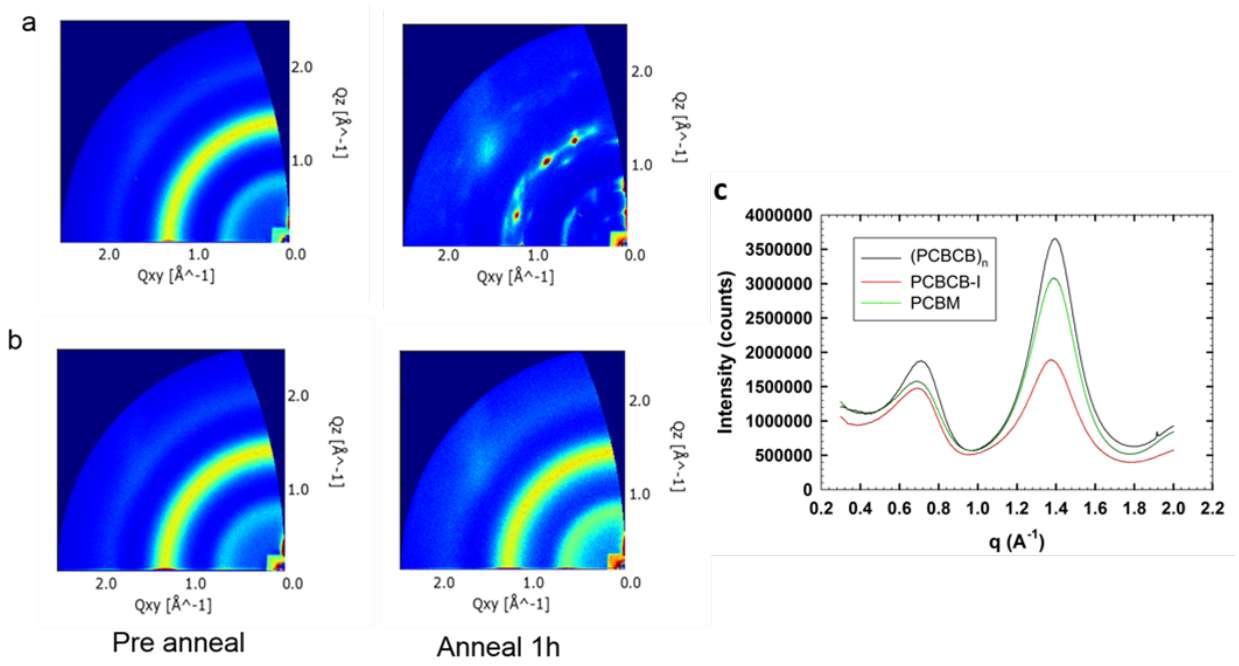

Figure 6.13 GIWAXS patterns for thin films of a) PCBM and b) $(PCBCB)_n$ before and after one hour of annealing at 150 ºC c) 2-d integration plots (I vs q) for the fullerenes PCBM, PCBCB-I, $(PCBCB)_n$.

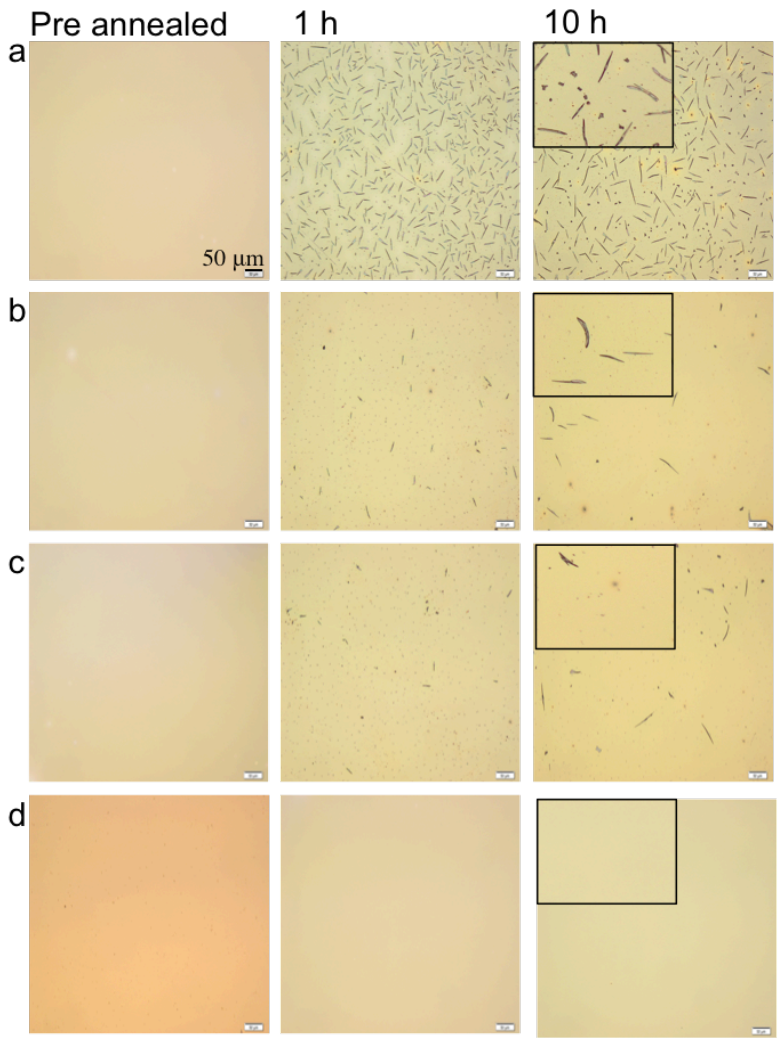

Figure 6.14 Optical microscopy images of P3HT-Fullerene thin films, before and after annealing at 150 ^{o}C for 1 h, 10 h a) P3HT-PCBM b)P3HT-$(PCBCB)_n$:PCBM (1:3) c) P3HT-$(PCBCB)_n$:PCBM (1:1) d) P3HT-$(PCBCB)_n$ (insets of the images at 10 hrs show zoom of a part of the image).

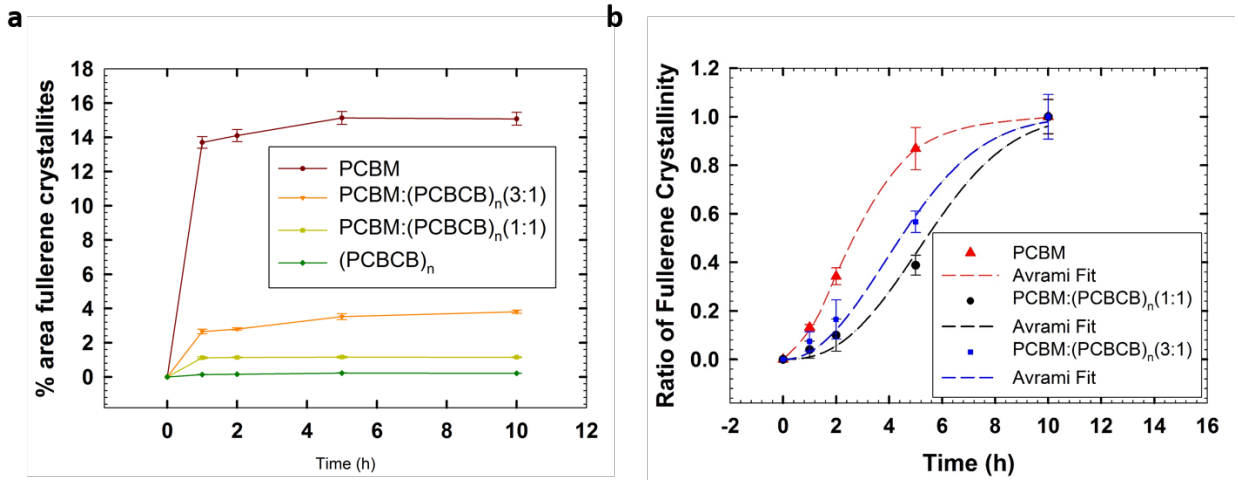

Figure 6.15 Relative area of fullerene crystallites in BHJs with time, annealed at 150 °C b) Avrami Fits for fullerene crystallization rates in BHJs.

Table 6.4 Avrami exponent and Rate constants from Avrami Fits.

Sample	Avrami Exponent	Rate Constant
P3HT-PCBM	1.89	0.31
P3HT-(PCBM: $(PCBCB)_n$) (3:1)	2.01	0.19
P3HT-(PCBM: $(PCBCB)_n$) (1:1)	2.11	0.16

6.5 SUMMARY – EFFECT OF FULLERENE CROSS-LINKING OF OPV DEVICE MORPHOLOGY AND PERFORMANCE

A new type of thermal cross-linking PCBM based molecule was synthesized, which was thermally cross-linked in-situ to obtain a fullerene derivative with electron mobility comparable to the original PCBM. Systematic studies on the effect of annealing time on the diffusion behavior

showed a decreased diffusion of the fullerene through the polymer after cross-linking. The effect of the annealing temperature and time on degree of cross-linking was measured using UV-vis absorption spectra, and could potentially be studied further in future studies. The use of these cross-linked fullerenes in bulk heterojunction based OPVs show comparable device efficiencies as well as a significant improvement in the device lifetime on being subjected to simulate high temperature annealing conditions. This behavior has been attributed to the reduction in the diffusion, physical mobility and aggregation of this new fullerene in the devices. This could pave way for similar fullerene based oligomeric acceptors to be synthesized in the future with other BCB based cross-linker groups. Future studies could look at cross-linking these fullerenes at even lower temperatures as well as conducting further in-depth studies on effect of processing conditions on the BHJ devices made with these materials.

7 OVERALL CONCLUSIONS

7.1 MORPHOLOGICAL STUDIES IN AMORPHOUS POLYMER-FULLERENE BLENDS

The interaction between PCBM and the aromatic side chains was shown to affect its miscibility with greater number of interactions allowing the PCBM to be more soluble in polymers with higher aromaticity (miscibility in P9VPh>P2VN>PS). This in turn drove the phase morphology of the system, with a shape independent two phase DAB model used to describe the phase composition and correlation lengths. The two phases in the system are believed to comprise of regions of differing concentration of fullerene thus causing fluctuations in the scattering pattern from the sample. The correlation lengths obtained are shown to be greatest in the least miscible PS system as one would expect. In addition, at a concentration of PCBM beyond the miscibility limit, the DAB model shows a sudden increase in pre-factor which is commensurate with formation of regions with differing SLDs, i.e. phase separation.

In addition to the DAB model, a mass fractal model was also fitted to the scattering profile, which provided us additional useful information regarding the surfaces of these phases, suggesting that they are more like rough surfaces with fractal dimension of 3. The other information regarding the phase in this case was however believed to be less reliable due to assumption of the size of the fractal (fullerene molecule) needed for the model. In the event of a small change in the radius, the fits could give us extremely different answers for the correlation lengths.

Previous studies have looked at interaction of C_{60} fullerenes in amorphous polymers, and concluded that the increased miscibility was associated with increased interactions of aromatic chains with the C_{60} ring.[174] We however believe that the interaction of the phenyl group on the

PCBM side chain with the aromatic side chains of the polymer contribute to it being even more miscible than C_{60}. In addition, the PCBM follows the same trend as C_{60} in terms of the miscibility with increasing aromatic side chains on the polymer. Further simulations on these systems could definitely help confirm the exact nature of interaction between the small molecule and polymer and explanation for the trend in miscibility and phase development.

7.2 MORPHOLOGICAL STUDIES IN POLYALKYLTHIOPHENE-FULLERENE BHJS

While interactions in the amorphous polymers fullerene blends were mainly with the side chain, in the case of polyalkylthiophene fullerene blends, it is believed to be mainly with the backbone with both the fullerene cage and its ligand interacting with the backbone to give its lowest energy conformation.[207] It can thus explain the values of binding energy we obtained for the different side-chain polymer and fullerene combinations, with the shortest polymer side chain (P3BT) allowing the greatest interaction of the fullerene with its backbone. Consequently, we expect the miscibility values of the fullerenes in the polymers to follow the same trend. However, polyalkylthiophenes are, as many other semiconducting polymers, semicrystalline in nature. Thus the dependence of the phase morphology goes beyond the effect of molecular interactions and miscibility. The amount of polymer crystalline content also comes into play and the phase behavior of such blends have been known to show eutectic like behavior.[56, 58]

Keeping this in mind, the wide angle and small angle scattering data, in combination give us detailed information about the morphology of these systems. The WAXS measurement shows that while polymers crystallize quite well even in bulk, the crystallization of the fullerene is only visible in the case of C_{60}. Since the fullerenes are believed to be miscible in the amorphous part of

these polymers,[60] appearance of their crystalline peaks suggest phase segregation and immiscibility. This in turn would make C_{60} the least soluble fullerene in the polymers, later confirmed by the DFT calculations on these system. In terms of the polymer crystal domain, while P3BT had the largest percentage crystallinity among the different polymers due to its ease in packing, the P3OT had the larger domain sizes owing to the longer side chains assisting in the lamellar stacking as seen previously in other studies with OFETs.[196] SANS measurements on the other hand showed that the phase behavior in mixtures of semicrystalline polymer-fullerene blends were more complex than the previously studied amorphous polymer-fullerene blends. Several individual two-phase models were initially used to fit the scattering profiles for these systems but were not found to be satisfactory. However with the knowledge that a significant amount of fullerene is miscible in the amorphous part of the fullerene polymer, a combined model was used. The two phase shape independent DAB model was combined with the hard sphere model to give an accurate representation of the phase morphology having 3 phases in total. These included a crystalline polymer phase, a mixed amorphous phase with minimal fullerene mixed in amorphous polymer, and a phase segregated pure fullerene phase. The amorphous regions of the polymer with fullerene miscible in it were modeled by the DAB model, whereas the immiscible part of the fullerene can be fitted using a hard sphere model. The size and volume fraction of the hard spheres in turn were dominated by the miscibility limits of the fullerene in the polymer. C_{60} having the least miscibility showed the greatest volume fraction of hard spheres. The correlation lengths of the amorphous part of the polymers in turn showed the reverse trend. Larger amounts of miscible fullerene tended to increase the size of the corresponding amorphous regime and so P3OT based blends had the largest mixed amorphous domains.

Both the wide and small angle scattering analysis of the bulk films provided a good estimate of the morphology we expected in our final BHJ thin films. However, for an accurate representation of a device, the thin film behavior of BHJ blends needed to be analyzed, complete with the electrode interfaces.

The fourth Chapter then showed the effect of interfacial energy, thermal annealing and length of the alkyl side chain on the diffusion of various fullerenes in different polyalkylthiophene based BHJ devices. The amount of fullerene diffusion to the electrode/active layer interface was seen to be driven by contributions from surface energy differences, miscibility and amorphous content of the polymer. Not all contributions were found to have the same effect for the different fullerenes. It was seen that bis-PCBM diffuses the most towards the top aluminum electrode, but in other films, the greatest amount of C_{60} was found at the lower PEDOT: PSS electrode. The segregated amount of these fullerenes showed good correlations with the short circuit current and fill factor of devices made with these mixtures. While greater fullerene segregation at the aluminum electrode served as an electron transport layer and improved the J_{sc}, at the opposing electrode interface fullerene acts as a hole blocking layer and this is manifested in negative correlation between segregated fullerene and the fill factor.

To derive information regarding the in-plane phase behavior, the scattering measurement in thin films had to be conducted in grazing incident geometry. These measurements also showed the effect of interfacial surface energy as well as kinetic factors (effect of spin coating parameters) being dominant in driving the morphological structure. The overall blend and polymer crystallinity in the systems were seen to be significantly lower owing to the lower time scale for solvent evaporation in spin coating. In addition, time-of-flight grazing incidence scattering was used to study the in-plane phase morphology at three different effect depths. This showed that phase

morphology varied with the depth as expected from our phase segregation studies in Chapter 4. While a three phase morphology is present near the top electrode (Zone 1) owing to fullerene enrichment, the bulk region (Zone 2) has mostly an amorphous mixture of polymer and a reduced amount of fullerene owing to depletion of fullerene. In the region near the bottom-most interface with the PEDOT PSS, a simple two phase system is observed, however in this case with fullerene enrichment similar to the top layer of the film.

The NR studies combined with the GIWAXS and GISANS measurements thus allowed us to derive an overall morphological structure within bulk heterojunctions, with specific details regarding all the phases present, their length scales and composition. Future experiments to provide additional information to this morphological model might be achieved by obtaining higher quality grazing incidence scattering data of the near PEDOT PSS surface, given the current model is based on certain assumptions. This could be achieved by measuring the GISANS and GIWAXS patterns from the bottom surface by floating the active layer from the substrate onto water and then flipping it over onto another substrate. The bottom interface, now exposed can be studied in further detail and help confirm our hypothesis for the phase behavior in that region.

7.3 THERMO-CROSS-LINKABLE FULLERENE

Chapters 4 and 5 showed the effect of fullerene diffusion and segregation on the morphology and eventual device performance. With this in mind, a strategy for limiting the diffusion by cross-linking a fullerene in-situ was developed, thereby imparting slower diffusion of the fullerenes within the BHJ layers. The fullerene synthesized in this work was based on a PCBM molecule, modified with the cross-linker molecule BCB-OH. Thermal annealing tests confirmed the occurrence of a cross-linking reaction starting at 150 °C and was confirmed through mass

spectroscopy. While the exact nature of the cross-linking could not be elucidated, partly due to the insolubility of the cross-linked fullerene, characterization showed that there was only evidence of the dimer in the mass spectroscopy. The diffusion behavior of these cross-linked fullerenes showed a rate of diffusion decrease by an order of magnitude compared to PCBM, whilst the electronic properties (electron mobility) were still comparable to PCBM. In addition, these cross-linked fullerenes greatly improve the lifetime of BHJ OPVs, with no visible degradation at elevated temperatures even after 48 hours of annealing. While these desirable properties were attributed to a propensity of the dimers not to aggregate, optical microscopy showed that they also had the capability to hinder the PCBM aggregation and crystallization when used in a mixture with it. At the present time the mechanism of enhancing BHJ device stability is not fully understood and further research is required in order to be to design other more efficient acceptor molecules as well. Whilst some of the effects of cross-linking fullerenes have been studied in this thesis with potentially useful application including improvement the long-term stability, future systematic studies with similar or higher oligomeric fullerene systems could fully expose the potential of these systems. In addition, the insolubility of cross-linked fullerenes would allow the use of these compounds as templates for designing new architectures from BHJ devices and doing controlled studies on them.

Chapters in these thesis have served as major parts of work submitted for publications in the following research journals:

- Gabriel Bernardo, Nabankur Deb, Stephen M. King, David G. Bucknall, Phase behavior of blends of PCBM with amorphous polymers with different aromaticity, 2015*, Manuscript submitted for publication to the Journal of Polymer Science B:Polymer Physics* – Based on Chapter 3

- Nabankur Deb, Bohao Li, Maximilian Skoda, Sarah Rogers, Yan Sun, Xiong Gong, Alamgir Karim, Bobby Sumpter and David G Bucknall, Phase Morphology correlations in model bulk heterojunction based thin film devices, 2015*, Manuscript submitted for publication to Advance Functional Materials* – Based on Chapter 4 and 5
- Nabankur Deb, Raghunath R. Dasari, Karttikay Moudgill, Jeffrey L. Hernandez, Seth R. Marder, Alamgir Karim and David G. Bucknall, Thermo-cross-linkable fullerene for long-term stability of photovoltaic devices, 2015, *Manuscript submitted for publication to Energy and Environmental Science* – Based on Chapter 6
- Bernardo, G., N. Deb, P. Pereira, L. Brandão, J. Viana and D. Bucknall (2014). "Solid-state low-temperature extrusion of P3HT ribbons." Applied Physics A: 117:2079-2086 - Work shown in Appendix
- Rodrigues, A., N. Deb, L. Hilliou, J. Viana, D. G. Bucknall and G. Bernardo (2013). "Low temperature solid state processing of pure P3HT fibers." AIP Advances 3(5), 052116 – Work shown in Appendix

APPENDIX A

Crystal Morphology of NDI based small molecules using WAXS

a

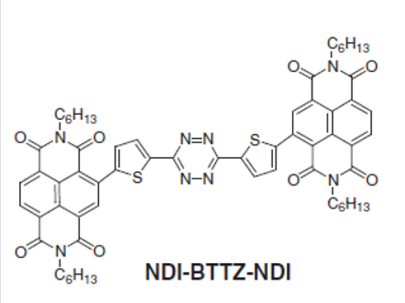

b

Substrate	Deposition	Solvent[b)]	Electrode (S/D)	μ ($cm^2 V^{-1} s^{-1}$)[d)]	V_T (V)[e)]	I_{on}/I_{off}[f)]
Glass	Spin-coating	TCE	Au	5.3 (±2.1) × 10^{-3} (7.4 × 10^{-3})	8.2 ± 0.3	10^3
Glass	Spin-coating	DCB	Au	0.13 ± 0.01 (0.15)	4.9 ± 0.4	10^4

Figure 1. a) Structure of NDI-BTTZ-NDI b) comparison of OFET parameters for devices built from different solvents (reproduced from reference[208])

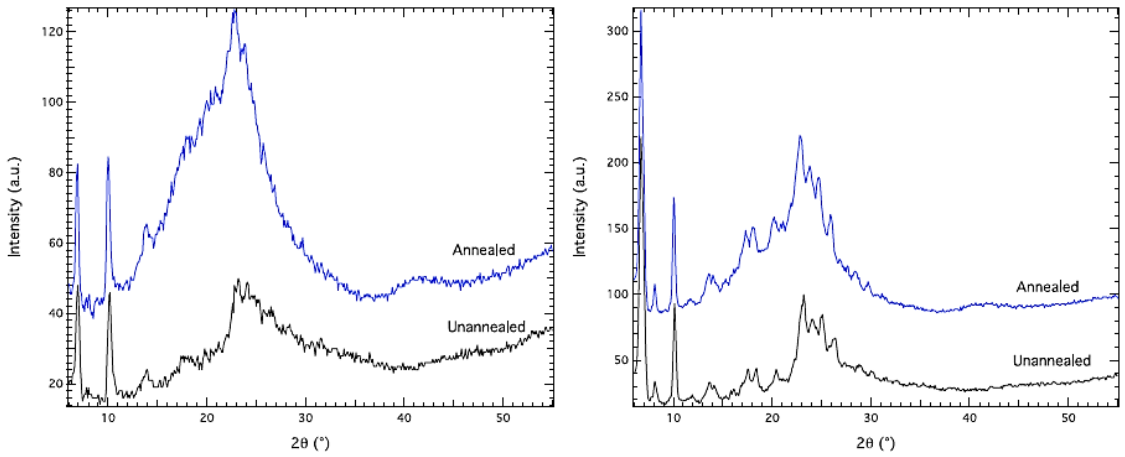

Figure 2. Wide angle X-ray scattering patterns of NDI-BTTZ-NDI thin-films prepared by spin-coating of TCE (left) and o-DCB (right) solutions onto a quartz glass substrate before/after annealing at 120 °C for 10 minutes (reproduced from reference[208]).

As part of this project, a new solution-processable small-molecule containing electron-poor naphthalene diimide and tetrazine moieties was synthesized by Dr. D. K. Hwang and Dr. Raghunath R. Dasari, Department of Chemistry, Georgia Institute of Technology. The compound synthesized was the (thienyl)tetrazine-bridged naphthalene diimide, NDI-BTTZ-NDI (Figure 1a) Optimized spin- coated OFETs based on the NDI-BTTZ-NDI molecules processed from o-DCB showed electron mobility values up to 0.15 cm^2/Vs . Inkjet-printed OFETs have also been fabricated in ambient atmosphere on flexible plastic substrates, and exhibit mobility values up to 0.17 cm^2/Vs (Fig 1 b)

Wide-angle X-ray scattering (WAXS) measurements were carried out to further investigate differences in crystallinity of films processed from TCE and o-DCB. The scattering patterns (Fig 2 a and b) indicated the film processed from o-DCB was more crystalline than that processed from TCE, the scattering pattern of which indicated the presence of a significant portion of amorphous material. Upon peak fitting, the sample made from o-DCB seemed to have up to 60% crystallinity, while the toluene had ~ 20%

Furthermore, the distinct electrical properties of OFETs processed from DCB and TCE are also correlated with the WAXS results, the higher electron mobility values being observed in the more crystalline films which were made from o-DCB (Fig 1b and Fig 2)

Crystal orientation in low temperature extrusion of P3HT fibers

A simple new approach for producing pure P3HT fibers without the use of solvents and at temperatures well below the polymer's melting temperature was developed by Alexandre Rodrigues, Institute for Polymers and Composites/I3N, University of Minho. The setup was as shown in Figure 3. The solid extrusion of poly3hexylthiophene through this setup was studied as a function of the processing temperature.

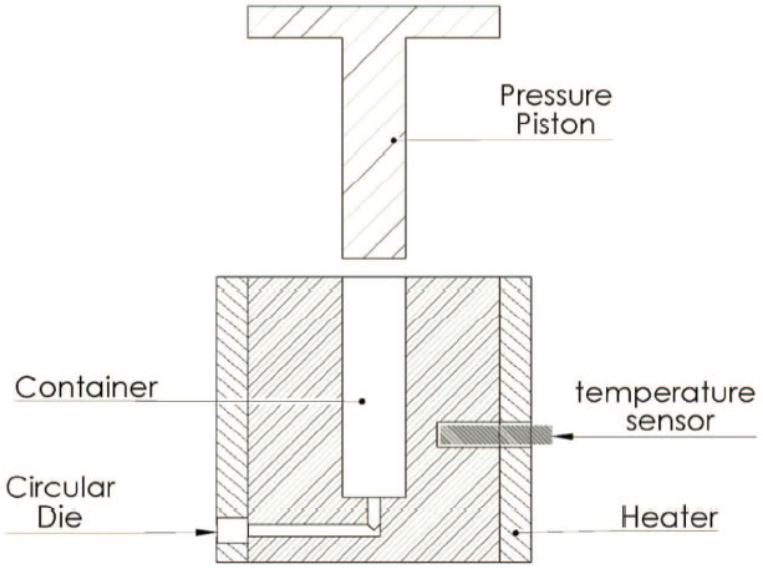

Figure 3. Setup for low temperature extrusion of P3HT fibers (reproduced from reference[209])

WAXS measurements were carried out on the extruded P3HT fibers to obtained information about the crystalline orientation induced in them as a function of the processing temperature. Subsequently azimuthal scans of the 2D WAXS patterns were obtained and the Herman's orientation factors were calculated (Figure 4). The orientation was seen to be maximum at 150 °C processing temperature where it is believed to have a balance between the least amount of wall slip and enough chain mobility (due to high temperature) to cause chain reorientation. The

percentage crystallinity in this case was also found to be comparable to previously made solution cast P3HT samples, thus making it a good alternative for a solution free process of generating P3HT fibers.

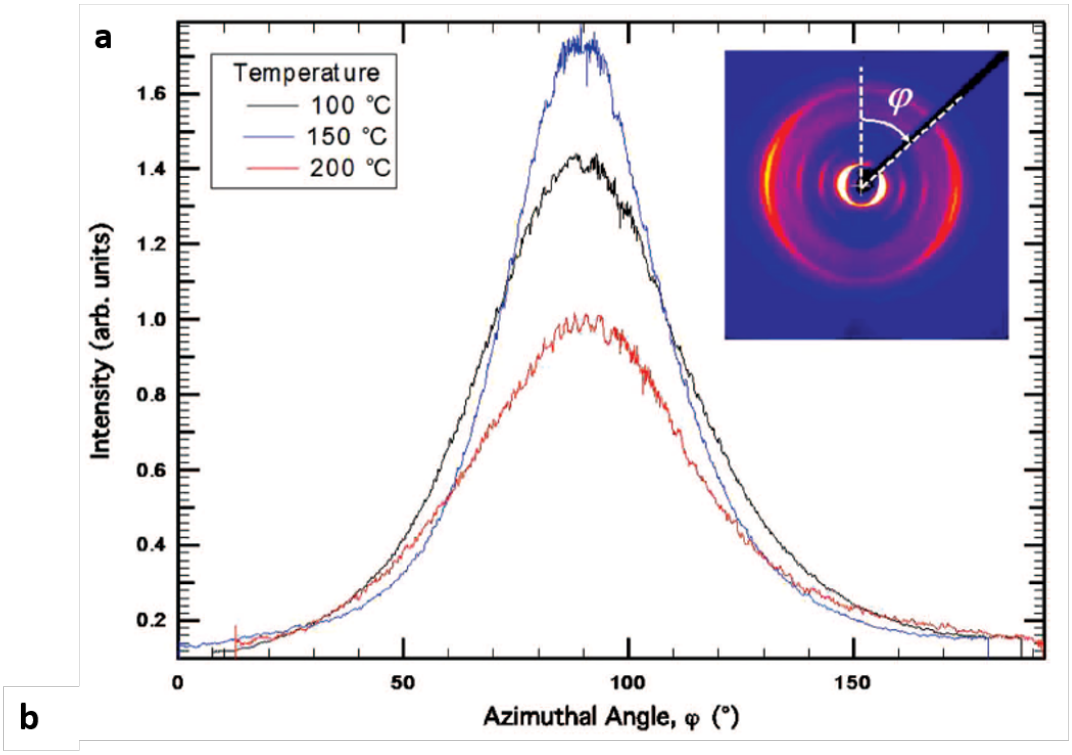

Processing Temp (C)	(100) d-spacing (Å) (± 0.02)	Hermann's Orientation parameter (*F*)	Percentage crystallinity (%)	Average Crystalline Domain size (Å)
Solution (DCB)	16.82		43.7 ± 0.5	
100	16.64	0.60 ± 0.03	38.9 ± 0.5	121 ± 4
150	16.55	0.76 ± 0.02	40.0 ± 0.5	144 ± 3
200	16.14	0.61 ± 0.03	30.8 ± 0.5	186 ± 5

Figure 4 P3HT fiber WAXS patterns (inset) at different processing temperatures a) Azimuthal scans b) Values for d-spacing, Herman's orientation parameter, percentage crystallinity and crystal domain size (reproduced from reference[209])

Crystal orientation in low temperature extrusion of P3HT ribbons

A new approach for producing P3HT ribbons was developed through extrusion, without the use of solvents. Temperatures of processing were much below the melting point of the polymer and different die thicknesses were also taken to see the effect of processing temperature and die thickness on the crystal morphology of the final ribbons. Ribbons were made by simple compression moulding of the polymer as well to compare with and observe the improvements in crystal orientation in the extruded samples. The setup for the extrusion process was as shown in figure 5.

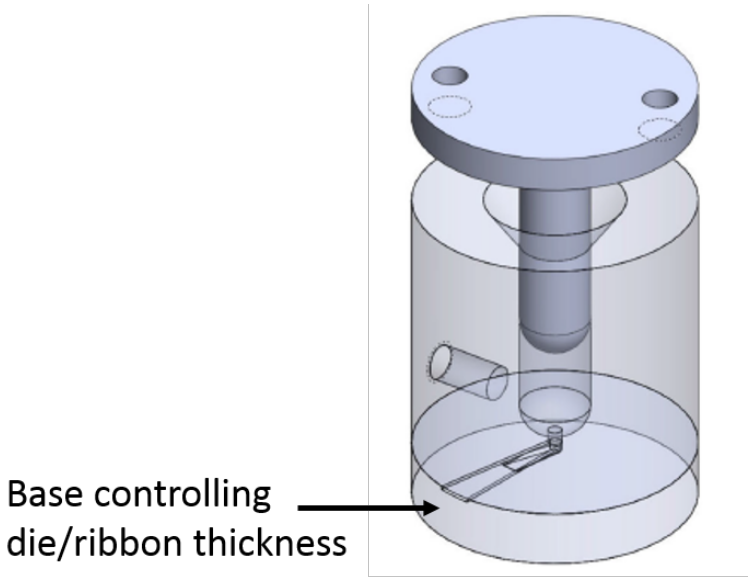

Figure 5. Setup for low temperature extrusion of P3HT ribbons (reproduced from reference[210])

WAXS measurements were carried out on these ribbons with different thicknesses and compared to compression moulded ribbons. The 1-D azimuthal scans from these were also obtained to look at the preferred direction of P3HT crystal orientation (figure 6). While the samples extruded from the melt (250 C) showed isotropic properties with no preferred orientation of the crystal planes. The compression moulded samples in turn had some induced orientation in the direction of the

ribbon long axis (fh = 0.45). The extruded ribbon with width 0.15 mm didn't show any significant orientation either in the flow or perpendicular to it with a fh value of 0.28 in the perpendicular direction. This probably arose because of the wall slip causing it to align perpendicular to the flow and domination the force in the flow direction itself. Consequently, in the thicker ribbon (0.30mm), both the wall slip and flow behavior are observe with relatively higher orientation (0.78 in the flow and 0.66 perpendicular to it) in both the directions.

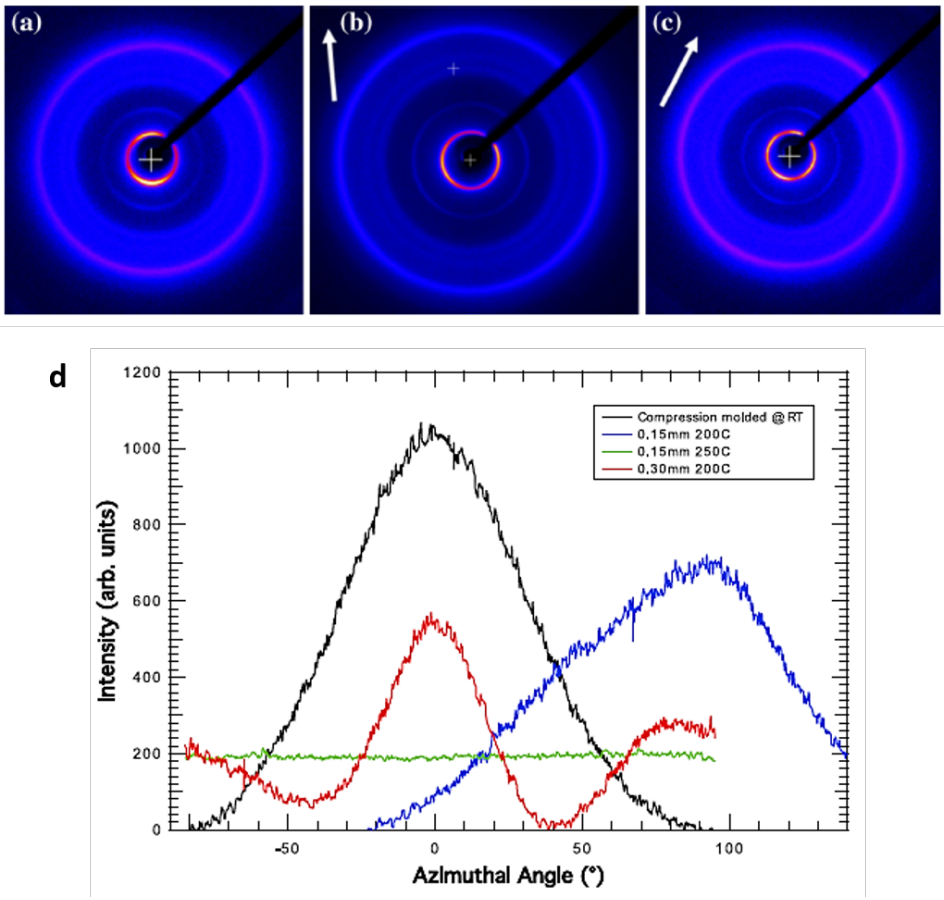

Figure 6. a) 2D WAXS patterns for a compression molding at RT, b extrusion through 0.15-mm die at 200 C and c extrusion through 0.30-mm die at 200 ºC. d) Azimuthal scans for the different P3HT ribbons with vertical axis = 0° (reproduced from reference[210])

DFT simulations of polyalkylthiophene-fullerene blends

All DFT calculations for the polyalkylthiophene-fullerene miscibility studies (Chapter 4) were carried out by Dr. Bobby G. Sumpter at the Oakridge National Laboratory. All-electron DFT calculations within the local density (LDA) and generalized gradient approximations (GGA) as implemented in NWChem[211] was used to determine geometries for fullerene and its derivatives interacting with oligomers of the polyalkylthiophene structures shown in Figure 14. The initial geometries for the different polymer-fullerene systems were obtained by optimizing the geometry via energy minimization of the fullerene-alkylthiophene oligomers using Materials Studio 5.0 (Accelrys). The Fletcher Reeves algorithm and the Newton (BFGS algorithm) methods were used to achieve the initial minimization. Subsequently, a NVT molecular dynamics simulation was run on the lowest energy structures using a Nose-Hoover thermostat at 298 K. These local energy minimum structures were run through the energy minimization protocol again to obtain the initial input structures for the DFT calculations. For DFT calculations, the DFT-D method[212] was used to obtain the non-bonded interactions between the fullerene-polymer pairs. The gas phase fullerene-alkylthiophene monomer interaction energies were computed by

$$E_B B = E_{mf} - E_{BSSE} - E_{def} \quad (2)$$

where E_b is the binding energy[174, 213]. E_{mf} is the energy of the optimized polymer-fullerene pair and E_{BSSE} is a calculation of the basis set superposition error (BSSE) defined by $E_{BSSE} = \sum i\ E_i\ (g)$, where E_i (g) is the energy of the alkylthiophene monomer or fullerene at the geometry in the pair (fullerene-alkylthiophene) with pair basis functions present. E_{def} was the deformation energy, calculated by the equation $Edef = \sum i\ [E_i\ (opt) - E_i]$, where E_i (opt) is the energy of the optimized species (fullerene or oligomer).

Neutron Reflectivity plots and fits

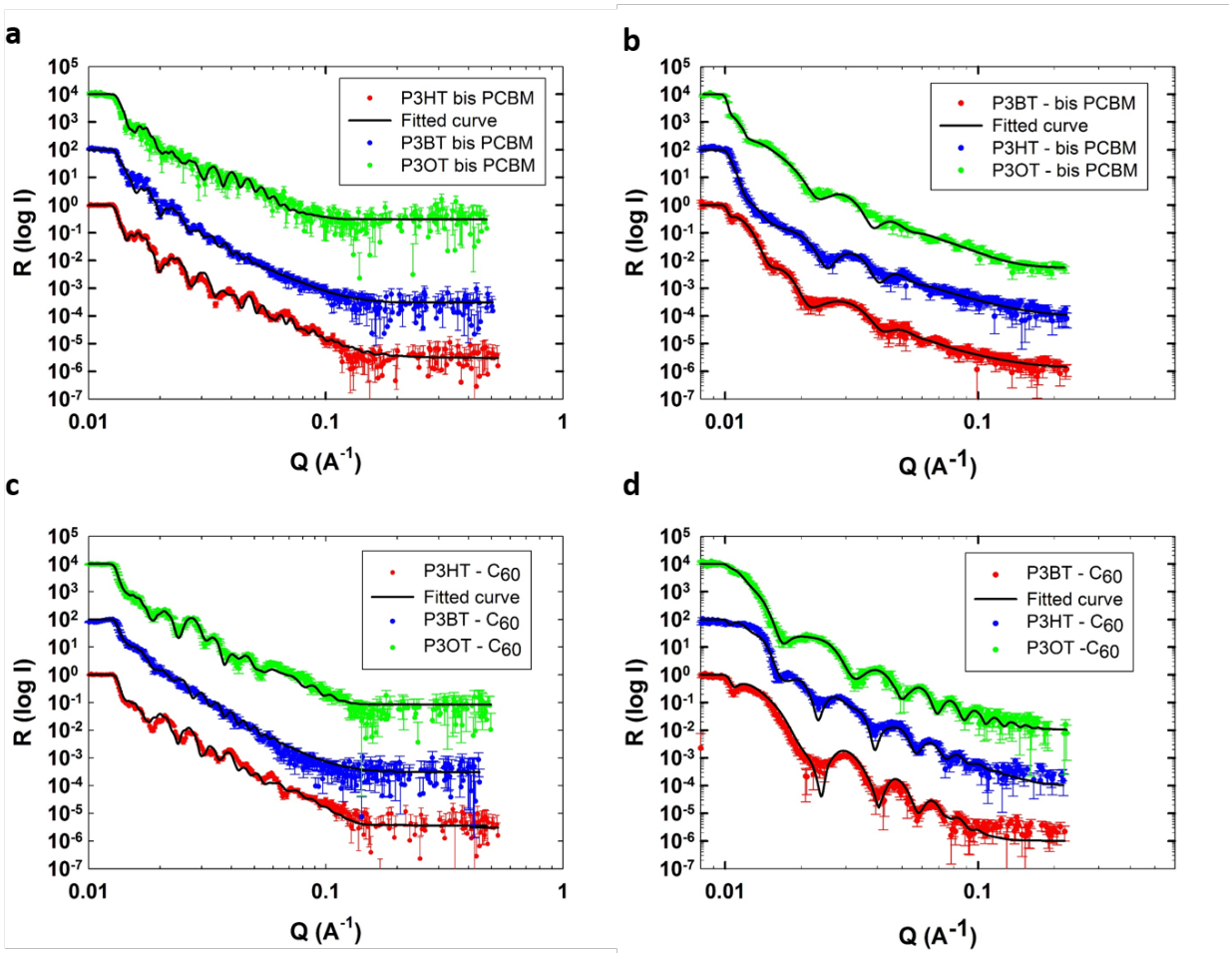

Figure 7. Neutron reflectivity plots and fits for various P3AT with bis-PCBM and C_{60} a) and c) post annealed without Ca b) and d) pre annealed with Ca

Synthesis of benzocyclobutene hydroxide

Benzocyclobutene hydroxide (BCB-OH) used for subsequent formation of thermos-cross-linkable fullerene PCBCB-I (Chapter 6) was synthesized by Karttikay Moudgill at the department of Chemistry, Georgia institute of Technology.

Synthesis of bicyclo[4.2.0]octa-1,3,5-trien-7-ol was accomplished according to published procedure.[214] Anthranilic acid was reacted with vinyl actetate in presence of amyl nitrite to obtain brown oil which was purified via vacuum distillation to give bicyclo[4.2.0]octa-1,3,5-trien-7-yl acetate in 40% yield. Hydrolysis of the ester with sodium carbonate in methanol gives desired alcohol in 90 % yield, which was easily purified by recrystallization with DCM/ Pentane to yield yellowish white crystals.

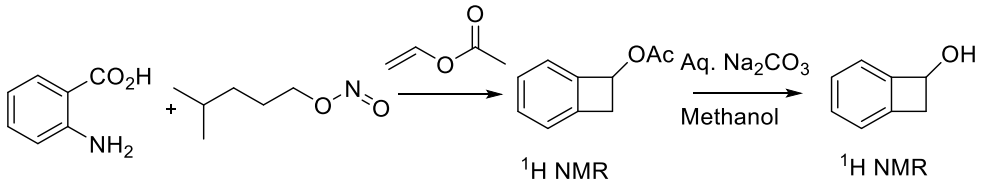

Figure 8. Schematic for synthesis of BCB-OH.

AFM images for P3HT: (PCBCB)n

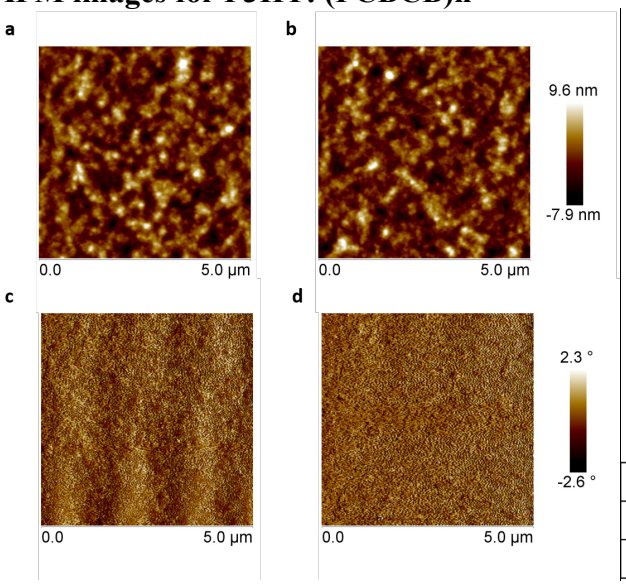

Roughness (nm)		Phase dimension (µm)	
Before annealing	After annealing	Before annealing	After annealing
3.47	2.83	0.040	0.044

Figure 9. AFM height images a)&b) and phase images c)&d)for P3HT-(PCBCB)n films before a)&c) and after annealing b)&d).

REFERENCES

1. Liu, C.; Yi, C.; Wang, K.; Yang, Y.; Bhatta, R. S.; Tsige, M.; Xiao, S.; Gong, X. Single-Junction Polymer Solar Cells with Over 10% Efficiency by a Novel Two-Dimensional Donor–Acceptor Conjugated Copolymer. *ACS Applied Materials & Interfaces* 2015, 7, 4928-4935.
2. Kim, J. Y.; Lee, K.; Coates, N. E.; Moses, D.; Nguyen, T.-Q.; Dante, M.; Heeger, A. J. Efficient Tandem Polymer Solar Cells Fabricated by All-Solution Processing. *Science* 2007, 317, 222-225.
3. Dennler, G.; Forberich, K.; Ameri, T.; Waldauf, C.; Denk, P.; Brabec, C. J.; Hingerl, K.; Heeger, A. J. Design of efficient organic tandem cells: On the interplay between molecular absorption and layer sequence. *Journal of Applied Physics* 2007, 102, 123109.
4. http://www.heliatek.com/wp-content/uploads/2013/01/130116_PR_Heliatek_achieves_record_cell_effiency_for_OPV.pdf.
5. *NREL efficiency chart*; NREL: 2014.
6. Chen, L.-M.; Hong, Z.; Li, G.; Yang, Y. Recent Progress in Polymer Solar Cells: Manipulation of Polymer:Fullerene Morphology and the Formation of Efficient Inverted Polymer Solar Cells. *Advanced Materials* 2009, 21, 1434-1449.
7. Thompson, B. C.; Fréchet, J. M. J. Polymer–Fullerene Composite Solar Cells. *Angewandte Chemie International Edition* 2008, 47, 58-77.
8. Tang, C. W. Two-layer organic photovoltaic cell. *Applied Physics Letters* 1986, 48, 183-185.
9. Wöhrle, D.; Meissner, D. Organic Solar Cells. *Advanced Materials* 1991, 3, 129-138.
10. Sariciftci, N. S.; Braun, D.; Zhang, C.; Srdanov, V. I.; Heeger, A. J.; Stucky, G.; Wudl, F. Semiconducting polymer-buckminsterfullerene heterojunctions: Diodes, photodiodes, and photovoltaic cells. *Applied Physics Letters* 1993, 62, 585-587.
11. Tsuzuki, T.; Shirota, Y.; Rostalski, J.; Meissner, D. The effect of fullerene doping on photoelectric conversion using titanyl phthalocyanine and a perylene pigment. *Solar Energy Materials and Solar Cells* 2000, 61, 1-8.
12. Günes, S.; Neugebauer, H.; Sariciftci, N. S. Conjugated Polymer-Based Organic Solar Cells. *Chemical Reviews* 2007, 107, 1324-1338.
13. Hoppe, H.; Sariciftci, N. S. Organic solar cells: An overview. *Journal of Materials Research* 2004, 19, 1924-1945.
14. Yu, G.; Gao, J.; Hummelen, J. C.; Wudl, F.; Heeger, A. J. Polymer Photovoltaic Cells: Enhanced Efficiencies via a Network of Internal Donor-Acceptor Heterojunctions. *Science* 1995, 270, 1789-1791.
15. Yang, C. Y.; Heeger, A. J. Morphology of composites of semiconducting polymers mixed with C60. *Synthetic Metals* 1996, 83, 85-88.
16. Padinger, F.; Rittberger, R. S.; Sariciftci, N. S. Effects of Postproduction Treatment on Plastic Solar Cells. *Advanced Functional Materials* 2003, 13, 85-88.
17. Meskers, S. C. J.; van Hal, P. A.; Spiering, A. J. H.; Hummelen, J. C.; van der Meer, A. F. G.; Janssen, R. A. J. Time-resolved infrared-absorption study of photoinduced charge transfer in a polythiophene-methanofullerene composite film. *Physical Review B* 2000, 61, 9917-9920.

18. Ma, W.; Yang, C.; Gong, X.; Lee, K.; Heeger, A. J. Thermally Stable, Efficient Polymer Solar Cells with Nanoscale Control of the Interpenetrating Network Morphology. *Advanced Functional Materials* 2005, 15, 1617-1622.
19. Schilinsky, P.; Waldauf, C.; Brabec, C. J. Recombination and loss analysis in polythiophene based bulk heterojunction photodetectors. *Applied Physics Letters* 2002, 81, 3885-3887.
20. Gebeyehu, D.; Brabec, C. J.; Padinger, F.; Fromherz, T.; Hummelen, J. C.; Badt, D.; Schindler, H.; Sariciftci, N. S. The interplay of efficiency and morphology in photovoltaic devices based on interpenetrating networks of conjugated polymers with fullerenes. *Synthetic Metals* 2001, 118, 1-9.
21. Shaheen, S. E.; Brabec, C. J.; Sariciftci, N. S.; Padinger, F.; Fromherz, T.; Hummelen, J. C. 2.5% efficient organic plastic solar cells. *Applied Physics Letters* 2001, 78, 841-843.
22. Brown, T. M.; Kim, J. S.; Friend, R. H.; Cacialli, F.; Daik, R.; Feast, W. J. Built-in field electroabsorption spectroscopy of polymer light-emitting diodes incorporating a doped poly(3,4-ethylene dioxythiophene) hole injection layer. *Applied Physics Letters* 1999, 75, 1679-1681.
23. Cao, Y.; Yu, G.; Zhang, C.; Menon, R.; Heeger, A. J. Polymer light-emitting diodes with polyethylene dioxythiophene–polystyrene sulfonate as the transparent anode. *Synthetic Metals* 1997, 87, 171-174.
24. Brabec, C. J.; Shaheen, S. E.; Winder, C.; Sariciftci, N. S.; Denk, P. Effect of LiF/metal electrodes on the performance of plastic solar cells. *Applied Physics Letters* 2002, 80, 1288-1290.
25. Kippelen, B.; Bredas, J.-L. Organic photovoltaics. *Energy & Environmental Science* 2009, 2, 251-261.
26. Bube, R. H.; Bube, R. H. *Photovoltaic materials*. World Scientific: 1998; Vol. 1.
27. Brabec, C. J.; Gowrisanker, S.; Halls, J. J. M.; Laird, D.; Jia, S.; Williams, S. P. Polymer–Fullerene Bulk-Heterojunction Solar Cells. *Advanced Materials* 2010, 22, 3839-3856.
28. Scharber, M. C.; Mühlbacher, D.; Koppe, M.; Denk, P.; Waldauf, C.; Heeger, A. J.; Brabec, C. J. Design Rules for Donors in Bulk-Heterojunction Solar Cells—Towards 10 % Energy-Conversion Efficiency. *Advanced Materials* 2006, 18, 789-794.
29. Qi, B.; Wang, J. Fill factor in organic solar cells. *Physical Chemistry Chemical Physics* 2013, 15, 8972-8982.
30. Bundgaard, E.; Krebs, F. C. Low band gap polymers for organic photovoltaics. *Solar Energy Materials and Solar Cells* 2007, 91, 954-985.
31. Liu, F.; Gu, Y.; Jung, J. W.; Jo, W. H.; Russell, T. P. On the morphology of polymer-based photovoltaics. *Journal of Polymer Science Part B: Polymer Physics* 2012, 50, 1018-1044.
32. Verploegen, E.; Miller, C. E.; Schmidt, K.; Bao, Z.; Toney, M. F. Manipulating the Morphology of P3HT–PCBM Bulk Heterojunction Blends with Solvent Vapor Annealing. *Chemistry of Materials* 2012, 24, 3923-3931.
33. Blouin, N.; Michaud, A.; Leclerc, M. A Low-Bandgap Poly(2,7-Carbazole) Derivative for Use in High-Performance Solar Cells. *Advanced Materials* 2007, 19, 2295-2300.
34. Park, S. H.; Roy, A.; Beaupre, S.; Cho, S.; Coates, N.; Moon, J. S.; Moses, D.; Leclerc, M.; Lee, K.; Heeger, A. J. Bulk heterojunction solar cells with internal quantum efficiency approaching 100%. *Nat Photon* 2009, 3, 297-302.
35. Amb, C. M.; Chen, S.; Graham, K. R.; Subbiah, J.; Small, C. E.; So, F.; Reynolds, J. R. Dithienogermole As a Fused Electron Donor in Bulk Heterojunction Solar Cells. *Journal of the American Chemical Society* 2011, 133, 10062-10065.

36. Small, C. E.; Chen, S.; Subbiah, J.; Amb, C. M.; Tsang, S.-W.; Lai, T.-H.; Reynolds, J. R.; So, F. High-efficiency inverted dithienogermole-thienopyrrolodione-based polymer solar cells. *Nat Photon* 2012, 6, 115-120.
37. Liang, Y.; Xu, Z.; Xia, J.; Tsai, S.-T.; Wu, Y.; Li, G.; Ray, C.; Yu, L. For the Bright Future—Bulk Heterojunction Polymer Solar Cells with Power Conversion Efficiency of 7.4%. *Advanced Materials* 2010, 22, E135-E138.
38. Liang, Y.; Feng, D.; Wu, Y.; Tsai, S.-T.; Li, G.; Ray, C.; Yu, L. Highly Efficient Solar Cell Polymers Developed via Fine-Tuning of Structural and Electronic Properties. *Journal of the American Chemical Society* 2009, 131, 7792-7799.
39. Yuan, T.; Zhu, X.; Zhou, L.; Zhang, J.; Tu, G. Efficient inverted polymer solar cells based on conjugated polyelectrolyte and zinc oxide modified ITO electrode. *Applied Physics Letters* 2015, 106, 083302.
40. Troshin, P. A.; Hoppe, H.; Renz, J.; Egginger, M.; Mayorova, J. Y.; Goryochev, A. E.; Peregudov, A. S.; Lyubovskaya, R. N.; Gobsch, G.; Sariciftci, N. S.; Razumov, V. F. Material Solubility-Photovoltaic Performance Relationship in the Design of Novel Fullerene Derivatives for Bulk Heterojunction Solar Cells. *Advanced Functional Materials* 2009, 19, 779-788.
41. Lopez, A. M.; Mateo-Alonso, A.; Prato, M. Materials chemistry of fullerene C(60) derivatives. *Journal of Materials Chemistry* 2011, 21, 1305-1318.
42. Zhao, G.; He, Y.; Xu, Z.; Hou, J.; Zhang, M.; Min, J.; Chen, H.-Y.; Ye, M.; Hong, Z.; Yang, Y.; Li, Y. Effect of Carbon Chain Length in the Substituent of PCBM-like Molecules on Their Photovoltaic Properties. *Advanced Functional Materials* 2010, 20, 1480-1487.
43. Matsumoto, F.; Moriwaki, K.; Takao, Y.; Ohno, T. Investigation of novel PCBM analogs containing thienyl groups for organic photovoltaic devices. *Synthetic Metals* 2010, 160, 961-966.
44. Mikroyannidis, J. A.; Kabanakis, A. N.; Sharma, S. S.; Sharma, G. D. A Simple and Effective Modification of PCBM for Use as an Electron Acceptor in Efficient Bulk Heterojunction Solar Cells. *Advanced Functional Materials* 2011, 21, 746-755.
45. Treat, N. D.; Varotto, A.; Takacs, C. J.; Batara, N.; Al-Hashimi, M.; Heeney, M. J.; Heeger, A. J.; Wudl, F.; Hawker, C. J.; Chabinyc, M. L. Polymer-Fullerene Miscibility: A Metric for Screening New Materials for High-Performance Organic Solar Cells. *Journal of the American Chemical Society* 2012, 134, 15869-15879.
46. Troshin, P. A.; Susarova, D. K.; Khakina, E. A.; Goryachev, A. A.; Borshchev, O. V.; Ponomarenko, S. A.; Razumov, V. F.; Sariciftci, N. S. Material solubility and molecular compatibility effects in the design of fullerene/polymer composites for organic bulk heterojunction solar cells. *Journal of Materials Chemistry* 2012, 22, 18433-18441.
47. Mackay, M. E.; Tuteja, A.; Duxbury, P. M.; Hawker, C. J.; Van Horn, B.; Guan, Z.; Chen, G.; Krishnan, R. S. General Strategies for Nanoparticle Dispersion. *Science* 2006, 311, 1740-1743.
48. Waller, J. H.; Bucknall, D. G.; Register, R. A.; Beckham, H. W.; Leisen, J.; Campbell, K. C60 fullerene inclusions in low-molecular-weight polystyrene–poly(dimethylsiloxane) diblock copolymers. *Polymer* 2009, 50, 4199-4204.
49. Mueller, C.; Ferenczi, T. A. M.; Campoy-Quiles, M.; Frost, J. M.; Bradley, D. D. C.; Smith, P.; Stingelin-Stutzmann, N.; Nelson, J. Binary organic photovoltaic blends: A simple rationale for optimum compositions. *Advanced Materials* 2008, 20, 3510-+.
50. Kim, J. Y.; Frisbie, D. Correlation of Phase Behavior and Charge Transport in Conjugated Polymer/Fullerene Blends. *Journal of Physical Chemistry C* 2008, 112, 17726-17736.

51. Zhao, J.; Swinnen, A.; Van Assche, G.; Manca, J.; Vanderzande, D.; Van Mele, B. Phase Diagram of P3HT/PCBM Blends and Its Implication for the Stability of Morphology. *Journal of Physical Chemistry B* 2009, 113, 1587-1591.
52. Hopkinson, P. E.; Staniec, P. A.; Pearson, A. J.; Dunbar, A. D. F.; Wang, T.; Ryan, A. J.; Jones, R. A. L.; Lidzey, D. G.; Donald, A. M. A Phase Diagram of the P3HT:PCBM Organic Photovoltaic System: Implications for Device Processing and Performance. *Macromolecules* 2011, 44, 2908-2917.
53. Zhao, J.; Bertho, S.; Vandenbergh, J.; Van Assche, G.; Manca, J.; Vanderzande, D.; Yin, X.; Shi, J.; Cleij, T.; Lutsen, L.; Van Mele, B. Phase behavior of PCBM blends with different conjugated polymers. *Physical Chemistry Chemical Physics* 2011, 13, 12285-12292.
54. Ballantyne, A. M.; Ferenczi, T. A. M.; Campoy-Quiles, M.; Clarke, T. M.; Maurano, A.; Wong, K. H.; Zhang, W.; Stingelin-Stutzmann, N.; Kim, J.-S.; Bradley, D. D. C.; Durrant, J. R.; McCulloch, I.; Heeney, M.; Nelson, J.; Tierney, S.; Duffy, W.; Mueller, C.; Smith, P. Understanding the Influence of Morphology on Poly(3-hexylselenothiophene):PCBM Solar Cells. *Macromolecules* 2010, 43, 1169-1174.
55. Bernardo, G.; Bucknall, D. G. *Recent Progress in the Understanding and Manipulation of Morphology in Polymer: Fullerene Photovoltaic Cells*. 2013.
56. Müller, C.; Ferenczi, T. A. M.; Campoy-Quiles, M.; Frost, J. M.; Bradley, D. D. C.; Smith, P.; Stingelin-Stutzmann, N.; Nelson, J. Binary Organic Photovoltaic Blends: A Simple Rationale for Optimum Compositions. *Advanced Materials* 2008, 20, 3510-3515.
57. Kim, J. Y.; Frisbie, C. D. Correlation of Phase Behavior and Charge Transport in Conjugated Polymer/Fullerene Blends. *The Journal of Physical Chemistry C* 2008, 112, 17726-17736.
58. Zhao, J.; Swinnen, A.; Van Assche, G.; Manca, J.; Vanderzande, D.; Mele, B. V. Phase Diagram of P3HT/PCBM Blends and Its Implication for the Stability of Morphology. *The Journal of Physical Chemistry B* 2009, 113, 1587-1591.
59. Eitouni, H.; Balsara, N. Thermodynamics of Polymer Blends. In *Physical Properties of Polymers Handbook*, Mark, J., Ed. Springer New York: 2007; pp 339-356.
60. Yin, W.; Dadmun, M. A New Model for the Morphology of P3HT/PCBM Organic Photovoltaics from Small-Angle Neutron Scattering: Rivers and Streams. *ACS Nano* 2011, 5, 4756-4768.
61. Kozub, D. R.; Vakhshouri, K.; Orme, L. M.; Wang, C.; Hexemer, A.; Gomez, E. D. Polymer Crystallization of Partially Miscible Polythiophene/Fullerene Mixtures Controls Morphology. *Macromolecules* 2011, 44, 5722-5726.
62. Woo, C. H.; Thompson, B. C.; Kim, B. J.; Toney, M. F.; Fréchet, J. M. J. The Influence of Poly(3-hexylthiophene) Regioregularity on Fullerene-Composite Solar Cell Performance. *Journal of the American Chemical Society* 2008, 130, 16324-16329.
63. Collins, B. A.; Gann, E.; Guignard, L.; He, X.; McNeill, C. R.; Ade, H. Molecular Miscibility of Polymer−Fullerene Blends. *The Journal of Physical Chemistry Letters* 2010, 1, 3160-3166.
64. Peumans, P.; Yakimov, A.; Forrest, S. R. Small molecular weight organic thin-film photodetectors and solar cells. *Journal of Applied Physics* 2003, 93, 3693-3723.
65. Hoppe, H.; Niggemann, M.; Winder, C.; Kraut, J.; Hiesgen, R.; Hinsch, A.; Meissner, D.; Sariciftci, N. S. Nanoscale Morphology of Conjugated Polymer/Fullerene-Based Bulk-Heterojunction Solar Cells. *Advanced Functional Materials* 2004, 14, 1005-1011.

66. Guo, J.; Liang, Y.; Szarko, J.; Lee, B.; Son, H. J.; Rolczynski, B. S.; Yu, L.; Chen, L. X. Structure, Dynamics, and Power Conversion Efficiency Correlations in a New Low Bandgap Polymer: PCBM Solar Cell. *The Journal of Physical Chemistry B* 2010, 114, 742-748.
67. Li, G.; Shrotriya, V.; Huang, J.; Yao, Y.; Moriarty, T.; Emery, K.; Yang, Y. High-efficiency solution processable polymer photovoltaic cells by self-organization of polymer blends. *Nat Mater* 2005, 4, 864-868.
68. Campoy-Quiles, M.; Ferenczi, T.; Agostinelli, T.; Etchegoin, P. G.; Kim, Y.; Anthopoulos, T. D.; Stavrinou, P. N.; Bradley, D. D. C.; Nelson, J. Morphology evolution via self-organization and lateral and vertical diffusion in polymer:fullerene solar cell blends. *Nat Mater* 2008, 7, 158-164.
69. Vanlaeke, P.; Vanhoyland, G.; Aernouts, T.; Cheyns, D.; Deibel, C.; Manca, J.; Heremans, P.; Poortmans, J. Polythiophene based bulk heterojunction solar cells: Morphology and its implications. *Thin Solid Films* 2006, 511–512, 358-361.
70. Kim, Y.; Choulis, S. A.; Nelson, J.; Bradley, D. D. C.; Cook, S.; Durrant, J. R. Device annealing effect in organic solar cells with blends of regioregular poly(3-hexylthiophene) and soluble fullerene. *Applied Physics Letters* 2005, 86, 063502.
71. Al-Ibrahim, M.; Ambacher, O.; Sensfuss, S.; Gobsch, G. Effects of solvent and annealing on the improved performance of solar cells based on poly(3-hexylthiophene): Fullerene. *Applied Physics Letters* 2005, 86, 201120.
72. Dang, M. T.; Wantz, G.; Bejbouji, H.; Urien, M.; Dautel, O. J.; Vignau, L.; Hirsch, L. Polymeric solar cells based on P3HT:PCBM: Role of the casting solvent. *Solar Energy Materials and Solar Cells* 2011, 95, 3408-3418.
73. Baek, W.-H.; Yang, H.; Yoon, T.-S.; Kang, C. J.; Lee, H. H.; Kim, Y.-S. Effect of P3HT:PCBM concentration in solvent on performances of organic solar cells. *Solar Energy Materials and Solar Cells* 2009, 93, 1263-1267.
74. Chirvase, D.; Parisi, J.; Hummelen, J. C.; Dyakonov, V. Influence of nanomorphology on the photovoltaic action of polymer–fullerene composites. *Nanotechnology* 2004, 15, 1317.
75. Zhao, Y.; Xie, Z.; Qu, Y.; Geng, Y.; Wang, L. Solvent-vapor treatment induced performance enhancement of poly(3-hexylthiophene):methanofullerene bulk-heterojunction photovoltaic cells. *Applied Physics Letters* 2007, 90, 043504.
76. Li, G.; Yao, Y.; Yang, H.; Shrotriya, V.; Yang, G.; Yang, Y. "Solvent Annealing" Effect in Polymer Solar Cells Based on Poly(3-hexylthiophene) and Methanofullerenes. *Advanced Functional Materials* 2007, 17, 1636-1644.
77. Reyes-Reyes, M.; Kim, K.; Carroll, D. L. High-efficiency photovoltaic devices based on annealed poly(3-hexylthiophene) and 1-(3-methoxycarbonyl)-propyl-1- phenyl-(6,6)C61 blends. *Applied Physics Letters* 2005, 87, 083506.
78. Mihailetchi, V. D.; Xie, H. X.; de Boer, B.; Koster, L. J. A.; Blom, P. W. M. Charge Transport and Photocurrent Generation in Poly(3-hexylthiophene): Methanofullerene Bulk-Heterojunction Solar Cells. *Advanced Functional Materials* 2006, 16, 699-708.
79. Li, G.; Shrotriya, V.; Yao, Y.; Yang, Y. Investigation of annealing effects and film thickness dependence of polymer solar cells based on poly(3-hexylthiophene). *Journal of Applied Physics* 2005, 98, 043704.
80. Agostinelli, T.; Lilliu, S.; Labram, J. G.; Campoy-Quiles, M.; Hampton, M.; Pires, E.; Rawle, J.; Bikondoa, O.; Bradley, D. D. C.; Anthopoulos, T. D.; Nelson, J.; Macdonald, J. E. Real-Time Investigation of Crystallization and Phase-Segregation Dynamics in P3HT:PCBM Solar Cells During Thermal Annealing. *Advanced Functional Materials* 2011, 21, 1701-1708.

81. Hoppe, H.; Sariciftci, N. S. Morphology of polymer/fullerene bulk heterojunction solar cells. *Journal of Materials Chemistry* 2006, 16, 45-61.
82. Dennler, G.; Scharber, M. C.; Brabec, C. J. Polymer-Fullerene Bulk-Heterojunction Solar Cells. *Advanced Materials* 2009, 21, 1323-1338.
83. Treat, N. D.; Brady, M. A.; Smith, G.; Toney, M. F.; Kramer, E. J.; Hawker, C. J.; Chabinyc, M. L. Interdiffusion of PCBM and P3HT Reveals Miscibility in a Photovoltaically Active Blend. *Advanced Energy Materials* 2011, 1, 82-89.
84. Lee, K. H.; Schwenn, P. E.; Smith, A. R. G.; Cavaye, H.; Shaw, P. E.; James, M.; Krueger, K. B.; Gentle, I. R.; Meredith, P.; Burn, P. L. Morphology of All-Solution-Processed "Bilayer" Organic Solar Cells. *Advanced Materials* 2011, 23, 766-770.
85. Chen, D.; Liu, F.; Wang, C.; Nakahara, A.; Russell, T. P. Bulk Heterojunction Photovoltaic Active Layers via Bilayer Interdiffusion. *Nano Letters* 2011, 11, 2071-2078.
86. Wu, W.-R.; Jeng, U. S.; Su, C.-J.; Wei, K.-H.; Su, M.-S.; Chiu, M.-Y.; Chen, C.-Y.; Su, W.-B.; Su, C.-H.; Su, A.-C. Competition between Fullerene Aggregation and Poly(3-hexylthiophene) Crystallization upon Annealing of Bulk Heterojunction Solar Cells. *ACS Nano* 2011, 5, 6233-6243.
87. Yang, X.; Loos, J.; Veenstra, S. C.; Verhees, W. J. H.; Wienk, M. M.; Kroon, J. M.; Michels, M. A. J.; Janssen, R. A. J. Nanoscale Morphology of High-Performance Polymer Solar Cells. *Nano Letters* 2005, 5, 579-583.
88. Rochester, C. W.; Mauger, S. A.; Moulé, A. J. Investigating the Morphology of Polymer/Fullerene Layers Coated Using Orthogonal Solvents. *The Journal of Physical Chemistry C* 2012, 116, 7287-7292.
89. Parnell, A. J.; Dunbar, A. D. F.; Pearson, A. J.; Staniec, P. A.; Dennison, A. J. C.; Hamamatsu, H.; Skoda, M. W. A.; Lidzey, D. G.; Jones, R. A. L. Depletion of PCBM at the Cathode Interface in P3HT/PCBM Thin Films as Quantified via Neutron Reflectivity Measurements. *Advanced Materials* 2010, 22, 2444-2447.
90. Kiel, J. W.; Eberle, A. P. R.; Mackay, M. E. Nanoparticle Agglomeration in Polymer-Based Solar Cells. *Physical Review Letters* 2010, 105, 168701.
91. Germack, D. S.; Chan, C. K.; Hamadani, B. H.; Richter, L. J.; Fischer, D. A.; Gundlach, D. J.; DeLongchamp, D. M. Substrate-dependent interface composition and charge transport in films for organic photovoltaics. *Applied Physics Letters* 2009, 94, 233303-3.
92. Chen, D.; Nakahara, A.; Wei, D.; Nordlund, D.; Russell, T. P. P3HT/PCBM Bulk Heterojunction Organic Photovoltaics: Correlating Efficiency and Morphology. *Nano Letters* 2010, 11, 561-567.
93. van Bavel, S. S.; Bärenklau, M.; de With, G.; Hoppe, H.; Loos, J. P3HT/PCBM Bulk Heterojunction Solar Cells: Impact of Blend Composition and 3D Morphology on Device Performance. *Advanced Functional Materials* 2010, 20, 1458-1463.
94. Kiel, J. W.; Kirby, B. J.; Majkrzak, C. F.; Maranville, B. B.; Mackay, M. E. Nanoparticle concentration profile in polymer-based solar cells. *Soft Matter* 2010, 6, 641-646.
95. Lu, H.; Akgun, B.; Russell, T. P. Morphological Characterization of a Low-Bandgap Crystalline Polymer:PCBM Bulk Heterojunction Solar Cells. *Advanced Energy Materials* 2011, 1, 870-878.
96. Kim, H.; So, W.-W.; Moon, S.-J. The importance of post-annealing process in the device performance of poly(3-hexylthiophene): Methanofullerene polymer solar cell. *Solar Energy Materials and Solar Cells* 2007, 91, 581-587.

97. Treat, N. D.; Shuttle, C. G.; Toney, M. F.; Hawker, C. J.; Chabinyc, M. L. In situ measurement of power conversion efficiency and molecular ordering during thermal annealing in P3HT:PCBM bulk heterojunction solar cells. *Journal of Materials Chemistry* 2011, 21, 15224-15231.
98. Ruderer, M. A.; Guo, S.; Meier, R.; Chiang, H.-Y.; Körstgens, V.; Wiedersich, J.; Perlich, J.; Roth, S. V.; Müller-Buschbaum, P. Solvent-Induced Morphology in Polymer-Based Systems for Organic Photovoltaics. *Advanced Functional Materials* 2011, 21, 3382-3391.
99. Verploegen, E.; Mondal, R.; Bettinger, C. J.; Sok, S.; Toney, M. F.; Bao, Z. Effects of Thermal Annealing Upon the Morphology of Polymer–Fullerene Blends. *Advanced Functional Materials* 2010, 20, 3519-3529.
100. Perez, L. A.; Chou, K. W.; Love, J. A.; van der Poll, T. S.; Smilgies, D.-M.; Nguyen, T.-Q.; Kramer, E. J.; Amassian, A.; Bazan, G. C. Solvent Additive Effects on Small Molecule Crystallization in Bulk Heterojunction Solar Cells Probed During Spin Casting. *Advanced Materials* 2013, 25, 6380-6384.
101. Rogers, J. T.; Schmidt, K.; Toney, M. F.; Bazan, G. C.; Kramer, E. J. Time-Resolved Structural Evolution of Additive-Processed Bulk Heterojunction Solar Cells. *Journal of the American Chemical Society* 2012, 134, 2884-2887.
102. Chou, K. W.; Yan, B.; Li, R.; Li, E. Q.; Zhao, K.; Anjum, D. H.; Alvarez, S.; Gassaway, R.; Biocca, A.; Thoroddsen, S. T.; Hexemer, A.; Amassian, A. Spin-Cast Bulk Heterojunction Solar Cells: A Dynamical Investigation. *Advanced Materials* 2013, 25, 1923-1929.
103. Chiu, M.-Y.; Jeng, U. S.; Su, C.-H.; Liang, K. S.; Wei, K.-H. Simultaneous Use of Small- and Wide-Angle X-ray Techniques to Analyze Nanometerscale Phase Separation in Polymer Heterojunction Solar Cells. *Advanced Materials* 2008, 20, 2573-2578.
104. Liao, H.-C.; Tsao, C.-S.; Lin, T.-H.; Chuang, C.-M.; Chen, C.-Y.; Jeng, U. S.; Su, C.-H.; Chen, Y.-F.; Su, W.-F. Quantitative Nanoorganized Structural Evolution for a High Efficiency Bulk Heterojunction Polymer Solar Cell. *Journal of the American Chemical Society* 2011, 133, 13064-13073.
105. Lilliu, S.; Agostinelli, T.; Pires, E.; Hampton, M.; Nelson, J.; Macdonald, J. E. Dynamics of Crystallization and Disorder during Annealing of P3HT/PCBM Bulk Heterojunctions. *Macromolecules* 2011, 44, 2725-2734.
106. Schmidt-Hansberg, B.; Sanyal, M.; Klein, M. F. G.; Pfaff, M.; Schnabel, N.; Jaiser, S.; Vorobiev, A.; Müller, E.; Colsmann, A.; Scharfer, P.; Gerthsen, D.; Lemmer, U.; Barrena, E.; Schabel, W. Moving through the Phase Diagram: Morphology Formation in Solution Cast Polymer–Fullerene Blend Films for Organic Solar Cells. *ACS Nano* 2011, 5, 8579-8590.
107. Nielsen, T. D.; Cruickshank, C.; Foged, S.; Thorsen, J.; Krebs, F. C. Business, market and intellectual property analysis of polymer solar cells. *Solar Energy Materials and Solar Cells* 2010, 94, 1553-1571.
108. Lloyd, M. T.; Olson, D. C.; Lu, P.; Fang, E.; Moore, D. L.; White, M. S.; Reese, M. O.; Ginley, D. S.; Hsu, J. W. P. Impact of contact evolution on the shelf life of organic solar cells. *Journal of Materials Chemistry* 2009, 19, 7638-7642.
109. Rivaton, A.; Chambon, S.; Manceau, M.; Gardette, J.-L.; Lemaître, N.; Guillerez, S. Light-induced degradation of the active layer of polymer-based solar cells. *Polymer Degradation and Stability* 2010, 95, 278-284.
110. Seemann, A.; Egelhaaf, H. J.; Brabec, C. J.; Hauch, J. A. Influence of oxygen on semi-transparent organic solar cells with gas permeable electrodes. *Organic Electronics* 2009, 10, 1424-1428.

111. Schafferhans, J.; Baumann, A.; Deibel, C.; Dyakonov, V. Trap distribution and the impact of oxygen-induced traps on the charge transport in poly(3-hexylthiophene). *Applied Physics Letters* 2008, 93, 093303.
112. Tournebize, A.; Bussière, P.-O.; Rivaton, A.; Gardette, J.-L.; Medlej, H.; Hiorns, R. C.; Dagron-Lartigau, C.; Krebs, F. C.; Norrman, K. New Insights into the Mechanisms of Photodegradation/Stabilization of P3HT:PCBM Active Layers Using Poly(3-hexyl-d13-Thiophene). *Chemistry of Materials* 2013, 25, 4522-4528.
113. Kawano, K.; Pacios, R.; Poplavskyy, D.; Nelson, J.; Bradley, D. D. C.; Durrant, J. R. Degradation of organic solar cells due to air exposure. *Solar Energy Materials and Solar Cells* 2006, 90, 3520-3530.
114. Miyanishi, S.; Tajima, K.; Hashimoto, K. Morphological Stabilization of Polymer Photovoltaic Cells by Using Cross-Linkable Poly(3-(5-hexenyl)thiophene). *Macromolecules* 2009, 42, 1610-1618.
115. De Bettignies, R.; Leroy, J.; Firon, M.; Sentein, C. Accelerated lifetime measurements of P3HT:PCBM solar cells. *Synthetic Metals* 2006, 156, 510-513.
116. Schuller, S.; Schilinsky, P.; Hauch, J.; Brabec, C. J. Determination of the degradation constant of bulk heterojunction solar cells by accelerated lifetime measurements. *Appl Phys A* 2004, 79, 37-40.
117. Jo, J.; Kim, S.-S.; Na, S.-I.; Yu, B.-K.; Kim, D.-Y. Time-Dependent Morphology Evolution by Annealing Processes on Polymer:Fullerene Blend Solar Cells. *Advanced Functional Materials* 2009, 19, 866-874.
118. Sivula, K.; Ball, Z. T.; Watanabe, N.; Fréchet, J. M. J. Amphiphilic Diblock Copolymer Compatibilizers and Their Effect on the Morphology and Performance of Polythiophene:Fullerene Solar Cells. *Advanced Materials* 2006, 18, 206-210.
119. Hummelen, J. C.; Knight, B. W.; LePeq, F.; Wudl, F.; Yao, J.; Wilkins, C. L. Preparation and Characterization of Fulleroid and Methanofullerene Derivatives. *The Journal of Organic Chemistry* 1995, 60, 532-538.
120. Yang, X.; van Duren, J. K. J.; Janssen, R. A. J.; Michels, M. A. J.; Loos, J. Morphology and Thermal Stability of the Active Layer in Poly(p-phenylenevinylene)/Methanofullerene Plastic Photovoltaic Devices. *Macromolecules* 2004, 37, 2151-2158.
121. Cheng, Y.-J.; Hsieh, C.-H.; Li, P.-J.; Hsu, C.-S. Morphological Stabilization by In Situ Polymerization of Fullerene Derivatives Leading to Efficient, Thermally Stable Organic Photovoltaics. *Advanced Functional Materials* 2011, 21, 1723-1732.
122. Drees, M.; Hoppe, H.; Winder, C.; Neugebauer, H.; Sariciftci, N. S.; Schwinger, W.; Schaffler, F.; Topf, C.; Scharber, M. C.; Zhu, Z.; Gaudiana, R. Stabilization of the nanomorphology of polymer-fullerene "bulk heterojunction" blends using a novel polymerizable fullerene derivative. *Journal of Materials Chemistry* 2005, 15, 5158-5163.
123. Li, Z.; Wong, H. C.; Huang, Z.; Zhong, H.; Tan, C. H.; Tsoi, W. C.; Kim, J. S.; Durrant, J. R.; Cabral, J. T. Performance enhancement of fullerene-based solar cells by light processing. *Nat Commun* 2013, 4.
124. Wong, H. C.; Li, Z.; Tan, C. H.; Zhong, H.; Huang, Z.; Bronstein, H.; McCulloch, I.; Cabral, J. T.; Durrant, J. R. Morphological Stability and Performance of Polymer–Fullerene Solar Cells under Thermal Stress: The Impact of Photoinduced PC60BM Oligomerization. *ACS Nano* 2014, 8, 1297-1308.
125. Schroeder, B. C.; Li, Z.; Brady, M. A.; Faria, G. C.; Ashraf, R. S.; Takacs, C. J.; Cowart, J. S.; Duong, D. T.; Chiu, K. H.; Tan, C.-H.; Cabral, J. T.; Salleo, A.; Chabinyc, M. L.; Durrant,

J. R.; McCulloch, I. Enhancing Fullerene-Based Solar Cell Lifetimes by Addition of a Fullerene Dumbbell. *Angewandte Chemie International Edition* 2014, 53, 12870-12875.
126. Liu, J.; Guo, X.; Qin, Y.; Liang, S.; Guo, Z.-X.; Li, Y. Dumb-belled PCBM derivative with better photovoltaic performance. *Journal of Materials Chemistry* 2012, 22, 1758-1761.
127. Rumer, J. W.; Ashraf, R. S.; Eisenmenger, N. D.; Huang, Z.; Meager, I.; Nielsen, C. B.; Schroeder, B. C.; Chabinyc, M. L.; McCulloch, I. Dual Function Additives: A Small Molecule Crosslinker for Enhanced Efficiency and Stability in Organic Solar Cells. *Advanced Energy Materials* 2015, n/a-n/a.
128. Kadish, K. M.; Ruoff, R. S. *Fullerenes: Chemistry, Physics, and Technology*. Wiley: 2000.
129. Marchiori, C. F. N.; Koehler, M. Dipole assisted exciton dissociation at conjugated polymer/fullerene photovoltaic interfaces: A molecular study using density functional theory calculations. *Synthetic Metals* 2010, 160, 643-650.
130. Li, S.; Lei, M.; Lv, M.; Watkins, S. E.; Tan, Z. a.; Zhu, J.; Hou, J.; Chen, X.; Li, Y. [6,6]-Phenyl-C61-Butyric Acid Dimethylamino Ester as a Cathode Buffer Layer for High-Performance Polymer Solar Cells. *Advanced Energy Materials* 2013, 3, 1569-1574.
131. Hong, D.; Lv, M.; Lei, M.; Chen, Y.; Lu, P.; Wang, Y.; Zhu, J.; Wang, H.; Gao, M.; Watkins, S. E.; Chen, X. N-Acyldithieno[3,2-b:2′,3′-d]pyrrole-Based Low-Band-Gap Conjugated Polymer Solar Cells with Amine-Modified [6,6]-Phenyl-C61-butyric Acid Ester Cathode Interlayers. *ACS Applied Materials & Interfaces* 2013, 5, 10995-11003.
132. Lee, J. U.; Jung, J. W.; Emrick, T.; Russell, T. P.; Jo, W. H. Synthesis of C60-end capped P3HT and its application for high performance of P3HT/PCBM bulk heterojunction solar cells. *Journal of Materials Chemistry* 2010, 20, 3287-3294.
133. Lee, J. U.; Cirpan, A.; Emrick, T.; Russell, T. P.; Jo, W. H. Synthesis and photophysical property of well-defined donor-acceptor diblock copolymer based on regioregular poly(3-hexylthiophene) and fullerene. *Journal of Materials Chemistry* 2009, 19, 1483-1489.
134. Coolidge, W. D. A Powerful R\"ontgen Ray Tube with a Pure Electron Discharge. *Physical Review* 1913, 2, 409-430.
135. Nave, C. http://hyperphysics.phy-astr.gsu.edu/hbase/quantum/bragg.html.
136. ISIS, O., UK. http://pd.chem.ucl.ac.uk/pdnn/inst3/pulsed.htm.
137. Jackson, A. J. Introduction to Small-Angle Neutron Scattering and Neutron Reflectometry. 2008.
138. Cowley, J. M. CHAPTER 4 - Radiations and their scattering by matter. In *Diffraction Physics (Third Revised Edition)*, Cowley, J. M., Ed. North-Holland: Amsterdam, 1995; pp 77-92.
139. Feigin, L. A.; Svergun, D. I.; Taylor, G. Principles of the Theory of X-Ray and Neutron Scattering. In *Structure Analysis by Small-Angle X-Ray and Neutron Scattering*, Taylor, G., Ed. Springer US: 1987; pp 3-24.
140. Lifshin, E. *X-ray Characterization of Materials*. Wiley: 2008.
141. Jenkins, R.; Snyder, R. L. Diffraction Theory. In *Introduction to X-ray Powder Diffractometry*, John Wiley & Sons, Inc.: 1996; pp 47-95.
142. Leng, Y. Materials characterization introduction to microscopic and spectroscopic methods. 2013.
143. Patterson, A. L. The Scherrer Formula for X-Ray Particle Size Determination. *Physical Review* 1939, 56, 978-982.
144. He, B. B. *Two-dimensional X-Ray Diffraction*. Wiley: 2011.
145. Levine, J.; Cohen, J.; Chung, Y.; Georgopoulos, P. Grazing-incidence small-angle X-ray scattering: New tool for studying thin film growth. 1989.

146. Muller-Buschbaum, P.; S. Gutmann, J.; Stamm, M. Dewetting of confined polymer films: an X-ray and neutron scattering study. *Physical Chemistry Chemical Physics* 1999, 1, 3857-3863.
147. Müller-Buschbaum, P.; Gutmann, J. S.; Stamm, M.; Cubitt, R.; Cunis, S.; von Krosigk, G.; Gehrke, R.; Petry, W. Dewetting of thin polymer-blend films examined with GISAS. *Physica B: Condensed Matter* 2000, 283, 53-59.
148. Muller-Buschbaum, P. Grazing incidence small-angle neutron scattering: challenges and possibilities. *Polym J* 2013, 45, 34-42.
149. Smilgies, D.-M. http://staff.chess.cornell.edu/~smilgies/gisaxs/GISAXS.php.
150. Kampmann, R.; Haese-Seiller, M.; Kudryashov, V.; Nickel, B.; Daniel, C.; Fenzl, W.; Schreyer, A.; Sackmann, E.; Rädler, J. Horizontal ToF-neutron reflectometer REFSANS at FRM-II Munich/Germany: First tests and status. *Physica B: Condensed Matter* 2006, 385–386, Part 2, 1161-1163.
151. Müller-Buschbaum, P.; Metwalli, E.; Moulin, J. F.; Kudryashov, V.; Haese-Seiller, M.; Kampmann, R. Time of flight grazing incidence small angle neutron scattering. *Eur. Phys. J. Spec. Top.* 2009, 167, 107-112.
152. Kaune, G.; Haese-Seiller, M.; Kampmann, R.; Moulin, J.-F.; Zhong, Q.; Müller-Buschbaum, P. TOF-GISANS investigation of polymer infiltration in mesoporous TiO2 films for photovoltaic applications. *Journal of Polymer Science Part B: Polymer Physics* 2010, 48, 1628-1635.
153. Müller-Buschbaum, P.; Maurer, E.; Bauer, E.; Cubitt, R. Surface versus Confinement Induced Morphology Transition in Triblock Copolymer Films: A Grazing Incidence Small Angle Neutron Scattering Investigation. *Langmuir* 2006, 22, 9295-9303.
154. Müller-Buschbaum, P.; Schulz, L.; Metwalli, E.; Moulin, J. F.; Cubitt, R. Lateral Structures of Buried Interfaces in ABA-Type Triblock Copolymer Films. *Langmuir* 2008, 24, 7639-7644.
155. http://www.isis.stfc.ac.uk/.
156. http://www.mantidproject.org/Main_Page.
157. Wignall, G. D.; Bates, F. S. Absolute Calibration of Small-Angle Neutron-Scattering Data. *Journal of Applied Crystallography* 1987, 20, 28-40.
158. http://www.sasview.org/.
159. Park, C.-D.; Fleetham, T. A.; Li, J.; Vogt, B. D. High performance bulk-heterojunction organic solar cells fabricated with non-halogenated solvent processing. *Organic Electronics* 2011, 12, 1465-1470.
160. Sariciftci, N. S.; Braun, D.; Zhang, C.; Srdanov, V. I.; Heeger, A. J.; Stucky, G.; Wudl, F. Semiconducting Polymer-Buckminsterfullerene Heterojunctions - Diodes, Photodiodes, and Photovoltaic Cells. *Applied Physics Letters* 1993, 62, 585-587.
161. Sariciftci, N. S.; Smilowitz, L.; Heeger, A. J.; Wudl, F. Photoinduced Electron-Transfer From a Conducting Polymer to Buckminsterfullerene. *Science* 1992, 258, 1474-1476.
162. Yu, G.; Gao, J.; Hummelen, J. C.; Wudl, F.; Heeger, A. J. Polymer Photovoltaic Cells - Enhanced Efficiencies Via a Network of Internal Donor-Acceptor Heterojunctions. *Science* 1995, 270, 1789-1791.
163. Bucknall, D. G.; Bernardo, G.; Shofner, M. L.; Nabankur, D.; Raghavan, D.; Sumpter, B. G.; Sides, S.; Huq, A.; Karim, A. Phase-Morphology and Molecular Structure Correlations in Model Fullerene-Polymer Nanocomposites. In *Polymer Composite Materials: From Macro, Micro to Nanoscale*, Boudenne, A., Ed. Trans Tech Publications Ltd: Stafa-Zurich, 2012; Vol. 714, pp 63-66.

164. Campbell, K.; Gurun, B.; Sumpter, B. G.; Thio, Y. S.; Bucknall, D. G. Role of Conformation in pi-pi Interactions and Polymer/Fullerene Miscibility. *Journal Of Physical Chemistry B* 2011, 115, 8989-8995.
165. Mens, R.; Chambon, S.; Bertho, S.; Reggers, G.; Ruttens, B.; D'Haen, J.; Manca, J.; Carleer, R.; Vanderzande, D.; Adriaensens, P. Description of the nanostructured morphology of 6,6 -phenyl-C(61)-butyric acid methyl ester (PCBM) by XRD, DSC and solid-state NMR. *Magnetic Resonance in Chemistry* 2011, 49, 242-247.
166. Rispens, M. T.; Meetsma, A.; Rittberger, R.; Brabec, C. J.; Sariciftci, N. S.; Hummelen, J. C. Influence of the solvent on the crystal structure of PCBM and the efficiency of MDMO-PPV:PCBM 'plastic' solar cells. *Chemical Communications* 2003, 2116-2118.
167. Mortuza, S. M.; Banerjee, S. Molecular modeling study of agglomeration of [6,6]-phenyl-C61-butyric acid methyl ester in solvents. *The Journal of Chemical Physics* 2012, 137, 244308.
168. Hammouda, B. SANS from Polymers-Review of the Recent Literature. *Polymer Reviews* 2010, 50, 14-39.
169. Debye, P.; Bueche, A. M. Scattering by an Inhomogeneous Solid. *Journal of Applied Physics* 1949, 20, 518-525.
170. Debye, P.; Anderson, H. R.; Brumberger, H. Scattering by an Inhomogeneous Solid. II. The Correlation Function and Its Application. *Journal of Applied Physics* 1957, 28, 679-683.
171. Mildner, D. F. R.; Hall, P. L. Small-Angle Scattering From Porous Solids With Fractal Geometry. *Journal of Physics D-Applied Physics* 1986, 19, 1535-1545.
172. Ruoff, R. S.; Tse, D. S.; Malhotra, R.; Lorents, D. C. Solubility of fullerene (C60) in a variety of solvents. *The Journal of Physical Chemistry* 1993, 97, 3379-3383.
173. Machui, F.; Langner, S.; Zhu, X.; Abbott, S.; Brabec, C. J. Determination of the P3HT:PCBM solubility parameters via a binary solvent gradient method: Impact of solubility on the photovoltaic performance. *Solar Energy Materials and Solar Cells* 2012, 100, 138-146.
174. Campbell, K.; Gurun, B.; Sumpter, B. G.; Thio, Y. S.; Bucknall, D. G. Role of conformation in pi-pi interactions and polymer/fullerene miscibility. *J Phys Chem B* 2011, 115, 8989-95.
175. Lenes, M.; Wetzelaer, G.-J. A. H.; Kooistra, F. B.; Veenstra, S. C.; Hummelen, J. C.; Blom, P. W. M. Fullerene Bisadducts for Enhanced Open-Circuit Voltages and Efficiencies in Polymer Solar Cells. *Advanced Materials* 2008, 20, 2116-2119.
176. Nguyen, L. H.; Hoppe, H.; Erb, T.; Günes, S.; Gobsch, G.; Sariciftci, N. S. Effects of Annealing on the Nanomorphology and Performance of Poly(alkylthiophene):Fullerene Bulk-Heterojunction Solar Cells. *Advanced Functional Materials* 2007, 17, 1071-1078.
177. Ruderer, M. A.; Meier, R.; Porcar, L.; Cubitt, R.; Müller-Buschbaum, P. Phase Separation and Molecular Intermixing in Polymer–Fullerene Bulk Heterojunction Thin Films. *The Journal of Physical Chemistry Letters* 2012, 3, 683-688.
178. Paci, B.; Generosi, A.; Rossi Albertini, V.; Perfetti, P.; de Bettignies, R.; Sentein, C. Time-resolved morphological study of organic thin film solar cells based on calcium/aluminium cathode material. *Chemical Physics Letters* 2008, 461, 77-81.
179. Jørgensen, M.; Norrman, K.; Krebs, F. C. Stability/degradation of polymer solar cells. *Solar Energy Materials and Solar Cells* 2008, 92, 686-714.
180. Meier, R.; Ruderer, M. A.; Diethert, A.; Kaune, G.; Körstgens, V.; Roth, S. V.; Müller-Buschbaum, P. Influence of Film Thickness on the Phase Separation Mechanism in Ultrathin Conducting Polymer Blend Films. *The Journal of Physical Chemistry B* 2011, 115, 2899-2909.

181. Brand, V.; Bruner, C.; Dauskardt, R. H. Cohesion and device reliability in organic bulk heterojunction photovoltaic cells. *Solar Energy Materials and Solar Cells* 2012, 99, 182-189.
182. Sun, Z.; Xiao, K.; Keum, J. K.; Yu, X.; Hong, K.; Browning, J.; Ivanov, I. N.; Chen, J.; Alonzo, J.; Li, D.; Sumpter, B. G.; Payzant, E. A.; Rouleau, C. M.; Geohegan, D. B. PS-b-P3HT Copolymers as P3HT/PCBM Interfacial Compatibilizers for High Efficiency Photovoltaics. *Advanced Materials* 2011, 23, 5529-5535.
183. Jung, J. W.; Jo, J. W.; Jo, W. H. Enhanced Performance and Air Stability of Polymer Solar Cells by Formation of a Self-Assembled Buffer Layer from Fullerene-End-Capped Poly(ethylene glycol). *Advanced Materials* 2011, 23, 1782-1787.
184. Vitos, L.; Ruban, A. V.; Skriver, H. L.; Kollár, J. The surface energy of metals. *Surface Science* 1998, 411, 186-202.
185. Krevelen, D. W. V.; Nijenhuis, K. T. *Properties of Polymers: Their Correlation with Chemical Structure; their Numerical Estimation and Prediction from Additive Group Contributions*. Fourth Edition ed.; Elsevier Science: 2009; p 1032.
186. Petrosino, M.; Rubino, A. The effect of the PEDOT:PSS surface energy on the interface potential barrier. *Synthetic Metals* 2012, 161, 2714-2717.
187. Brédas, J.-L.; Norton, J. E.; Cornil, J.; Coropceanu, V. Molecular Understanding of Organic Solar Cells: The Challenges. *Accounts of Chemical Research* 2009, 42, 1691-1699.
188. Mauer, R.; Howard, I. A.; Laquai, F. Effect of Nongeminate Recombination on Fill Factor in Polythiophene/Methanofullerene Organic Solar Cells. *The Journal of Physical Chemistry Letters* 2010, 1, 3500-3505.
189. Tremolet de Villers, B.; Tassone, C. J.; Tolbert, S. H.; Schwartz, B. J. Improving the Reproducibility of P3HT:PCBM Solar Cells by Controlling the PCBM/Cathode Interface. *The Journal of Physical Chemistry C* 2009, 113, 18978-18982.
190. Wang, T.; Pearson, A. J.; Lidzey, D. G.; Jones, R. A. L. Evolution of Structure, Optoelectronic Properties, and Device Performance of Polythiophene:Fullerene Solar Cells During Thermal Annealing. *Advanced Functional Materials* 2011, 21, 1383-1390.
191. Moule, A. J.; Bonekamp, J. B.; Meerholz, K. The effect of active layer thickness and composition on the performance of bulk-heterojunction solar cells. *Journal of Applied Physics* 2006, 100, 094503-7.
192. Jin, H.; Tuomikoski, M.; Hiltunen, J.; Kopola, P.; Maaninen, A.; Pino, F. Polymer−Electrode Interfacial Effect on Photovoltaic Performances in Poly(3-hexylthiophene):Phenyl-C61-butyric Acid Methyl Ester Based Solar Cells. *The Journal of Physical Chemistry C* 2009, 113, 16807-16810.
193. van Bavel, S.; Sourty, E.; de With, G.; Frolic, K.; Loos, J. Relation between Photoactive Layer Thickness, 3D Morphology, and Device Performance in P3HT/PCBM Bulk-Heterojunction Solar Cells. *Macromolecules* 2009, 42, 7396-7403.
194. Sauve, G.; Javier, A. E.; Zhang, R.; Liu, J.; Sydlik, S. A.; Kowalewski, T.; McCullough, R. D. Well-defined, high molecular weight poly(3-alkylthiophene)s in thin-film transistors: side chain invariance in field-effect mobility. *Journal of Materials Chemistry* 2010, 20, 3195-3201.
195. Huang, W. Y.; Lee, C. C.; Wang, S. G.; Han, Y. K.; Chang, M. Y. Side Chain Effects of Poly(3-alkylthiophene) on the Morphology and Performance of Polymer Solar Cells. *Journal of The Electrochemical Society* 2010, 157, B1336-B1342.
196. Park, Y. D.; Kim, D. H.; Jang, Y.; Cho, J. H.; Hwang, M.; Lee, H. S.; Lim, J. A.; Cho, K. Effect of side chain length on molecular ordering and field-effect mobility in poly(3-alkylthiophene) transistors. *Organic Electronics* 2006, 7, 514-520.

197. Shaw, P. E.; Ruseckas, A.; Samuel, I. D. W. Exciton Diffusion Measurements in Poly(3-hexylthiophene). *Advanced Materials* 2008, 20, 3516-3520.
198. Ma, B.; Lauterwasser, F.; Deng, L.; Zonte, C. S.; Kim, B. J.; Fréchet, J. M. J.; Borek, C.; Thompson, M. E. New Thermally Cross-Linkable Polymer and Its Application as a Hole-Transporting Layer for Solution Processed Multilayer Organic Light Emitting Diodes. *Chemistry of Materials* 2007, 19, 4827-4832.
199. Dobish, J. N.; Hamilton, S. K.; Harth, E. Synthesis of low-temperature benzocyclobutene cross-linker and utilization. *Polymer Chemistry* 2012, 3, 857-860.
200. Bubb, W.; Sternhell, S. Proton NMR spectra of 1-substituted benzocyclobutenes (Bicyclo [4, 2, 0] octa-1, 3, 5-trienes). *Australian Journal of Chemistry* 1976, 29, 1685-1697.
201. Segura, J. L.; Martín, N. o-Quinodimethanes: Efficient Intermediates in Organic Synthesis. *Chemical Reviews* 1999, 99, 3199-3246.
202. Pugh, C.; Baker, J. S.; Storms, W. K. Synthesis of a Polymerizable Benzocyclobutene that Undergoes Ring-Opening Isomerization at Reduced Temperature. *Synlett* 2014, 25, 148-152.
203. Gügel, A.; Belik, P.; Walter, M.; Kraus, A.; Harth, E.; Wagner, M.; Spickermann, J.; Müllen, K. The repetitive Diels-Alder reaction: A new approach to [60]fullerene maindashchain polymers. *Tetrahedron* 1996, 52, 5007-5014.
204. Treat, N. D.; Mates, T. E.; Hawker, C. J.; Kramer, E. J.; Chabinyc, M. L. Temperature Dependence of the Diffusion Coefficient of PCBM in Poly(3-hexylthiophene). *Macromolecules* 2013, 46, 1002-1007.
205. Zhang, Y.; Yip, H.-L.; Acton, O.; Hau, S. K.; Huang, F.; Jen, A. K. Y. A Simple and Effective Way of Achieving Highly Efficient and Thermally Stable Bulk-Heterojunction Polymer Solar Cells Using Amorphous Fullerene Derivatives as Electron Acceptor. *Chemistry of Materials* 2009, 21, 2598-2600.
206. Camaioni, N.; Catellani, M.; Luzzati, S.; Migliori, A. Morphological characterization of poly(3-octylthiophene):plasticizer:C60 blends. *Thin Solid Films* 2002, 403–404, 489-494.
207. Marchiori, C. F. N.; Koehler, M. Density functional theory study of the dipole across the P3HT : PCBM complex: the role of polarization and charge transfer. *Journal of Physics D: Applied Physics* 2014, 47, 215104.
208. Hwang, D. K.; Dasari, R. R.; Fenoll, M.; Alain-Rizzo, V.; Dindar, A.; Shim, J. W.; Deb, N.; Fuentes-Hernandez, C.; Barlow, S.; Bucknall, D. G.; Audebert, P.; Marder, S. R.; Kippelen, B. Stable Solution-Processed Molecular n-Channel Organic Field-Effect Transistors. *Advanced Materials* 2012, 24, 4445-4450.
209. Rodrigues, A.; Nabankur, D.; Hilliou, L.; Viana, J.; Bucknall, D. G.; Bernardo, G. Low temperature solid state processing of pure P3HT fibers. *AIP Advances* 2013, 3, 052116.
210. Bernardo, G.; Nabankur, D.; Pereira, P.; Brandão, L.; Viana, J.; Bucknall, D. Solid-state low-temperature extrusion of P3HT ribbons. *Appl Phys A* 2014, 117, 2079-2086.
211. Kendall, R. A.; Aprà, E.; Bernholdt, D. E.; Bylaska, E. J.; Dupuis, M.; Fann, G. I.; Harrison, R. J.; Ju, J.; Nichols, J. A.; Nieplocha, J.; Straatsma, T. P.; Windus, T. L.; Wong, A. T. High performance computational chemistry: An overview of NWChem a distributed parallel application. *Computer Physics Communications* 2000, 128, 260-283.
212. Burns, L. A.; Mayagoitia, Á. V.-.; Sumpter, B. G.; Sherrill, C. D. Density-functional approaches to noncovalent interactions: A comparison of dispersion corrections (DFT-D), exchange-hole dipole moment (XDM) theory, and specialized functionals. *The Journal of Chemical Physics* 2011, 134, 084107.

213. Linton, D.; Driva, P.; Sumpter, B.; Ivanov, I.; Geohegan, D.; Feigerle, C.; Dadmun, M. D. The importance of chain connectivity in the formation of non-covalent interactions between polymers and single-walled carbon nanotubes and its impact on dispersion. *Soft Matter* 2010, 6, 2801-2814.
214. Bubb, W.; Sternhell, S. Proton N.M.R. spectra of 1-substituted benzocyclobutenes (Bicyclo[4,2,0]octa-1,3,5-trienes). *Australian Journal of Chemistry* 1976, 29, 1685-1697.

VITA

Nabankur Deb was born in Kolkata, India and raised in the city of New Delhi, India. He completed his schooling from the Mother's International School following which he enrolled in the Indian Institute of Technology Delhi, New Delhi to obtain his Bachelor of Technology degree in Textile Technology. There, he got to work under Dr. Ashwini Agarwal and Dr. Manjeet Jassal in the field of nano-finishing of textile materials under the SMITA fellowship program. This led to his interest in pursuing graduate studies in the field of materials science, for which he was accepted into the PhD Program of the erstwhile department of Polymer, textile and fiber engineering (now Materials science and engineering). There under the guidance of Dr. David Bucknall, he pursued his thesis research on the topic of morphological studies of bulk heterojunction based organic photovoltaics. He is planning to graduate in 2015 and looking to possibly conduct further research in related areas in the future.